

# Quality Assurance of the VELO Modules and Analysis of the $B_d \rightarrow K^* \mu^+ \mu^-$ Rare Decay on LHCb.

Franciole da Cunha Marinho



University  
*of*  
Glasgow

September 2008

CERN-THESIS-2008-107  
01/09/2008



A thesis submitted for the degree of Doctor of Philosophy  
at the University of Glasgow

# Quality Assurance of the VELO Modules and Analysis of the $B_d \rightarrow K^* \mu^+ \mu^-$ Rare Decay on LHCb.

## Abstract

The LHCb experiment is a high energy physics detector at the Large Hadron Collider. The experiment has been designed and built to search for new physics in the  $b$  hadron sector.

This thesis discusses a contribution to the detector construction and preparatory studies for a rare decay analysis.

### Quality assurance of the silicon modules of LHCb vertex detector

One of the critical components of the LHCb experiment is the silicon vertex locator (VELO), which is used to measure the decay distance of the  $b$ -hadrons and is a principal component of the tracking of the experiment. This thesis describes the quality assurance tests of the VELO silicon modules. A facility was designed to operate the VELO modules in vacuum and thermally stress the modules. To verify the suitability of the modules for the experiment a range of studies were performed including measurements of the silicon leakage current and the identification of bad channels through a noise analysis. A full set of 42 modules (and spares) suitable for use in the experiment were successfully tested.

### Analysis of the $B_d \rightarrow K^* \mu^+ \mu^-$ decay

The  $B_d \rightarrow K^* \mu^+ \mu^-$  decay is a flavour changing neutral current process which occurs only via loop diagrams. This is a rare process with a measured branching ratio of  $1.10^{+0.29}_{-0.26} \times 10^{-6}$ . The  $B_d \rightarrow K^* \mu^+ \mu^-$  rare decay is sensitive to new physics (NP) effects. Through the measurement of the so-called forward backward asymmetry distribution a clear signature of NP can be found in this channel.

The estimated number of signal events expected per year in LHCb ( $2\text{fb}^{-1}$ ) was estimated to be  $7.0 \pm 0.1 \times 10^3$ . The sensitivity to the zero point of the forward backward asymmetry was calculated as  $0.4 \text{ GeV}^2/c^4$ , assuming the estimated annual yield. Degradation of the sensitivity due to background events was estimated to be  $\sim 10 - 15\%$ . Potential systematic effects due to acceptance and background mismeasurement are also presented. The results on the forward backward asymmetry were obtained using a non-parametric unbinned method.

# Acknowledgements

A number of people contributed directly or indirectly to the work presented in this thesis, therefore influenced my life in the last three years. They contributed in a positive way and I here acknowledge their professionalism, help and friendship during this period.

- To Chris Parkes for the great support and supervision during these years. You always made an effort to know what I was working on and provided me with great ideas and suggestions. Thank you very much for reading all my work along these years and proof reading this thesis. I'm pretty sure it was a lot of hard work.
- To Paul Soler for all the advice and help throughout my PhD studies. You were one of those who made it possible for me to come to Glasgow. Thank you very much.
- To Andrew, Liam and Lisa for showing me the surroundings of the nice and interesting Glasgow.
- To Aldo Saavedra for all the lessons and fun. I reckon your support allowed me to develop many of the skills that I was looking forward to learn. I enjoyed each moment in the lab including those of high stress levels. Thanks for the "burn-in experience" and friendship. You're a good pal!
- To the chinese gang for all the fun in the flat, although sometimes I did not have a clue on what was going on. Special thanks to Wei and Bo with whom I made a great friendship.
- To Alison Bates for the friendship, partnership and patience during the burn-in operation and developing the data analysis at CERN. Thanks a lot.
- To the VELO team. Thanks guys for the support with the VELO DAQ and occasional hardware issues. Special thanks goes to Paula Collins and Themis Bowcock for the suggestions and fruitful discussions on the burn-in operation and analysis.
- To Sebastien Viret for the help with the toy MC production and for the rich range of subjects during lunch at CERN. That was really helpful.
- Thanks to Laurence, Barinjaka, Marco, Mark, Andrew, Jason, Lars and Bruno for the good time in Glasgow and/or at CERN.
- Special thanks to my friend Kazu. I will never forget the quick instructions on how to survive in Ferney.
- To Hans and Susan for saving me from boredom in Ferney-Voltaire many times. Whoever lived there knows what it means.

- To Bernardo, Alberto and Gabriel for the fun in Saint Genis. Next time I promise I will help with the Christmas tree. Perhaps in SP.
- To my friends Luis, Fernando, Johanna, Dima, Arthur and Taynara for all the support and friendship back in Glasgow.
- To Vava and Tomasz for all the coffee breaks and fun during the writing up period.
- To the examiners Craig Buttar, Roger Barlow and Tony Doyle for the fruitful discussion on this thesis results.

This work was supported by SUPA.



## **Agradecimentos**

- Aos meus queridos em São Paulo: Jane, Ary, Dona Angelina e Roberta. Obrigado pelo carinho e cuidado nas minhas visitas.
- Aos meus irmãos Max e Rita, por sempre me apoiarem e por compartilharem muita coisa boa comigo.
- A minha Laura, por todo o amor, carinho e compreensão durante esses três anos. Só você sabe o quanto foi difícil chegar aqui.
- Aos meus pais, pelo amor e dedicação ao longo de toda a minha vida. Sem vocês nada disso seria possível. Amo vocês.

# Preface

The studies presented in this thesis can be divided in two parts: Development and operation of a burn-in facility to perform long term evaluation of the LHCb VELO modules; and preparatory studies for the analysis of the  $B_d \rightarrow K^* \mu^+ \mu^-$  decay channel in LHCb.

The main studies performed in the first part of this thesis are:

- Design and development of the burn-in facility for long term testing of the LHCb VELO modules;
- Results from the characterisation of the VELO modules in this facility.

The main results from the  $B_d \rightarrow K^* \mu^+ \mu^-$  studies are:

- Estimation of the signal efficiency and expected event yield;
- Evaluation of the sensitivity to measure the forward backward asymmetry using an unbinned approach with simulated events;
- Evaluation of the potential distortions on the forward backward asymmetry from selection cuts and background events.

## Overview

This section briefly describes the contents and structure of this thesis.

Chapter 1 introduces the Standard Model. It emphasises the aspects of the Standard Model which are relevant to the LHCb physics programme. It first discusses the basic concepts and features of the Quantum Chromodynamics and Electroweak theory. Then it introduces the flavour changing neutral current mechanism and CP symmetry violation in the  $b$  hadron's system. It also discusses the rare  $b \rightarrow s$  transitions emphasising the  $B_d \rightarrow K^* \mu^+ \mu^-$  decay. A review of the recent experimental results on the  $B_d \rightarrow K^* \mu^+ \mu^-$  decays is also presented.

Chapter 2 provides a description of the LHCb detector focusing on the aspects relevant or required for the discussions presented in the following chapters. The LHCb detector has a total of six different sub-detectors and two global systems to select the interesting events, reconstruct vertices, reconstruct the particle tracks, and identify the particles. Particular emphasis is given to the VELO system since part of the work presented in this thesis is related to the long term testing of the silicon modules of the VELO.

Chapter 3 discusses the design and implementation of the Glasgow burn-in facility. The burn-in system was developed to perform long term tests of the LHCb VELO modules in an environment similar to the LHCb experiment. The aim of the burn-in system was to uncover any weaknesses introduced into the modules during manufacturing or in the components

themselves. The burn-in system had a set of subsystems to reproduce the LHCb environment. The main components of this setup were the cooling system, vacuum system, interlocks and DAQ. The design and performance of each of these components are discussed in chapter 3. The software used to monitor and control the burn-in system is also described.

Chapter 4 presents the results obtained by testing the LHCb VELO modules using the burn-in facility described in chapter 3. The LHCb VELO modules were received and visually inspected in the burn-in laboratory. The following measurements were performed during the long term operation of the modules: measurements of the silicon leakage current, identification of bad channels, measurement of noise, estimates of the signal to noise ratio and an attempt to correlate metrology parameters with leakage current behaviour. These measurements were performed several times during the burn-in procedure in order to characterise the performance of the modules and to verify the stability of the behaviour of the modules.

Chapter 5 discusses the analysis performed on simulated data for the measurement of the forward backward asymmetry (FBA) of the  $B_d \rightarrow K^* \mu^+ \mu^-$  decay. In this chapter an estimate of the efficiency and annual yield obtained using the LHCb software simulation is presented. The dependence of these quantities on the instantaneous luminosity is also discussed. A non-parametric unbinned method developed to evaluate the dimuon mass squared distribution and forward backward asymmetry is described. Results on the expected LHCb sensitivity to measure the zero point of the forward backward asymmetry are presented. Potential effects on these results due to acceptance selections and background contamination are also discussed.

Chapter 6 contains the conclusions. It briefly summarises and discusses the achievements presented in the previous chapters of this thesis. Prospects for the future operation of the burn-in system and development of the  $B_d \rightarrow K^* \mu^+ \mu^-$  analysis are also discussed.

All figures in this thesis were made by the author with exception of figures: 1.2, 1.3, 1.11, 1.12, 1.13, 1.14, 2.1, 2.2, 2.3, 2.4, 2.5, 2.6, 2.10, 2.11, 2.12, 2.13, 2.14, 2.15, 2.16, 2.17, 2.18, 2.19, 2.20, 2.21, 2.22, 2.23, 2.24, 2.25, 2.26, 6.1.

The origin of these figures is given in their corresponding captions.

# Contents

|          |  |           |
|----------|--|-----------|
| <b>1</b> | <b>Theory Review</b>   | <b>1</b>  |
| 1.1      | The Standard Model . . . . .   | 2         |
| 1.2      | The Electroweak Model . . . . .  | 4         |
| 1.2.1    | The Leptonic Sector . . . . .  | 4         |
| 1.2.2    | The Quark Sector . . . . .   | 7         |
| 1.2.3    | Discrete Symmetries . . . . .  | 10        |
| 1.2.3.1  | P Violation . . . . .  | 10        |
| 1.2.3.2  | CP Violation . . . . .   | 11        |
| 1.2.3.3  | T Violation . . . . .  | 11        |
| 1.2.3.4  | CPT Theorem . . . . .  | 11        |
| 1.2.4    | The CKM matrix and CP Violation . . . . .                                | 11        |
| 1.3      | Quantum Chromodynamics . . . . .   | 15        |
| 1.4      | Rare B Decays . . . . .  | 16        |
| 1.4.1    | Motivation . . . . .   | 17        |
| 1.4.2    | Exclusive and Inclusive Analyses of $b \rightarrow sll$ decays . . . . . | 18        |
| 1.4.3    | The OPE Formalism of Semileptonic $B$ Decays . . . . .                   | 19        |
| 1.4.3.1  | Short Distance Effects . . . . .   | 20        |
| 1.4.3.2  | Long Distance Effects . . . . .  | 21        |
| 1.5      | The $B_d \rightarrow K^* \mu^+ \mu^-$ Rare Decay . . . . .               | 25        |
| 1.5.1    | Search for New Physics . . . . .   | 26        |
| 1.5.2    | Observables in $B_d \rightarrow K^* \mu^+ \mu^-$ Analysis . . . . .      | 28        |
| 1.5.2.1  | Double Differential Branching Ratio . . . . .                            | 28        |
| 1.5.2.2  | Dimuon Distribution . . . . .  | 28        |
| 1.5.2.3  | Forward Backward Asymmetry . . . . .                                     | 29        |
| 1.5.2.4  | Wilson Coefficients . . . . .  | 30        |
| 1.5.3    | Recent Experimental Results . . . . .                                    | 32        |
| 1.6      | Conclusions . . . . .  | 34        |
| <b>2</b> | <b>The LHCb Experiment</b>   | <b>35</b> |
| 2.1      | The LHC Project . . . . .  | 35        |

|          |  |           |
|----------|--|-----------|
| 2.1.1    | The LHC Experiments . . . . .  | 37        |
| 2.2      | The LHCb Experiment . . . . .  | 38        |
| 2.2.1    | Vertex Locator . . . . .   | 39        |
| 2.2.1.1  | Overview . . . . .   | 40        |
| 2.2.1.2  | Requirements . . . . .   | 41        |
| 2.2.1.3  | Silicon Sensors . . . . .  | 43        |
| 2.2.1.4  | The VELO Modules . . . . .   | 47        |
| 2.2.1.5  | Vacuum System . . . . .  | 49        |
| 2.2.1.6  | Cooling System . . . . .   | 49        |
| 2.2.1.7  | Low Voltage & High Voltage Systems . . . . .                                   | 49        |
| 2.2.2    | Ring Imaging Cherenkov Detectors . . . . .                                     | 50        |
| 2.2.2.1  | RICH1 . . . . .  | 50        |
| 2.2.2.2  | RICH2 . . . . .  | 51        |
| 2.2.2.3  | The Hybrid Photon Detectors . . . . .  | 51        |
| 2.2.3    | Magnet . . . . .   | 52        |
| 2.2.4    | Tracking System . . . . .  | 54        |
| 2.2.4.1  | Tracker Turicensis . . . . .   | 54        |
| 2.2.4.2  | Tracking Stations . . . . .  | 55        |
| 2.2.5    | Calorimeters . . . . .   | 55        |
| 2.2.5.1  | SPD and PS . . . . .   | 56        |
| 2.2.5.2  | Electronic Calorimeter . . . . .   | 56        |
| 2.2.5.3  | Hadronic Calorimeter . . . . .   | 57        |
| 2.2.6    | Muon System . . . . .  | 58        |
| 2.2.6.1  | Gas Electron Multipliers . . . . .   | 59        |
| 2.2.6.2  | Multiple Wire Proportional Chambers . . . . .                                  | 60        |
| 2.2.7    | Trigger System . . . . .   | 60        |
| 2.2.7.1  | Trigger Requirements . . . . .   | 61        |
| 2.2.7.2  | The L0 trigger . . . . .   | 62        |
| 2.2.7.3  | The High Level Trigger . . . . .   | 63        |
| 2.2.8    | Online System . . . . .  | 64        |
| 2.2.8.1  | Data Acquisition . . . . .   | 64        |
| 2.2.8.2  | Timing and Fast Control . . . . .  | 65        |
| 2.2.8.3  | Experiment Control System . . . . .  | 65        |
| 2.3      | Conclusions . . . . .  | 66        |
| <b>3</b> | <b>A facility for long term evaluation of the LHCb Vertex Detector modules</b> | <b>67</b> |
| 3.1      | Overview . . . . .   | 68        |
| 3.2      | Reception and Visual Inspection . . . . .                                      | 69        |
| 3.2.1    | Module Handling . . . . .  | 70        |

|          |  |           |
|----------|--|-----------|
| 3.3      | Burn-in Setup . . . . .                                | 72        |
| 3.3.1    | Vacuum System . . . . .                                | 73        |
| 3.3.2    | Cooling System . . . . .                               | 75        |
| 3.3.3    | Voltage Supplies and Monitoring Devices . . . . .      | 80        |
| 3.3.4    | Control and Monitoring Software System . . . . .       | 80        |
| 3.3.5    | Interlock System . . . . .                             | 83        |
| 3.3.5.1  | Temperature Monitoring . . . . .                       | 84        |
| 3.3.5.2  | Pressure Monitoring . . . . .                          | 84        |
| 3.3.5.3  | Interlock Unit Devices . . . . .                       | 85        |
| 3.3.6    | Control and Data Acquisition . . . . .                 | 88        |
| 3.3.6.1  | Data Readout . . . . .                                 | 91        |
| 3.3.6.2  | Software . . . . .                                     | 93        |
| 3.4      | Conclusion . . . . .                                   | 94        |
| 3.5      | Future Improvements . . . . .                          | 95        |
| <b>4</b> | <b>VELO Modules Characterisation</b>                   | <b>97</b> |
| 4.1      | Burn-in Procedures . . . . .                           | 98        |
| 4.1.1    | Reception . . . . .                                    | 98        |
| 4.1.2    | Visual Inspection . . . . .                            | 99        |
| 4.1.3    | Electrical and Thermal Tests . . . . .                 | 100       |
| 4.1.3.1  | Electrical Data and Leakage Current Measurements . . . | 101       |
| 4.1.3.2  | Burn-in Data Processing . . . . .                      | 102       |
| 4.1.4    | Burn-in Time Scale . . . . .                           | 103       |
| 4.2      | Visual Inspections . . . . .                           | 104       |
| 4.2.1    | Kapton Damage . . . . .                                | 104       |
| 4.2.2    | HV Return Lines . . . . .                              | 105       |
| 4.2.3    | Silicon Surfaces . . . . .                             | 105       |
| 4.2.4    | Pitch Adaptors . . . . .                               | 105       |
| 4.2.5    | Bonding . . . . .                                      | 105       |
| 4.3      | Thermal Images . . . . .                               | 106       |
| 4.4      | Signal to Noise Ratio . . . . .                        | 107       |
| 4.4.1    | High Voltage Scans . . . . .                           | 112       |
| 4.5      | Leakage Current . . . . .                              | 113       |
| 4.5.1    | Temperature Corrections . . . . .                      | 114       |
| 4.5.2    | Current Degradation . . . . .                          | 116       |
| 4.6      | Metrology . . . . .                                    | 121       |
| 4.7      | Pulse Shape Studies . . . . .                          | 128       |
| 4.8      | Bad Channels Analysis . . . . .                        | 136       |
| 4.8.1    | Liverpool Classifications . . . . .                    | 137       |

|          |   |            |
|----------|---|------------|
| 4.8.2    | Burn-in Electrical Tests . . . . .  | 139        |
| 4.9      | Conclusions . . . . .   | 145        |
| <b>5</b> | <b>Analysis of the <math>B_d \rightarrow K^* \mu^+ \mu^-</math> decay</b> | <b>147</b> |
| 5.1      | The LHCb Simulation . . . . .   | 148        |
| 5.2      | Trigger . . . . .   | 149        |
| 5.3      | Particle Identification . . . . .   | 150        |
| 5.4      | Event Selection and Efficiency . . . . .                                  | 150        |
| 5.4.1    | Selection Efficiency and Yield . . . . .                                  | 154        |
| 5.5      | Luminosity Dependence of Selection Efficiency . . . . .                   | 155        |
| 5.6      | Resolution . . . . .  | 158        |
| 5.6.1    | Momentum Resolution . . . . .   | 158        |
| 5.6.2    | Dimuon Mass Resolution . . . . .  | 159        |
| 5.6.3    | $\theta_1$ Resolution . . . . .   | 159        |
| 5.6.4    | $\theta_1$ Uncertainty . . . . .  | 164        |
| 5.7      | The Forward Backward Asymmetry in LHCb . . . . .                          | 164        |
| 5.7.1    | Simplified Monte Carlo . . . . .  | 165        |
| 5.7.2    | Unbinned Method . . . . .   | 165        |
| 5.7.2.1  | Kernel Density Estimator . . . . .  | 166        |
| 5.7.2.2  | Method Convergence . . . . .  | 168        |
| 5.7.2.3  | $h$ Estimate . . . . .  | 169        |
| 5.7.2.4  | FBA Estimate . . . . .  | 171        |
| 5.8      | Acceptance Effects . . . . .  | 173        |
| 5.8.1    | Selection Cuts . . . . .  | 174        |
| 5.8.2    | Muon Identification . . . . .   | 176        |
| 5.8.3    | L0 Trigger . . . . .  | 176        |
| 5.8.4    | Proposal for Single Muon Calibration . . . . .                            | 177        |
| 5.9      | Background Effects . . . . .  | 180        |
| 5.9.1    | Background Subtraction . . . . .  | 182        |
| 5.9.2    | Symmetric Background . . . . .  | 183        |
| 5.9.3    | Asymmetric Background . . . . .   | 185        |
| 5.10     | Conclusions . . . . .   | 189        |
| 5.11     | LHCb Outlook . . . . .  | 190        |
| <b>6</b> | <b>Conclusions &amp; Outlook</b>  | <b>192</b> |
| 6.1      | Summary . . . . .   | 192        |
| 6.2      | Outlook . . . . .   | 195        |
| 6.2.1    | VELO Commissioning and Physics Analysis Preparation . . . . .             | 195        |
| 6.2.2    | First Phase of Operation . . . . .  | 196        |
| 6.2.3    | LHCb Replacement and Upgrade . . . . .                                    | 197        |

# List of Tables

|     |   |     |
|-----|---|-----|
| 1.1 | FCNC decay channels to be studied at LHCb . . . . .                         | 18  |
| 1.2 | Theoretical results for the Wilson Coefficients . . . . .                   | 20  |
| 1.3 | Different values of Wilson coefficients used for FBA calculations . . . . . | 30  |
| 1.4 | Luminosity, signal yields and estimated branching ratios. . . . .           | 32  |
| 1.5 | Wilson coefficients measured by the Belle collaboration. . . . .            | 33  |
| 2.1 | LHC accelerator parameters. . . . .   | 36  |
| 2.2 | Characteristics of the radiators used in the RICH system. . . . .           | 52  |
| 2.3 | Parameters of the calorimeters. . . . .                                     | 58  |
| 3.1 | The specification parameters for the chiller. . . . .                       | 77  |
| 3.2 | Specification parameters of the silica coolant liquid. . . . .              | 77  |
| 3.3 | List of devices, drivers and protocols in the monitoring software. . . . .  | 83  |
| 3.4 | BROICE relay parameters list. . . . .                                       | 88  |
| 4.1 | Module metrology parameters . . . . .                                       | 122 |
| 4.2 | Sensor metrology parameters . . . . .                                       | 125 |
| 4.3 | The standard values and the tested set of Beetle chip parameters. . . . .   | 131 |
| 4.4 | Test pulse fit parameters and fractional uncertainties. . . . .             | 138 |
| 4.5 | Rejection criteria for bad strips on the R and $\Phi$ -sensors. . . . .     | 143 |
| 4.6 | Number of bad channels found in the burn-in. . . . .                        | 143 |
| 5.1 | $B_d \rightarrow K^* \mu^+ \mu^-$ selection criteria. . . . .               | 152 |
| 5.2 | Parameters used in the annual yield evaluation. . . . .                     | 154 |
| 5.3 | Background events types. . . . .  | 181 |



# List of Figures

|      |   |    |
|------|---|----|
| 1.1  | $K_L \rightarrow \mu^+ \mu^-$ box diagrams. . . . .   | 9  |
| 1.2  | Unitary triangles representing CP violation in the $b$ sector. . . . .                            | 12 |
| 1.3  | Constraints on the CKM triangle . . . . .   | 14 |
| 1.4  | Feynman diagrams corresponding to $Q_1$ and $Q_2$ operators . . . . .                             | 22 |
| 1.5  | Feynman diagrams corresponding to $Q_3, Q_4, Q_5, Q_6$ operators . . . . .                        | 23 |
| 1.6  | Feynman diagrams corresponding to the $Q_7, Q_8, Q_9, Q_{10}$ operators. . . . .                  | 23 |
| 1.7  | Feynman diagrams corresponding to $Q_{9V}, Q_{10A}$ and $Q_{11}$ semileptonic operators . . . . . | 24 |
| 1.8  | Feynman diagrams corresponding to $Q_{7\gamma}$ and $Q_{8g}$ operators . . . . .                  | 24 |
| 1.9  | Box and Penguin diagrams for $B_d \rightarrow K^* \mu^+ \mu^-$ . . . . .                          | 25 |
| 1.10 | Examples of SUSY Feynman diagrams for $B_d \rightarrow K^* \mu^+ \mu^-$ . . . . .                 | 27 |
| 1.11 | Dimuon mass squared distribution. . . . .   | 29 |
| 1.12 | Forward backward asymmetry distribution. . . . .  | 31 |
| 1.13 | B mass distribution fit for Belle and CDF. . . . .  | 33 |
| 1.14 | Forward Backward Asymmetry distribution at Belle and Babar . . . . .                              | 34 |
| 2.1  | LHC accelerator and its experiments . . . . .   | 37 |
| 2.2  | LHCb detector. . . . .  | 38 |
| 2.3  | $b\bar{b}$ quark pair production in a proton-proton collision. . . . .                            | 39 |
| 2.4  | VELO detector cutaway. . . . .  | 41 |
| 2.5  | Expanded view of the VELO. . . . .  | 41 |
| 2.6  | VELO station front view . . . . .   | 42 |
| 2.7  | p-on-n microstrip detector diagram. . . . .   | 45 |
| 2.8  | Comparison between p-on-n and n-on-n microstrip detectors. . . . .                                | 46 |
| 2.9  | $\Phi$ glued LHCb VELO module. . . . .  | 48 |
| 2.10 | Schematic diagram of the RICH1. . . . .   | 51 |
| 2.11 | Schematic diagram of the RICH2. . . . .   | 52 |
| 2.12 | Hybrid Photon Detector . . . . .  | 53 |
| 2.13 | LHCb Magnet. . . . .  | 53 |
| 2.14 | Tracker Turicensis layers. . . . .  | 54 |
| 2.15 | Outer tracker module diagram. . . . .   | 55 |

|      |   |     |
|------|---|-----|
| 2.16 | Tracking station diagram. . . . .   | 56  |
| 2.17 | Lateral segmentation scheme of the SPD, PS, ECAL and HCAL. . . . .  | 57  |
| 2.18 | ECAL modules and complete ECAL detector. . . . .  | 57  |
| 2.19 | M1 transverse segmentation layout. . . . .  | 59  |
| 2.20 | Triple GEM detector. . . . .  | 59  |
| 2.21 | MWPC layer. . . . .   | 60  |
| 2.22 | Muon chamber pictures. . . . .  | 61  |
| 2.23 | Diagram of the trigger system. . . . .  | 62  |
| 2.24 | HLT alleys structure. . . . .   | 63  |
| 2.25 | Online architecture. . . . .  | 64  |
| 2.26 | ECS architecture. . . . .   | 65  |
|      |   |     |
| 3.1  | Burn-in setup diagram. . . . .  | 69  |
| 3.2  | Burn-in area layout. . . . .  | 70  |
| 3.3  | Visual inspection setup. . . . .  | 71  |
| 3.4  | LHCb VELO Module mounted in the mechanical frame. . . . .   | 72  |
| 3.5  | Picture of the stainless steel vacuum tank. . . . .   | 74  |
| 3.6  | Photographs of the vacuum pump system. . . . .  | 74  |
| 3.7  | Photographs of the cooling system. . . . .  | 76  |
| 3.8  | Flexible hoses inside vacuum chamber. . . . .   | 78  |
| 3.9  | Cooling block attached to the module frame. . . . .   | 81  |
| 3.10 | Interlock system diagram. . . . .   | 86  |
| 3.11 | Temperature interlock schematic. . . . .  | 87  |
| 3.12 | Pressure interlock schematic. . . . .   | 89  |
| 3.13 | Diagram of the DAQ system in the burn-in. . . . .   | 90  |
| 3.14 | DAQ setup in the burn-in system. . . . .  | 91  |
|      |   |     |
| 4.1  | Burn-in time scale. . . . .   | 104 |
| 4.2  | Thermal images of a VELO module. . . . .  | 107 |
| 4.3  | Beetle chips temperature obtained with thermal camera. . . . .  | 107 |
| 4.4  | Distribution of the Beetle chips temperature. . . . .   | 108 |
| 4.5  | Raw noise and common mode corrected noise plots for a VELO module. . . . .                                  | 109 |
| 4.6  | Signal to noise distribution per link of a VELO module. . . . .   | 110 |
| 4.7  | Estimated signal to noise ratio from the Beetle chips header as a function of<br>the module number. . . . . | 111 |
| 4.8  | Signal to noise ratio as a function of the bias voltage applied. . . . .                                    | 112 |
| 4.9  | Depletion voltage for the R and $\Phi$ -sensors as a function of the module number. . . . .                 | 113 |
| 4.10 | Temperature dependence of the leakage current of module 64. . . . .   | 115 |
| 4.11 | Temperature dependence of the leakage current of module 26. . . . .   | 115 |
| 4.12 | Temperature dependence of the leakage current of the $\Phi$ -sensor of module 26. . . . .                   | 116 |

|      |   |     |
|------|---|-----|
| 4.13 | Leakage current as a function of VELO module number for the R-sensors. .  | 118 |
| 4.14 | Leakage current as a function of VELO module number for the $\Phi$ -sensors. .  | 119 |
| 4.15 | Temperature dependence of the leakage current measured on the $\Phi$ -sensor of module 64. . . . .  | 121 |
| 4.16 | Leakage current measured on $\Phi$ -sensor of module 75 for 3 different temperatures. . . . .   | 122 |
| 4.17 | Leakage current and percentage change in the leakage current versus the various metrology parameters. . . . .                                 | 123 |
| 4.18 | Leakage current and percentage change in the leakage current versus the various metrology parameters. . . . .                                 | 124 |
| 4.19 | Plot of sensor metrology variables. . . . .   | 126 |
| 4.20 | Residuals of position measured on the sensors as a function of the module number. . . . .   | 127 |
| 4.21 | Sagitta of the sensor as function of the module number. . . . .   | 127 |
| 4.22 | Silicon sensor's wafer masks. . . . .   | 128 |
| 4.23 | Leakage current and percentage change in the leakage current as a function of the module number. . . . .                                      | 129 |
| 4.24 | Leakage current of the $\Phi$ -sensors as a function of the date of the first leakage current measurement at University of Liverpool. . . . . | 130 |
| 4.25 | Test pulse of a Beetle chip installed in a VELO module. . . . .   | 130 |
| 4.26 | Signal measured in response to test pulses in the Beetle chips using the default Beetle parameters. . . . .                                   | 133 |
| 4.27 | Pulse shapes for different values of $V_{fp}$ . . . . .   | 134 |
| 4.28 | Pulse shapes for different values of $V_{fs}$ . . . . .   | 135 |
| 4.29 | Pulse shapes for different values of $I_{pre}$ . . . . .  | 136 |
| 4.30 | Pulse shapes for different values of $I_{sha}$ . . . . .  | 137 |
| 4.31 | Plots of the measured signal from test pulses as a function of $V_{fp}$ on both the $R$ and the $\Phi$ -sides of the module. . . . .          | 138 |
| 4.32 | Plots of the measured signal from test pulses as a function of $V_{fs}$ on both the $R$ and the $\Phi$ -sides of the module. . . . .          | 139 |
| 4.33 | Plots of the measured signal from test pulses as a function of $I_{pre}$ on both the $R$ and the $\Phi$ -sides of the module. . . . .         | 140 |
| 4.34 | Plots of the measured signal from test pulses as a function of $I_{sha}$ on both the $R$ and the $\Phi$ -sides of the module. . . . .         | 141 |
| 4.35 | Test pulse peak and spillover as a function of the strips length on R-sensors. .  | 141 |
| 4.36 | Ratio between the pulse amplitude as a function of the time and the pulse peak expressed as a percentage. . . . .                             | 142 |
| 4.37 | Number of bad channels as a function of the module number for both the $R$ and the $\Phi$ -sensors. . . . .                                   | 144 |

|      |   |     |
|------|---|-----|
| 5.1  | Diagram of a $B_d \rightarrow K^* \mu^+ \mu^-$ event. . . . .   | 151 |
| 5.2  | Reconstructed mass distribution of the $K^*$ and $B_d$ mesons. . . . .  | 153 |
| 5.3  | Number of selected events and efficiency. . . . .   | 156 |
| 5.4  | Efficiency and annual yields as a function of the luminosity. . . . .   | 157 |
| 5.5  | L0 trigger yield as a function of the luminosity. . . . .   | 158 |
| 5.6  | Momentum resolution of the muon and pion from the $B_d \rightarrow K^* \mu^+ \mu^-$ decay. . . . .                                  | 160 |
| 5.7  | Momentum resolution of the kaon and reconstructed $B_d$ . . . . .   | 161 |
| 5.8  | Momentum uncertainties of the muons . . . . .   | 162 |
| 5.9  | Dimuon mass squared resolution distribution. . . . .  | 162 |
| 5.10 | Dimuon mass resolution broadening. . . . .  | 163 |
| 5.11 | $\theta_l$ angle resolution. . . . .  | 163 |
| 5.12 | $\theta_l$ angle uncertainty estimate. . . . .  | 164 |
| 5.13 | Comparison between kernel density estimator and histogram. . . . .  | 167 |
| 5.14 | Dimuon mass squared distribution. . . . .   | 169 |
| 5.15 | FBA distribution. . . . .   | 170 |
| 5.16 | $h$ optimisation. . . . .   | 171 |
| 5.17 | $h$ as a function of $M_{\mu^+ \mu^-}^2$ . . . . .  | 172 |
| 5.18 | FBA obtained with $2 \text{ fb}^{-1}$ data sets. . . . .  | 173 |
| 5.19 | FBA zero point distribution. . . . .  | 174 |
| 5.20 | FBA distribution after selection cuts. . . . .  | 175 |
| 5.21 | Ratio between the dimuon mass squared distribution before and after the muon $P_T$ cut at selection level. . . . .                  | 176 |
| 5.22 | Ratio between the dimuon mass squared distribution before and after the muon $P$ cut or $IP/\sigma$ cut at selection level. . . . . | 177 |
| 5.23 | Correlation between the muon $P_T$ and $DLL$ variables. . . . .   | 178 |
| 5.24 | Ratio between the dimuon mass squared distribution before and after the muon $P_T$ and $DLL$ cuts. . . . .                          | 178 |
| 5.25 | Ratio between the dimuon mass squared distribution before and after the muon $P_T$ cuts on the L0 trigger. . . . .                  | 179 |
| 5.26 | Comparison of muon $P_T$ distributions before and after particle identification. . . . .  | 180 |
| 5.27 | Background $M_{\mu^+ \mu^-}^2$ distributions. . . . .   | 182 |
| 5.28 | Effect on FBA due to symmetric background. . . . .  | 184 |
| 5.29 | Zero point sensitivity degradation due to symmetric background. . . . .   | 185 |
| 5.30 | FBA zero point value and sensitivity as a function of the fraction of background subtracted. . . . .                                | 186 |
| 5.31 | FBA zero point value and sensitivity as a function of the $\sqrt{B}/S$ ratio. . . . .   | 186 |
| 5.32 | Diagram illustrating the asymmetric background mismeasurement algorithm. . . . .  | 187 |
| 5.33 | FBA zero point shift as a function of the fraction of asymmetric background mismeasured. . . . .                                    | 188 |

---

|      |  |     |
|------|--|-----|
| 5.34 | FBA comparison with and without asymmetric background subtraction. . . | 188 |
| 6.1  | Tracks induced by the LHC beam reconstructed by the VELO detector. . . | 196 |

# Chapter 1

## Theory Review

In this chapter a theoretical review of the aspects of the Standard Model (SM) which are significant to the physics programme of the LHCb experiment is presented. In general it emphasises the physics involved in the  $b \rightarrow s$  quark transitions and in particular the rare decay  $B_d \rightarrow K^* \mu^+ \mu^-$ . It also contains a discussion on New Physics (NP) models, sensitivity of the  $b \rightarrow s$  transitions to these models and the current experimental constraints given by recent measurements.

The SM is an effective theory which describes very well the interactions of the elementary particles. It has been extensively and successfully tested in the past decades but important questions in high energy physics need to be answered. Why are there three generations of quarks and leptons? What are the additional sources of Charge-Parity symmetry (CP) violation required to explain the matter-antimatter asymmetry in the universe? Is the SM a low-energy description of a more fundamental theory given that it does not explain the existence of dark matter in the universe? To answer those questions precise measurements of the CP violation and rare decays in the b-hadron sector together with the search for the Higgs boson, will be the key to confirm the SM and to pave the way to a new physics era at the LHC.

CP violation is one of the ingredients necessary to explain the imbalance between matter and antimatter in the universe [1]. It was found that CP symmetry violation occurs in Electroweak interactions. CP violation is introduced through the CKM matrix in the SM [2, 3]. The elements of the CKM matrix describe the strength of the flavour changing weak transitions of the quarks. The LHCb experiment was developed to perform measurements of the b-hadrons decays in order to significantly improve the current knowledge of the CKM matrix and to search for possible NP signatures.

The  $b \rightarrow s$  transitions are important processes to study because they allow us to make precise tests of the SM and to search for NP effects. In the SM these decays are tree suppressed and only occur via loop diagrams. Additional diagrams can exist with new particles occurring in these loops. These NP diagrams can potentially contribute to physical quantities such as differential branching ratios as much as the SM ones. Hence one can expect signifi-

cant changes to occur with respect to the SM theoretical expectations. These transitions are not experimentally well constrained yet [4, 5].

The  $B_d \rightarrow K^* \mu^+ \mu^-$  decay is a flavour changing neutral current process (FCNC) which occurs only via loop diagrams. Its branching ratio is estimated to be  $1.19 \pm 0.39 \times 10^{-6}$  with next-to-next leading order calculations in the SM [6]. Other quantities can be measured in this decay such as the dimuon mass distribution, forward-backward asymmetry and Wilson coefficients. These measurements will be explained in section 1.5.2. This decay has been measured and its experimental branching ratio was found to be  $1.10^{+0.29}_{-0.26} \times 10^{-6}$  [7]. Initial angular analyses were also performed and the results are in agreement with the SM. However, the uncertainties are still large due to the statistics available and more precise measurements are necessary. In many extensions of the SM, the differential branching ratio and the angular distributions can drastically change [8, 9]. Measurements of the  $B_d \rightarrow K^* \mu^+ \mu^-$  decay at LHCb will allow searches for NP to be performed.

This chapter is organised as the following: Section 1.1 describes the fundamentals of the SM. Section 1.2 describes the Electroweak Model in more detail discussing FCNC processes and CP violation. Section 1.3 describes the main features of Quantum Chromodynamics. Section 1.4 presents the theoretical aspects of the Rare  $B$  decays. Section 1.5 reviews the phenomenology of the  $B_d \rightarrow K^* \mu^+ \mu^-$  decay and summarises the experimental status of this channel.

## 1.1 The Standard Model

The SM describes with great precision the phenomena related to the elementary particles and their fundamental interactions. This model has undergone precise tests with uncertainties ranging from  $\sim 10^{-5}\%$  to  $\sim 2\%$  [7, 10, 11]\*.

The elementary particles are understood to be the smallest constituents of matter, and are known to not have any structure down to the limits of  $\leq 10^{-19}\text{m}$  [12]†. In the SM the elementary particles are classified within two basic sets: fermions and bosons.

The particles in the first set have half-integer spin and obey the Pauli exclusion principle. They are classified into two subsets, the leptons and quarks. The leptons are: the electron  $e$ , the muon  $\mu$ , and the tau  $\tau$ , with electric charge  $Q = -1$  and their corresponding neutrinos are  $\nu_e$ ,  $\nu_\mu$  and  $\nu_\tau$  with electric charge  $Q = 0$ . The six flavors of quarks are:  $u$ ,  $d$ ,  $c$ ,  $s$ ,  $t$  and  $b$  with electric charges  $Q_{u,c,t} = \frac{2}{3}$  and  $Q_{d,s,b} = -\frac{1}{3}$  (in units of the electron charge with the  $e = -1$ ).

The quarks possess another quantum number called *colour*. This quantum number is represented as  $q_i$ ,  $i = 1, 2, 3$ . Quarks are not observed isolated in nature but confined as

---

\*The minimum of this range corresponds to  $(g - 2)/2$  measurements and the maximum corresponds to the measurements of the strong coupling constant  $\alpha_s(M_Z)$ .

†Limit refers to the quarks radius.

constituents of the observed particles. The arrangement of the quark colours that compose a given particle is such that the resulting colour is always null either by combining the three colours together or by a combination of a colour with its anticolor, therefore this quantity is never observed. The particles composed of quarks are called hadrons and are classified according to their number of valence quarks. Those particles composed by three valence quarks are called baryons and those composed by two valence quarks are called mesons. Protons and neutrons are examples of baryons composed respectively of the valence quarks  $uud$  and  $ddu$ . Pions and Kaons are typical examples of mesons with respectively  $u\bar{d}$  and  $u\bar{s}$  valence quarks.

The second set of elementary particles is composed of the particles that mediate the interactions, these are called bosons. These particles have integer spin and obey Bose-Einstein statistics. For each known type of interaction there is a set of interaction carriers. In the electromagnetic forces the mediator is the photon  $\gamma$ , to mediate the strong interactions there are 8 gluons ( $A^\alpha$ ;  $\alpha=1,\dots,8$ ) and in the weak interactions the carriers are the  $W^\pm$  and  $Z$ . There is an additional scalar boson (spin 0), called the Higgs boson, which is discussed in section 1.2.1.

The SM contains the Quantum Chromodynamics (QCD) and the Electroweak (EW) Standard Model. QCD is the part of the theory which describes the strong interactions, whereas the EW model describes the weak and electromagnetic interactions [13, 14]. All these interactions are envisaged in terms of a gauge theory. The SM is a quantum field theory based on the gauge symmetry of the group  $SU(3)_c \times SU(2)_L \times U(1)_Y$ , which contains the symmetry group of the strong interactions  $SU(3)_c$  and the symmetry group of the EW interactions  $SU(2)_L \times U(1)_Y$ . The weak interaction and the electromagnetic interaction are said to be unified in the sense that the symmetry group of the electromagnetic interactions  $U(1)_{em}$  enters in the SM as a subgroup of the  $SU(2)_L \times U(1)_Y$  group.

In the LHC experiments, both the QCD and EW theory play important roles. The relevance of QCD rises from the fact that the  $b$  quarks will be produced by means of the strong interactions in the proton-proton collisions, then these quarks will hadronise forming mesons and baryons by combinations of the  $b$  quarks with the other type of quarks.

The EW model is of paramount importance because it describes the decays of the  $b$  mesons which are the subject of analysis of the LHCb experiment. Although QCD effects have always to be taken into account, it is in the EW Model where the LHC physics programme primarily resides and where NP is most likely to be found. The less well explored sectors of the Higgs mechanism, CP violation and FCNC processes are all in the EW Model.

The work of this thesis is strongly related to the EW Model therefore this is the focus of this theory chapter. A short section describing the main features of QCD is provided to illustrate its importance for the calculations of hadronic uncertainties in the FCNC processes.



## 1.2 The Electroweak Model

The S.L. Glashow, S. Weinberg and A. Salam model describes both the electromagnetic interactions and the weak interactions as an unified theory [15, 16, 17]. The weak interactions violate parity: they are not symmetric under transformations between fermions of left and right-handed helicity. The Dirac field representing a fermion can be expressed as a combination of a left-handed component,  $\Psi_L$ , and a right-handed component,  $\Psi_R$ .

$$\Psi = a\Psi_L + b\Psi_R, \quad (1.1)$$

where

$$\begin{aligned} \Psi_L &= P_L \Psi, \\ P_L &= \frac{1 - \gamma_5}{2}, \end{aligned} \quad (1.2)$$

$$\begin{aligned} \Psi_R &= P_R \Psi, \\ P_R &= \frac{1 + \gamma_5}{2}, \end{aligned} \quad (1.3)$$

and  $P_L$  and  $P_R$  are helicity projectors. The  $\gamma_5$  matrix is given by

$$\gamma_5 = i\gamma_0\gamma_1\gamma_2\gamma_3,$$

where the  $\gamma_\mu$  are the Dirac matrices [18].

The kinetic terms of the Lagrangian and the interaction terms of the Dirac fields can also be written as a sum of two terms each involving states of unique helicity.

### 1.2.1 The Leptonic Sector

The electrons, muons and taus are organised in weak isospin doublets since the weak interactions occur between fermions of left-handed helicity.

$$L_l = \begin{pmatrix} \nu \\ l \end{pmatrix}_L, \quad (1.4)$$

where the states  $\nu$  and  $l$  left are:

$$\begin{aligned} \nu_L &= \frac{1}{2}(1 - \gamma_5)\nu, \\ l_L &= \frac{1}{2}(1 - \gamma_5)l. \end{aligned} \quad (1.5)$$

It is important to notice that when the SM was envisaged there was no evidence for the mass of neutrinos. However, in the last decade experimental evidence has shown that neutrinos have mass and there is oscillation between the families [19]. In this chapter the

SM is discussed in the traditional picture where neutrinos are massless. This implies the neutrinos right helicity state are written as

$$\nu_R = \frac{1}{2}(1 + \gamma_5)\nu = 0. \quad (1.6)$$

Hence there are only 3 leptons of right helicity which are singlets of weak isospin denoted as  $R_l$ . The coupling of the weak isospin gauge group  $SU(2)_L$  is denoted  $g$ .

The abelian group  $U(1)_Y$  is used to incorporate the electromagnetic interactions to the theory. The hypercharge  $Y$  is related to the electric charge  $Q$  and the third weak isospin component  $I_3$  as follows:

$$Q = I_3 + \frac{1}{2}Y, \quad (1.7)$$

and by construction

$$[I_3, Y] = 0. \quad (1.8)$$

The coupling of the  $U(1)_Y$  group is defined as  $g'/2$  where the factor  $1/2$  is chosen for simplicity: this way the transformations given by the  $I$  and  $Y$  generators are represented by the  $SU(2)_L \times U(1)_Y$  gauge group<sup>‡</sup>. The gauge bosons introduced are denoted as:

$$b_\mu^1, b_\mu^2, b_\mu^3 \quad \text{for } SU(2)_L, \quad (1.9)$$

$$\mathcal{A}_\mu \quad \text{for } U(1)_Y. \quad (1.10)$$

The Lagrangian is written as

$$\mathcal{L} = \mathcal{L}_{leptons} + \mathcal{L}_{gauge}. \quad (1.11)$$

The  $\mathcal{L}_{leptons}$  term is given by

$$\mathcal{L}_{leptons} = \bar{R}_l i\gamma^\mu \left( \partial_\mu + \frac{ig'}{2} \mathcal{A}_\mu Y \right) R_l + \bar{L}_l i\gamma^\mu \left( \partial_\mu + \frac{ig'}{2} \mathcal{A}_\mu Y + \frac{ig}{2} \boldsymbol{\tau} \cdot \mathbf{b}_\mu \right) L_l, \quad (1.12)$$

where  $\tau$  are the generators of the  $SU(2)_L$  group.

The  $\mathcal{L}_{gauge}$  term is given by

$$\mathcal{L}_{gauge} = -\frac{1}{4} F_{\mu\nu}^l F^{l\mu\nu} - \frac{1}{4} f_{\mu\nu} f^{\mu\nu}, \quad (1.13)$$

where

$$F_{\mu\nu}^l = \partial_\nu b_\mu^l - \partial_\mu b_\nu^l + g\epsilon_{jkl} b_\mu^j b_\nu^k, \quad f_{\mu\nu} = \partial_\nu \mathcal{A}_\mu - \partial_\mu \mathcal{A}_\nu. \quad (1.14)$$

This Lagrangian is not yet satisfactory to describe the electroweak interactions as it does not contain any mass term. In nature only one of the interaction bosons is found to be massless. Similarly, the muons, electrons and taus are also massless. In order to acquire mass a symmetry breaking mechanism is employed keeping the group's gauge invariance. One doublet of scalar complex fields is introduced. This doublet transforms as a  $SU(2)_L$

---

<sup>‡</sup>The notation used in this chapter is mostly the same as in [13].

doublet with hypercharge  $Y = 1$  [20]. It is the so called Higgs field. Three terms are added to the original Lagrangian: the interaction term of the Higgs field with the fermions

$$\mathcal{L}_{Yukawa} = -G_l[(\bar{L}_l\phi)R_l + \bar{R}_l(\phi^\dagger L_l)], \quad (1.15)$$

where  $G_l$  are the Fermi constants and  $\phi$  is the Higgs field;  
the interaction term between the Higgs field and bosons

$$\mathcal{D}\phi^\dagger\mathcal{D}\phi = \left| \left( \partial_\mu + \frac{ig'}{2}\mathcal{A}_\mu Y + \frac{ig}{2}\boldsymbol{\tau} \cdot \mathbf{b}_\mu \right) \right|^2; \quad (1.16)$$

and a self-interaction term of  $\phi$ ,

$$\mathcal{L}_H = -V(\phi^\dagger\phi) = -\mu^2(\phi^\dagger\phi) - |\lambda|(\phi^\dagger\phi)^2, \quad (1.17)$$

where the part with the  $\mu^2$  parameter is a mass-like term and the part with the  $|\lambda|$  term was designed to be negative. If  $\mu^2 < 0$  the Higgs potential has a minimum when

$$\phi^\dagger\phi = -\frac{\mu^2}{2|\lambda|}. \quad (1.18)$$

The vacuum expectation value for  $\phi$  is chosen as

$$\langle \phi \rangle_0 = \begin{pmatrix} 0 \\ v/\sqrt{2} \end{pmatrix}. \quad (1.19)$$

The generators  $\boldsymbol{\tau}$  and  $Y$  do not satisfy the necessary condition to keep the vacuum invariant because

$$Y_i \langle \phi \rangle_0 \neq 0, \quad \tau_i \langle \phi \rangle_0 \neq 0. \quad (1.20)$$

This implies that all gauge bosons acquire mass. However the linear combination corresponding to the electric charge  $Q$  does not break this invariance: the photon does not acquire mass. By expanding the  $\phi$  field at the minimum of the potential  $V$  the masses of the fermions and bosons are obtained directly from the Lagrangian.

The mass of the fermions is obtained from the Yukawa interaction term,

$$m_l = \frac{G_l v}{\sqrt{2}}. \quad (1.21)$$

The charged fields are defined directly from the scalar term of the Lagrangian,

$$W_\mu^\pm = \frac{b_\mu^1 \mp ib_\mu^2}{\sqrt{2}}, \quad (1.22)$$

with masses given by

$$M_{W_\mu^\pm} = \frac{gv}{2}. \quad (1.23)$$

The following orthogonal combinations correspond to the neutral fields

$$Z_\mu = \frac{-g' \mathcal{A}_\mu + g b_u^3}{\sqrt{g^2 + g'^2}}, \quad A_\mu = \frac{g \mathcal{A}_\mu + g' b_u^3}{\sqrt{g^2 + g'^2}}, \quad (1.24)$$

where  $A_\mu$  is the photon (massless) and the  $Z_\mu$  boson has mass given by  $M_{Z_0} = M_W \sqrt{1 + g'^2/g^2}$ .

To parametrise the mixing between the neutral gauge fields it is convenient to introduce an angle  $\theta_W$  (Weinberg angle) so that

$$g'/g = \tan \theta_W. \quad (1.25)$$

That allows the Lagrangian to be re-written in terms of the fields  $W^\pm$ ,  $Z$  and  $A$ . Through this procedure it is possible to express the coupling constants in terms of the elementary electric charge and the  $\theta_W$  angle.

$$g = e/\sin \theta_W, \quad g' = e/\cos \theta_W. \quad (1.26)$$

The electromagnetic and weak currents are also explicitly identified in the Lagrangian.

### 1.2.2 The Quark Sector

The quarks are introduced into the EW Model in a similar manner as to the leptons. Quarks are incorporated in the GWS model by the addition of quark left-handed doublets and right-handed singlets. The first family consists of one  $u$  quark and one  $d$  quark. The doublet is then defined as

$$q_L = \begin{pmatrix} u \\ d \end{pmatrix}_L, \quad (1.27)$$

and the singlets are  $u_R$  and  $d_R$ .

Note that for each family three copies of these quarks are introduced but for simplicity the colour index is suppressed. The quarks also acquire mass by means of the symmetry breaking mechanism via their coupling with the scalar fields. However the conjugated complex of the  $\phi$  field must also appear in the Lagrangian in order to give mass to the upper components. That term does not appear in the leptonic sector due to the fact that the EW Standard Model was conceived assuming the neutrinos are massless. It is given by

$$\bar{\phi} = i\sigma_2 \phi^*, \quad (1.28)$$

which is also a field of the  $SU(2)_L$  group with hypercharge  $Y_{\bar{\phi}} = -1$ .

In the quark sector the Yukawa interaction term generates mass to both quarks of each generation.

The second quark family consists of a  $c$  quark and a  $s$  quark. Including pure copies of quark doublets and singlets in the theory brings some extra complications because there are mixing terms between the quarks in the interaction Lagrangian. This problem is resolved by

making the convenient choice that the mass matrix is diagonal and the interaction states are mixtures of the mass states. This way the doublets are written as

$$\begin{pmatrix} u \\ \tilde{d} \end{pmatrix}, \quad \begin{pmatrix} c \\ \tilde{s} \end{pmatrix}, \quad (1.29)$$

where

$$\begin{pmatrix} \tilde{d} \\ \tilde{s} \end{pmatrix} = \begin{pmatrix} d \cos\theta_c + s \sin\theta_c \\ -d \sin\theta_c + s \cos\theta_c \end{pmatrix}. \quad (1.30)$$

The  $\theta_c$  angle is known as the Cabibbo angle [2]. It indicates that two types of eigenstates must be defined. The quarks  $d$  and  $s$  are mass eigenstates while  $\tilde{d}$  and  $\tilde{s}$  are interaction eigenstates given by orthogonal combinations of the mass eigenstates. It is important to emphasise that these mixtures mean that transitions between the different families are allowed. In fact the  $\theta_c$  angle was introduced to allow those transitions. The  $c$  quark was introduced by Glashow, Iliopoulos and Maiani[21] in such a manner that the interaction terms of the  $Z$  boson are not changed by a unitary transformation because

$$\bar{\tilde{d}}\gamma_5\tilde{d} + \bar{\tilde{s}}\gamma_5\tilde{s} = \bar{d}\gamma_5d + \bar{s}\gamma_5s, \quad (1.31)$$

where the cross terms cancel. This way flavour changes in neutral interactions can happen only in higher order processes where there is no  $Z$  boson exchanges but  $W$  boson pairs. This mechanism is called the GIM mechanism. One of the motivations for the introduction of the GIM mechanism was to explain the branching ratio of the  $K_L \rightarrow \mu^+\mu^-$ . The box diagrams for this decay are illustrated in figure 1.1. The first theoretical value obtained without taking into account the  $c$  quark was inconsistent with the observed rate. These diagrams differ in the exchange of  $u$  and  $c$  quarks. Because the  $c$  quark mass is much bigger than the  $u$  quark the contribution of the two diagrams do not cancel out but yield a small branching ratio value. The same procedure is used to include the third family of quarks. The doublets are then written as

$$\begin{pmatrix} u \\ \tilde{d} \end{pmatrix}, \quad \begin{pmatrix} c \\ \tilde{s} \end{pmatrix}, \quad \begin{pmatrix} t \\ \tilde{b} \end{pmatrix}, \quad (1.32)$$

where  $\tilde{d}, \tilde{s}$  and  $\tilde{b}$  are given by

$$\begin{pmatrix} \tilde{d} \\ \tilde{s} \\ \tilde{b} \end{pmatrix} = V_{CKM} \begin{pmatrix} d \\ s \\ b \end{pmatrix}, \quad \text{with} \quad V_{CKM} = \begin{pmatrix} V_{ud} & V_{us} & V_{ub} \\ V_{cd} & V_{cs} & V_{cb} \\ V_{td} & V_{ts} & V_{tb} \end{pmatrix}. \quad (1.33)$$

$V_{CKM}$  is the Cabibbo-Kobayashi-Maskawa unitary matrix and its  $V_{q_i q_j}$  elements are transition amplitudes between the different quark flavours [3].

A complex  $n \times n$  unitary matrix has a total  $2n^2$  parameters. Given that  $n^2$  unitarity constraints are established the number of free parameters is then  $n^2$ . In a theory such as the

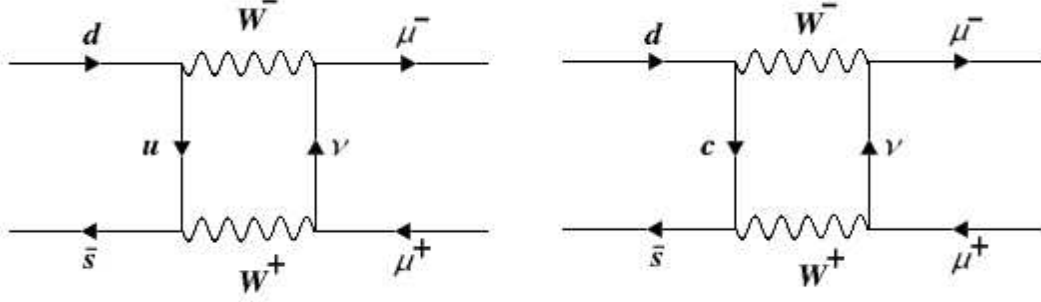


Figure 1.1:  $K_L \rightarrow \mu^+ \mu^-$  box diagrams. By including the  $c$  quark it was possible to calculate the correct branching ratio of this decay.

SM with  $2n$  quarks the total number free parameters is given by

$$n^2 - (2n - 1). \quad (1.34)$$

A global phase is omitted keeping the  $V_{CKM}$  matrix invariance. The remaining real parameters can be described as rotation angles and the number of phases is given by

$$n^2 - (2n - 1) - \frac{1}{2}n(n - 1) = \frac{1}{2}(n - 1)(n - 2). \quad (1.35)$$

For example, the two doublets model has one real parameter, the Cabibbo angle. With the inclusion of the third family the SM obtained three real parameters and a phase giving a total of 4 parameters. The three real parameters are associated to the three mixing angles between the flavours. These angles can be written as generalised Cabibbo angles. In the Kobayashi-Maskawa conjecture, the complex phase is the source of CP violation in the SM.

The following list contains the experimental values for the CKM matrix elements. A brief description of the measurements is also given [7].

- $|V_{ud}| = 0.97418 \pm 0.00027$  (Nuclear  $\beta$  decay measurements where the error is dominated by theoretical uncertainties);
- $|V_{us}| = 0.2255 \pm 0.0019$  (High statistic measurements from semileptonic kaon decays. Measurements were also carried out with leptonic kaon decays, hyperon decays and  $\tau$  decays whose results have similar uncertainties);
- $|V_{cd}| = 0.230 \pm 0.011$  (Measurements based on charm production from neutrino and anti-neutrino nucleus interactions. Measurements with semileptonic charm decays were also performed but the error is subject to theoretical uncertainties. The error with this method is a factor of  $\sim 2$  bigger than the previous measurements);

- $|V_{cs}| = 0.957 \pm 0.017 \pm 0.093$  (Combined results from  $D$  and  $D_s$  semileptonic decays and  $W$  decays. The  $D$  and  $D_s$  decays provide the far more precise result on this measurement);
- $|V_{cb}| = 0.0416 \pm 0.0006$  (Combined results from  $B$  to charm semileptonic decays. The methods used employ both inclusive and exclusive measurements);
- $|V_{ub}| = 0.00431 \pm 0.00030$  (Measurements of semileptonic decays of  $b \rightarrow ul^- \bar{\nu}_l$  type);
- $|V_{td}| = 0.0081 \pm 0.0006$  and  $|V_{ts}| = 0.0387 \pm 0.0023$  (Obtained from  $B - \bar{B}$  oscillations or K and B rare decays);
- $|V_{tb}| > 0.74$  at 95% CL (Measurements from top decays using branching ratio fractions, providing direct access to  $|V_{tb}|^2$ ).

### 1.2.3 Discrete Symmetries

Symmetries are an important concept in high energy physics. They help to understand the laws of nature in different ways. They are used to identify conservation laws and to understand how particles interact. For example, space-time symmetries lead to energy-momenta conservation and gauge symmetries are used to describe the EW model and QCD in the SM. Symmetries can be classified as continuum symmetries and discrete symmetries.

In this section three discrete symmetries of the space-time are reviewed: charge conjugation (C), parity (P) and time-reversal (T). The combinations of the symmetries given by CP and CPT are also discussed.

- Charge conjugation: This operation takes a particle into its antiparticle by inverting the sign of the internal quantum numbers (Electric charge, lepton number, baryon number and strangeness).
- Parity: This transformation inverts the sign of the coordinate system (left-handed system  $\leftrightarrow$  right-handed system).
- Time-reversal: As the name suggests this transformation makes  $t \rightarrow -t$  reversing particle's momenta and angular momenta.

#### 1.2.3.1 P Violation

For a long period it was believed that parity symmetry should be preserved by all interactions. However, in 1957 C. S. Wu observed the  $\beta$  decay  $^{60}\text{Co} \rightarrow ^{60}\text{Ni} + e^- + \nu_e$  with an asymmetric number of electrons emitted in the directions parallel and anti-parallel to the applied magnetic field [22]. This result was a clear signature of parity violation by weak interactions contradicting the expected symmetric distribution in the direction of the polarisation of the atoms according to the parity conservation hypothesis.

### 1.2.3.2 CP Violation

In the same year as P violation was observed the combination of the C and P symmetries was proposed as the correct symmetry between matter and antimatter [23]. The CP operation transforms a left-handed particle into right-handed antiparticle. However CP symmetry is also violated by weak interactions. Its violation was first observed in neutral Kaon decays by Cronin and Fitch in 1964 [24]. CP violation has also been observed in the b-meson sector [25, 26].

CP violation is introduced in the SM by the complex phase in the CKM matrix because its sign inverts under CP transformation. Section 1.2.4 details this phenomenon in the  $b$  sector.

### 1.2.3.3 T Violation

Measurements of T violation are very difficult since weak reactions which proceed in both directions at reasonable rate are suppressed due to phase space. CPLEAR has observed this effect by measuring the oscillation probability of  $K^0$  to  $\bar{K}^0$  and vice-versa [27]. T and CP violation tests are equivalent.

### 1.2.3.4 CPT Theorem

This theorem states that any relativistic quantum field theory preserves CPT if Lorentz invariance and locality are kept. Therefore CPT conservation is a valid assumption. The equality of masses and lifetimes of particles and corresponding antiparticles provide the best experimental evidence for the validity of the CPT theorem. The mass difference between  $K^0$  and  $\bar{K}^0$  provides the most precise measurement of CPT conservation ( $M_{\bar{K}^0} - M_{K^0}/M_{K^0} \leq 10^{-18}$ ) [7].

## 1.2.4 The CKM matrix and CP Violation

As mentioned in section 1.2.3, CP symmetry violation is explained by making the CKM matrix elements complex numbers. It is convenient to use the CKM matrix unitarity to describe CP violation in the SM. These constraints are written in the following way:

$$\sum_k^3 V_{ik} V_{kj}^* = \delta_{ij}. \quad (1.36)$$

The relevant relations for CP violation studies are

$$\sum_k^3 V_{kj} V_{ki}^* = 0. \quad (1.37)$$

With these relations geometrical parameters can be associated to physical processes. The relations that are significant for physics involving the  $b$  quark are



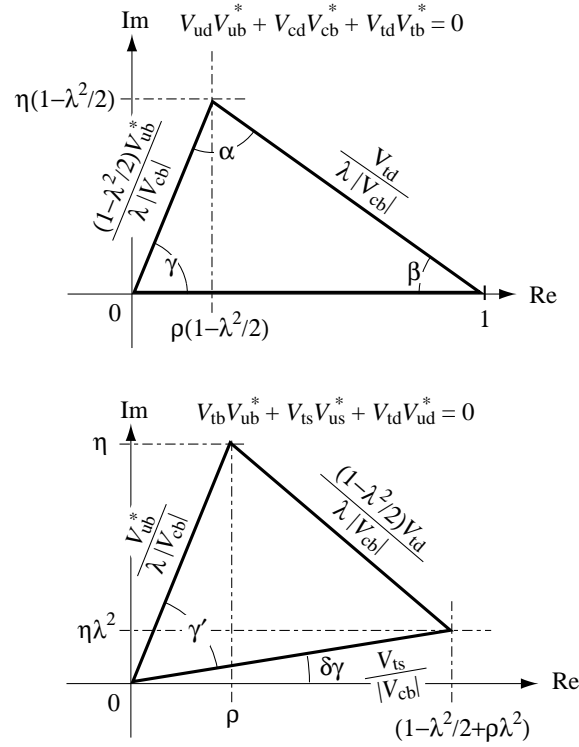


Figure 1.2: Unitary triangles representing CP violation in the  $b$  sector. Figure reproduced from [28].

$$\begin{aligned} V_{ud}V_{ub}^* + V_{cd}V_{cb}^* + V_{td}V_{tb}^* &= 0, \\ V_{td}V_{ud}^* + V_{ts}V_{us}^* + V_{tb}V_{ub}^* &= 0. \end{aligned} \quad (1.38)$$

By using these relations it is possible to construct two unitary triangles as an Argand diagram. The triangles illustrated in figure 1.2 represent the complex part of the CKM matrix. The area of the triangle represents the amount of CP violation.

Another convenient way of representing the  $V_{CKM}$  matrix is by means of the Wolfenstein parametrisation [29]. This representation uses three parameters. Two real numbers and a complex parameter. The two real parameters are  $A \sim 1.0$  and  $\lambda = \sin\theta_C$  and the complex number is usually written as  $\rho + i\eta$ . In terms of these parameters the CKM matrix is written in the following way

$$V_{CKM} = V_{CKM}^{(3)} + \delta V_{CKM} + \mathcal{O}(\lambda^6), \quad (1.39)$$

where  $V_{CKM}^{(3)}$  is the matrix expansion up to the third order in the  $\lambda$  parameter and  $\delta V_{CKM}$  is the matrix correction up to the fifth order in  $\lambda$ .

$$V_{CKM}^{(3)} = \begin{pmatrix} 1 - \lambda^2/2 & \lambda & A\lambda^3(\rho - i\eta) \\ -\lambda & 1 - \lambda^2/2 & A\lambda^2 \\ A\lambda^3(1 - \rho - i\eta) & -A\lambda^2 & 1 \end{pmatrix}, \quad (1.40)$$

$$\delta V_{CKM} = \begin{pmatrix} 0 & 0 & 0 \\ -iA^2\lambda^5\eta & 0 & 0 \\ A\lambda^5(\rho + i\eta)/2 & A\lambda^4(1/2 - \rho) - iA\lambda^4\eta & 0 \end{pmatrix}. \quad (1.41)$$

The angles of the triangle are written in terms of the length of its sides by using trigonometric relations and the CKM matrix unitarity. The angles  $\alpha$ ,  $\beta$  and  $\gamma$  are defined as

$$\begin{aligned} \alpha &= \arg \left( -\frac{V_{tb}^* V_{td}}{V_{ub}^* V_{ud}} \right), \\ \beta &= \arg \left( -\frac{V_{cb}^* V_{cd}}{V_{tb}^* V_{td}} \right), \\ \gamma &= \arg \left( -\frac{V_{ub}^* V_{ud}}{V_{cb}^* V_{cd}} \right). \end{aligned}$$

All the sides of these two triangles have lengths of the order of  $\mathcal{O}(\lambda^3)$  which means the internal angles  $\alpha$ ,  $\beta$  and  $\gamma$  have similar values.

The  $\alpha$  angle between  $V_{tb}^* V_{td}$  and  $V_{ub}^* V_{ud}$  is obtained via time-dependent measurements of CP asymmetry in  $b \rightarrow u\bar{u}d$  transitions. Measurements have been performed with the  $B \rightarrow \pi\pi$ ,  $B \rightarrow \rho\rho$  and  $B \rightarrow \rho\pi$  decay modes. The current combined result for this angle is  $\alpha = (99_{-8}^{+13})^\circ$  [30].

It is possible to extract the  $\beta$  angle via charmonium modes ( $b \rightarrow c\bar{c}s$ ) and penguin dominated modes ( $b \rightarrow q\bar{q}s$ ). The penguin decays are dominated by single phase terms, with any new physics CP violating phases introduced only in higher order terms, and therefore expected to be negligible. The current world average for the angle  $\beta$  is  $\sin(2\beta) = 0.687 \pm 0.032$  [31], and is dominated by measurements in  $B \rightarrow J/\Psi K$  modes.

The  $\gamma$  angle can be measured in tree level  $B$  decays. It implies that direct measurements of this angle are unlikely to be affected by new physics. The current range for the value of the angle is  $40^\circ < \gamma < 110^\circ$  with 95% confidence level [30].

A global fit can be performed by using all the independent measurements of the CKM matrix elements and requiring unitarity in order to determine the CKM matrix with better precision. Other CP violation measurements are also used in this fit to obtain the parameters of the Wolfenstein parametrisation. The most important measurements in the combined fit are: the mass difference  $\Delta m_d$  and  $\Delta m_s$  between the  $B_d$ - $\bar{B}_d$  and  $B_s$ - $\bar{B}_s$  mesons (respectively) obtained from oscillation measurements;  $\sin(2\beta)$ ; and the direct CP violation parameter  $|\epsilon_k|$  measured from the neutral kaon system. The current results from the CKM fitter collaboration for the coordinates of the apex of the unitary triangle in the Argand diagram are illustrated in figure 1.3 [32]:

The Wolfenstein parameters values from the fit are:

$$\begin{aligned} A &= 0.818_{-0.017}^{+0.007}, & \lambda &= 0.2272 \pm 0.0010, \\ \bar{\rho} &= 0.141_{-0.017}^{+0.029}, & \bar{\eta} &= 0.343_{-0.016}^{+0.016}, \end{aligned} \quad (1.42)$$

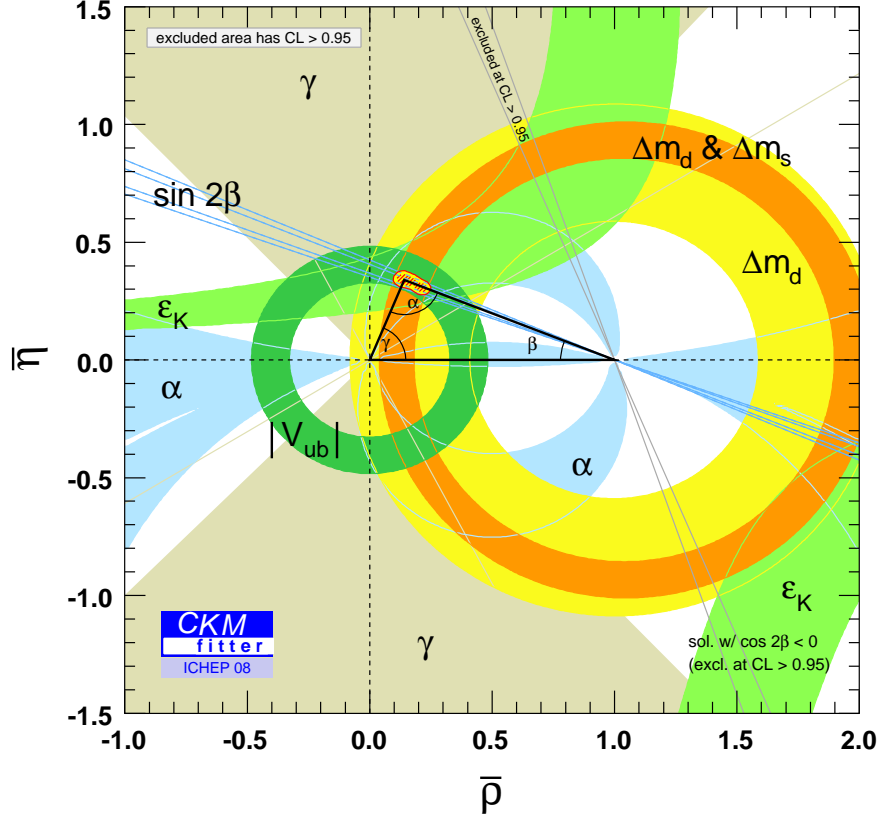


Figure 1.3: Constraints for the possible values for the apex coordinates of the CKM unitary triangle. The different regions of constraint with corresponding measurement indicated are also shown. All constraint bounds shown on the figure are at 95% confidence level. Figure reproduced from [32].

where  $\bar{\rho} = \rho(1 - \lambda^2/2)$  and  $\bar{\eta} = \eta(1 - \lambda^2/2)$ .

The fitted values for the absolute values of the CKM matrix elements are

$$V_{CKM} = \begin{pmatrix} 0.97383^{+0.00024}_{-0.00023} & 0.2272^{+0.0010}_{-0.0010} & 3.96^{+0.09}_{-0.09} \times 10^{-3} \\ 0.2271^{+0.0010}_{-0.0010} & 0.97296^{+0.00024}_{-0.00024} & 42.21^{+0.10}_{-0.80} \times 10^{-3} \\ 8.14^{+0.32}_{-0.64} \times 10^{-3} & 41.61^{+0.12}_{-0.78} \times 10^{-3} & 0.999100^{+0.000034}_{-0.000004} \end{pmatrix}. \quad (1.43)$$

Figure 1.3 shows the CKM triangle and its different regions of constraint with corresponding measurement indicated. All constraint bounds shown on the figure are at 95% confidence level.

### 1.3 Quantum Chromodynamics

This section introduces the basic concepts of QCD required for the discussions in this chapter, and in particular for the arguments of section 1.4.3. It briefly describes the main features of the theory which are *confinement* and *asymptotic freedom*.

QCD theory is based in the gauge symmetry of the strong interactions, which means local transformations of this group keep the Lagrangian invariant[33]. The symmetry group generated by these transformations is the  $SU(3)_C$  non-Abelian Lie group, where  $C$  refers to the colours and 3 is the number of possible quarks eigenstates. According to the gauge principle, to promote a global symmetry of the  $SU(3)_C$  to a local symmetry one has to introduce  $3^2 - 1 = 8$  gauge bosons in order to transform the free particle theory into an interaction theory. These bosons are called gluons. The number of gauge bosons is equal to the number of generators in the group.

The construction of the QCD Lagrangian is made by applying the gauge principle to the structure of the  $SU(3)$  non-Abelian group. The global symmetry of  $SU(3)$  of the strong interaction Lagrangian is then promoted to a local symmetry by changing the ordinary space-time derivative by its covariant derivative. In the QCD case this is

$$D_\mu q = \left( \partial_\mu - ig_s \left( \frac{\lambda_\alpha}{2} \right) A_\mu^\alpha \right) q, \quad (1.44)$$

where

$$q = \begin{pmatrix} q_1 \\ q_2 \\ q_3 \end{pmatrix},$$

$$\begin{aligned} q_i &= \text{quark fields; } (i = 1, 2, 3), \\ g_s &= \text{strong coupling constant,} \\ \frac{\lambda_\alpha}{2} &= SU(3)_C \text{ generators,} \\ A_\mu^\alpha &= \text{gluon fields; } (\alpha = 1, \dots, 8). \end{aligned}$$

The Lagrangian is then written in terms of the quarks and their covariant derivatives, and contains also the kinetic term of the gluon fields.

$$\mathcal{L}_{\text{QCD}} = \sum_q \bar{q}(x)(i\not{D} - m_q)q(x) - \frac{1}{4}G_{\mu\nu}^\alpha G_{\alpha}^{\mu\nu}, \quad (1.45)$$

where  $G_{\mu\nu}^\alpha$  is QCD strength tensor given by

$$G_{\mu\nu}^\alpha = \partial_\mu A_\nu^\alpha(x) - \partial_\nu A_\mu^\alpha(x) + g_s f^{\alpha\beta\gamma} A_{\mu\beta} A_{\nu\gamma}, \quad (1.46)$$

containing a bilinear term in the gluon fields, and where  $f^{\alpha\beta\gamma}$  are the structure constants.

The coupling of the strong interactions is usually written as

$$\alpha_s = \frac{g_s^2}{4\pi}. \quad (1.47)$$

Given the observed nature of strong interactions at low energies it could be expected that the  $\alpha_s$  coupling would have a large value. In this case the use of the Feynman rules would be impossible since they rely on a perturbation theory approach. However in non-abelian gauge theories the coupling decreases as the energy increases and this problem is naturally solved at high energies. This is called the asymptotic freedom principle. The dependence of the effective coupling with the energy scale is given by the equation:

$$\frac{\partial \alpha_s(Q^2)}{\partial \ln(Q^2)} = \beta(\alpha_s(Q^2)), \quad (1.48)$$

where  $Q$  is the momenta scale and  $\beta$  is expanded as

$$\beta(\alpha) = -\beta_0 \alpha^2 + \mathcal{O}(\alpha^3) + \dots \quad (1.49)$$

The equation 1.48 is the renormalisation group equation for the coupling constant  $\alpha_s(Q^2)$ .

Corrections of higher order correspond to including loop diagrams in the calculation. This self-interaction of the gluons gives rise to many higher order diagrams. This complicated gluon exchange system is responsible for keeping quarks and gluons confined in hadrons. The more one tries to separate the quarks the more the effective coupling becomes stronger requiring more and more energy to increase the distance between quarks. Hence two QCD calculation regimes are identified:

- Perturbative: Characterises short distance processes and energies above the QCD scale;
- Non-perturbative: Characterises long distance processes and low energy scales.

QCD plays a major role in LHC physics when it is necessary to describe the production mechanisms and the decays of the hadrons. Even though the LHCb programme focuses primarily on processes that occur via weak interactions, one needs to consider the strong forces between the hadron's components. In the case of rare FCNC decays the hadronic uncertainties involved can be significant.

## 1.4 Rare B Decays

In this section an overview of the phenomenology of the rare semileptonic  $B$  decays is provided. A general approach to describe the theory of the  $b \rightarrow s$  transitions is given. This description applies to the  $B_d \rightarrow K^* \mu^+ \mu^-$  decay, discussed in this thesis, and also to other channels of the  $b \rightarrow s$  type.

This section discuss different aspects of the  $b \rightarrow s$  transitions. First it discusses the type of physics effects that can be observed with these transitions. A list of channels which will be studied in LHCb is presented. It also discuss the advantages of *exclusive* and *inclusive* measurements. An inclusive analysis consists roughly in performing measurements with the multiple channels which have the same Feynman diagrams in the quark transition level (for example:  $b \rightarrow sll$ ). It potentially allows a more accurate understanding of the decay because the theoretical uncertainties due to hadronic effects are reduced. Exclusive analyses tend to be theoretically more challenging because the hadronic uncertainties involved are in general difficult to calculate. However there are few cases where this is not true: the exclusive channels  $B_d \rightarrow K^* \mu^+ \mu^-$  and  $B_s \rightarrow \mu^+ \mu^-$  are examples which are well described by theory and can provide clean measurements.

The formalism used to predict the weak decays of the B mesons is briefly described. This approach allows the analysis of the  $b \rightarrow s$  decays by factorising the EW and perturbative QCD from the non-perturbative QCD. In this method testing the SM or searching for NP becomes a matter of checking whether or not the perturbative and non-perturbative parts of the theory agree with the SM predictions.

More details on the analysis of the  $B_d \rightarrow K^* \mu^+ \mu^-$  decay is given. It is discussed how NP effects can be identified within the theoretical framework and which variables should be used to identify those effects. An update on the current experimental status of the  $B_d \rightarrow K^* \mu^+ \mu^-$  measurements is also presented.

### 1.4.1 Motivation

In the SM FCNC occur only via penguin and box diagrams. Since they are forbidden in tree decays it is possible that NP effects can contribute as much as the SM to the decay amplitudes. A whole family of decay channels which occur in transitions like  $b \rightarrow sll$ ,  $b \rightarrow s\gamma$  and  $B \rightarrow ll'$  provide excellent observables for NP searches. According to different SM extensions observables related to those channels could change considerably with respect to the SM predictions. It is part of the LHCb physics programme to reveal and quantify such differences by making precise measurements of these decays.

The flavour changing processes are usually classified according to the number of quark transitions in the event. FCNC  $\Delta F = 2$  for example were extensively observed in  $K - \bar{K}$  and  $B - \bar{B}$  systems, in particular with  $\Delta m_d$  and  $\Delta m_s$  measurements from  $B - \bar{B}$  [7, 34]. However precise measurements of  $\Delta F = 1$  have not been made with FCNC  $b \rightarrow s$  transitions. These transitions only became accessible with the B factories [4, 5].

Table 1.1 lists a set of channels which are members of this family of decays and will be studied in LHCb.

To measure all these processes is an important task because they are in some manner complementary and can be used to constrain the space of parameters of the many existing

Table 1.1: FCNC rare decay channels to be studied at LHCb. Some of the semileptonic decays are listed on the first row, radiative decays are listed on the second row and leptonic decays on the third row.

| Transition              | Exclusive Channels   | Measurement                                |
|-------------------------|--|--|
| $b \rightarrow sll$     | $B_d \rightarrow K^* \mu^+ \mu^-$ , $B_d \rightarrow K^* e^+ e^-$ ,<br>$B^+ \rightarrow K^+ \mu^+ \mu^-$ , $B^+ \rightarrow K^+ e^+ e^-$ ,<br>$B_s \rightarrow \phi \mu^+ \mu^-$                                     | Branching ratios,<br>angular distributions |
| $b \rightarrow s\gamma$ | $B \rightarrow K^* \gamma$ , $B_s \rightarrow \phi \gamma$ ,<br>$\Lambda_b \rightarrow \Lambda \gamma$ , $\Lambda_b \rightarrow \Lambda^* \gamma$ ,<br>$B \rightarrow \rho^0 \gamma$ , $B \rightarrow \omega \gamma$ | CP Asymmetry,<br>$\gamma$ polarisation     |
| $B \rightarrow ll'$     | $B_s \rightarrow \mu^+ \mu^-$ , $B_d \rightarrow \mu^+ \mu^-$ ,<br>$B \rightarrow \mu e$   | Branching ratios,<br>LF violation          |

SM extensions. This will be discussed in more detail in sections 1.5.1 and 1.5.2.

It is also important to measure different channels because they can provide extra information to be used within other analyses. For example the  $B \rightarrow K^* \gamma$  decay can be used to fix the hadronic uncertainties on the  $B_d \rightarrow K^* \mu^+ \mu^-$  channel as discussed in section 1.5.2.

#### 1.4.2 Exclusive and Inclusive Analyses of $b \rightarrow sll$ decays

The exclusive and inclusive measurements of the rare semileptonic  $B$  decays are complementary to each other. Theoretical uncertainties are more controlled in inclusive decays and they can usually provide a complete picture of the decays. However they are experimentally more difficult. On the other hand, exclusive searches are interesting because usually they can be used to test the theory and the experimental uncertainties tend to be less significant.

In inclusive analyses it is a challenge to define the number of different channels that are sufficient to claim an inclusive measurement. It is also necessary to take into account that the experimental detection efficiencies will depend on the event multiplicity. Hence the experimental uncertainties will tend to be significantly higher and more difficult to calculate than with exclusive decays. It is not proven whether it will be possible to make inclusive measurements in LHCb: it is well known inclusive measurements in hadronic machines are very difficult. However, LHCb has features such as very good mass resolution, good proper time resolution and particle identification which may allow the control of the problems arising from multiplicities, background rejection and efficiency [35].

Studying exclusive decays in LHCb is very attractive, for those channels where the theoretical quantities are well estimated. This is the case in  $B_d \rightarrow K^* \mu^+ \mu^-$  where its branching ratio and angular distributions are theoretically well determined. This process can be measured with high statistics in LHCb, and will be discussed in detail in chapter 5.

In section 1.4.3 a qualitative discussion on the sources of theoretical uncertainties on  $b \rightarrow sll$  decays is made. It also provides more details on the theoretical advantages and disadvantages of exclusive and inclusive analyses.

### 1.4.3 The OPE Formalism of Semileptonic $B$ Decays

This section describes the formalism used to describe the semileptonic  $B$  decays. Remarkable features of this method are: it factorises the EW and perturbative QCD from non-perturbative QCD; it also allows to identify NP and provide some information about its structure (see section 1.5.1).

In order to predict the weak decays of the  $B$  mesons it is necessary to take into account the strong interaction effects on the quarks in the meson, as already mentioned in section 1.3. A formalism which describes the interplay between the weak interaction and the strong interaction on the semileptonic  $B$  decays is required. This formalism is called the Operators Product Expansion (OPE) [36].

The aim of the OPE method is to separate into two distinct terms the so called short-distance effects from the long-distance effects. The effective Hamiltonian is then based on the OPE method and the renormalisation group approach. At scales much lower than  $1/\Lambda_{QCD}^{\S}$  the strong interactions are treated in perturbative expansions by dressing the lowest order quark diagrams with gluons. Above  $1/\Lambda_{QCD}$  the quarks and gluons will hadronise and QCD becomes non-perturbative. It means that physics from different length scales must be treated differently.

As the name suggests, the OPE formalism is a tool to factorise the EW and QCD perturbative effects from the non-perturbative QCD effects. In other words, it allows the amplitude of a given process  $I \rightarrow F$  to be obtained as a series expansion of products given by

$$\mathcal{A}(I \rightarrow F) = \langle F | \mathcal{H}_{eff} | I \rangle = \sum_i \mathcal{C}_i(\mu) \langle F | \mathcal{Q}_i(\mu) | I \rangle, \quad (1.50)$$

where  $\mathcal{C}_i$  are known as Wilson coefficients and  $\mathcal{Q}_i$  are local operators. Both  $\mathcal{C}_i$  and  $\mathcal{Q}_i$  depend on the scale of normalisation  $\mu$ .  $\mathcal{C}_i$  also depend on the  $W$  boson mass and other heavy particles such as the  $t$  quark. The amplitude in equation 1.50 can be considered as a Hamiltonian where  $\mathcal{Q}_i$  are the effective vertices and  $\mathcal{C}_i$  are the coupling constants. The particle fields such as the  $W$ , and the  $t$ ,  $b$  and  $c$  quarks which have masses larger than  $\mu$  are integrated out. That means these degrees of freedom are removed from the theory but taken into account in the  $\mathcal{C}_i$  coefficients. Hence, the interactions carried out by the massive  $W$  bosons on hadrons can be considered as a point-like interaction, just as in the original weak decay theory proposed by Fermi [13].

This effective Hamiltonian expansion attempts to isolate the short-distance effects in the Wilson coefficients and the long-distance effects are contained in the matrix elements of the

---

<sup>\S</sup>  $\Lambda_{QCD}$  is the QCD scale.



local operators. The separation between these two ranges is given by the renormalisation scale  $\mu$  which for B decays is of the order of 1 GeV. It is expected that the decay amplitudes do not depend on the renormalisation scale. The scale dependence of the Wilson coefficients and the dependence of the local operators should cancel out. This cancellation involves the various terms of the effective Hamiltonian expansion.

#### 1.4.3.1 Short Distance Effects

The short-distance effects are analysed through well established methods in quantum field theory [37]. Due to the QCD asymptotic freedom principle, strong interaction effects at short-distance can be calculated in terms of a perturbative series in the coupling constant  $\alpha(\mu)$ . This approach works fine in the range between  $\mathcal{O}(1 \text{ GeV})$  up to  $\mathcal{O}(M_W)$ . However terms of the form  $\ln(M_W/\mu)$  appear in products with  $\alpha(\mu)$  making the usual perturbative series invalid [18]. The renormalisation group analysis is used in order to recover the perturbative series including the logarithmic terms in the calculation (see equation 1.48). This way the usual perturbative theory is substituted by a renormalised theory.

It is important to note that in the OPE approach the Wilson coefficients are independent of the external fermion lines. Hence, the numerical values of the  $C_i$  are the same for any  $F$  state. The Wilson coefficients have mostly been calculated up to next-to-next-leading order. In table 1.2 the most relevant Wilson Coefficients for the rare  $B$  decays are listed. The values of the coefficients are given according to the operator basis proposed in [38]. An alternative scheme for the coefficients proposed in [39] is also often used.

Table 1.2: Next-to-next leading order calculation results for the Wilson Coefficients, as given in [38].

|               | $\mu = 2.35\text{GeV}$ | $\mu = 4.7\text{GeV}$ | $\mu = 9.4\text{GeV}$ |
|---------------|------------------------|-----------------------|-----------------------|
| $C_1(\mu)$    | -0.4642                | -0.2880               | -0.1506               |
| $C_2(\mu)$    | 1.019                  | 1.007                 | 1.001                 |
| $C_3(\mu)$    | -0.0096                | -0.0043               | -0.0017               |
| $C_4(\mu)$    | -0.1247                | -0.0795               | -0.0508               |
| $C_5(\mu)$    | 0.00069                | 0.00029               | 0.00009               |
| $C_6(\mu)$    | 0.00205                | 0.00081               | 0.00026               |
| $C_7(\mu)$    | -0.3637                | -0.3293               | -0.2982               |
| $C_8(\mu)$    | -0.2012                | -0.1778               | -0.1598               |
| $C_9(\mu)$    | 4.504                  | 4.209                 | 3.790                 |
| $C_{10}(\mu)$ | 4.175                  | 4.175                 | 4.175                 |

### 1.4.3.2 Long Distance Effects

The calculation of the long-distance effects are an extreme challenge once a perturbation theory cannot be used. Different theoretical approaches are available and quantitative results have been obtained for both CP violating and FCNC decays of experimental interest. The most common techniques used are lattice QCD and QCD sum rules [40, 41]. The latter have been used to estimate the hadronic contributions to the  $b \rightarrow sl\bar{l}$  decays. The long-distance effects are, in general, the biggest uncertainty sources on the Hamiltonian calculations for rare  $B$  decays.

The amplitude for the weak decay of the  $B$  whose final state is denoted by  $F$  can be written as

$$\mathcal{A}(I \rightarrow F) = \frac{G_F}{\sqrt{2}} V_{CKM} \sum_i \mathcal{C}_i(\mu) \langle F | \mathcal{Q}_i(\mu) | I \rangle, \quad (1.51)$$

where  $G_F/\sqrt{2}$  is the Fermi coupling constant and  $V_{CKM}$  represents the CKM matrix elements. Note that equation 1.51 is exactly the same as equation 1.50 but  $(G_F/\sqrt{2})V_{CKM}$  is factorised out from the Wilson coefficients. The amplitude  $\mathcal{A}$  defined at a scale of  $m_b$  reproduces the SM result with a precision of the order of  $(m_b/M_W)^2$  [42].

The matrix elements  $\langle F | \mathcal{Q}_i | I \rangle$  contain the contributions due to the complicated gluon exchanges between the external fermion lines. The calculation of the  $\mathcal{Q}_i$  operators strongly depend on the components of the hadrons in the  $I$  and  $F$  states and the interaction between these components.

Now, recalling the previous discussion on the inclusive and exclusive measurements in section 1.4.2, the following deductions can be made. If the inclusive measurement is possible then one can make the rough approximation

$$\langle F | \mathcal{Q}_i | I \rangle \sim \langle s | \mathcal{Q}_i | b \rangle, \quad (1.52)$$

where  $\langle s | \mathcal{Q}_i | b \rangle$  are the matrix elements for the free quark transition which can be evaluated. In the case of exclusive measurements this assumption is no longer valid. However, if the final state of interest is a semileptonic state it is possible to simplify the matrix elements as

$$\langle F | \mathcal{Q}_i | I \rangle \propto \langle H | \mathcal{Q}_i | I \rangle, \quad (1.53)$$

where  $H$  ( $L$ ) is the hadronic (leptonic) part of the final state  $F = HL$ . The term  $\langle H | \mathcal{Q}_i | I \rangle$  contains the hadronic part of the decay. It is possible to factorise the operators in hadronic and leptonic parts because leptons do not contribute to the long-distance effects.

The following operators are those of relevance to the case of  $\Delta B = 1$  transitions [43]. This is a list of operators which describe all decays in the  $b \rightarrow s$  family.

Note that figures 1.4-1.8 are the lowest order diagrams for these transitions. The internal lines are shown just to illustrate how the operators are obtained. As already discussed in

section 1.4.3.1 the internal lines in these diagrams are integrated out and condensed in the  $\mathcal{C}_i$ .

### Current-Current operators

$$\begin{aligned} \mathcal{Q}_1^c &= \bar{q}_L^\alpha \gamma_\mu c_L^\beta \bar{c}_L^\beta \gamma^\mu b_L^\alpha, \\ \mathcal{Q}_1^u &= \bar{q}_L^\alpha \gamma_\mu u_L^\beta \bar{u}_L^\beta \gamma^\mu b_L^\alpha, \\ \mathcal{Q}_2^c &= \bar{q}_L^\alpha \gamma_\mu c_L^\alpha \bar{c}_L^\beta \gamma^\mu b_L^\beta, \\ \mathcal{Q}_2^u &= \bar{q}_L^\alpha \gamma_\mu u_L^\alpha \bar{u}_L^\beta \gamma^\mu b_L^\beta, \end{aligned} \quad (1.54)$$

where  $q_L = P_L q$  and  $\bar{q}_L = P_L \bar{q}$  with  $P_L$  being the chiral operator defined in equation 1.2. To emphasise the differences between the operators the colour indexes  $\alpha$  and  $\beta$  are shown.

Figure 1.4 shows two examples of tree level Feynman diagrams which represent these operators. The diagrams describe  $W$  exchange and also QCD corrections to it. Note that  $\mathcal{Q}_1^c$  and  $\mathcal{Q}_2^c$  are the tree operators for the  $b \rightarrow sc\bar{c}$  decays.

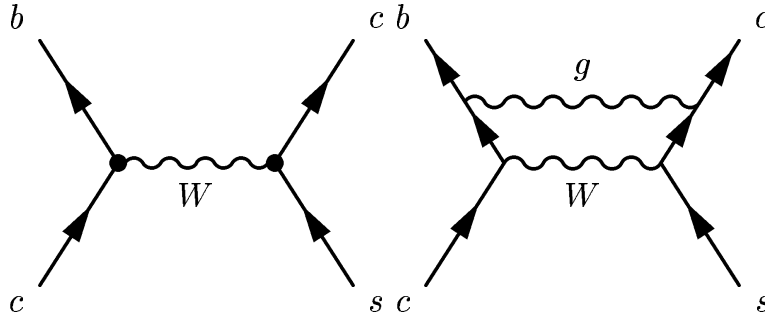


Figure 1.4: Lowest order Feynman diagrams with  $W$  exchange corresponding to current-current  $\mathcal{Q}_1$  and  $\mathcal{Q}_2$  operators.

It is also necessary to take into account the different penguin operators. These contributions are given by the following four-quark diagrams.

### QCD Operators for Quarks

The QCD operators are given by the equations in 1.55. Figure 1.5 shows the lowest order diagrams which correspond to the  $\mathcal{Q}_3$ ,  $\mathcal{Q}_4$ ,  $\mathcal{Q}_5$ ,  $\mathcal{Q}_6$  QCD operators.

$$\begin{aligned} \mathcal{Q}_3 &= \sum_{q' \neq t} (\bar{q}_L^\alpha \gamma_\mu b_L^\alpha) (\bar{q}'_L^\beta \gamma^\mu q'_L^\beta), \\ \mathcal{Q}_4 &= \sum_{q' \neq t} (\bar{q}_L^\alpha \gamma_\mu b_L^\beta) (\bar{q}'_L^\beta \gamma^\mu q'_L^\alpha), \\ \mathcal{Q}_5 &= \sum_{q' \neq t} (\bar{q}_L^\alpha \gamma_\mu b_L^\alpha) (\bar{q}'_R^\beta \gamma^\mu q'_R^\beta), \\ \mathcal{Q}_6 &= \sum_{q' \neq t} (\bar{q}_L^\alpha \gamma_\mu b_L^\beta) (\bar{q}'_R^\beta \gamma^\mu q'_R^\alpha). \end{aligned} \quad (1.55)$$

where  $q'_R = P_R q'$  and  $\bar{q}'_R = P_R \bar{q}'$  with  $P_R$  as defined in equation 1.3.

### Electroweak Operators for Quarks

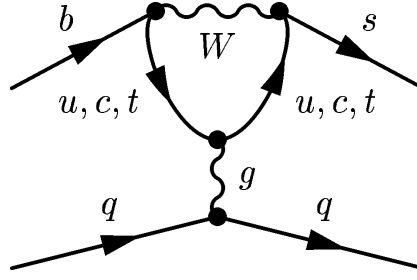


Figure 1.5: Lowest order Feynman diagram corresponding to the  $\mathcal{Q}_3, \mathcal{Q}_4, \mathcal{Q}_5, \mathcal{Q}_6$  four-quark QCD penguin operators.

The Electroweak Operators are:

$$\begin{aligned}\mathcal{Q}_7 &= \frac{3}{2} \sum_{q' \neq t} \epsilon_{q'} (\bar{q}'_L \gamma_\mu b_L^\alpha) (\bar{q}'_R \gamma^\mu q'_R^\beta), \\ \mathcal{Q}_8 &= \frac{3}{2} \sum_{q' \neq t} \epsilon_{q'} (\bar{q}'_L \gamma_\mu b_L^\beta) (\bar{q}'_R \gamma^\mu q'_R^\alpha), \\ \mathcal{Q}_9 &= \frac{3}{2} \sum_{q' \neq t} \epsilon_{q'} (\bar{q}'_L \gamma_\mu b_L^\alpha) (\bar{q}'_L \gamma^\mu q'_L^\beta), \\ \mathcal{Q}_{10} &= \frac{3}{2} \sum_{q' \neq t} \epsilon_{q'} (\bar{q}'_L \gamma_\mu b_L^\beta) (\bar{q}'_L \gamma^\mu q'_L^\alpha).\end{aligned}\tag{1.56}$$

Here  $\epsilon_{q'}$  is the electric charge of the  $q'$  quark. Figure 1.6 shows the Feynman diagrams for these operators. Note the diagram on the left-hand side differs from the QCD diagram only by the internal boson exchanged.

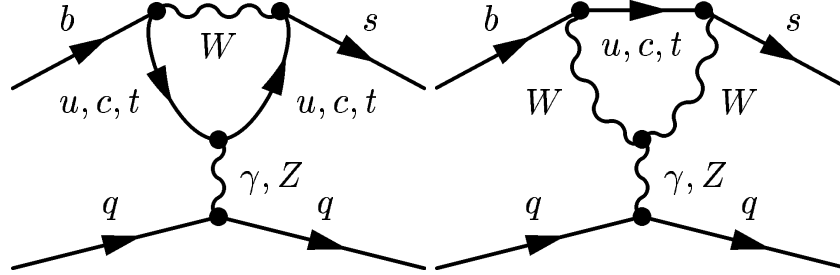


Figure 1.6: Lowest order Feynman diagrams corresponding to the  $\mathcal{Q}_7, \mathcal{Q}_8, \mathcal{Q}_9, \mathcal{Q}_{10}$  operators.

### Electroweak Operators for Semileptonic Final States

These operators are evaluated in a similar manner to the electroweak operators for quarks. They differ only in the outgoing leptons as can be seen in figure 1.7.

$$\begin{aligned}\mathcal{Q}_{9V} &= \frac{e^2}{16\pi^2} (\bar{q}'_L \gamma_\mu b_L^\alpha) (\bar{l} \gamma^\mu l), \\ \mathcal{Q}_{10A} &= \frac{e^2}{16\pi^2} (\bar{q}'_L \gamma_\mu b_L^\alpha) (\bar{l} \gamma^\mu \gamma_5 l), \\ \mathcal{Q}_{11} &= \frac{e^2}{32\pi^2 \sin^2 \theta_W} (\bar{q}'_L \gamma_\mu b_L^\alpha) (\bar{\nu}_L \gamma^\mu \nu_L).\end{aligned}\tag{1.57}$$

The operators  $\mathcal{Q}_{9V}$  and  $\mathcal{Q}_{10A}$  are mainly used on the semileptonic  $b \rightarrow sll$  decays analyses.

### Operators for Radiative Decays

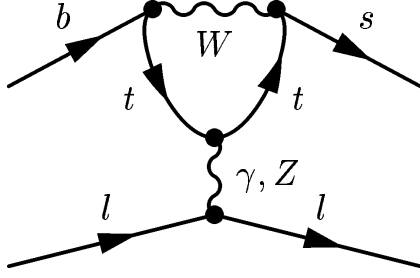


Figure 1.7: Lowest order Feynman diagram corresponding to the  $\mathcal{Q}_{9V}$ ,  $\mathcal{Q}_{10A}$  and  $\mathcal{Q}_{11}$  operators.

There are two types of operators which govern radiative transitions.  $\mathcal{Q}_{7\gamma}$  is the main operator on the  $B \rightarrow K^* \gamma$  decay and is also important for the  $B_d \rightarrow K^* \mu^+ \mu^-$  decay. Their operators are given by

$$\begin{aligned} \mathcal{Q}_{7\gamma} &= \frac{e^2}{16\pi^2} m_b (\bar{q}_L^\alpha \sigma^{\mu\nu} F_{\mu\nu} b_R^\alpha), \\ \mathcal{Q}_{8g} &= -\frac{g}{32\pi^2} m_b (\bar{q}_L^\alpha \sigma^{\mu\nu} G_{\mu\nu}^a \lambda_{\alpha\beta}^a b_R^\beta), \end{aligned} \quad (1.58)$$

where  $F_{\mu\nu}$  is the electromagnetic strength tensor,  $G_{\mu\nu}$  is the QCD strength tensor and  $\lambda_{\alpha\beta}^a$  are the  $SU(3)$  group generators.

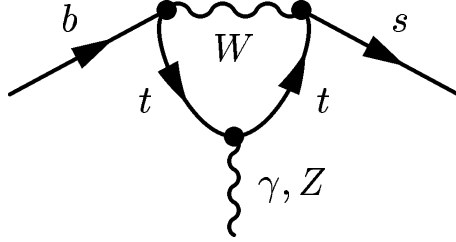


Figure 1.8: Lowest order Feynman diagram corresponding to the  $\mathcal{Q}_{7\gamma}$  and  $\mathcal{Q}_{8g}$  radiative operators.

In summary, the most important operators for the  $B_d \rightarrow K^* \mu^+ \mu^-$  analyses are  $\mathcal{Q}_{7\gamma}$ ,  $\mathcal{Q}_{9V}$  and  $\mathcal{Q}_{10A}$ . The studies performed with the  $B_d \rightarrow K^* \mu^+ \mu^-$  decay in LHCb will consist in comparing the measured values of the Wilson coefficients  $\mathcal{C}_7$ ,  $\mathcal{C}_9$ ,  $\mathcal{C}_{10}$  with the expected SM values for these coefficients. Any significant discrepancy between these numbers can potentially be due to NP effects. In order to make a coherent comparison the hadronic uncertainties calculated via the matrix elements have to be reduced. It is possible to fix these uncertainties through combination of experimental data from  $B \rightarrow K^* \gamma$  and theory [44]. Section 1.5 presents the current status of the theoretical predictions for the  $B_d \rightarrow K^* \mu^+ \mu^-$  decay.

## 1.5 The $B_d \rightarrow K^* \mu^+ \mu^-$ Rare Decay

This section details the phenomenology of the  $B_d \rightarrow K^* \mu^+ \mu^-$  decay emphasising how the SM can be tested and NP identified using the OPE formalism. It presents the current status of the theoretical predictions for this decay and also its experimental status.

The amplitude of a given decay can be deduced using the effective Hamiltonian given by equation 1.50. From the amplitude it is also interesting to calculate the differential branching ratio in order to characterise the decay process in terms of meaningful quantities which can actually be measured. Figure 1.9 shows two of the lowest order Feynman diagrams of the  $B_d \rightarrow K^* \mu^+ \mu^-$  decay. On the left-hand side a penguin diagram with a  $\gamma$  or  $Z$  emission going into two leptons is shown. In the right-hand side a box diagram with double  $W$  exchange and the emission of two leptons is shown.

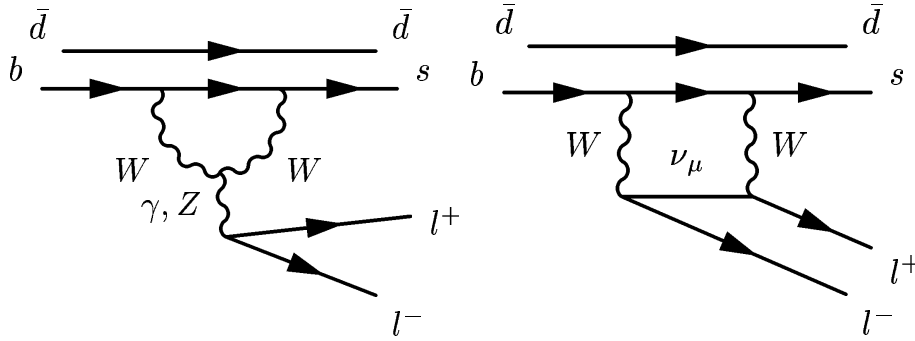


Figure 1.9: Box and Penguin diagrams for  $B_d \rightarrow K^* \mu^+ \mu^-$ .

As already mentioned in the introduction of this chapter, the short-distance of the effective Hamiltonian is calculated at next-to-next leading order also for the  $B_d \rightarrow K^* \mu^+ \mu^-$  exclusive analysis with uncertainties of  $\sim 10\%$  [38]. The long-distance components are evaluated via the QCD sum rules approach. Because the mass of the  $b$  quark is much heavier than the  $d$  quark the non-perturbative effect is small. However the long-distance effects due to the operators involving  $c\bar{c}$  loops near the  $J/\Psi$  mass can be significant. So in order to control the hadronic uncertainties the region  $\sqrt{s}^\P \sim J/\Psi$  mass has to be avoided.

The main reason to perform analyses on rare  $B$  decays is to make precise tests of the SM and to search for NP via indirect measurements. If new physics is found the next step would be to evaluate if it contains a flavour structure and to provide a first attempt to map this structure.

Hence, for an experimental analysis it is necessary to identify which quantities are potentially sensitive to NP. It is also important to reduce the theoretical and experimental uncertainties to a minimum. In the case of the  $B_d \rightarrow K^* \mu^+ \mu^-$  decay the theoretical uncertainties are mainly due to the hadronic matrix elements as discussed earlier in section 1.4.3. The

<sup>\P</sup> In this case  $\sqrt{s}$  is the invariant dimuon mass.

experimental uncertainties are initially simply due to statistics with systematic uncertainties becoming significant only after  $2 - 8 \text{ fb}^{-1}$  in LHCb. The experimental issues of analysing this decay will be discussed in chapter 5.

### 1.5.1 Search for New Physics

Even though the SM is a very successfully model it is not a complete theory. For example, it does not explain the existence of dark matter in the universe. The experimental evidence for dark matter as a major component of the matter in the universe requires new explanations from the theoretical point of view. However, to develop this new theory extra information from the LHC experiments is needed. Heavy flavour physics is expected to be one of the main windows for NP searches [45, 46].

Amongst the many proposed NP models the Supersymmetric extensions of the SM are the most promising in terms of predictions [9, 47]. The Supersymmetric models are also far more developed than the other alternative theories. They already propose specific solutions to the dark matter problem. A family of hypothetical particles have been proposed as candidates to compose the non-baryonic dark matter in the universe. The favourite candidates are the so called Neutralinos, the Gravitinos and the Axinos [48]. Experimental searches for these particles via astroparticle, cosmology and collider experiments [49] are being carried out, but no evidence for their existence has yet been obtained.

In general, heavy flavour physics is unique in its potential for new physics searches. The B sector does not provide searches for direct production of new particles but is a good probe for indirect searches of NP signatures. For example, in many models of Supersymmetry the CKM approach as proposed in the SM would not provide a complete description since new particles could include  $\sim 10$ -100 new couplings and complex phases. Those couplings and phases could interfere with the SM ones such that the CKM unitary triangle would not close perfectly. In this case a better understanding of the nature of these effects would be necessary to include the new fields in a more general theory.

As already mentioned the  $B_d \rightarrow K^* \mu^+ \mu^-$  decay is an interesting place to look for NP signals. Since FCNC occur just via penguin and box diagrams in the SM additional loop diagrams with new particles inside the loops can contribute at the same level as the SM. Those new contributions would significantly affect quantities such as the branching ratio. Angular distributions are also likely to be changed. Figure 1.10 shows some of the possible diagrams with new particles in the loop which can contribute to the  $B_d \rightarrow K^* \mu^+ \mu^-$  decay ratio.

Within the OPE approach new physics can be identified in three different ways each depending on how NP affects the effective Lagrangian. A list of the possible NP signatures is listed as:

- i - Wilson coefficients: The most obvious NP signature would be the case where new

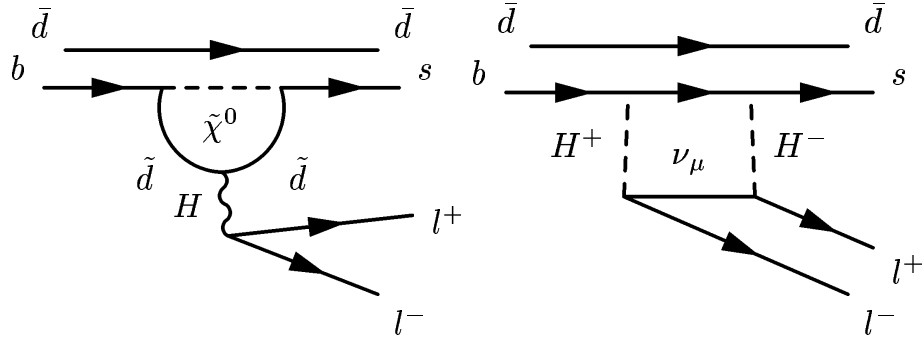


Figure 1.10: Examples of SUSY Feynman diagrams for  $B_d \rightarrow K^* \mu^+ \mu^-$ . A penguin diagram with virtual Neutralino and squarks is shown on the left-hand side. A box diagram with charged Higgs bosons is shown on the right-hand side.

particles couple exactly as the SM particles. The overall effect would be a considerable change on the  $\mathcal{C}_i$  absolute values due to the existence of new particles contributing with new loop diagrams.

- ii - Local Operators: It is possible that new particles might not couple exact as the SM particles then it would be necessary to include new operators similar to the SM ones but with chirality swapped. Hence, new Wilson coefficients  $\mathcal{C}'_i$  would be required too. A maximum of 10 new extra terms in the Lagrangian can be written down. For each  $\mathcal{C}'_i$  there would be an operator with swapped chirality.
- iii - New Phases: New FCNC transitions could be allowed if NP includes new complex phases. This would be observed through studies of the CKM unitary triangles.

In models with Minimal Flavor Violation [50] and SUGRA [51]  $\mathcal{C}_7$  can have the opposite sign compared to the SM value. In Mass Insertion Approximation (MIA-SUSY) [52] the coefficient changed is  $\mathcal{C}_{10}$ .

In principle it should not be expected that just one of these effects will appear isolated. It might be possible that NP contributes by changing all of these quantities. However, theoretical and experimental results already constrain the possible NP signature considerably. From the theoretical point of view terms with new operators should not contribute significantly because of the inverse power law type of dependence of such operators with the NP scale [53]. Because new operators are very suppressed their contribution might be too small to be experimentally identified. New phases also seem to be unlikely to be found in the  $B_d \rightarrow K^* \mu^+ \mu^-$ . This can be concluded because new phases would affect the CKM picture significantly and experimental results already constrain this [32]. The main NP contribution is expected to come from the Wilson coefficients, although part of these coefficients are already strongly constrained. The  $\mathcal{C}_i$  coefficients with  $i \leq 6$  are not affected by NP otherwise those contributions would have been already identified in the various hadronic decays described by these



terms. Hence, the  $\mathcal{C}_{7\gamma}$ ,  $\mathcal{C}_{9V}$  and  $\mathcal{C}_{10}$  coefficients are the quantities most likely to be sensitive to NP effects in rare semileptonic  $B$  decays.  $\mathcal{C}_{7\gamma}$ ,  $\mathcal{C}_{9V}$  and  $\mathcal{C}_{10}$  are not yet well measured [4].

## 1.5.2 Observables in $B_d \rightarrow K^* \mu^+ \mu^-$ Analysis

A number of quantities that can provide good estimates to confirm the SM predictions or to spot NP have been identified in many theory papers (see [50, 9, 52, 6, 53, 8]). This section describes those quantities that are also interesting from an experimental point of view as they are relatively easy to measure. All formulas and quantities shown in this section were calculated in [39, 38] and assume that new particles do not introduce new operators in the effective Hamiltonian (see section 1.5.1).

### 1.5.2.1 Double Differential Branching Ratio

It is convenient to express the differential spectrum in terms of an angular decomposition. This decomposition provides direct access to measurable quantities of interest [38]. This method also allows the extraction of the Wilson coefficients without  $q^2$  dependence and reasonable  $\mu$  freedom. The double-differential spectrum formula is given by

$$\frac{d^2\Gamma}{dq^2 d\cos\theta_l} = \frac{3}{8} [(1 + \cos^2\theta_l)H_T(q^2) + 2\cos\theta_l H_A(q^2) + 2(\sin^2\theta_l)H_L(q^2)], \quad (1.59)$$

where  $q$  is the dimuon invariant mass and  $\theta_l$  is the angle between  $l^+$  and the  $B$  meson calculated in the dimuon rest frame. The  $H_X$  functions can be written as quadratic combinations of transversity amplitudes. These amplitudes are given in terms of the Wilson coefficients and hadronic form factors. The hadronic form factors are functions which contain all the information from the non-perturbative part of the Hamiltonian.

From the double differential branching ratio it is possible to derive the quantities described in the following sections and then finally extract the Wilson coefficients.

### 1.5.2.2 Dimuon Distribution

The differential branching ratio as a function of the dimuon mass is obtained by simply integrating over the angle  $\theta_l$  in equation 1.59,

$$\frac{d^2\Gamma}{dq^2} = H_T(q^2) + H_L(q^2). \quad (1.60)$$

Figure 1.11 shows the squared dimuon mass distribution calculated in the SM and also in some Supersymmetry models [9]. The SM, SUGRA and MIA-SUSY models are shown. The shaded area illustrates the typical hadronic uncertainties. The peaks are due to the  $c\bar{c}$  resonances. The two main peaks are due to the  $J/\Psi$  and  $\psi'$  resonances.

On first impression it may appear straight forward from figure 1.11 to distinguish the SM distribution from the SUSY models. However, the only significant difference between the

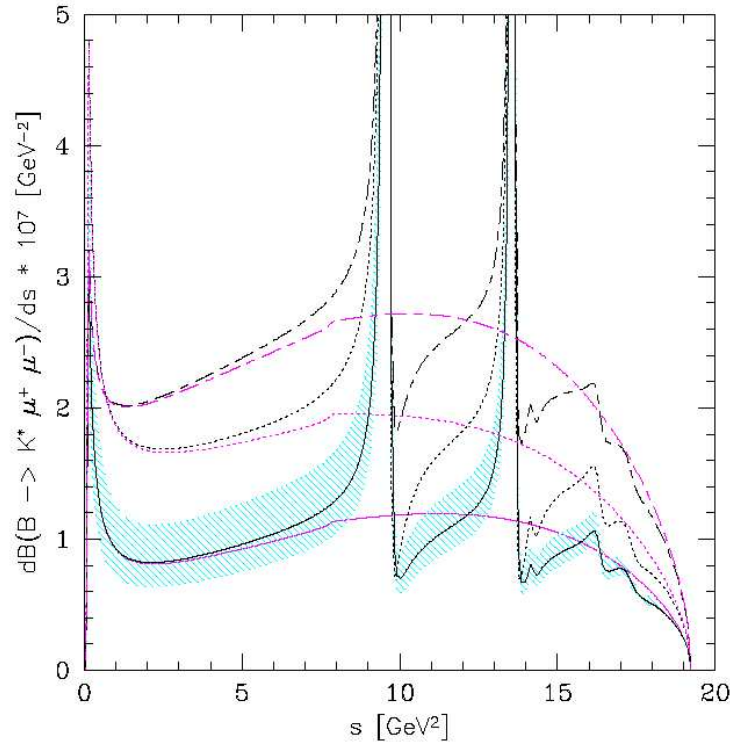


Figure 1.11: Squared dimuon mass distribution for SM and various SUSY models. The solid line represents the SM. The dashed line represents a SUGRA model and long-short dashed line represents a MIA-SUSY model. The purple lines correspond to the pure short-distance spectra. Figure reproduced from [9].

curves is the overall rate. In LHCb it could be difficult to obtain the normalisation constant of the curve using early data. Extracting the Wilson coefficients directly from the dimuon distribution would be difficult due to possible detector acceptance effects as it is discussed in chapter 5. These uncertainties could be partially reduced by using ratios between distributions as discussed in the following subsection.

### 1.5.2.3 Forward Backward Asymmetry

A cleaner measurement with the  $B_d \rightarrow K^* \mu^+ \mu^-$  decays is the so-called Forward Backward Asymmetry (FBA). The FBA can be interpreted as the difference between the number of forward events and the number of backward events as a function of the dimuon mass squared. An event is classified as forward if  $\theta_l \leq \pi/2$  and backward if  $\theta_l > \pi/2$ . This quantity provides a powerful measurement to test the SM and to search for NP. This curve has a particular shape that could change significantly as NP enters the Hamiltonian.

The FBA is defined as

$$\mathcal{A}_{FB}(q^2) = \int_{-1}^1 \frac{d^2\Gamma}{dq^2 d\cos\theta_l} \text{sgn}(\cos\theta_l) \mathbb{I} d\cos\theta_l, \quad (1.61)$$

and by substituting the expression given in equation 1.59 it is possible to write the FBA as

$$\mathcal{A}_{FB}(q^2) = \frac{3}{4} H_A(q^2). \quad (1.62)$$

Not only the shape of the FBA distribution is important but also the point where its value is zero. This point is commonly referred to as the FBA zero point. The FBA zero point provides the ratio between the coefficients  $C_7$  and  $C_9$  with the theoretical uncertainties reduced to a minimum. The expected value for the FBA zero point in the SM has been calculated through different methods. The results obtained are in reasonable agreement.

This measurement is important because both  $C_7$  and  $C_9$  Wilson coefficients are susceptible to NP contribution and a considerable shift on their expected values would be an indication of a NP signature.

Figure 1.12 shows the FBA calculated in the SM. Results using different values for the Wilson coefficients are shown. The values in table 1.3 have been used to make the three extra curves in the graph.

Table 1.3: Different values of Wilson coefficients used for FBA calculations.

|        |   |
|--------|---|
| case 1 | $C_7 = -C_7^{SM}, C_9 = C_9^{SM}, C_{10} = C_{10}^{SM}$ |
| case 2 | $C_7 = C_7^{SM}, C_9 C_{10} = -C_9^{SM} C_{10}^{SM}$    |
| case 3 | $C_7 = -C_7^{SM}, C_9 C_{10} = -C_9^{SM} C_{10}^{SM}$   |

The value for the zero point with form factors calculated purely with QCD sum rules is [54].

$$q_0^2 = 4.36_{-0.31}^{+0.33} \text{ GeV}^2/\text{c}^4. \quad (1.63)$$

The parallel component of the form factors was also fixed by measurements of the  $\gamma$  polarisation in the  $B \rightarrow K^* \gamma$  decay as discussed in [44]. This results in a value for the zero point of

$$q_0^2 = 4.07_{-0.13}^{+0.16} \text{ GeV}^2/\text{c}^4. \quad (1.64)$$

Both results are in reasonable agreement with each other and with the previous calculations of the zero point [6]. As seen, fixing the form factor experimentally reduces the uncertainties by a factor of  $\sim 2$ .

#### 1.5.2.4 Wilson Coefficients

A set of measurements have been proposed in order to access the values of the Wilson coefficients in the  $B_d \rightarrow K^* \mu^+ \mu^-$  decays. These methods consist of using partially integrated

---

$\mathbb{I} \text{sgn}(x) = x/|x|.$

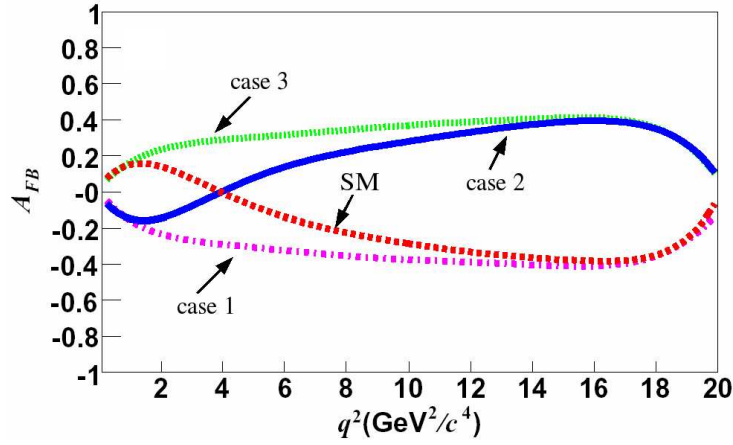


Figure 1.12: Forward backward asymmetry distribution calculated in the SM. Each case assume different values for the Wilson coefficients (see table 1.3). Figure reproduced from [5].

values of the differential branching ratio in the low  $q^2$  regime, the shape of the FBA curve (and its zero point). Some methods also propose the use of integrated values of the FBA curve.

These partially integrated quantities are usually defined within ranges of  $q^2$  which do not contain the  $c\bar{c}$  resonance contributions. That means the distributions are integrated in the low range  $0 \text{ GeV}^2 < q^2 < 8 \text{ GeV}^2$ .

The integrated quantities provide the following numbers which, combined as ratios, can provide sensitivity to  $\mathcal{C}_9/\mathcal{C}_7$  and  $\mathcal{C}_{10}/\mathcal{C}_7$

$$\begin{aligned} H_T(0.1, 4.0) &= \int_{q_1^2=0.1}^{q_2^2=4.0} H_T(q^2) dq^2, & H_T(4.0, 8.0) &= \int_{q_1^2=4.0}^{q_2^2=8.0} H_T(q^2) dq^2, \\ H_A(0.1, 4.0) &= \int_{q_1^2=0.1}^{q_2^2=4.0} H_A(q^2) dq^2, & H_A(4.0, 8.0) &= \int_{q_1^2=4.0}^{q_2^2=8.0} H_A(q^2) dq^2. \end{aligned} \quad (1.65)$$

The various ratios between these integrals can be used to constrain the actual values of the Wilson coefficients. It is possible that this method may be as accurate as measuring the zero point of the FBA itself. These constraints become more obvious if  $H_T$  and  $H_A$  are explicitly expressed as

$$\begin{aligned} H_T(q^2) &\propto \left\{ \mathcal{C}_{10}^2 |\zeta_{\perp}(\mathbf{s})|^2 + \left| \mathcal{C}_9 \zeta_{\perp}(\mathbf{s}) + \frac{2\mathcal{C}_7}{s} \frac{m_b}{m_B} [\zeta_{\perp}(\mathbf{s}) + (1-s)\zeta_{\perp}^J(\mathbf{s})] \right|^2 \right\}, \\ H_A(q^2) &\propto (-2)\mathcal{C}_{10}\zeta_{\perp}(\mathbf{s})\mathcal{R} \left\{ \mathcal{C}_9 \zeta_{\perp}(\mathbf{s}) + \frac{2\mathcal{C}_7}{s} \frac{m_b}{m_B} [\zeta_{\perp}(\mathbf{s}) + (1-s)\zeta_{\perp}^J(\mathbf{s})] \right\}. \end{aligned} \quad (1.66)$$

The  $B \rightarrow K^*\gamma$  decay can be used in these ratio methods to improve the measurements of the Wilson coefficients. The improvement is obtained by taking the ratio between  $\Gamma(B \rightarrow K^*\gamma)$  and the quantities in equation 1.65 for  $B_d \rightarrow K^*\mu^+\mu^-$ .  $B \rightarrow K^*\gamma$  could also be used to fix the form factors, as already discussed in the zero point calculations in section 1.5.2.3.

### 1.5.3 Recent Experimental Results

The  $B_d \rightarrow K^* \mu^+ \mu^-$  decay has already been detected by the Belle, Babar and CDF experiments [4, 5, 55]. All these collaborations were able to provide values for the branching ratios with similar statistics. On table 1.4 the luminosity, signal yields and estimated branching ratios are quoted for this decay.

Table 1.4: Luminosity, signal yields and estimated branching ratios for  $B_d \rightarrow K^* \mu^+ \mu^-$ .

| Experiment | Luminosity            | Yields               | $\text{Br}(B \rightarrow K^* \mu^+ \mu^-)$               |
|------------|-----------------------|----------------------|--|
| Belle      | $140 \text{ fb}^{-1}$ | $17.1^{+5.4}_{-4.7}$ | $(1.33^{+0.42}_{-0.37} \pm 0.1 \pm 0.05) \times 10^{-6}$ |
| Babar      | $208 \text{ fb}^{-1}$ | $15.9^{+7.0}_{-5.9}$ | $(0.73^{+0.20}_{-0.18} \pm 0.11) \times 10^{-6}$         |
| CDF        | $924 \text{ pb}^{-1}$ | $\sim 35$            | $(0.82 \pm 0.31 \pm 0.11) \times 10^{-6}$                |

In these experiments the following types of background were identified.

- Charmonium  $B$  decays: This is basically due to  $B \rightarrow J/\Psi X_s$  and  $B \rightarrow \psi' X_s$  decays. To avoid such contamination cuts on the dimuon invariant mass close to the  $\Psi$  and  $\psi'$  mass were applied;
- Continuum Background: Due to  $u, d, s$  or  $c$  pair production. This was estimated from the  $B$  mass side bands and subtracted afterwards;
- Combinatorial Background: The decay products of the two  $B$ 's, which can decay via semileptonic processes, were wrongly combined as a signal event;
- Misidentification: Decays of the type  $B \rightarrow K^* h^+ h^-$  where the hadrons were misidentified as leptons.

Figure 1.13 shows the fit to the mass distribution of the  $B_d \rightarrow K^* \mu^+ \mu^-$  data and background for Belle and CDF experiments. The significances obtained from the mass fit are 4.2 and 2.9 respectively.

The B factory collaborations have performed initial angular analyses. Figure 1.14 shows the measured FBA on both Belle and Babar experiments. On the left hand side the FBA calculated with the data from the Belle detector is shown. To perform these measurements the Belle experiment has increased the integrated luminosity of the data set used to  $357 \text{ fb}^{-1}$  [56]. On the right-hand side the analogous analysis made by the Babar experiment is shown. On both plots the solid line represents the expected distribution in the SM. The other curves represent the FBA with values for Wilson coefficients similar to those given in table 1.3<sup>||</sup>.

The results obtained for the Wilson coefficients given by Belle are summarised in table 1.5. Note the values quoted are strongly related to the model dependent analysis based on

<sup>||</sup>Analyses on Belle and Babar experiments continue under development with preliminary results presented in [57, 58]. Belle:  $\text{BR} = 10.8 \pm 0.9 \pm 1.0 \times 10^{-7}$ , Babar:  $\text{BR} = 11.1 \pm 1.9 \pm 0.7 \times 10^{-7}$ .

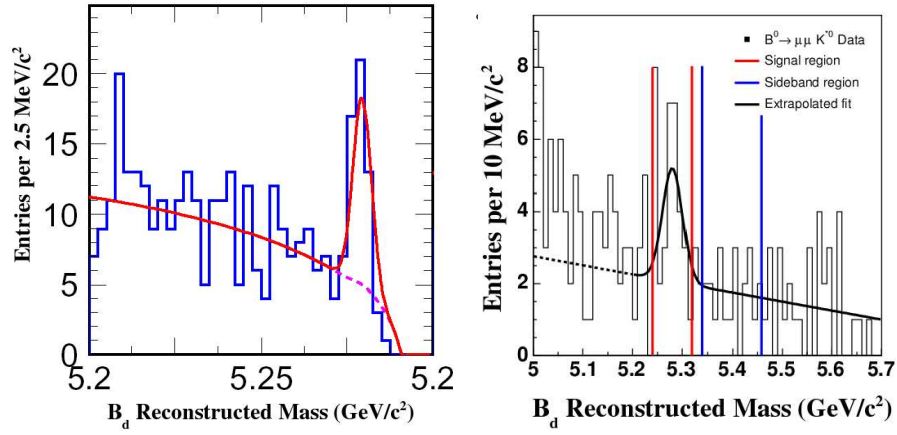


Figure 1.13: B mass distribution fit for Belle and CDF experiments. In the left-hand side the Belle plot is shown. This figure is reproduced from [4]. The red solid line shows the signal plus background fit and the purple dashed line shows the fit of the background. In the right-hand side the CDF plot is shown. This figure is reproduced from [55]. The solid black line shows the signal plus background fit and the black dotted line shows the background fit. The red vertical lines indicate the signal mass window and the blue vertical lines indicate the background sideband region.

the SM expectations. Both the FBA and Wilson coefficients obtained in these analyses are in agreement with the SM. Unfortunately the experimental uncertainties are too large to spot any signal of NP. Future measurements should have the prospect to much better constrain NP models. In chapter 5 a discussion of the measurements and uncertainties that LHCb will perform is presented.

Table 1.5: Wilson coefficients measured by the Belle collaboration. The SM values are also listed.

|                | $C_9/C_7$                     | $C_{10}/C_7$                  |
|----------------|-------------------------------|-------------------------------|
| negative $C_7$ | $-15.3^{+3.4}_{-4.8} \pm 1.1$ | $-10.3^{+5.2}_{-3.5} \pm 1.8$ |
| positive $C_7$ | $-16.3^{+3.7}_{-5.7} \pm 1.4$ | $-11.1^{+6.0}_{-3.9} \pm 2.4$ |
| SM             | -12.4                         | -11.5                         |

The Babar collaboration have recently presented interesting measurements with  $B \rightarrow K^{(*)}l^+l^-$  decays, where  $l$  can be muons or electrons. These measurements are: direct CP violation ( $\mathcal{A}_{CP}^{K^{(*)}}$ ), ratio of rates to dimuon and dielectron final states ( $R_{K^{(*)}}$ ), and isospin asymmetries ( $\mathcal{A}_I^{K^{(*)}}$ ) [59]. All these measurements were performed in two ranges of dilepton mass squared: low  $q^2$  ( $0.1 < q^2 < 7.02 \text{ GeV}^2/c^4$ ); and high  $q^2$  ( $q^2 > 10.24 \text{ GeV}^2/c^4$ ). The measurements of direct CP violation and the ratio of rates are in agreement with the SM expected values. The isospin analyses have shown that the  $\mathcal{A}_I^{K^{(*)}}$  values in the high range

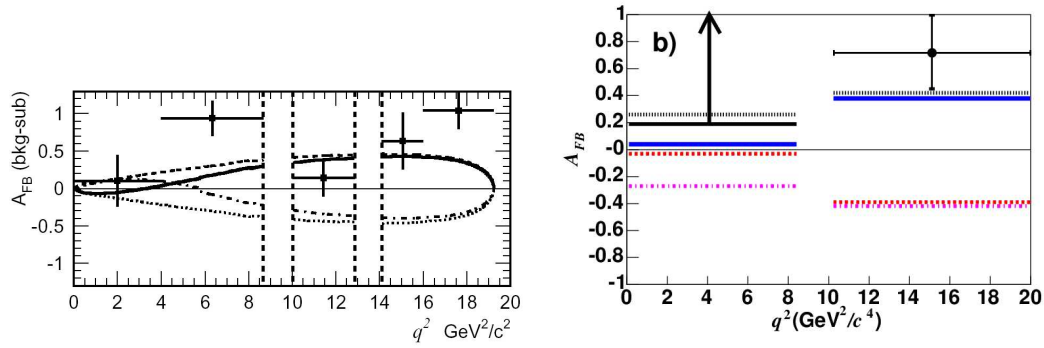


Figure 1.14: FBA distribution of the  $B_d \rightarrow K^* \mu^+ \mu^-$  decay in Belle and Babar experiment. On both plots the solid line represents the expected distribution in the SM. The other curves represent the FBA with values for Wilson coefficients similar to those given in table 1.3. These figures are reproduced from [56, 5].

are also in agreement with the SM predictions. For the low  $q^2$  range,  $\mathcal{A}_I^{K^{(*)}}$  is about  $3.2 \sigma$  and  $2.7 \sigma$  different from the SM predictions for the  $B \rightarrow K l^+ l^-$  and  $B \rightarrow K^* l^+ l^-$  decays, respectively. In the case of the  $B \rightarrow K^* l^+ l^-$  decays,  $\mathcal{A}_I^{K^* \mu^+ \mu^-} = -0.26^{+0.50}_{-0.34} \pm 0.05$  and  $\mathcal{A}_I^{K^{*e^+e^-}} = -0.66^{+0.19}_{-0.17} \pm 0.05$ . When using the range  $0.0 < q^2 < 7.02$  the value was  $\mathcal{A}_I^{K^{*e^+e^-}} = -0.25^{+0.20}_{-0.18} \pm 0.03$ .

## 1.6 Conclusions

A review of the SM was presented in this chapter. This included a description of the main features of the EW and QCD theories. Aspects of the LHCb physics programme were also discussed, focusing on the rare  $b \rightarrow s$  transitions. The phenomenology of the  $B_d \rightarrow K^* \mu^+ \mu^-$  decay was presented. The most interesting quantities to measure in the  $B_d \rightarrow K^* \mu^+ \mu^-$  decay are the branching ratio, dimuon mass squared distribution, FBA distribution and Wilson coefficients. These quantities are all sensitive to NP and should be measured in LHCb. A summary of the recent experimental results of the  $B_d \rightarrow K^* \mu^+ \mu^-$  decay was given. A discussion on the LHCb sensitivity to measure these quantities is given in chapter 5.

# Chapter 2

## The LHCb Experiment

The Large Hadron Collider (LHC) accelerator at CERN will start colliding protons in the spring of 2009. The LHCb experiment is one of the four LHC detectors and will search for signs of new physics by investigating the decays of B mesons. The construction of the LHCb detector has been finished and its final commissioning stage will be completed with early data, which will be used for calibration and alignment.

This chapter presents a review of the LHC project emphasising the description of the LHCb experiment. Section 2.1 describes the LHC project and its four experiments. Section 2.2 details the LHCb detector. Each of the LHCb sub-systems is described in sections 2.2.1-2.2.8.3. A more detailed description of the VELO system is given in section 2.2.1 since part of the work of this thesis is related to the long term tests of the LHCb VELO modules.

### 2.1 The LHC Project

The Large Hadron Collider (LHC) [60] built at CERN [61] in Geneva is the largest particle accelerator in the world. It will collide hadrons with a maximum centre of mass energy of 14 TeV with crossing intervals of  $\sim 25$  ns\*. This section briefly describes the LHC accelerator and introduces its four experiments.

The existing infrastructure, much of it previously used for the Large Electron Positron (LEP) [62], will be used to produce, store and accelerate protons. This infrastructure comprises the pre-acceleration system, injection system and tunnel. The protons are accelerated through many stages. This process starts with the Linear Accelerator (LINAC2) [63] accelerating protons up to an energy of 50 MeV. These particles are delivered to the Proton Synchrotron Booster (PSB) [64] which accelerates the protons up to 1.4 GeV. The Proton Synchrotron (PS) [65] accelerates the protons up to 26 GeV which are transported to the Super Proton Synchrotron (SPS) [66]. The SPS accelerates the protons to an energy of

---

\*Particles are distributed in bunches along the accelerator line. The crossing time is defined as the time interval between two consecutive bunch crossings in the region of collision.



Table 2.1: LHC accelerator parameters. Numbers are taken from [67].

| Parameter                                       | value          |
|---|----------------|
| Ring Circumference (km)                         | 27             |
| Centre of mass energy (TeV)                     | 14             |
| Field of main bends (T)                         | 8.4            |
| Luminosity ( $\text{cm}^{-2}\text{s}^{-1}$ )    | $\sim 10^{34}$ |
| Number of bunches                               | 2808           |
| Number of particles per bunch                   | $\sim 10^{11}$ |
| Time between beam crossings (ns)                | 25             |
| Crossing angle ( $\mu\text{rad}$ ) <sup>†</sup> | 200            |
| Beam size ( $\mu\text{m}$ ) <sup>†</sup>        | 70.9           |
| Bunch length (cm)                               | 7.55           |

450 GeV. The protons are finally injected in the LHC accelerator where they reach 7 TeV.

The LHC tunnel is located 100 m underground. It has a circular shape with a perimeter of 27 km. The LHC has two independent accelerating pipes in order to circulate protons in both directions. A total of 1700 magnetic dipoles with 8.4 T are used to keep the protons in their approximately circular trajectory inside the beam pipe. These dipoles are used to bend the proton trajectory in the so-called deflection points. Table 2.1 list some of the various LHC parameters.

The high energy scale and high crossing rates will allow measurements of new physical processes and access to very rare decays by the LHC detectors. A quantity that describes the rate of collisions in a high energy collider is the luminosity,  $\mathcal{L}$ . The luminosity is given approximately by the product of the number of particles in each of the colliding bunches divided by the cross section of the interaction region and divided by the time between beam crossings. The value for the luminosity obtained using the parameters given in table 2.1 is  $\sim 10^{34} \text{ cm}^{-2}\text{s}^{-1}$ . The luminosity is a parameter necessary to evaluate signal yields and to estimate background (see chapter 5).

Figure 2.1 shows the LHC accelerator and its experiments. The circular blue-white line illustrates the LHC tunnel. There are four interaction points, one for each detector. The purpose of each of these experiments is described in section 2.1.1. The SPS and the injection system are also shown in this picture. They are represented by the red-white line.

---

<sup>†</sup> At the LHCb collision point.

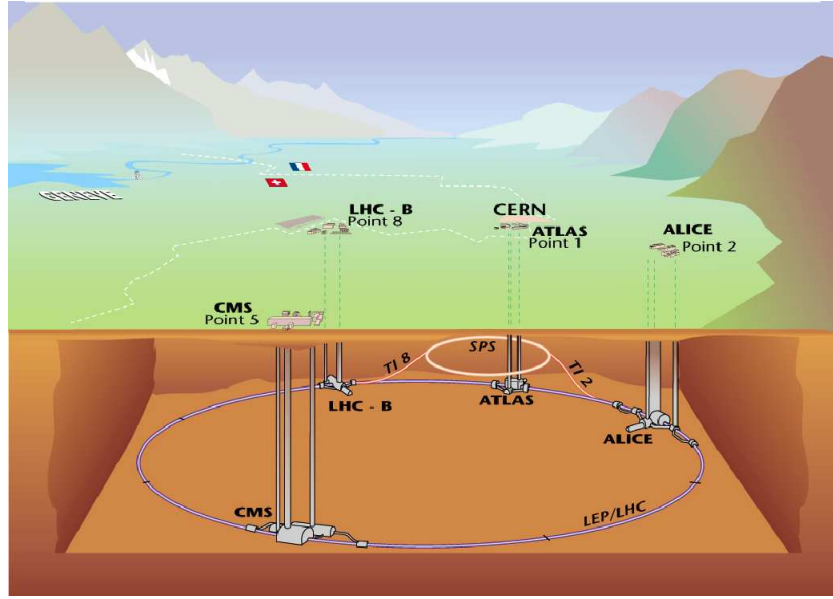


Figure 2.1: The LHC accelerator and its experiments. The SPS and the injection system are also shown. Picture taken from [60].

### 2.1.1 The LHC Experiments

The LHC project has four main experiments in order to investigate the different aspects of the SM in the TeV scale and to search for NP. This section summarises the main goals of these experiments.

- **LHCb:** It is primarily dedicated to CP violation and rare decays studies in the  $b$  sector. This experiment will test the flavour sector of the SM and search for NP by making precise measurements of  $B$  meson decays. To perform these measurements the detector has to reconstruct the particle tracks, recognise the interaction and decay vertices and identify the type of the particles detected [68].
- **ATLAS:** It is a general purpose experiment which will search for the Higgs boson, supersymmetric particles, investigate possible alternative spontaneous symmetry breaking mechanisms and perform heavy flavour physics analyses [69].
- **CMS:** It is also a general purpose detector. This experiment has a physics programme similar to ATLAS [70].
- **ALICE:** The main goal of this experiment is to produce, detect and study the nature of the quark-gluon plasma. Different from the other three experiments, ALICE will have Pb-Pb collisions in its interaction region. This investigation is considered fundamental to the understanding of the evolution of the early universe [71].

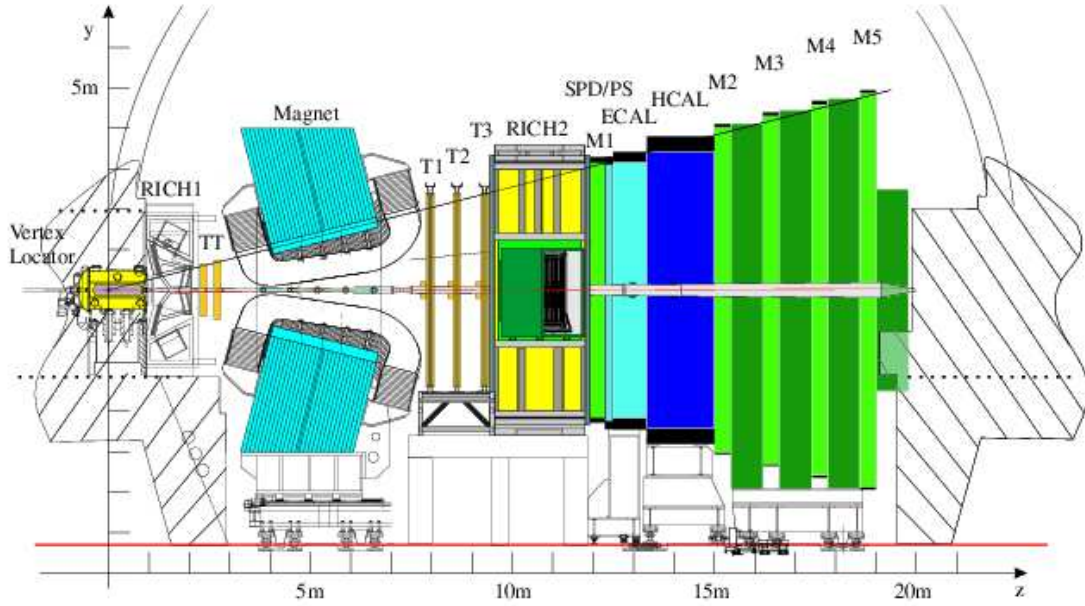


Figure 2.2: The LHCb detector and its sub-detectors. Figure reproduced from [72].

## 2.2 The LHCb Experiment

The LHCb experiment [28, 72, 68] will search for NP in the heavy flavour sector of the SM. To achieve its goals it will perform precise measurements of CP violation and rare decays of the  $B$  mesons. The LHCb detector is designed to reconstruct and identify individually produced particles and to select the interesting events. To perform these measurements LHCb has a total of 6 different sub-detectors and 2 critical global systems. In this chapter the LHCb detector and its sub-systems are described. Sections 2.2.1-2.2.6 describe the sub-detectors. Sections 2.2.7 and 2.2.8.3 describe the trigger system and the online system respectively.

The LHCb detector is a collider detector but its geometry resembles a fixed target detector. Figure 2.2 shows a schematic diagram of the detector and its components. It has an angular acceptance of  $\pm 250$  mrad in the  $yz$  plane and  $\pm 300$  mrad in the  $xz$  plane. The length of the detector is 20 m in the beam direction ( $z$ ). Its design is based on the kinematics of production of  $b\bar{b}$  quarks in proton-proton collisions. The colliding protons have the same momentum but the interactions occur between the partons that constitute the protons. This means that the probability to have partons with different momentum interacting is high while the likelihood of having partons with similar momentum interacting is almost negligible. Therefore  $b\bar{b}$  quarks pairs are produced in a direction quite close to the beam direction. Figure 2.3 shows the angular distribution of the produced  $b$  and  $\bar{b}$  quarks in proton-proton collisions at the LHC energy scale. It also shows an example of a  $b\bar{b}$  production collision.

LHCb will operate with an instantaneous luminosity  $\sim 2 \times 10^{32} \text{ cm}^{-2}\text{s}^{-1}$ . This lumi-

osity is a factor of 50 below the maximum design luminosity of the LHC. This reduced luminosity at LHCb is obtained by having a comparatively defocused beam. This value of luminosity ensures an average number of proton-proton collisions per crossing of  $\sim 1$ . This lower value for luminosity ensures a small number of primary vertices per event and reduces radiation damage in the detectors closest to the interaction vertex (see section 2.2.1). It allows good signal selection efficiencies and background rejection [28, 72].

In figure 2.2 each sub-detector of the LHCb experiment is shown. From the left-hand side to the right-hand side of the diagram the following systems can be seen: Vertex Locator (VELO), Ring Image Cherenkov 1 (RICH1), Tracker Turicensis (TT), Magnet, Tracking stations (T1, T2, T3), Ring Image Cherenkov 2 (RICH2), Muon Station 1 (M1), Electronic and Hadronic Calorimeters (ECAL, HCAL) and Muon Stations (M2, M3, M4, M5). In the following sections each detector or sub-system is described.

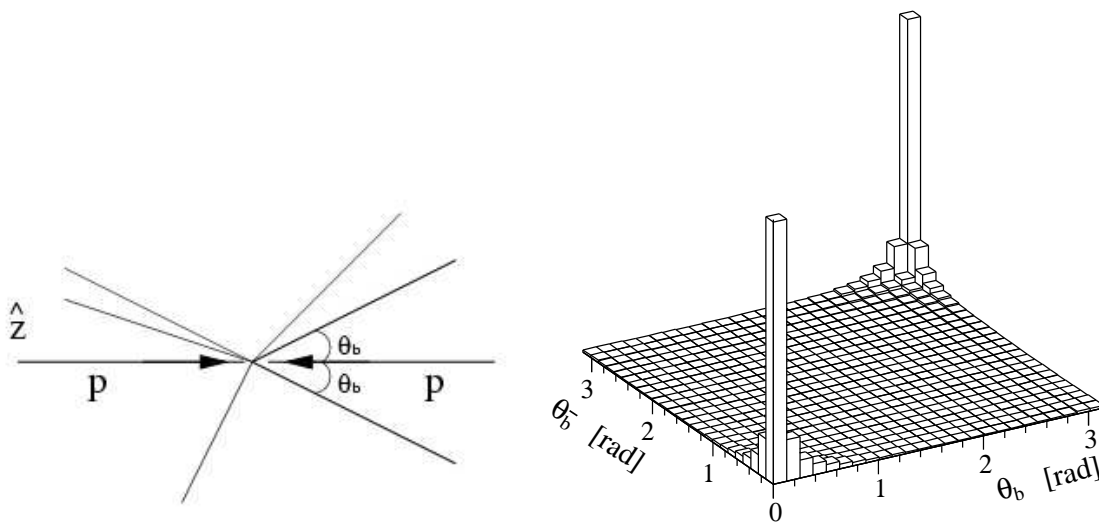


Figure 2.3: (a)  $b\bar{b}$  quark pair production in a proton-proton collision. The  $b$ -hadrons are more likely to be produced in directions close to the beam. (b) Angular distribution of the  $b$  and  $\bar{b}$  quarks. Reproduced from [72].

### 2.2.1 Vertex Locator

The LHCb detector is a detector primarily designed to study CP violation and rare decays in the  $b$ -hadron sector. It is essential for these investigations that the detector reconstructs the particle tracks to a great precision inside its volume and locates the primary interaction and decay vertices. The flight distance is used to identify  $B_s$  mesons. Excellent resolution is needed for time dependent mixing studies in the  $B_s$  system. The vertex reconstruction is performed by the VELO [73]. This section describes the VELO system and its components.

### 2.2.1.1 Overview

The VELO detector was designed to reconstruct the position of the vertices with high precision. For primary vertices the resolution is about  $42\text{ }\mu\text{m}$  in the beam direction ( $z$  axis) and  $10\text{ }\mu\text{m}$  in the transverse plane ( $xy$  plane). Such measurements are necessary for accurate calculations of the lifetime and impact parameter of the  $b$ -hadrons. The decay length resolution ranges from  $220\text{ }\mu\text{m}$  to  $330\text{ }\mu\text{m}$  depending on the decay process of interest. An impact parameter resolution of  $20\text{ }\mu\text{m}$  is expected for those tracks with higher values of transverse momentum ( $> 10\text{ GeV}/c$ ) [73].

The VELO is designed to make precise measurements of the coordinates of the tracks close to the interaction region. The VELO covers not only the angular aperture of the LHCb spectrometer but also has limited coverage in the opposite hemisphere. Using these measurements it is possible to determine the position of the primary and secondary vertices in the observed events.

The VELO system is composed of a series of silicon detector stations placed along the beam direction. There are two halves of the VELO detector. Each half contains 21 modules. The nominal distance of the sensors to the beam during operation will be  $8\text{ mm}$  (closed position). The halves must be retracted during LHC beam injection by  $30\text{ mm}$  each side (opened position) since the aperture required by the LHC machine increases.

Each module has two sensors back to back. The sensors are strip detectors with a half disk shape. The strip pattern depends on the kind of measurement that the sensor performs. It can be an  $R$  or  $\Phi$  measurement and every module contains both types of sensors. The  $R/\Phi$  design matches the strip pitch to the occupancy and allows  $R - Z$  track reconstruction to speed up the trigger. Section 2.2.1.3 discusses the technology of the VELO silicon sensors and the LHCb VELO modules are described in section 2.2.1.4. The main features of the module readouts are discussed in section 3.3.6.

Figure 2.4 shows a cutaway of the VELO detector. Each detector half is mounted in a vacuum vessel made from a  $200\text{ }\mu\text{m}$  thin aluminium sheet. The box geometry allows the two halves to overlap when in the closed position. The corrugations on the surface of the vessel close to the beam axis also minimise material. The VELO detector halves are kept in a secondary vacuum separated from the beam vacuum (also known as the primary vacuum) as shown in the picture. The modules are operated in vacuum in order to minimise the material traversed by the charged particles produced.

Figure 2.5 shows an expanded view of the VELO system. Each VELO half is also equipped with two pile-up VETO stations. The pile-up system aims at distinguishing between crossings with single and multiple interactions. The pile-up is shown at the left-hand side of the picture. The diagram shows the interaction region in blue inside the VELO. The angular acceptance of the detector is also indicated in the diagram.

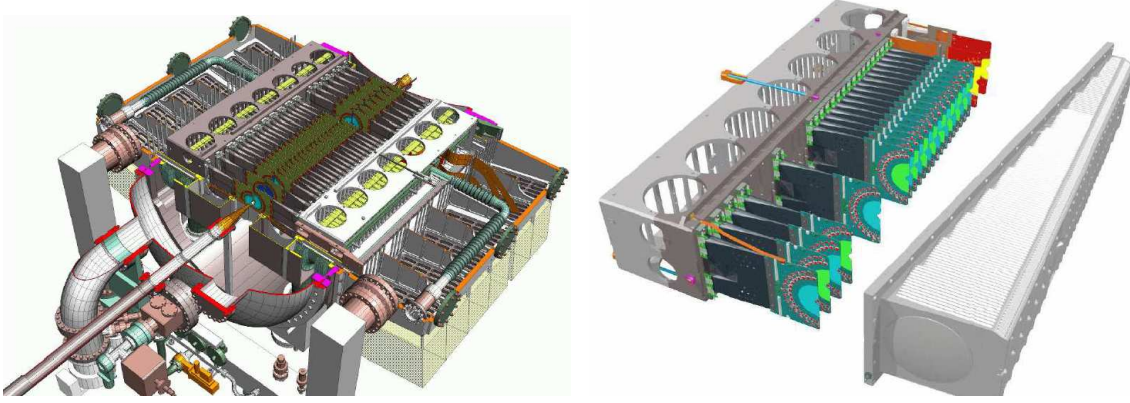


Figure 2.4: On the left-hand side a cutaway of the VELO detector is shown. On the right-hand side one half of the detector with its vacuum vessel is shown. Reproduced from [68].

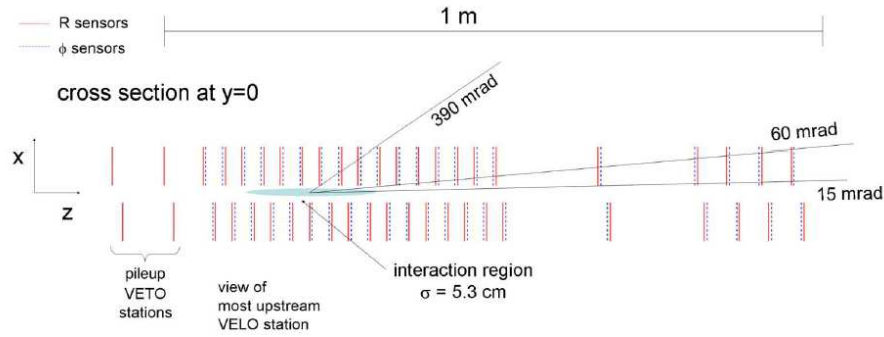


Figure 2.5: Expanded view of the VELO. The position of the VELO modules and the position of the pile-up modules is shown. Reproduced from [68].

### 2.2.1.2 Requirements

The VELO is designed to measure the track coordinates close to the interaction point. It allows the determination of the interaction vertex and the decay vertex of the  $b$ -hadron mesons. These measurements are necessary to obtain the decay time of the  $b$ -mesons and to calculate the impact parameter (IP) of the particles<sup>†</sup>. The distance between the interaction vertex and decay vertex is also used by the high level trigger and offline analysis to select  $b$ -meson events and reject the background events (see chapter 5). To achieve its goals the VELO system must satisfy various requirements. This section discusses the constraints of the VELO system.

### Performance

The VELO system is constrained by the following performance requirements: high signal

<sup>†</sup>In LHCb the impact parameter of a particle with respect to a vertex is defined as the distance of closest approach between the particle track and the vertex.

to noise ratio ( $S/N > 14$ ); channel efficiency higher than 99%; and good spatial resolution <sup>‡</sup>.

### Geometry

The VELO should detect particles with pseudo-rapidities within the range of  $1.6 < \eta < 4.9$ . The primary vertex position in the collisions should be within the  $|z| < 10.6$  cm limit.

Note the distances between the silicon stations on figure 2.5 are such that the track reconstruction can be performed efficiently over the whole angular acceptance of the detector.

Figure 2.6 shows the overlap between two silicon detectors of the VELO. This overlap allows complete coverage of the azimuth angle and is also used on the alignment of the VELO.

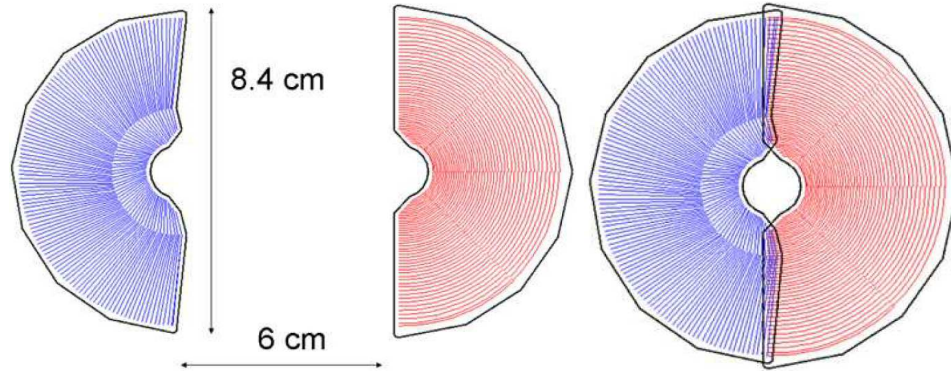


Figure 2.6: VELO station front view. On the left-hand side a VELO station is shown open as during the LHC beam injection. On the right-hand side a VELO station is shown closed. Reproduced from [68].

### Environment

The LHCb VELO modules are designed to operate in a harsh radiation environment with non-uniform particle fluences. The expected fluence range after accumulating  $2 \text{ fb}^{-1}$  is  $5 \times 10^{12} - 1.3 \times 10^{14} \text{ n}_{\text{eq}}/\text{cm}^2$ <sup>§</sup> from the outermost region to the innermost region of the silicon. The VELO system is expected to work for three years of data taking sustaining radiation damage without having its main features significantly changed. Damage effects on the silicon sensors due to radiation exposure are briefly discussed in section 2.2.1.3.

In order to operate the modules it is necessary to use a cooling system to transfer the heat generated by the electronics. This cooling system maintains the silicon sensor temperature between  $-10^\circ\text{C}$  and  $0^\circ\text{C}$ . This temperature range also limits the effects of radiation damage of the silicon sensors.

<sup>‡</sup>The cluster spatial resolution is  $\sim 4 \mu\text{m}$  for 100 mrad tracks within the smaller pitch region.

<sup>§</sup> $\text{n}_{\text{eq}}$  stands for 1 MeV neutron equivalents.



## Integration

The integration of the VELO system to the LHC machine also constrains the detector design. The main VELO features dictated by the LHC requirements are:

- **Box material:** the VELO boxes also have the purpose to protect the modules against Radio Frequency pidiagrammagckup (RF) from the beam and to withstand the pressure difference between the detector vacuum and beam vacuum systems. It protects the LHC vacuum from any outgassing of the detector modules (section 2.2.1.5);
- **Beam - silicon sensors minimum distance:** although the beam size during LHC operation is  $100\text{ }\mu\text{m}$  the closest approach allowed is  $5\text{ mm}$ . Taking into account the VELO box thickness and distance between the sensors and the inner surface of the boxes, the minimum beam-silicon distance allowed is  $8\text{ mm}$ ;
- **Wake field suppression:** the particle bunches crossing the VELO structure induce wake fields which can affect the beam. The wake field suppressors and the VELO boxes provide a continuous surface which controls the action of these electromagnetic fields;
- **VELO positioning:** the VELO halves are mounted in a mechanical positioning system, which is remotely controlled. This system is used to retract the VELO halves in to a safe position during the beam injection, and to centre the VELO around the beam during operation.

Details on the integration of the LHCb detector into the LHC machine can be found at [68].

### 2.2.1.3 Silicon Sensors

The use of semiconductor silicon detectors on LHCb<sup>¶</sup> relies on the fact that these technologies meet the requirements necessary to reconstruct the particle tracks close to the interaction region. This section briefly introduces the silicon sensors technology used in the VELO system. In the proton-proton collisions a number of charged particles are produced. These particles will propagate and pass through the VELO system hitting a certain number of silicon sensors. The position where the particles hit the sensors are measured. Combining these hit positions allows the reconstruction of the particle track.

The advantage of using silicon detectors to measure particle tracks is that they do not excessively disturb the direction of the particle trajectories nor reduce the particle energy significantly. The spatial resolution of these devices can be very good because they can be highly segmented ( $>40\text{-}100\text{ }\mu\text{m}$  for the VELO sensors).

---

<sup>¶</sup> Silicon detectors have been widely employed as vertex detectors. Some examples of collaborations which employed these technologies are: Aleph, Delphi, CDF, Babar, Belle, ATLAS, CMS, LHCb.



An ionising particle passing through the material of a semiconductor detector generates electron-hole pairs inside this material. Using appropriate electronics it is possible to determine if a particle hits the sensor by collecting the charge carriers in the material. The carriers are separated by applying an electric field avoiding the recombination of electrons and holes in the bulk of the detector.

### **The $pn$ junction and the p-on-n sensors**

The functioning principle of all silicon detectors is based on  $pn$  junctions [74]. A  $pn$  junction can be roughly defined as a combination of two semiconductor layers with different doping types. A semiconductor can have two types of impurities: donors or acceptors. Donors are atoms which have an extra valence electron when compared to silicon and acceptors are atoms with less one valence electron when compared to silicon. A silicon substrate doped with donors (acceptors) is called n-type (p-type).

Silicon lattices are formed through covalent bonds between the atoms. The multiple atomic interactions results in a structure of energy bands. Each band has many energy levels slightly different from each other. These bands can be considered as near continuous bands of energy. The highest filled band is usually referred to as the valence band and the lowest empty band is called the conduction band. The energy separation between these two bands is called the energy gap,  $E_g$ . The energy gap for silicon is  $\sim 1.12$  eV. If enough energy is provided one electron can be promoted from the valence band to the conduction band. A hole is left in the valence band.

The interface between the  $p$  and  $n$  layers in the  $pn$  junction is called the depletion region. In this region there are no carriers. It happens because the electrons in the n-type material available in the vicinity of the interface flow to the p-type layer recombining with the holes available. The flow of holes from the p-type layer to recombine with electrons in the n-type layer also occurs.

The depletion region is the active part of the silicon detectors. The width of the depletion region is usually very narrow but for particle detector purposes it is significantly increased by applying a bias voltage.

Figure 2.7 shows the schematics of a p-on-n strip detector. A particle passes through the silicon and deposits a small part of its energy in the depletion region generating pairs of electron-holes. These charge carriers flow according to the electric field and are collected on the p-type strips (anodes).

### **The n-on-n and n-on-p sensors**

The VELO silicon sensors are based on n-on-n technology. The approach used allows the production of sensors with higher radiation tolerance. The VELO sensors can operate fully depleted for a period of three full years ( $6 \text{ fb}^{-1}$ ) in the LHCb radiation environment.

Figure 2.8 shows a diagram which illustrates the difference between p-on-n and n-on-n

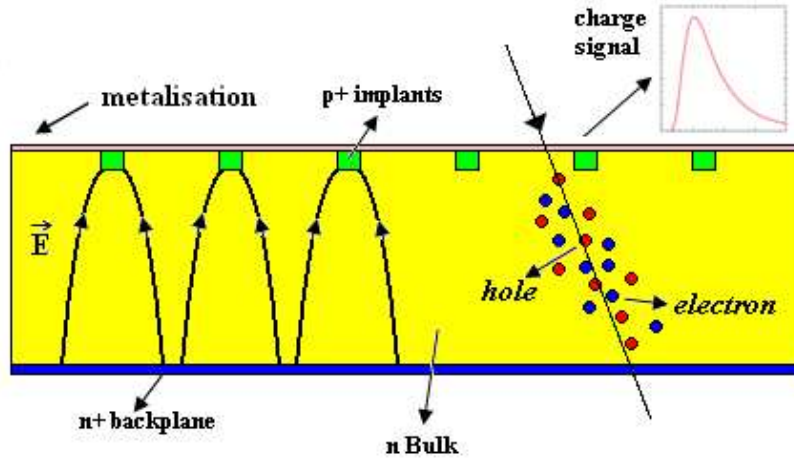


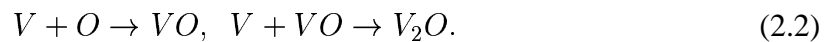
Figure 2.7: p-on-n microstrip detector diagram. In the diagram the p-type implants are denoted as  $p^+$  because they are heavily doped. Same applies to the  $n^+$  definition. The electric field lines within the depleted sensor are shown.

detectors. One of the advantages of the n-on-n or n-on-p detectors is that after the radiation exposure of these devices the spatial resolution and signal to noise ratio (S/N) are less degraded than for the p-on-n devices. This occurs because after the radiation exposure of the sensors the voltage depletion increases, effectively an undepleted region may appear in the material if the detector can not be fully depleted [75]. This becomes a problem if the voltage depletion increases considerably and it is not possible to supply this voltage without breakdown. This region is located in different sides of the devices as it is indicated on the bottom row of figure 2.8. For the p-on-n technology the effective undepleted region could appear in the vicinity of the readout strips while in the n-on-n technology the effective undepleted region could appear close to the backplane.

Another improvement on the silicon radiation hardness is achieved by incorporating impurities or defects in the material. The main idea is to reduce the effect of the radiation-induced vacancies by using a material rich in oxygen. Expression 2.1 indicates how di-vacancies are formed in the silicon without oxygen,



Note in this case the space charge favours type inversion from  $n$  to  $p$ . The presence of oxygen in the material reduces the di-vacancies formation as the following processes might occur:



The intermediate step which yields  $VO$  retards the formation of di-vacancies since the space charge is null. Therefore it slows down the type inversion until  $V_2O$  is formed. More details on the n-on-n or n-on-p technology can be found at [76].

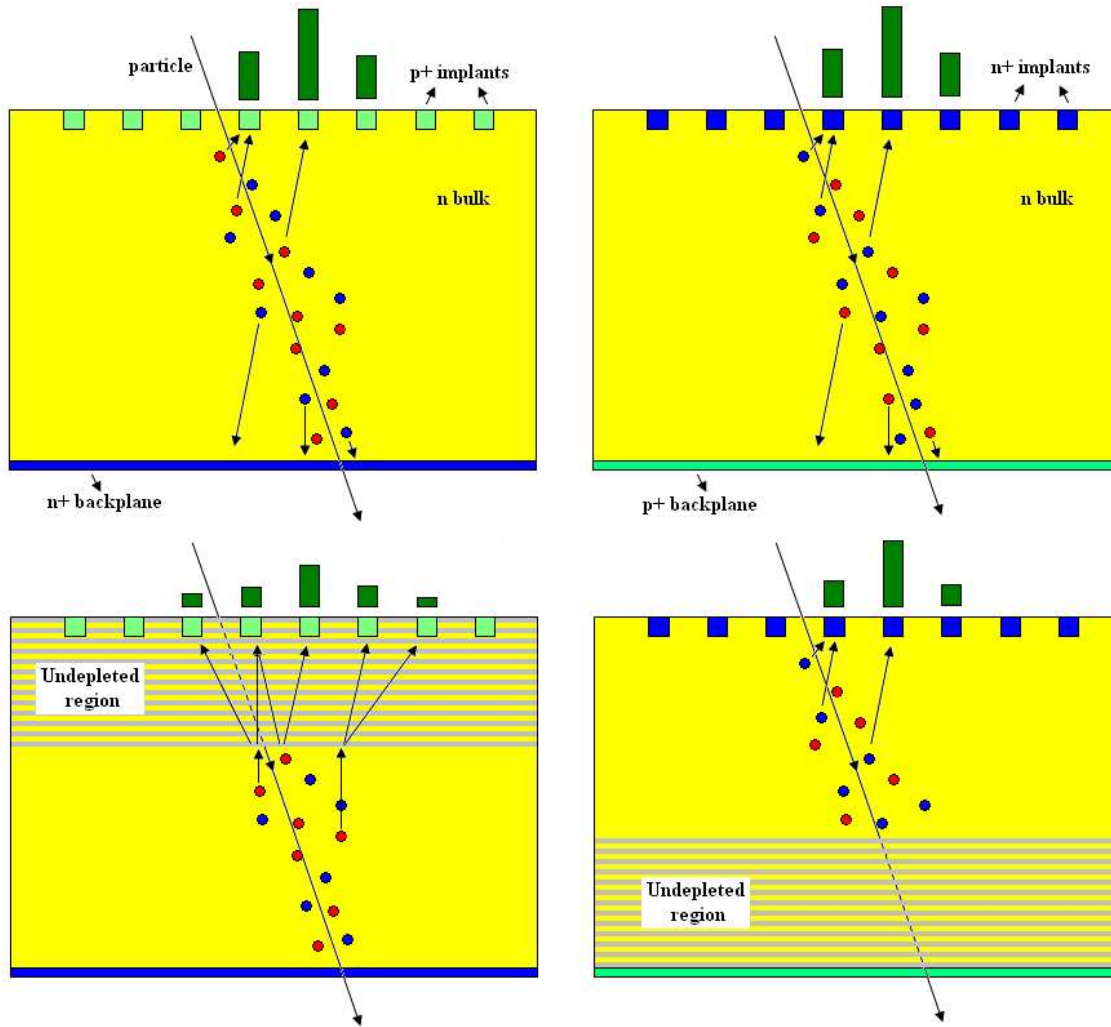


Figure 2.8: Comparison between p-on-n (left) and n-on-n (right) microstrip detectors before (top) and after (bottom) radiation exposure. The green bars on the top of each diagram illustrates the signal amplitude read out on each strip.

The VELO sensors are silicon n-on-n oxygenated sensors with  $300\text{ }\mu\text{m}$  thickness. They were optimised for long term operation under the LHCb radiation environment. The maximum fluence rates on this non-uniform environment were estimated to be  $\sim 1.3 \times 10^{14}\text{ n}_{\text{eq}}/\text{cm}^2$ <sup>||</sup> per year. After approximately  $6\text{ fb}^{-1}$  it might not be feasible to operate the VELO detectors. That is because the depletion voltage necessary to operate the modules will be too high ( $\sim 500\text{ V}$ ). The modules will be replaced and the n-on-p technology will be used in the new modules. The n-on-p sensors have similar performance when compared to the n-on-n. However, the production of the n-on-p sensors is simpler and  $\sim 40\%$  cheaper.

### The VELO sensors layout

<sup>||</sup>The radiation dose sustained by the VELO sensors is due to charged particles. However, it is given in  $\text{n}_{\text{eq}}$  which stands for 1 MeV neutron equivalents.

This section introduces the main features of the VELO sensors microstrip design. As already mentioned there are two different patterns of strips on the VELO silicon sensors. The sensor microstrips can be of R or  $\phi$  pattern. Figure 2.6 shows both patterns.

The strips on the R sensors have an annular shape with length increasing from 4.0 mm to 34.0 mm from the innermost region to the outermost region respectively. The inter-strip pitch size varies from 40  $\mu\text{m}$  to 100  $\mu\text{m}$ . The strips are set in an arrangement of 4 sectors. Each sector has the same size and contains the same number of strips.

The strips on the  $\Phi$  sensors have a radial geometry and are divided in inner and outer strips. The total of inner and outer strips are 683 and 1365 respectively. The length of the inner and outer strips are 9.3 mm and 24.9 mm respectively. The pitch size on the  $\Phi$  sensors varies between 37  $\mu\text{m}$  and 98  $\mu\text{m}$ . To improve pattern recognition the inner and outer strips of the  $\Phi$  sensors make a small angle with respect to the radial. At 8 mm from the beam the inner strips have 20 ° with respect to the radial. At 17 mm from the beam the outer strips have an angle of  $-10^\circ$  to the radial (see figure 2.6).

In LHCb the sensors are installed on modules. Each module has two sensors. The LHCb modules and its components are described in section 2.2.1.4.

#### 2.2.1.4 The VELO Modules

A description of the LHCb modules is given in this section. The VELO module is composed of two silicon strip detectors attached on a hybrid which is glued to a carbon fibre support paddle [77] \*. Figure 2.9 shows the  $\Phi$  sensor of a production module. The electronic components are also mounted and connected on the hybrid. The charge readout of each sensor is performed by 16 Beetle chips [78] whose location is indicated in figure 2.9. The main features of the Beetle chip and hybrid are presented below. Signals are sent to and read out from the modules through kapton cables which are connected to the modules via cable connectors. The power supply for the detector electronics is also supplied through these kapton cables. There are 4 negative temperature coefficient thermistors (NTCs) on the hybrid †. The kapton cable connectors and NTC positions on the hybrid are also shown in figure 2.9. The cooling interface, where the hybrid is glued to the paddle, has 5 captive screws to allow the cooling attachment (see section 2.2.1.6). For simplicity the modules can be referred to as R glued or  $\Phi$  glued because they can either have the R or  $\Phi$  side of the hybrid glued to the paddle. The module in figure 2.9 is a  $\Phi$  glued module. The paddle is made of a low mass carbon fibre piece attached to a carbon fibre base.

#### Beetle Chips

---

\* As explained in section 2.2.1.3 each module has two sensors. One of the sensors is used to perform  $\Phi$  measurements while the other performs R measurements.

† NTCs are solid-state temperature sensors that work like temperature-sensitive resistors. However, as the temperature increases the device resistance decreases.

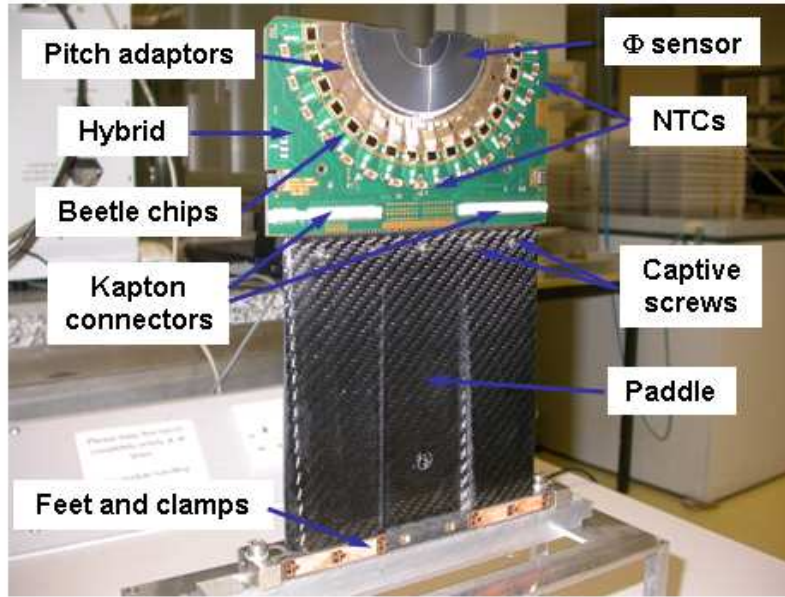


Figure 2.9: A photograph of a  $\Phi$  glued LHCb VELO module and its components.

The Beetle chip is a readout device for silicon strip detectors. It is a Bipolar CMOS ASIC fabricated in  $0.25\ \mu\text{m}$  technology designed to be radiation hard. It will operate in 40 MHz analogue readout mode and trigger rates up to 1.1 MHz can be sustained. Technical details on the design requirements and the specifications are found at [78].

The VELO module has a total of 4096 strips, with 2048 per sensor. The signals are read out from the strips using Beetle front-end chips. Each Beetle chip reads out 128 strips, hence 32 Beetle chips are necessary to read out the module, with 16 chips per sensor. One single Beetle chip has its readout channels arranged in a set of four ports on the readout multiplexing analogue mode<sup>‡</sup>. Therefore one port has 32 channels. In total 1344 chips will be operated on the 42 modules of the VELO.

The analogue signal collected in the strips of the silicon sensor is integrated through a pre-amplifier. The integrated signal is then delivered to a shaper amplifier which formats the pulse in order to obtain the appropriate response. After the shaper, the signal is sampled into an analogue pipeline (160 stages) to match the trigger latency (see section 2.2.7). The data is brought off chip at a clock frequency of 40 MHz, with 32 channels multiplexed on each of the 4 output lines.

## Hybrid

The hybrid is implemented as a flexible kapton circuit which encapsulates a substrate to

<sup>‡</sup>The Beetle chip can operate in analogue mode or binary mode. The analogue mode can operate onto 1 or 4 ports (40 MHz). The binary mode operates on two ports (80 MHz).

provide appropriate thermal conductivity to allow the removal of the heat from the front-end and sensors. The hybrid bulk is a Thermal Pyrolytic Graphite substrate (TPG) wrapped by layers of carbon fibre to provide it with strength and for safe handling. The main purpose of the hybrid of the VELO module is to provide electronic support for the sensors. The electronic components such as kapton connectors, thermistors, Beetle chips, pitch adaptors are mounted onto the hybrid. The bias voltage is also supplied to the sensors via the hybrid. In addition it mechanically supports the sensors.

#### **2.2.1.5 Vacuum System**

The LHC beam vacuum is designed to operate at very low pressures. The LHC pressure levels are of the order  $\sim 10^{-8}$  mbar. The VELO system has to operate in a secondary vacuum (pressure  $< 10^{-4}$  mbar) in order to minimise material and avoid any possible contamination of the LHC vacuum.

The VELO vacuum system has two requirements to meet: provide vacuum quality to the system and regulate the venting or evacuation of the system to guarantee no damage. The vacuum vessels can be easily damaged by a 20 mbar pressure difference between the primary and secondary vacuum. The vacuum system is designed to avoid pressure differences higher than 5 mbar during venting and evacuation of the VELO.

#### **2.2.1.6 Cooling System**

The cooling system allows the operation of the VELO detectors in vacuum by transferring the heat generated in the front-end electronics to outside the system. It is also necessary to operate the silicon at lower temperatures because it reduces radiation damage [68].

During operation each LHCb module consumes  $\sim 20$  W. In vacuum this power would raise the temperature and burn electronic components. The cooling system must transfer the heat produced in the electronic components inside vacuum and keep the silicon sensors at temperatures below  $-5$  °C. The cooling is served to the system through small cooling blocks attached to the VELO modules. Inside these cooling blocks a CO<sub>2</sub> coolant gas circulates. The CO<sub>2</sub> is used as coolant because it also presents good radiation tolerance properties.

#### **2.2.1.7 Low Voltage & High Voltage Systems**

To supply the modules with the appropriate voltages two systems were developed: low voltage system (LV); high voltage system (HV).

A multi-channel power supply system serves the low voltages to the VELO and pile-up. The low voltage is used to power on the module electronics and the repeater boards (see section 3.3.6). The high voltage system supplies the silicon sensors reverse bias voltage. The voltage provided to the modules will range from 100–500 V with the operating voltage being

increased as the sensors undergo radiation damage. The LV and HV systems are installed in the detector counting house. Both systems supply interface to the hardware interlock system.

## 2.2.2 Ring Imaging Cherenkov Detectors

One of the major requirements for a satisfactory performance of the LHCb experiment is good particle identification [28, 72]. The identification of hadronic particles in LHCb is important for B decay studies with hadronic particles in the final states. The identification of hadronic particles in LHCb is provided by a system composed of two Ring Imaging Cherenkov Detectors (RICH1 and RICH2)[79, 68]. The Ring Imaging Cherenkov Detector (RICH) system and its components are briefly described in this section.

The particle identification technique employed with RICH detectors is based on the detection of the light rings emitted through the Cherenkov effect. To cover the whole momentum spectrum it is necessary to use different materials with different refractive index. To detect low momenta particles silica aerogel is used. To detect particles within the intermediate momenta range  $C_4F_{10}$  gas is used. High momenta particles are detected using  $CF_4$  gas.

There is a well defined correlation between the particle momentum and polar angle between the particle track and the beam direction,  $\theta_c$ . Low momentum particles have high angles while high momentum particles have small angles. Hence two RICH detectors are used to cover the range completely.

### 2.2.2.1 RICH1

The RICH1 detector is designed to perform particle identification in the range of 1 GeV/c to 60 GeV/c. To cover this range two types of radiators are used, aerogel and  $C_4F_{10}$  gas. The aerogel layer is 5 cm thick with a refractive index of  $\sim 1.03$ . This material facilitates the identification of kaons and pions in the range of 1 GeV/c to 15 GeV/c. The second volume with  $C_4F_{10}$  gas is 85 cm thick with refraction index of  $\sim 1.0014$ . This gas allows the identification of pions and kaons with momentum ranging from 10 GeV/c to 60 GeV/c.

Figure 2.10 illustrates RICH1 and its functioning principle. Cherenkov radiation is emitted if a charged particle passes through a radiator with a speed higher than the light speed inside the radiator media. This light is then reflected and focused by spherical mirrors onto a set of plane mirrors. The light reflected by the plane mirrors is detected by the RICH photodetectors. The size of the ring provides the particle speed, which combined with the momenta measured by the tracker, allows the mass of the particle to be identified. Note the interaction point is on the left-hand side of the diagram. The RICH photodetectors are described in section 2.2.2.3. This combination of mirrors is used in order to minimise the amount of material inside the LHCb detector acceptance. The RICH1 has an iron shielding to protect the detector against the residual magnetic field effects of the LHCb magnetic dipole.

The right hand-side photo shows the gas enclosure of the RICH1. Note the interaction point is on the right-hand side in this photograph.

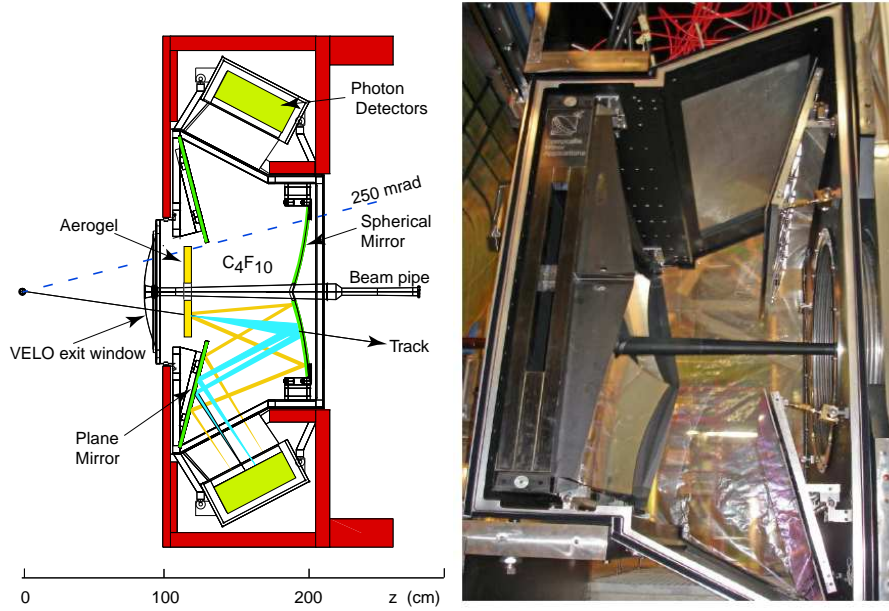


Figure 2.10: On the left-hand side a schematic diagram of the RICH1 is shown. On the right-hand side a photograph of the RICH1 gas enclosure is shown. Reproduced from [79, 68].

### 2.2.2.2 RICH2

RICH2 identifies the particles with momentum between 50 GeV/c and 150 GeV/c. It uses the CF<sub>4</sub> gas as a radiator material. The effective thickness of the radiator is  $\sim 167$  cm with a refractive index of 1.0005. The mirror arrangement is similar to that used in RICH1. Figure 2.11 shows the RICH2 detector. Note the angular acceptance is reduced to  $\sim 100$  mrad.

Table 2.2 shows the resolution obtained for the emission angle of the Cherenkov radiation. It also shows the average number of photons detected per particle for the three types of radiators used in LHCb.

The total area of the photodetector arrangement of the whole RICH system is  $\sim 3.5$  m<sup>2</sup> with an active area estimated to be  $\sim 2.24$  m<sup>2</sup>. The granularity of the detectors is expected to be  $2.5 \times 2.5$  mm<sup>2</sup> at the photocathode window providing detection of the Cherenkov radiation rings. The number of photodetectors installed in RICH1 and RICH2 are respectively 196 and 288.

### 2.2.2.3 The Hybrid Photon Detectors

Hybrid Photon Detectors (HPD) are photodetectors which combine vacuum photo-cathode technology with solid state technology [80]. Figure 2.12 shows a diagram of a HPD detector.



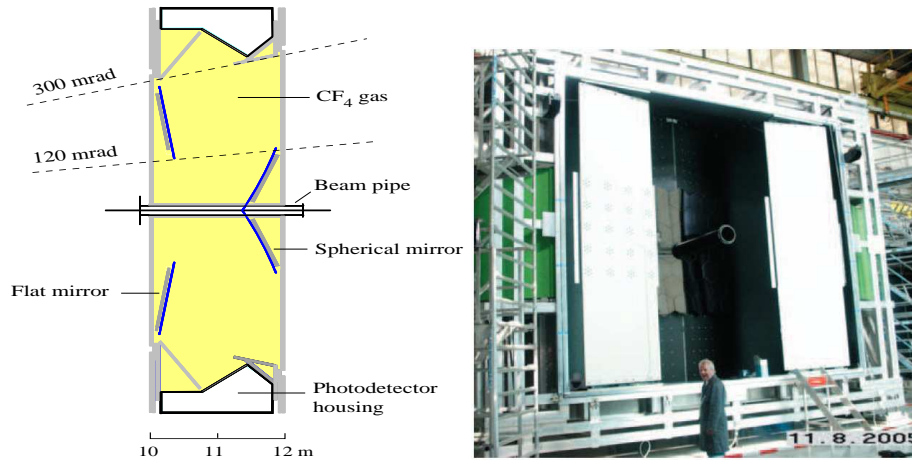


Figure 2.11: On the left-hand side a schematic diagram of the RICH2 is shown. On the right-hand side a photograph of the RICH2 partially assembled. Reproduced from [79, 68].

Table 2.2: Characteristics of the radiators used in the RICH system: radiator width  $L$ , refraction index  $n$ , maximum angle  $\theta_c^{max}$ , angular resolution  $\sigma_{\theta_c}$  and average number of detected photons per particle  $N_{photons}$ .

| Parameter           |        | $CF_4$ | $C_4F_{10}$ | Aerogel |
|---------------------|--------|--------|-------------|---------|
| $L$                 | (cm)   | 167    | 85          | 5       |
| $n$                 |        | 1.0005 | 1.0014      | 1.03    |
| $\theta_c^{max}$    | (mrad) | 32     | 53          | 242     |
| $\sigma_{\theta_c}$ | (mrad) | 0.58   | 1.45        | 2.00    |
| $N_{photons}$       |        | 18.4   | 32.7        | 6.6     |

When a photon from Cherenkov emission hits the photo-cathode of the detector it releases a photo-electron. This electron is accelerated towards the pixel silicon detector by an electric field (10 – 20 kV). The electric field acts as an optical system (lens). The electron hits the silicon surface and its kinetic energy is dissipated creating  $3 - 5 \times 10^3$  electron-hole pairs. By collecting this charge it is possible to reproduce the light pattern on the cathode.

The silicon detector is based on the pixel technology. It is segmented in a matrix of  $32 \times 256 = 8192$  pixels with  $500 \mu\text{m} \times 62.5 \mu\text{m}$  size. Eight consecutive pixels are combined in an electronic “OR” to produce 1024 super-pixels of  $500 \mu\text{m} \times 500 \mu\text{m}$  effective size. The electronics speed is compatible with the bunch crossing rate of 25 ns.

### 2.2.3 Magnet

The LHCb detector possesses a dipole magnet to perform measurements of the particle momenta [28, 81, 68]. This measurement is obtained through the analysis of the particle tracks

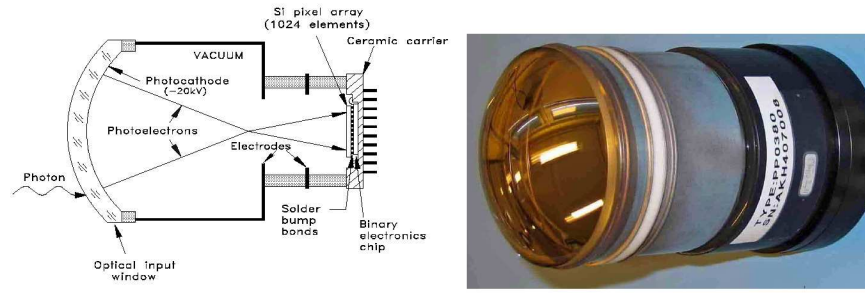


Figure 2.12: On the left-hand side a schematic diagram of the HPD is shown. On the right-hand side one HPD tube is shown. Reproduced from [68].

before and after the magnet region. The precision of the measurements of the particle momenta is  $\sim 0.4\%$  with values of momentum up to  $200 \text{ GeV}/c$ . To achieve this precision an integrated magnetic field of  $4 \text{ Tm}$  is necessary. Field uniformity along the transverse direction is also required. The system which performs the measurements of the particle momenta is detailed in section 2.2.4.

The magnet is a conventional (non-superconducting) warm dipole. Its magnetic field can be reversed regularly during LHCb data taking. This is a requirement to perform studies on systematic asymmetries. Figure 2.13 shows a diagram of the magnet.

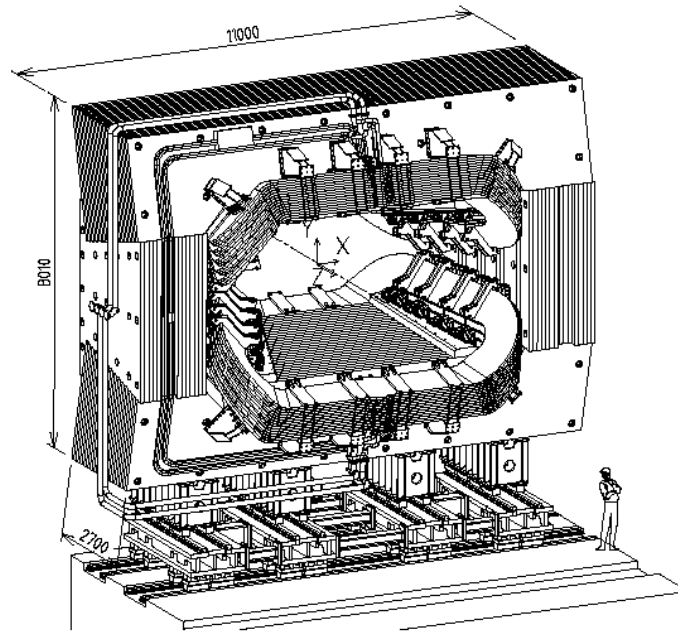


Figure 2.13: Diagram of the LHCb Magnet. Reproduced from [81].

## 2.2.4 Tracking System

The tracking system is designed to determine the particle tracks in the region between the two RICH detectors. It also performs the measurement of the particle momenta. In this section the tracking system is presented. More details are available at [82, 83, 68].

The tracking consists of 4 stations placed along the beam direction. It is divided in two parts: the first part is the so-called tracker turicensis (TT); the second part is composed by three stations (T1, T2, T3).

The measurements of the particle tracks on the tracking system can be combined with measurements from other sub-subsystems. For example, these tracks are used to associate the measurements of the VELO system with the measurements performed on the other sub-systems. This allows the reconstruction of the complete trajectory of each particle. The tracks obtained can also provide additional information for the RICH measurements. This allows the association of the tracks with their corresponding RICH identification.

### 2.2.4.1 Tracker Turicensis

The TT system and the VELO perform measurements of the particle tracks before the magnet. It also provides information to the displaced vertex component of the high level trigger [72] (see section 2.2.7).

The TT consists of four silicon detector layers arranged in two pairs,  $(x, u)$  and  $(v, x)$ . Figure 2.14 shows the layout of the silicon detector layers on the TT station. Each pair has one layer equipped with vertical readout strips ( $x$ ) and one layer equipped with readout strips rotated by a stereo angle of  $\pm 5^\circ$  with respect to the vertical direction. The  $u$  direction corresponds to a positive rotation ( $+5^\circ$ ) and the  $v$  direction corresponds a negative rotation ( $-5^\circ$ ). On the left-hand side the  $x$  layer is shown and on the right-hand side the  $u$  layer is shown. This arrangement avoids ambiguities between the measured hits and allows the measurement of the transverse component of the particle momenta. The active area of the TT is  $8.4 \text{ m}^2$  with 143360 readout strips.

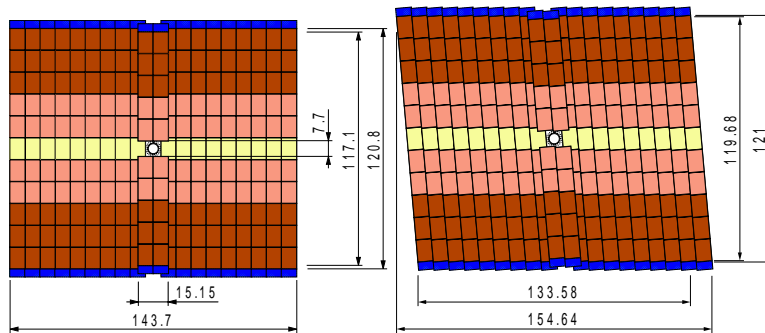


Figure 2.14: Tracker Turicensis layers. On the left-hand side the vertical  $x$  layer is shown and on the right-hand side the rotated  $u$  layer is shown. Reproduced from [72].

### 2.2.4.2 Tracking Stations

The tracking stations T1, T2, and T3 are each composed of two parts: inner tracker [82] and outer tracker [83]. The reason for this design is because different technologies are employed in the inner and outer regions to reconstruct the particles track in the tracking stations. The technologies used are described in the following sections.

#### Inner Tracker

The inner tracker is composed of layers of strip detectors with a design similar to the TT. Each of the 3 stations has 4 layers with the same layout described before  $(x, u, v, x)$ . This technology attends the requirements necessary to perform measurements in the inner region of the tracking system. The system has a spatial resolution of  $\sim 50 \mu\text{m}$  and  $\sim 1\%$  occupancy per channel.

#### Outer Tracker

The outer tracker is a drift-time detector. Each of the 3 stations is composed of 4 layers with the  $(x, u, v, x)$  layout. Each layer is composed of straw-tube modules. Figure 2.15 shows a module diagram. Each module contains two layers of drift-tubes with of 4.9 mm inner diameter. To guarantee fast drift time ( $\sim 50 \text{ ns}$ ) and spatial resolution of  $\sim 200 \mu\text{m}$  a mixture of Argon (70%) and  $\text{CO}_2$  (30%) is used.

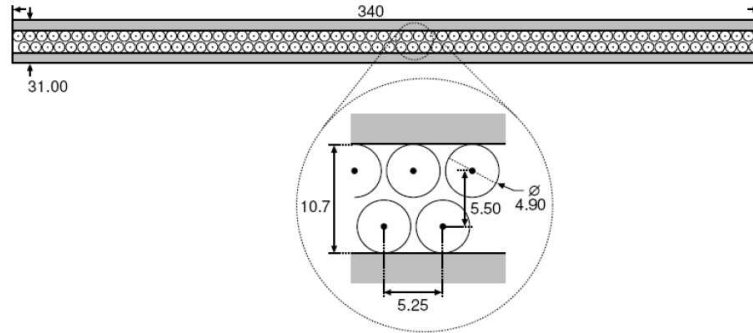


Figure 2.15: An outer tracker module diagram. Dimensions are given in cm. Reproduced from [72].

Figure 2.16 shows the assembly of a T station with its inner and outer components. The front view of the T station is shown on the left-hand side. The side view of the T station is shown on the right-hand side.

### 2.2.5 Calorimeters

The LHCb calorimeters are designed to measure energy and hit position of hadrons, photons and electrons providing fast information for the level 0 trigger [84, 68]. They are also

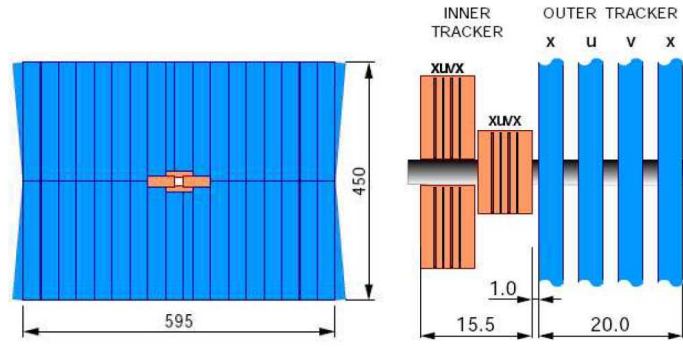


Figure 2.16: A tracking station diagram. The front view of the T station is shown on the left-hand side. The side view of the T station is shown on the right-hand side. Reproduced from [72].

part of the particle identification system. The calorimetry system is composed of Scintillator Pad Detector (SPD), Pre-shower (PS), Electromagnetic Calorimeter (ECAL) and Hadronic Calorimeter (HCAL). A description of the components of this system is given in the following sections.

### 2.2.5.1 SPD and PS

The SPD/PS system consists of two scintillator layers separated by a 15 mm lead plate. The SPD is the first layer of the calorimetry system of the LHCb. It detects charged particles separating electrons and photons. As a result it reduces the  $\pi^0$  contamination of the electron trigger. The lead plate induces electromagnetic showers. The PS is used to measure the initial position of the showers and separates electrons and charged pions.

The light signal from both SPD and PS are collected via Wave Length Shifter fibres and conducted to multianode photomultipliers outside the detectors through an optical system. The signal is then amplified and read out.

The SPD and PS have a variable lateral segmentation because the hit density varies by two orders of magnitude from the inner region to the outer region. The segmentation scheme for the SPD, PS and ECAL is shown in figure 2.17.

### 2.2.5.2 Electronic Calorimeter

The LHCb ECAL is designed to measure the energy of the photons and the electrons selecting these particles for the level 0 trigger. The technology used is based on the combination of layers of scintillator material and lead. The ECAL is composed of modules. The modules are composed of alternating layers of 2 mm lead and 4 mm scintillator tiles. Each module has 66 layers of lead and 66 scintillator tiles with a total radiation length of  $25X_0^{\parallel}$ .

$^{\parallel}X_0$  is the characteristic radiation length.

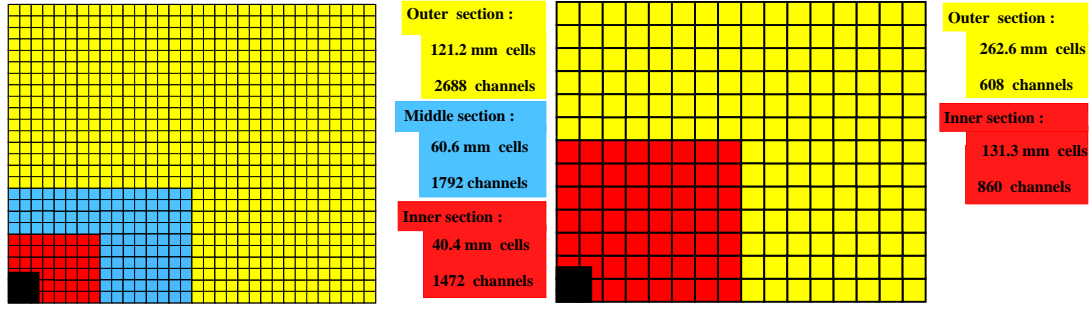


Figure 2.17: On the right-hand side the segmentation of the SPD, PS and ECAL is shown. It has 3 different regions. On the left-hand side the segmentation of the HCAL is shown. It has 2 different regions. Reproduced from [84].

The ECAL has a readout system similar to that used on the SPD/PS detectors. However the signals are amplified by phototubes. Figure 2.18 shows the different types of ECAL modules and the whole ECAL detector installed. The modules in the inner region have 9 cells, those in the intermediary region have 4 cells and in the outer region have a single cell. The energy resolution of the ECAL is

$$\frac{\sigma_E}{E} = \frac{10\%}{\sqrt{E}} \oplus 1\%, \quad (2.3)$$

where  $E$  is given in GeV.

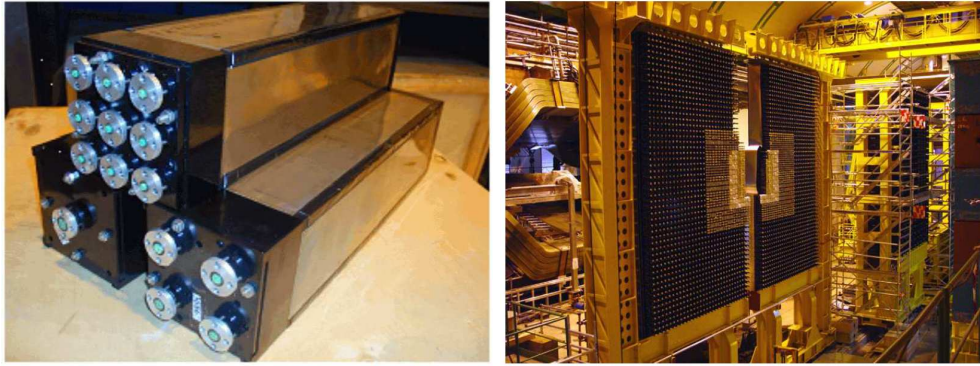


Figure 2.18: ECAL modules and the complete ECAL detector. Reproduced from [68].

### 2.2.5.3 Hadronic Calorimeter

The HCAL provides fast information to the hadronic level 0 trigger. It has to measure  $E_T^{**}$  with a time rate compatible with the bunch crossing time (25 ns). It also provides information on hadronic particle identification.

<sup>\*\*</sup>  $E_T$  is the transverse energy defined as  $E_T = E \sin \theta$  where  $E$  is the total energy deposited in the calorimeter, and  $\theta$  is the opening angle.

The HCAL structure alternates scintillator tiles and iron plates. Both scintillators and iron plates are parallel to the beam direction. The scintillators are 4 mm thick and the iron plates 12 mm thick. The lateral segmentation for the HCAL is shown in figure 2.17. The energy resolution is given by

$$\frac{\sigma_E}{E} = \frac{80\%}{\sqrt{E}} \oplus 10\%, \quad (2.4)$$

where  $E$  is the energy in GeV.

Table 2.3 summarises the main features of the different components of the calorimeters. The resolution of the calorimeters were obtained from analyses of test beam data.

Table 2.3: Parameters of the calorimeters.

| sub-detector       | SPD/PS               | ECAL   | HCAL  |
|--------------------|----------------------|--|---|
| number of channels | $2 \times 5952$      | 5952   | 1468  |
| dimensions $xy$    | 6.2 m $\times$ 7.6 m | 6.3 m $\times$ 7.8 m                                     | 6.3 m $\times$ 7.8 m                                      |
| length $z$         | 180 mm, $2X_0$ ,     | 835 mm, $25 X_0$ ,                                       | 1655 mm, $5.6 \lambda_I^{\dagger\dagger}$                 |
| resolution         | 20-30 $e/\text{MIP}$ | $\frac{\sigma(E)}{E} = \frac{10}{\sqrt{E}}\% \oplus 1\%$ | $\frac{\sigma(E)}{E} = \frac{80}{\sqrt{E}}\% \oplus 10\%$ |

## 2.2.6 Muon System

In this section the LHCb muon system is briefly described. This system provides fast information for the high  $p_T$  muon level 0 trigger. It also provides muon identification for the high level trigger and offline analysis (see section 2.2.7) [85, 68].

The muon system consists of 5 detector stations. These stations are referred to as M1-M5. The station M1 is located between the RICH2 and the calorimeters. The four stations M2-M5 are located after the calorimeters. The M1 station provides transverse momentum measurements for the trigger system. Iron filters with 80 cm thickness are used between the M2-M5 stations. The iron filters avoid any possible electron or hadron contamination. Only muons with energy above 6 GeV reach the M5 station.

Each station is divided in regions with different segmentation. According to the proximity to the beam these regions are called R1, R2, R3, R4. Figure 2.19 shows the transverse segmentation of the M1 station. Two different technologies are adopted for the muon detectors: Gas Electron Multipliers (GEM) and Multiple Wire Proportional Chambers (MWPC).

The GEM modules are used on the region R1 of the station M1. The occupancy on the M1 station is higher than on the other muon stations because it is placed in front of the calorimeters. To cope with this high particle flux in this specific region GEM is the most appropriate technology. On the other hand the simpler MWPC devices are suitable for the rest of the large muon system.



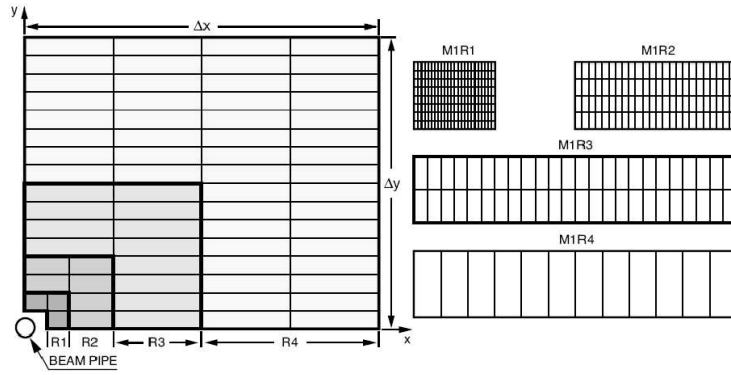


Figure 2.19: M1 segmentation layout. One quadrant of the M1 station is shown. It is divided in four regions as indicated in the figure. The segmentation of each region is also shown. Reproduced from [85].

### 2.2.6.1 Gas Electron Multipliers

The GEM detectors installed in the region M1R1 must satisfy the following requirements: particles flux of  $\sim 500 \text{ kHz/cm}^2$ ; efficiency above 96% within a 20 ns time interval; and radiation hardness [86].

The GEMs used in LHCb have a triple layer layout. Figure 2.20 shows a diagram of these devices. A single foil GEM is made of a  $50 \mu\text{m}$  thick Kapton sheet covered with  $5 \mu\text{m}$  copper layer on both sides. This foil has a high density of bi-conical holes with internal and external radius equals to  $50 \mu\text{m}$  and  $70 \mu\text{m}$  respectively. The distance between the holes is  $140 \mu\text{m}$ . The combination of multiple layers provides high signal gain. The values for the drift, transfer and induction electric fields indicated in the figure are  $E_d = 3.5 \text{ kV/cm}$ ,  $E_t = 3.5 \text{ kV/cm}$  and  $E_i = 5 \text{ kV/cm}$  respectively. The drift, transfer and induction layers are respectively  $g_d = 3 \text{ mm}$ ,  $g_t = 1$  and  $2 \text{ mm}$  and  $g_i = 1 \text{ mm}$  respectively. A gas mixture composed by  $\text{Ar}(45)\text{CO}_2(15)\text{CF}_4(40)$  is used in the detectors.

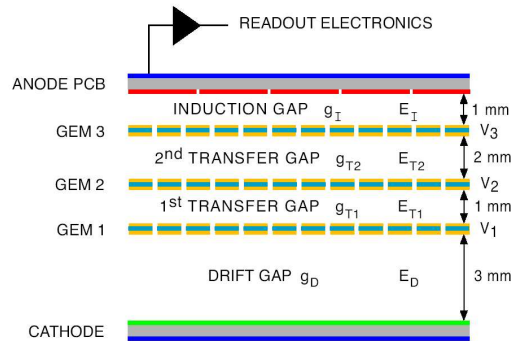


Figure 2.20: A triple GEM detector. The multiple layers provide high signal gain. Reproduced from [68].



In the M1R1 region 12 chambers with  $20\text{ cm} \times 24\text{ cm}$  active area are used. Each chamber has two triple GEMs to ensure redundancy. The total active area of the system is  $0.6\text{ m}^2$ .

### 2.2.6.2 Multiple Wire Proportional Chambers

Figure 2.21 shows a diagram of a MWPC layer. These chambers have a symmetric cell with a distance between anode to cathode of  $2.5\text{ mm}$ . The distance between wires is  $1.5\text{ mm}$ . The mixture  $\text{Ar}(40)\text{CO}_2(50)\text{CF}_4(10)$  is used as ionising gas. In the M2-M5 stations a MWPC chamber consists of four detector layers resulting in an efficiency higher than 95% with integrated time less than  $20\text{ ns}$ . Similar efficiency is obtained with the two layer chambers used in the outer regions of M1. The distance between wires is  $2.0\text{ mm}$  on these chambers.

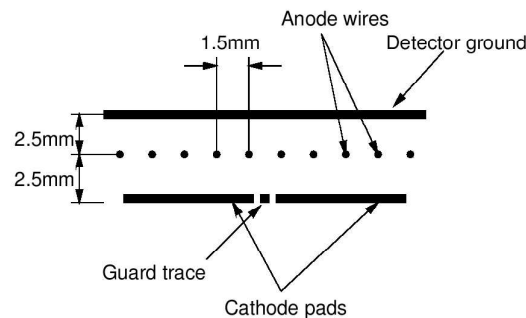


Figure 2.21: MWPC layer. The anode-cathode distance is  $2.5\text{ mm}$  and the distance between the wires is  $1.5\text{ mm}$ . Reproduced from [85].

Figure 2.22 shows the two types of MWPC used. On the left-hand side a diagram for a 4 layer chamber is shown. On the right-hand a photograph of a two layer chamber before its installation in a Faraday cage is shown.

## 2.2.7 Trigger System

The number of events to be generated in LHC is extremely high when compared to previous experiments in high energy physics. This vast amount of data cannot be recorded due to limited readout speed and storage capacity. However, from these events only a small fraction is interesting for physics analyses. The LHCb trigger is a global system which uses information from different detectors to select only the events interesting for physics analyses. The selected events are recorded on disk and the events which do not pass the trigger requirements are immediately discarded<sup>††</sup> [87, 68]. The LHCb trigger system is discussed in this section.

In LHCb, the event frequency with visible interactions is  $\sim 10\text{ MHz}$ . This rate is lower than the bunch crossing rate ( $1/25\text{ ns} = 40\text{ MHz}$ ) because of the LHC bunch structure and

<sup>††</sup>The data acquisition system is discussed in section 2.2.8.1.

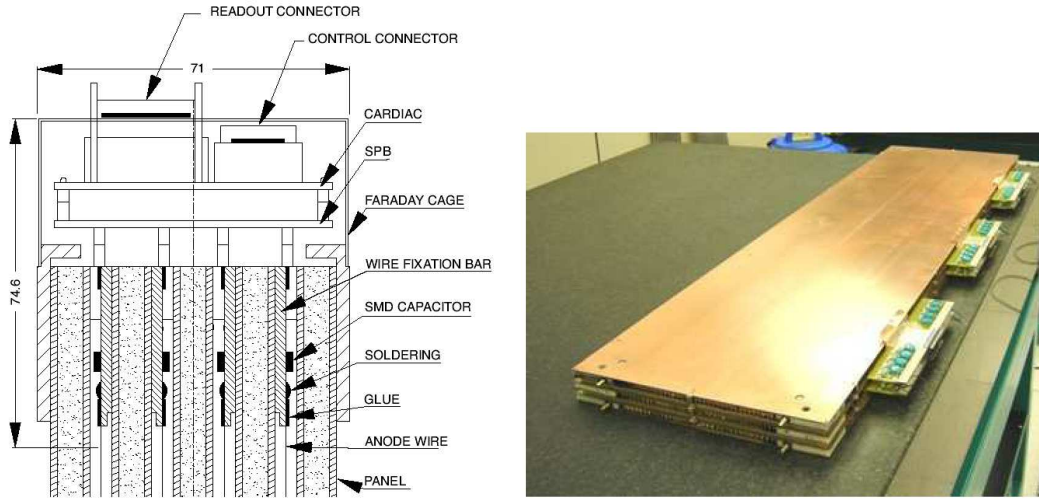


Figure 2.22: Muon chamber pictures. On the left-hand side a diagram for a 4 layer chamber is shown. On the right-hand a photograph of a two layer chamber is shown. Reproduced from [68].

the luminosity. The event rate is reduced to 2 kHz by the trigger system. This reduction is obtained by the two trigger levels: level 0 trigger (L0) and high level trigger (HLT). The L0 trigger is implemented in hardware in order to select events within the latency time ( $1 \mu\text{s}$ ). The HLT operates in asynchronous mode and is software implemented.

Figure 2.23 shows a diagram of the LHCb trigger system. The L0 reduces the input rate to 1 MHz. The HLT takes the 1 MHz rate of selected events by the L0 trigger and accepts 2 kHz. Both levels use information from different parts of the detector. Each level of the LHCb trigger is briefly described in the following sections.

### 2.2.7.1 Trigger Requirements

The LHCb trigger is defined by the topology of the  $B$  meson production inside the detector and by the requirement that its decay products must also be within the detector acceptance. This ensures the  $B$  decays can be completely reconstructed. The aim of the trigger system is to record only events that are of interest for physics analysis.

Among the total visible events in LHCb only a small fraction is expected to be  $b\bar{b}$  events. The estimated rate of  $b\bar{b}$  events is 100 kHz. From these events only 15% contains at least one  $B$  and its decay products inside the detector. To select only these kind of events the trigger system uses selection criteria based on the general characteristics of the  $B$  decays. For example, the decay products of the  $B$  mesons have high transverse momentum and high transverse energy. Through this method the trigger system can keep good efficiencies selecting a wide variety of final states.

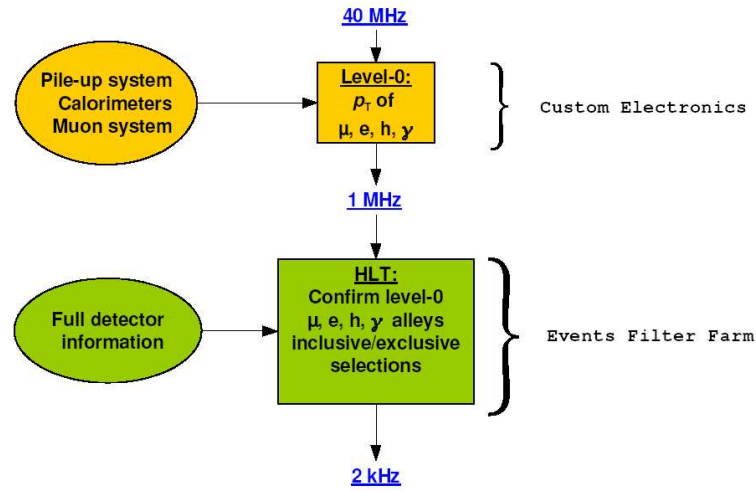


Figure 2.23: Diagram of the trigger system. The event rate is reduced from 10 MHz to 2 kHz. Reproduced from [68].

### 2.2.7.2 The L0 trigger

The L0 trigger reduces the event input rate from 40 MHz to the detector data acquisition rate of 1 MHz. The L0 trigger uses information from three different parts of the detector: pile-up, calorimeters and muon system. These are the only parts of the detector read out at 40 MHz. The following methods are used by the L0 trigger to select events.

- i **Decay product selection:** Hadrons, electrons, photons and muons with high  $E_T$  or  $p_T$  are selected. One event is accepted if at least one of the particles have  $E_T$  or  $p_T$  above certain threshold values. Otherwise the event is discarded. The  $E_T$  and  $p_T$  measurements are provided by the calorimeters and muon system.
- ii **Track Multiplicity selection:** Accurate event reconstruction is only performed if the number of tracks per event is not very high. The SPD provides an estimate of the number of charged tracks by counting the number of fired cells. The pile-up system also provides an estimate of the number of tracks produced in the opposite direction of the LHCb detector ( $-z$ ). The L0 takes into account this information to perform the trigger decision.
- iii **Multiple Interaction selection:** The pile-up system also provides an estimate of the number of interactions per event. Events with more than one interaction are rejected.

The so-called Level Zero Decision Unit (L0DU) process the information from the three L0 components to provide the L0 decision. This L0 decision is transmitted to the readout supervisor which forwards this information to the front-end electronics. If the L0 accepts then readout data from all subdetectors is sent to the LHCb processing farm and a more detailed analysis of the event is performed by the HLT.

### 2.2.7.3 The High Level Trigger

The HLT is a software system with algorithms implemented in C++ code. These algorithms run in the LHCb processing farm which contains up to 2000 computing nodes. The HLT receives the selected events from the L0 trigger at a rate of 1 MHz and accepts a reduced rate of these events. This system uses information from all the sub-detectors to perform event selection. The HLT also has to perform its selection fast in order to cope with the high amount of input events per second delivered by the L0. Therefore, it is implemented in terms of simple selection criteria.

Figure 2.24 illustrates the architecture of the HLT system. The HLT is divided in two stages: HLT1 and HLT2.

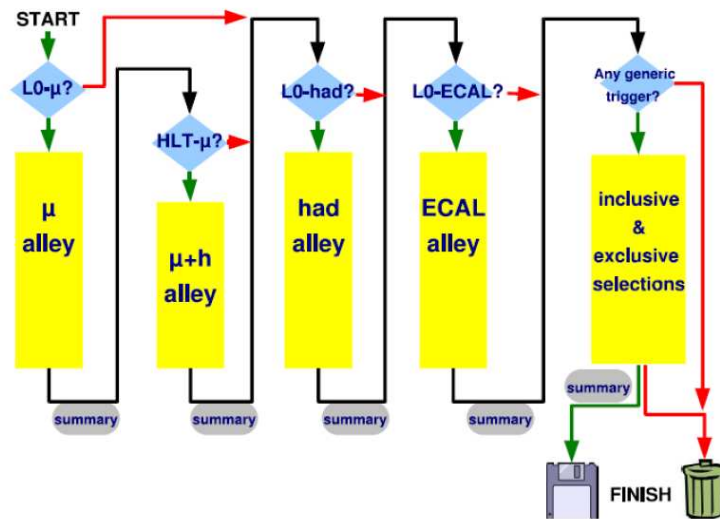


Figure 2.24: The HLT alleys structure. Reproduced from [68].

The HLT1 reconstructs the particles in the VELO and T-stations corresponding to the L0 objects. This part of the trigger is composed of the alley algorithms. According to the classification given by the L0 trigger the event is processed by the corresponding alley (for example: L0 single  $\mu$  decision  $\rightarrow \mu$ -alley; L0 hadron decision  $\rightarrow$  hadron-alley). About  $\sim 15\%$  of the events are accepted by multiple triggers therefore they are processed by more than one alley. The HLT1 reduces the event rate to a value of  $\sim 30$  kHz.

The HLT2 performs exclusive and inclusive triggers. The exclusive part of the algorithm aims to reconstruct specific  $B$  final states. The inclusive part of the algorithm reconstructs partial  $B$  decays, such as  $\phi X$ ,  $J/\psi X$ ,  $D^* X$ ,  $\mu^\pm X$ ,  $\mu^\pm h X$ ,  $\mu^+ \mu^- X$ .

The final trigger is given as the logical OR operation of the exclusive and inclusive selections. The output event rate of HLT is  $\sim 2$  kHz.

## 2.2.8 Online System

The Online system is a global system which is divided into three main sub-systems: Data Acquisition (DAQ), Timing and Fast Control (TFC) and Experiment Control System (ECS). Figure 2.25 illustrates the Online system architecture implemented on the LHCb experiment. Details of the Online system are given at [88, 89]. In this section a brief overview of the main features of each component of the Online system is presented.

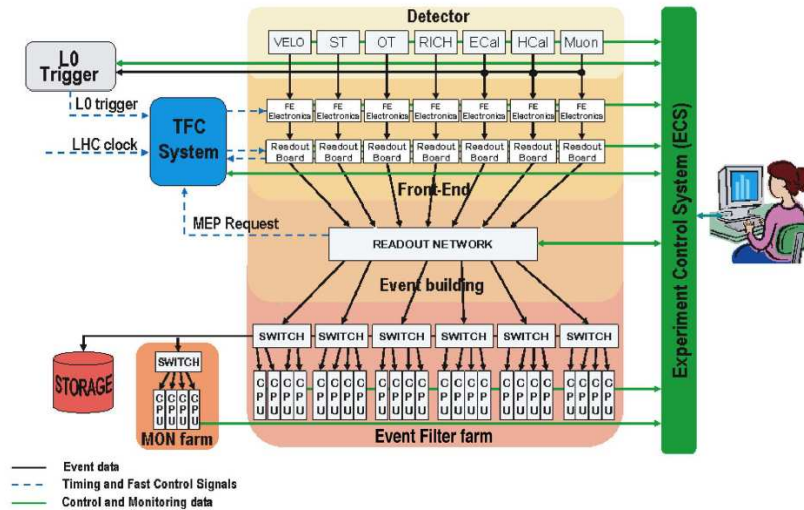


Figure 2.25: Online architecture. The interface of the online system with trigger system and front-end electronics is shown. Reproduced from [68].

### 2.2.8.1 Data Acquisition

The DAQ system delivers the data corresponding to the events selected by the trigger system to the Event Filter Farm (EFF). This system collects and transports the data from the front-end electronics to permanent storage. The main requirements this system satisfies is processing speed and flexibility. The DAQ must be fast in order to cope with the high event rate and able to work with a range of data rates. It must also be able to operate with different event sizes. The average size of a LHCb event is  $\sim 150$  kB.

In LHCb two types of motherboards are used to collect the data from the front-end electronics, to digitise and to perform pre-processing. The UKL1 boards are used on the RICH system data acquisition while the TELL1 boards [90] are used on all the other subdetectors. These boards perform data compactification and data transfer to the EFF computers.

The TELL1 boards and UKL1 boards are controlled by the readout supervisor [91] (see section 3.3.6). The readout supervisor delivers the trigger signal and the computer IP address to which the boards will send the data. The boards send the data to this specific machine in the EFF and a software algorithm is used to assemble the whole event combining all the parts

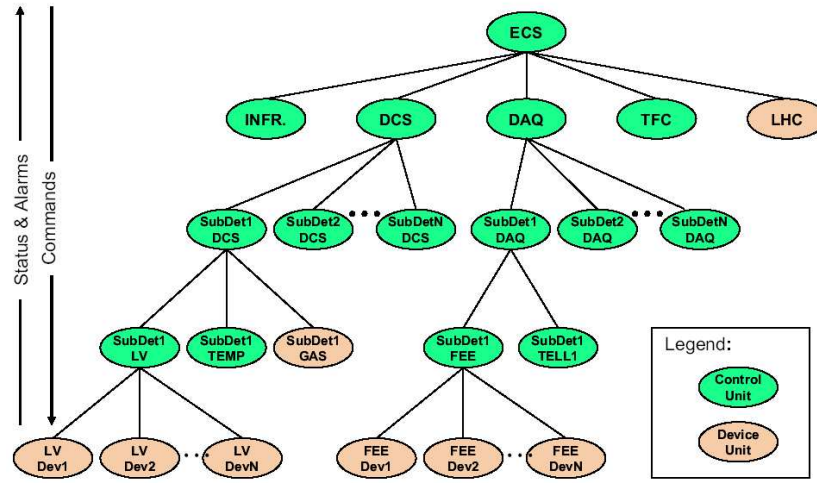


Figure 2.26: ECS architecture. Reproduced from [68].

received. The event is then available for the HLT processing stage. The event is recorded if it is accepted by the trigger system selection

### 2.2.8.2 Timing and Fast Control

The TFC system controls the data acquisition system. It provides the clock signals to the DAQ boards and front-end electronics. The L0 trigger decision is sent to the boards via the TFC system.

The TFC system also manages the addresses to where the data is sent on the EFF. In LHCb the events are sent in multiple event packs which reduces the used bandwidth. The size of these packs are defined by the TFC system.

### 2.2.8.3 Experiment Control System

The ECS performs the so-called slow control of the experiment. This system configures and controls different parts of the experiment. It monitors the performance of the different components and can also take actions in case of emergencies. Some of the different parts the ECS controls are: front-end electronics, power supplies, temperature and pressure monitoring and software interlock.

The sub-systems used to perform these tasks in each of the LHCb sub-detectors is developed according to the sub-detector characteristics. The ECS integrates all parts in a single framework. Figure 2.26 shows an example of the ECS system structure. Note the DCS control unit in this figure manages the power supplies, temperature monitoring, pressure monitoring, etc. The DAQ control unit is responsible for the operation of the front-end electronics and TELL1 boards.

## 2.3 Conclusions

The aim of this chapter, together with chapter 1, was to provide the background necessary to discuss the results presented in this thesis. A description of the LHCb detector and its 6 subdetectors was given. The main features of the trigger system and the online system were also described.

A detailed description of the VELO system was given because part of the work presented in the following chapters is related to the long term tests performed with the VELO modules. The technology of the silicon sensors and the VELO modules was discussed in detail in section 2.2.1. The design and development of the burn-in facility for long term evaluation of the VELO modules is discussed in chapter 3. The results of the tests performed with the VELO modules are presented in chapter 4. The estimated performance of the LHCb detector to measure the  $B_d \rightarrow K^* \mu^+ \mu^-$  decay is discussed in chapter 5. The LHCb sensitivity to measure the quantities that were described in section 1.5.2 are also presented.

## Chapter 3

# A facility for long term evaluation of the LHCb Vertex Detector modules

This chapter describes the system that was developed to exercise LHCb VELO modules under realistic conditions for long periods of time. This testing procedure is colloquially referred to as the *burn-in* of the module. The aim of the Glasgow burn-in system is to uncover any weaknesses introduced into the modules during manufacturing or in the components themselves. The system is able to verify that all the modules which are tested conform to a certain level of quality. The burn-in system was designed and constructed in Glasgow before being transported to a clean room at CERN where it was used.

The LHCb modules were produced at University of Liverpool and then transported to CERN where they were received, visually inspected and tested in the burn-in setup. This chapter is divided into a number of sections detailing these tests and describing each sub-system's purpose, construction and performance. An overview of the laboratory area and discussion of the tests performed is given in section 3.1. The different aims of these tests are also explained. Section 3.2 describes the hardware equipment used on the reception and visual inspection in more detail. It also lists all the items verified on the modules. Section 3.3 describes the burn-in setup and its components.

Each of the burn-in system components is described in separate sub-sections of section 3.3 where details on the construction and performance are given. The burn-in sub-systems were used together to replicate the environmental conditions of the experiment and to operate the modules. Section 3.4 concludes this chapter by providing an overview of the performance of the system and commenting on how the environmental conditions of the LHCb experiment were replicated. Section 3.5 addresses possible improvements for future use of the burn-in system.

The analysis of the results obtained from the testing of the modules in the burn-in facility are presented in chapter 4.



## 3.1 Overview

This section introduces the burn-in system. It discusses why the burn-in facility was built to test the VELO modules for long term operation and describes the main features of this facility.

As described in section 2.2.1.4 the VELO modules are comprised of a number of different materials with different physical properties and the functionality of the active components needed to be tested under long term operation. For example, latent defects could be hidden in its components or could be introduced during its assembly. Any dynamic component could also suffer from *infant mortality* which refers to the malfunction of the component after a short time of operation. The long term testing and stressing under realistic environmental conditions was one way to detect faulty components that could result in the compromise of the long term operation of the unit. The faulty components could then be fixed or replaced.

Verifying the long term operation of each VELO module was a primary concern due to the harsh and inaccessible environment that it operates in and the loss of coverage the vertex detector could suffer as a result of a malfunctioning unit. The main aspects to be covered by the long term stressing were the operation under vacuum, the temperature cycling the module is subjected to in LHCb, and any infant mortality that the electronic components may suffer. A number of guidelines were developed from experience to perform long term testing of electronic devices operated in vacuum and at different temperatures. Documents [92, 93] describe guidelines for similar applications, these were used in determining the procedure for the VELO module tests.

The other aspect that could affect the long term operation of a module was any physical damage that the module could suffer due to handling at the assembly stage, during transportation or testing. The damage could range from subtle effects such as misshaped wire bonds to serious damage such as chipped or scratched silicon sensors. The modules were transported from Liverpool, the assembly site, to Geneva where they were integrated into the VELO detector. The modules were received at the Glasgow test facility at CERN using procedures designed to verify the integrity and quality of the delivered modules\*. These tests consisted of a visual inspection using a high resolution microscope and a burn-in procedure.

The aim of the inspection was to verify the physical integrity of the module after transportation. It consisted of a high resolution visual inspection of all the bonds, components and silicon on both sides of the module for any visual signs of damage. Electronic components were verified. Photographs of the modules were taken for later analysis when necessary. The kapton cables were shipped with their corresponding module and were also inspected. The setup used for the modules reception and visual inspection is described in section 3.2.

The burn-in system was used to perform a series of tests to stress the modules when functioning in similar conditions to its normal operation in the experiment. It was built to

---

\* A transportation box was developed for the transportation of the modules [94].

perform periodic thermal cycles while the modules were operated as in the real experiment. To reproduce such conditions the modules were enclosed in a vacuum chamber and their temperature was controlled by a cooling system. The module was powered on and its front-end readout chips were exercised by providing a clock, commands and triggers. Figure 3.1 shows a diagram to illustrate the burn-in setup. It was composed of a vacuum system, cooling system, interlocks, DAQ system, low voltage supplies, high voltage supply and two PCs to control, monitor and perform data analysis. The burn-in components are described in section 3.3.

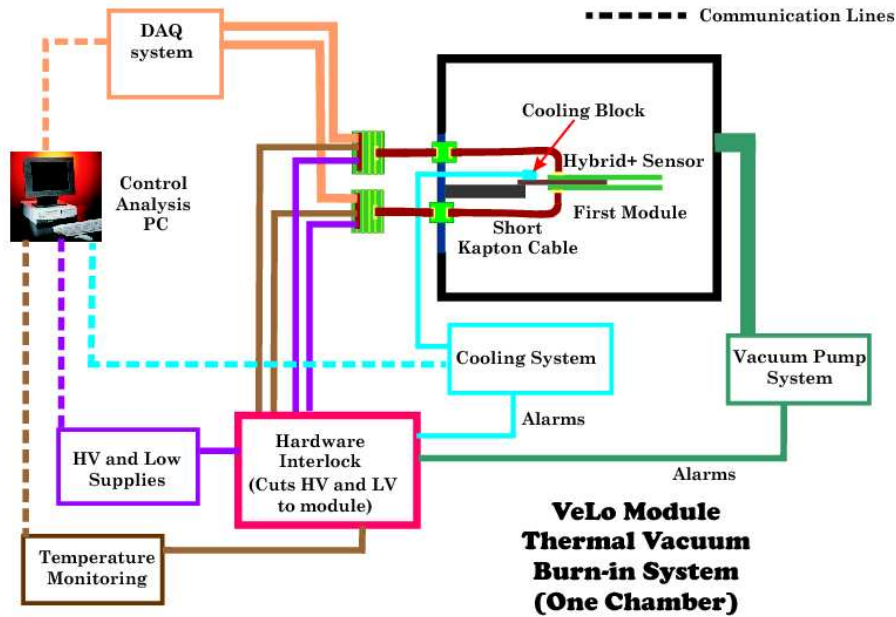


Figure 3.1: The burn-in setup was composed of vacuum system, cooling system, interlocks, DAQ system, low voltage supplies, high voltage supply and 2 PCs to control, monitor and perform data analysis.

The photograph in figure 3.2 shows the laboratory where the modules arrived and the burn-in took place. The visual inspection microscope, the data analysis PCs and the DAQ hardware are visible on the left-hand side. On the right-hand side the cooling system, the vacuum system and reception area are seen.

## 3.2 Reception and Visual Inspection

The VELO modules, on arrival in the burn-in setup, underwent a module reception procedure. A visual inspection was performed following a check list. This aimed to determine if any visible damage had occurred during the transportation from University of Liverpool to CERN. This reception procedure included a check on the clamps, feet, captive screws,

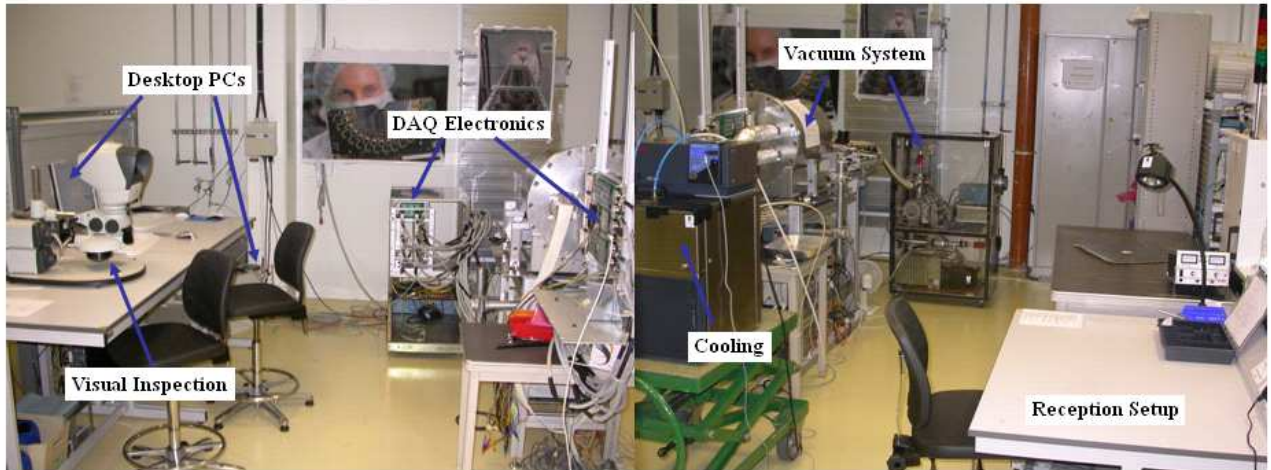


Figure 3.2: The burn-in area layout. On the left side the visual inspection microscope, the data analysis PCs and the DAQ hardware are shown. On the right side the cooling system, the vacuum system and reception area are shown.

paddle, cooling face, hybrid, bond wires, chips and silicon. The integrity of the module's kapton cables and cable clamps were also verified. These components are shown in figure 2.9 .

After the reception tests, a detailed high-resolution visual inspection was performed with a Lynx microscope equipped with a camera. Photographs were taken for further analysis. For the inspection the modules were mounted in an aluminium frame with clear plastic covers on both sides. Figure 3.3 shows the visual inspection setup. The visual inspection procedure consisted of a fine integrity verification of all the components of the modules. Some examples of typical problems that were found with the microscope such as lifted bonds and defects on the pitch adaptors are also shown in figure 3.3.

After the completion of the burn-in tests a second visual inspection was performed in order to determine if any changes had happened during the period of tests. The visual inspection procedures and results are presented in section 4.2.

### 3.2.1 Module Handling

An important aspect of the visual inspection procedures was enabling the safe handling of the VELO modules throughout the different stages of testing. A frame was designed to incorporate the following points, as well as being compatible with the burn-in setup:

- Easy and safe mounting and dismounting of modules to the frame.

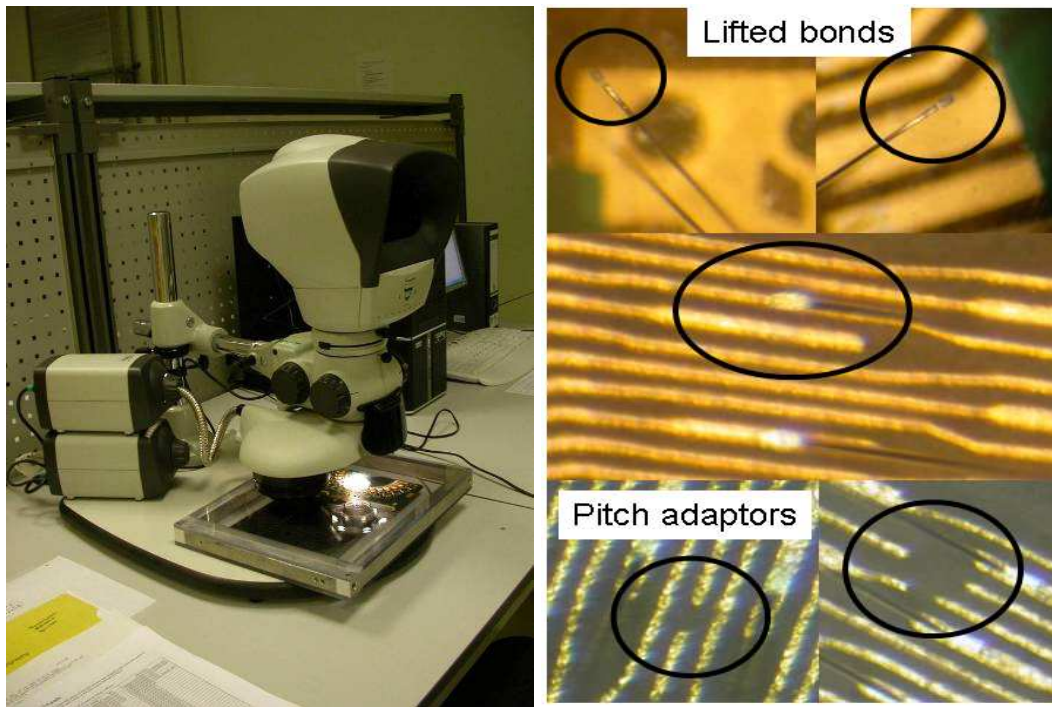


Figure 3.3: A Lynx microscope equipped with coolpix camera was used to perform the visual inspections. On the left side image a module is shown mounted on the visual inspection frame. Various items were verified on the visual inspection. Lifted bonds and defects on the pitch adaptors seen on the right-hand side picture are typical problems that were found during the visual inspection.

- Thin enough for the module to be placed underneath the visual inspection microscope.
- Allow access to either the R and  $\Phi$  faces of the module during visual inspection and burn-in.
- A mounting system compatible with the standard connections on the feet of the module.

The frame designed to meet all of these requirements is shown in figure 3.4 together with the transfer jig. The transfer jig was employed to transfer modules to and from the frame in a safe manner. The diagram shows how the sides of module frame could be removed allowing the module to be easily mounted or dismounted on its base as it was held by the transfer jig. The R and  $\Phi$  faces of the module were protected by clear plastic panels that were removed during visual inspection.

A similar aluminium frame was used to place the modules into the burn-in vacuum chamber. It had the same dimensions as the one used on the visual inspection but modifications were made in order to satisfy the mechanical requirements.

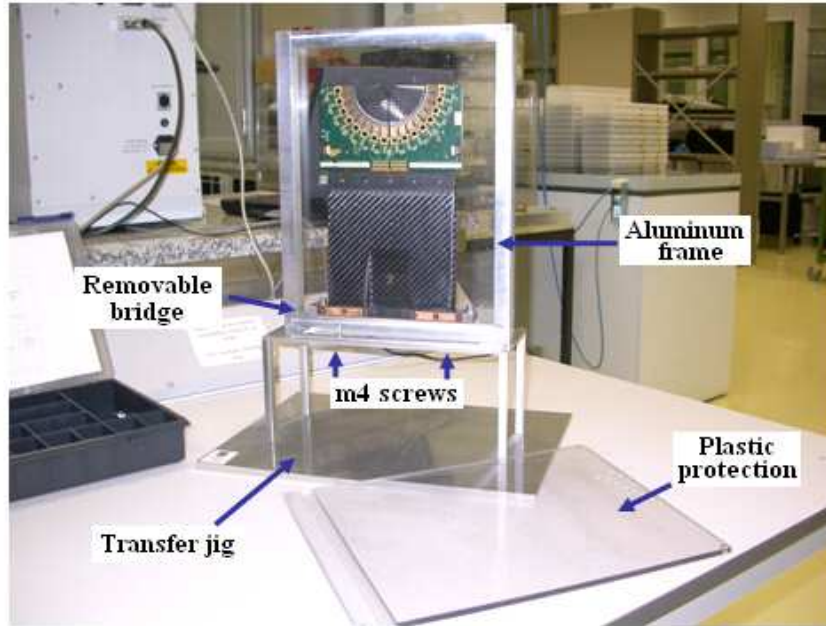


Figure 3.4: An LHCb VELO Module mounted in the mechanical frame on the transfer jig.

### 3.3 Burn-in Setup

The burn-in system was built to test the VELO modules in an environment similar to the LHCb experiment. This section describes each of the burn-in components explaining their function.

The most important design consideration of the VELO was to optimise the impact parameter resolution of the reconstructed tracks. This was achieved by keeping the material to a minimum and by placing the sensors as close as possible to the interaction point (see section 2.2.1). The first condition resulted in the modules being operated under vacuum in order to get close to the beam. The second condition resulted in high levels of radiation being incident on the sensors during operation. The sensors were designed to withstand high levels of radiation. In order to minimise the effects of radiation damage the sensors should be kept at temperatures around  $-5/ -10$  °C. This condition implied that during the lifetime of the modules they will undergo a large number of temperature cycles as either the cooling or the module front end electronics are switched on or off.

These two features were recreated in the burn-in by operating the modules inside a stainless steel vacuum chamber while in contact to an internal liquid cooling circuit. Achieving the vacuum and module cooling was only part of the challenge. The module handling, the monitoring of the environment, module parameters and interlocks to ensure safe module operation were all aspects of the burn-in system that also required development for the long



term testing to be performed. The purpose of each system together with its description is given in the following sections. Sections 3.3.1 and 3.3.2 describe the vacuum system and the cooling system of the burn-in facility respectively. Section 3.3.3 depicts the equipment used to power on the VELO modules and to monitor the burn-in system. Section 3.3.4 discusses the software developed to control the laboratory devices and to monitor the system. The interlock system implementation is explained in section 3.3.5. Section 3.3.6 describes the DAQ system used to read out the VELO modules.

### 3.3.1 Vacuum System

The burn-in of the LHCb modules is only fully effective if the operational environment in the experiment is approximately recreated during testing. Hence, in order to evaluate the functioning of the modules a vacuum system was constructed.

A vacuum environment was needed not only to mimic the experimental conditions but also to allow the operation of the modules with the same parameters as in the experiment. To safely apply the bias voltage on the silicon sensors it was necessary to have the module at very low pressure condition to avoid any discharge. Studies performed on the burn-in system have shown that discharges do not occur at atmospheric pressure or very low pressure conditions but a mid-pressure range should be avoided [95]. The heating and cooling of the module could be performed when the module was in vacuum with no concerns about the formation of condensation on the surface of the module.

The burn-in vacuum system consisted of a vacuum pump setup and stainless steel chamber. The vacuum pump system is based on the traditional arrangement of rotary pump and turbo pump. The turbo pump model was a Pfeiffer TPH 330 and the rotary pump was a Pfeiffer DUO 012A. Additional mechanics were developed to locate the module safely inside the vacuum chamber.

Figure 3.5 shows the vacuum tank. It has a diameter of 40 cm and length of 60 cm. Connection to the vacuum system was done through the back of the tank. A diaphragm valve and an air inlet valve were attached in a 4.0-2.5 cm reducing tee connection, which allowed air to be released inside the tank when tests were finished. A 4 cm ball valve was installed to close the connection between the vacuum pumps and tank. The diameter of the flexible hose is 4 cm and it has a length of 100 cm.

Figure 3.6 shows the vacuum pump system in the burn-in lab. The picture at the left side shows the pumps inside the plastic box used to isolate the system from the clean room since the pumps were not rated for operating in the clean room area. The rotary pump had its exhaust connected to outside of the clean room because of the toxic and contaminating nature of its gases. In order to avoid any oil reaching the vacuum chamber a foreline trap was placed between the rotary and turbo pump. In the centre photograph in figure 3.6, the header vessel mounted on the turbo pump is shown. It has one 2.5 cm connection to a vacuum

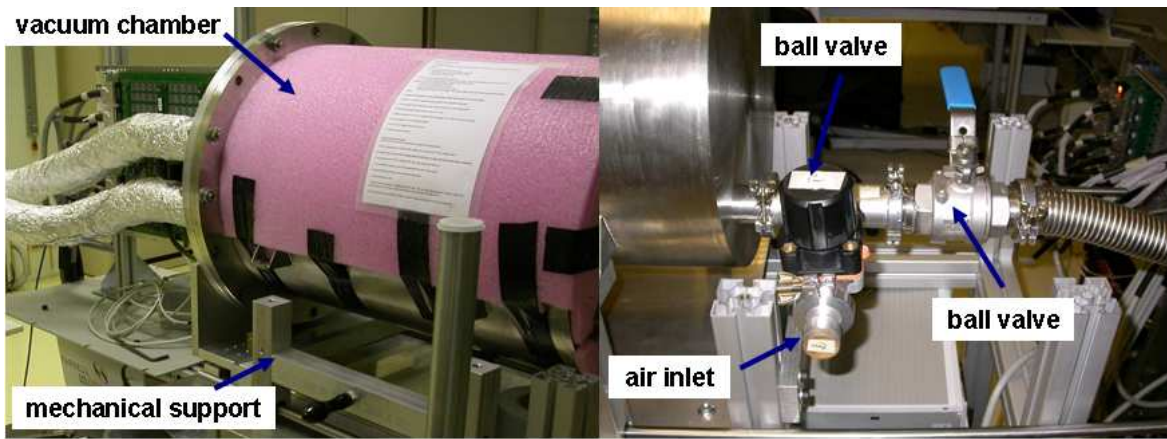


Figure 3.5: Picture of the stainless steel vacuum tank. Its dimensions are 40 cm diameter and 60 cm length. The tubing has a 4 cm diameter and a 100 cm length. A set of valves were installed to facilitate the vacuum operation procedures.

pressure reading penning gauge and four 4.0 cm connections available. One of the 4.0 cm connections was used to attach the flexible hose to the vacuum chamber. On the right hand side picture the control panel is shown.

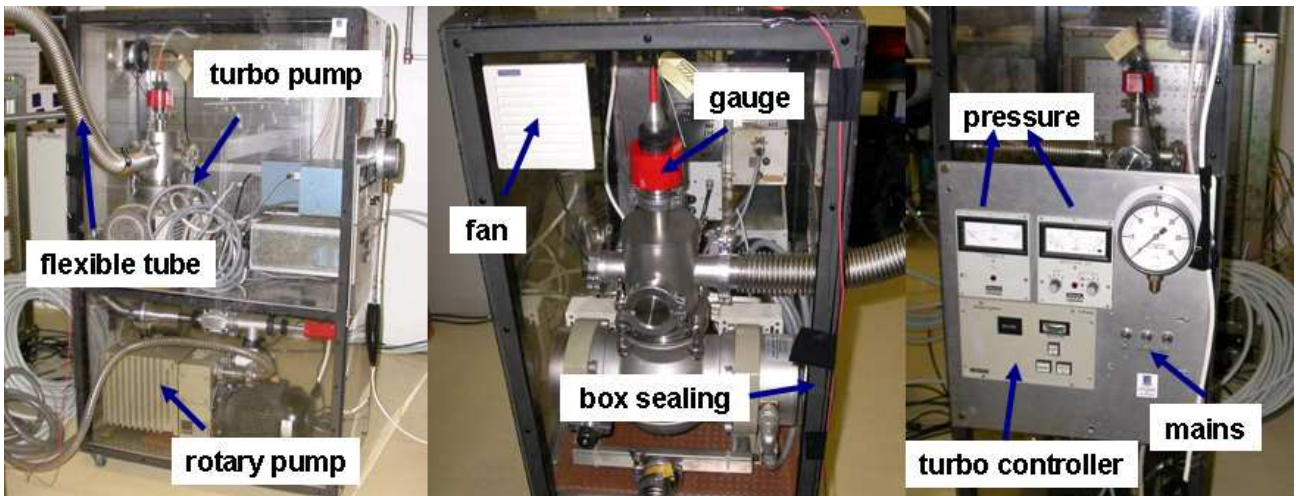


Figure 3.6: Three photographs showing the vacuum pump system. The left hand photograph shows both pumps and their respective accessories. The centre photograph shows the turbo pump and its connections. The right hand photograph shows the control panel.

To provide the appropriate vacuum environment to operate the VELO modules any leak in the vacuum system connections was avoided and the outgassing of the components used inside the vacuum was minimised. A set of measures were taken in order to achieve the desired vacuum quality.

- The additional mechanics and electronic components used inside the chamber were suitable for high quality vacuum applications.
- All the mechanics pieces were properly cleaned in an ultrasound bath, dried and baked before assembly. This cleaning procedure was repeated a few times for the plastic pieces of the mechanics.
- Gloves were always used when handling anything that was to be placed inside the vacuum and measures were taken to keep the vacuum tank clean.

The operation of the vacuum system with its mechanics inside the chamber achieved the appropriate vacuum quality and stability. The rotary pump sustained the secondary vacuum at levels of 0.1 Torr after 10 minutes of operation. The turbo pump reached levels of  $5 - 10 \times 10^{-5}$  mbar after 20 – 40 minutes of operation on the primary vacuum. Pressure values of the order of  $0.5 - 1.0 \times 10^{-5}$  mbar were obtained after overnight runs. No quality degradation of the vacuum or turbo pump failures were observed during the assembly, test phases and operation. The procedures to operate the vacuum system during the module testing are described in section 4.1.3.

### 3.3.2 Cooling System

The VELO cooling system was designed to keep the silicon detectors in a temperature range of  $-10.0$  °C to  $-5.0$  °C while the temperature of the Beetle chips and other electronics components should be kept below 40 °C. To mimic the environment in the LHCb experiment a cooling system was set up in the burn-in lab. It was used to control the temperature of the modules and to perform thermal cycles in order to stress the modules thermally and mechanically.

The cooling system developed for the burn-in consisted of a chiller, insulated hoses, cryogenic feedthroughs, flexible metallic hoses and a custom designed cooling block that was attached to the module. Figure 3.7 shows some pictures of the burn-in cooling system.

The thermal control was provided by a Huber CC415 circulator [96] controlled through a RS232 interface. The parameters of the chiller that suited the needs of the burn-in system are shown in table 3.1.

In order to avoid moisture condensation in the coolant bath of the chiller the reservoir was sealed and a nitrogen flow of about 4.5 l/h was used to keep the internal environment dry.

The coolant liquid used was a low viscosity silica oil also provided by Huber <sup>†</sup>. Its relevant properties for the burn-in operation, extracted from the safety data sheet, are listed in table 3.2. The liquid was cycled in the temperature range between  $-37.0$  °C and  $+30.0$  °C.

---

<sup>†</sup>The silica coolant type used in the burn-in was SilOil M60.115.05. Its specifications and safety data sheet can be found at [97].



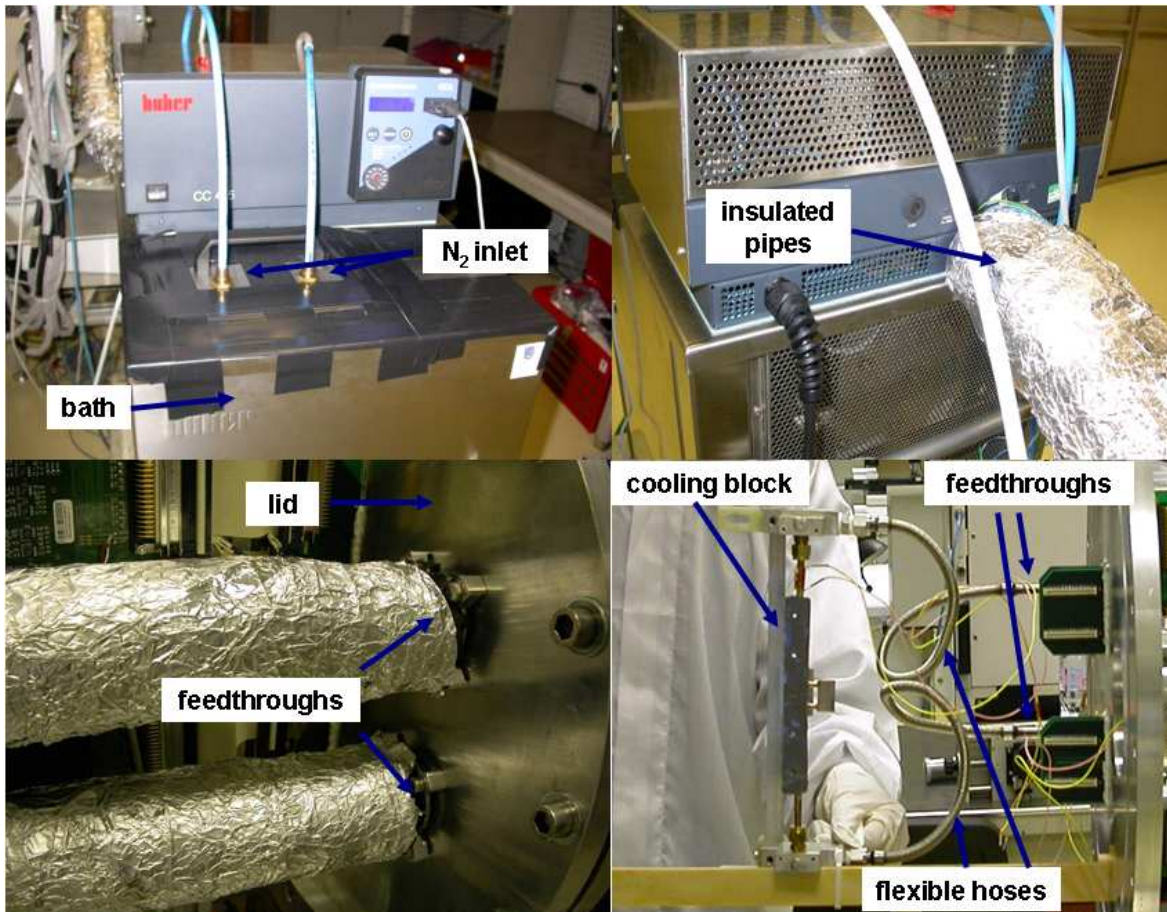


Figure 3.7: Four photographs of the cooling system in the burn-in setup. The top left picture shows the chiller front panel. Tubes were connected to the bath to provide nitrogen flow and keep a dry atmosphere. On the top right the hoses to conduct the coolant liquid connected at the back of the unit are shown. On the bottom left the cryogenic feedthroughs connected to the vacuum chamber lid are shown. On the bottom right the flexible hoses and cooling block located on the opposite side of the lid can be seen.

All safety measures for handling were followed when evacuating the bath container or replacing the coolant fluid.

The chiller had a number of hardware alarms, these included registering low or high fluid level in its bath, overheating and malfunctioning. It was possible to set all the safety parameters to values even more stringent than those proposed by the manufacturer given the small volume of coolant liquid necessary and the temperature requirements for the burn-in operation. For example, the heating power of the chiller was operated at values 50/80% lower than the power rate set by the manufacturer. The overheating temperature was set to 40 °C while the overheating threshold set by the manufacturer was 70 °C. These values were also chosen in order to fully satisfy the coolant specifications.

In the situation where one of these hardware alarms was triggered the chiller unit would

Table 3.1: The specification parameters for the chiller.

|                    |                                   |
|--------------------|-----------------------------------|
| Temperature range  | -40 °C - +200 °C                  |
| Cooling power      | 50 W at -40 °C<br>200 W at -30 °C |
| Heating power      | 1.5 kW                            |
| Maximum power      | 2.5 kW                            |
| Control Interface  | RS232/RS485 via CC3               |
| Tubing connections | male M16x1                        |

Table 3.2: Specification parameters of the silica coolant liquid.

|                                  |                                  |
|----------------------------------|----------------------------------|
| Boiling point                    | 300 °C at 1013 mbar              |
| Density                          | 0.923 g/cm <sup>3</sup> at 25 °C |
| Vapour pressure                  | 0.01 mbar at 20 °C               |
| Kinematic viscosity              | 5 mm <sup>2</sup> /s at 25 °C    |
| Heat capacity                    | 1.63 J/(g × K)                   |
| Thermal conductivity             | 0.133 W/(K × m)                  |
| Solubility in water              | insoluble                        |
| Flash point(DIN 51376)           | > 120 °C                         |
| Ignition temperature (DIN 51794) | > 400 °C                         |

turn off its cooling and stop pumping the coolant liquid through the cooling system. If the module was to overheat after a cooling system failure then the burn-in interlock system was triggered and the module voltage supplies were turned off. More details on the burn-in interlock system are discussed in section 3.3.5.

The coolant was conducted to the vacuum chamber via insulated hoses that were connected to the cryogenic feedthroughs on the lid of the vacuum chamber. The feedthroughs allowed the connection between the external part of the cooling system and the flexible metallic hoses attached to the cooling block inside the vacuum chamber. The cryogenic feedthroughs were required to minimise the thermal conductivity between the hoses carrying the coolant and the chamber lid.

Two triple insulated hoses of 1.5 m length were the most appropriate tubing choice to conduct the coolant from the chiller to the vacuum chamber. The hosing operational temperature range was  $-100\text{ °C}/200\text{ °C}$ . The fittings used were female  $M16 \times 1$ . External and internal diameters were respectively 42 mm and 10 mm. The hoses had 3 insulating layers made of glass silk (3 mm thick), silicon foam tubing (6 mm thick) and a black poly braiding

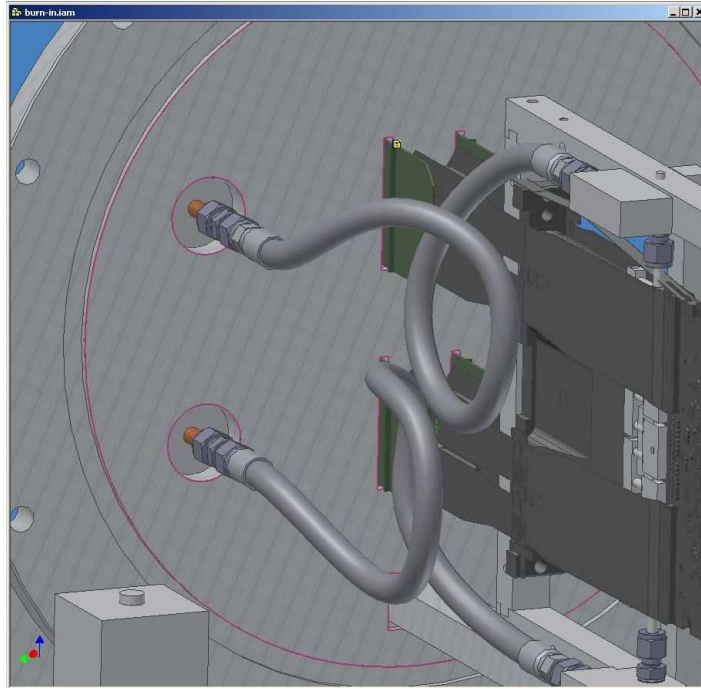


Figure 3.8: The flexible hoses were connected on the feedthroughs and cooling block. The length of the tubes was chosen such that low stress was applied to the cooling block. The curved shape of the hoses was such that the cooling block was not pushed against the module.

cover. An external layer of rubber insulation was also added to the tubes in order to reduce the heat loss as much as possible.

To connect the hoses to the swagelok fittings of the tube of the cryogenic feedthroughs a M16X1 to 3/8 inches adaptor was installed between them. The feedthroughs were connected to flexible metallic hoses inside the chamber with swagelok fittings. The flexible hoses could be bent with a minimum radius of 4.0 cm in dynamic applications. In the burn-in system the radius was estimated to be bigger than 5.0 cm and it was a quasi-static application. At the other end of the flexible hoses, the cooling block was attached as shown in figure 3.8. The length of the tubes was chosen such that low stress was applied to the cooling block. The curved shape of the hoses was designed to not push the cooling block against the module. In fact, the hoses tend to gently pull the cooling block toward the lid direction and not against the module.

The cooling block was the part of the cooling circuit that was attached to the module cooling face to remove the heat from the module. The mechanical design of the cooling block had to satisfy the following set of requirements:

- The thermal interface between the cooling block and the module should be such that the mechanical stress applied to the module was minimised.
- The cooling block shape should maximise the contact area with the module cooling

face.

- The cooling block should fit in the 5 mm gap between the module cooling face and the kapton cables.

The mechanical stress applied to the module had to be limited as otherwise it could cause a permanent deformation of the hybrid or damage the sensors. Displacements of the paddle or hybrid with respect to their original position were kept below 100  $\mu\text{m}$  in order to ensure no damage to the modules.

The second requirement could directly affect the performance of the cooling system to remove heat from the module. The size of the contact surface of the cooling block was mainly limited by the area of the module thermal interface. The size of the cooling block was also constrained by the distance between the module kapton cables and the module thermal interface. Figure 3.9 shows a 3D diagram of the cooling block attached on a module mounted on the burn-in frame.

The cooling block was composed of a copper pipe and two aluminium blocks as indicated in figure 3.9. The aluminium pieces made the connection between the metallic flexible tubes and the copper pipe closing the circuit where the coolant liquid flows inside. The design of the cooling pipe with two flat pieces connected by a copper U allowed the block to slightly deform due to temperature variations without applying any mechanical stress on the module. The two copper flat pieces were made of 6 mm copper blocks machined out and lids attached with high temperature brazing. This avoided any leaks while operating at low pressure. Thermal film COH-4000 with 0.5 mm thickness was used as a thermal interface to attach the copper pipe to the module cooling face. The film interface improved the thermal connection filling the small gaps due to the cooling block surface irregularities. The film low outgassing properties were compatible with the system.

Figure 3.9 shows the cooling block installed on the chamber lid and attached to one of the modules. The module was placed in the burn-in frame which had a hood to protect the silicon sensors during the procedure. The burn-in frame sat in a plastic cantilever attached to the vacuum chamber lid. This plastic piece was suitable for vacuum applications and prevented heat flow from the lid to the frame. The cooling block was attached to the frame using plastic L shapes to reduce the heat flow from the frame to the cooling block. A support at the opposite side was used to attach the cooling connection and position the cooling block correctly. Additional clamps were attached to the flexible tubes to avoid the mechanical stresses due to thermal expansions or contractions during the temperature cycles.

To achieve the required temperature for the thermal cycling, the circulator was operated at  $-38\text{ }^{\circ}\text{C}$ . The cooling block temperature at this point achieved a minimum of  $-30\text{ }^{\circ}\text{C}$  with and without a module mounted. No significant temperature difference was observed when the module low voltage was switched off. The minimum temperature measured on the hybrid with the readout electronics off was between  $-20\text{ }^{\circ}\text{C}$  to  $-25\text{ }^{\circ}\text{C}$ , showing that the cooling

system was capable of thermally stressing the modules. The cooling system was able to vary the temperature of the module hybrid from 30 °C to its minimum in about 20 minutes. It allowed the burn-in system to thermally cycle the modules in temperature ranges compatible to those in the experiment. The operating procedure of the cooling block for testing the modules is described in section 4.1.3.

### 3.3.3 Voltage Supplies and Monitoring Devices

A number of voltages are required to operate the VELO modules. Under normal operation conditions a module uses 24.5 W of power. A set of electronics devices were used to supply the electronics with appropriate voltages, currents and to read out the NTCs mounted on the modules hybrid, repeater boards, cooling block and vacuum chamber walls. To supply the modules with low voltage and high voltage two component units were used.

To supply the modules low voltage an Agilent E364BA unit with two channels was used. Each channel was used to supply 16 Beetle chips on each side of the module. Each Beetle chip was powered with 3.5 V and consumed 0.22 A.

An 8 channel Iseg GCH224L unit provided the bias voltage to deplete the module sensors. Each sensor was biased by an individual channel.

The voltages were supplied to the modules through the repeater boards. The repeater boards were the components of the burn-in DAQ which not only served the modules with the voltages but also drove and amplified the readout signals. More details on the DAQ electronics of the burn-in system is given in section 3.3.6.

A second Agilent E364BA was used to power on the repeater boards themselves. A channel was available for each of the two repeater boards used. A Keithley multimeter was used to monitor the NTCs on the modules hybrid, repeater boards, cooling block and vacuum chamber walls. The multimeter was equipped with two cards with 20 and 40 channels. The resistances of the NTCs were measured and the temperatures were calculated using the manufacturer's calibration formulas. The Iseg unit and the Keithley multimeter were controlled by the software suite described in section 3.3.4.

### 3.3.4 Control and Monitoring Software System

This section describes the software architecture used to develop the algorithms necessary to control and monitor the components of the burn-in system during the module testing. The code was written in C++ using a single set of technologies based on Qt [98] and ROOT [99]. For each device there was a graphical user interface application (GUI) running independently of the other algorithms. This allowed the user to operate each device separately. To display the data read out from the different devices a data display algorithm was developed. Table 3.3 lists the devices controlled by software, their function on the burn-in system, the driver names and the communication protocols used.



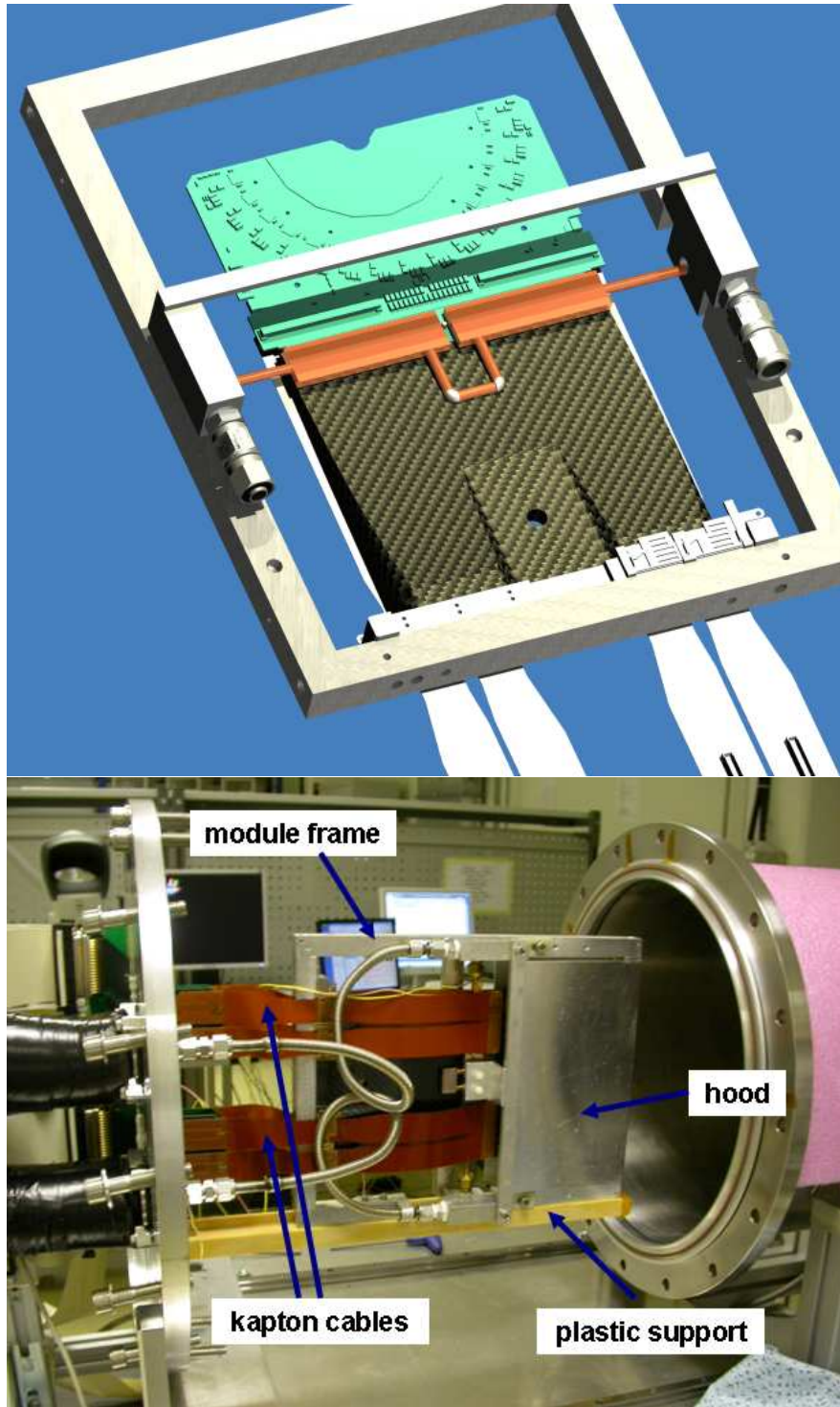


Figure 3.9: The cooling block had a two piece design connected by an U of copper that enabled deformation without buckling. It could bend inwards and outwards in the plane of the cooling block to take into account the expansion and contraction of the whole cooling block. The cooling block was attached to the module during the mounting procedure. The module was placed in a special frame which had a hood to protect the silicon during the mounting. The cooling block was attached to the frame and a support at the opposite side was used to optimise the cooling connection and position the cooling block correctly.

In order to optimise the GUI development Qt was taken as the main tool. Qt is a framework for cross-platform applications development provided by Trolltech. It includes a library with a rich set of classes and functionality for GUI programming. Manuals, tutorials, how-to lists, mailing lists and browsable documentation are available. A GUI layout designer is also available (Qt designer). As ROOT is the main framework for data analysis in HEP it was the straight forward choice to display data and to save it into a recognisable format. This set of tools and classes were proven to be easy to use and robust enough for the burn-in laboratory needs. To integrate both Qt and ROOT the so called QtROOT interface [100] developed and maintained by GSI was used. Nowadays this package is already built in ROOT versions above 5.11-02.

A simple software architecture was chosen in order to simplify the programming activities and maintenance. Each of the devices mentioned had an application that ran independent of the other applications. Each application was composed of a basic set of four classes: system class; GUI class; monitoring thread class; and device class. The system classes were developed to control the different parts of the applications. The GUI classes provided the interface between the user and the application. The monitoring thread were state machines implemented to perform the actual communication between software and hardware. The device classes embedded the drivers provided by the different unit manufacturers.

The GUI class read out the inputs and commands given by the user and reported the current status of the device. The GUI had a pointer to the system class such that the instructions given by the user could be delivered to the hardware device. The signal/slots mechanism provided by Qt was used for this purpose. When an action was requested by the user, the system class would pass the updates to the monitoring thread that ran independent of the GUI communicating with the hardware through the device class. To avoid conflicts when accessing memory the system class locked the address where the new command information was written to disable the thread from trying to access the same address at the same time. After the information was updated the memory location was unlocked and available. The device class was implemented with all the functionality provided by the drivers in a user friendly manner and tuned to the operation of the devices used in the lab.

Once the hardware status was obtained the information was written back and the system class notified that there was data to be updated. This information was delivered to the system class through a posted event sent by the thread. If required the data was passed to the GUI by the system class. The system class would also write the data in a memory address shared with the data display software. It used the signal/slots mechanism to notify the data display that there was more data available to be added to the graphs.

Additional features were implemented using ROOT I/O classes. The applications used to control the devices were able to save acquired data in ROOT files for further analysis. Configuration files to operate the devices could be saved in XML files. For example, configuration files were saved for the Keithley controller used to read out the NTCs on the module

Table 3.3: List of devices, drivers and protocols in the monitoring software.

| Device        | Function             | Driver             | Protocol |
|---------------|----------------------|--------------------|----------|
| Chiller Huber | Module cooling       | QextSerialPort 0.9 | RS232    |
| Keithley      | NTCs monitoring      | linux-gpib-3.1.101 | GPIB     |
| Agilent       | Hybrid low voltage   | linux-gpib-3.1.101 | GPIB     |
| Iseg          | Sensors high voltage | pcan-usb           | USB      |

and cooling block. After all the necessary channels were configured to perform the resistance measurements one could record the settings on disk and load it again afterwards.

The data display application allowed graphs of the monitored parameters to be displayed as a function of time. For each parameter it was simply necessary to set up in the software the electronic channel used to read out the device and insert a suitable calibration. An example is the calibration required to obtain temperatures from an NTC probe. To monitor a given NTC it was necessary to set the channel number of the Keithley multimeter which was connected to the NTC and the calibration that should be used. Then the channel configuration and corresponding calibrations could also be recorded in XML files.

### 3.3.5 Interlock System

The modules were protected by a hardware interlock system against any malfunction of the burn-in system that could harm their physical integrity. High voltage and low voltage interlocks were developed for monitoring the temperature on the hybrid and the pressure inside the tank. The burn-in interlock had two monitoring units in order to turn off both high voltage and low voltage supplies in case of a system failure.

As mentioned in section 3.3.3, an Agilent E364BA unit was used to power up the Beetle chips with 3.5V and an Iseg GCH 224L unit provided the high voltage applied to the silicon detectors. The Agilent unit could not be turned off via an external signal but only manually or via software commands. Hence it was decided to cut off the mains power of this unit in case of a burn-in system failure.

The high voltage unit had a safety loop mechanism to cut off the outputs in case this circuit was opened. The safety loop was the standard mechanism offered by the manufacturer and was adopted in the burn-in. The Iseg HV unit also had a current overflow protection system in its output.

Sections 3.3.5.1 and 3.3.5.2 explain why it was necessary to develop an interlock system in the burn-in. Section 3.3.5.3 describes the design of the interlock system and its units.



### 3.3.5.1 Temperature Monitoring

The temperature monitoring interlock was developed to protect the modules against any possible overheating. This could happen in four situations that were identified during the burn-in commissioning. All the situations were related to the cooling system operation.

- i The first possibility was when the chiller continues to function properly but the coolant liquid does not circulate inside the hoses and cooling block. It was observed that water condensation in the surroundings of the bath inside the chiller reservoir could occur since it was not a closed container. Ice could be formed in the mixture of the thermofluid and condensed water blocking the normal flow of the liquid through the thin cooling pipe. The efficiency of the final module cooling would then be drastically reduced. During operation of the chips the module would then overheat due to insufficient cooling.
- ii The thermal connection between the cooling block and the module in the burn-in was highly dependent on the cooling block positioning. Overheating could occur if the cooling block mounting was not done properly such that its surface was not fully attached to the module thermal interface. However, this problem would be rectified since it would be noticed and corrected during the start up of the burn-in procedures and before the interlock would be triggered.
- iii The third situation was when the chiller mains could be turned off due to the chiller drawing more power than that specified as maximum for operation or due to the mains fuse blocking if the drawn current was too high. The maximum current allowed in a standard fuse for mains is 10 A and the maximum current operation of the chiller is 11.5 A.
- iv Human error could also lead the interlock system to trigger if the module was turned on with the cooling system off or set up to run in a non safe temperature level.

In each of these four scenarios, the module temperature would rise and at a hybrid temperature of 50 °C both the low voltage and high voltage would be turned off by the interlock system, thereby reducing the temperature of the module to room temperature.

### 3.3.5.2 Pressure Monitoring

Monitoring of the pressure was necessary since a vacuum system failure could cause a rise in the pressure inside the chamber while the module was operated at high voltage and low temperature conditions. In this case condensation could occur over the silicon surface and electronic components of the modules if they were operated at low temperatures in an air environment. A pressure value of  $1 \times 10^{-4}$  mbar was set as a maximum threshold to safely

operate the modules with the sensor bias voltages higher than 100 V. A more detailed study of the module operation in vacuum was later performed with the burn-in setup and can be found at [95].

The Controller 201 unit in the vacuum system provided a relay to allow the monitoring of the vacuum system status. The contacts of the relay would be open or closed depending on the pressure read out by the controller unit. A voltage of 5 V was connected to the input of the relay in order to provide a step signal on the output of the relay in case the pressure went above the threshold set. A few situations where the pressure interlock system should take action were identified during the burn-in setup commissioning. All cases were related to the functioning of the vacuum pumps since all the potential air leaks were eliminated during the burn-in commissioning.

The most probable case was when the power supply of the vacuum system was turned off due to excessive power demands. In this case the relays in the pressure interlock system were triggered immediately and not when the pressure reached the maximum pressure level allowed for operation. The relays were used to interrupt the power supply to the high voltage and low voltage systems, as described in section 3.3.5.3.

The less probable cases would be of degradation of the vacuum making the turbo pump turn itself off. This could happen due to outgassing of the plastic arm that supports the module frame or, for example, some small piece of kapton tape that could be released and dragged into the vacuum tube causing a blockage. In these cases the relays would change their state if the pressure readings passed the maximum level allowed since the gauge unit was completely independent of the turbo pump.

### **3.3.5.3 Interlock Unit Devices**

The burn-in system had two independent devices to protect the modules in case of failure, which were a temperature unit and a pressure unit. They worked in a series arrangement such that the high voltage and low voltage supplies would be turned off both in the case of the temperature passing certain limits or the pressure being above the acceptable threshold. Figure 3.10 shows a diagram of the interlock system.

#### **Temperature Interlock Unit**

To protect the system against overheating accidents a temperature monitoring device was built. It used a regulator CAREL IR32 [101] with a resistance input. This regulator was simple to program and had a set of prearranged functions that allowed operation in different modes, parameter values and calibration offsets. Figure 3.11 illustrates how the unit was set.

The hybrid temperature was shown in the front panel display of the unit. The working parameters of the unit were set in the front panel. The temperature was obtained by converting the resistance readings from the NTC on the module through a calibration. The resistance

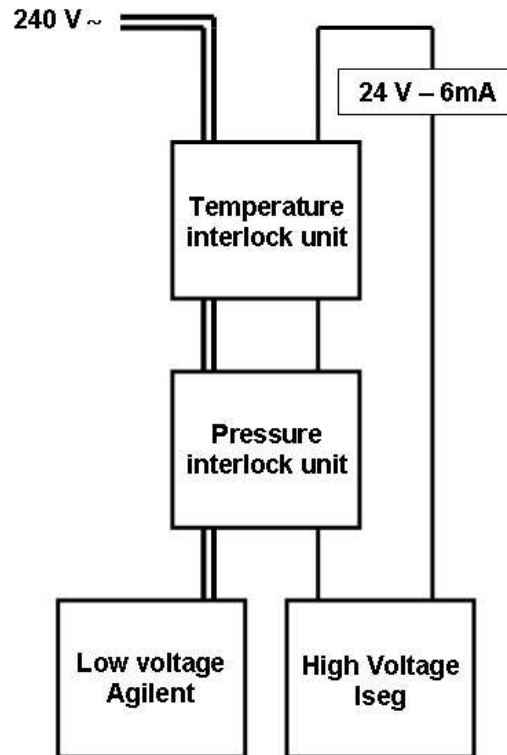


Figure 3.10: Interlock diagram. It used two units to protect the module inside the chamber. The arrangement of the interlock units ensured that high voltage and low voltage would be cut in case of a system failure.

input connectors were also located at the front panel of the unit. At the back of the device two 230 V plugs (INPUT/OUTPUT) and 2 banana plugs (INPUT/OUTPUT) were available to connect the Agilent and Iseg devices. The unit supply cable was also connected at the back.

In normal operation the temperature interlock unit had the HV safety loop and the power supply cables of the low voltage connected. When the temperature interlock detected an abnormal temperature on the hybrid, the connections were opened and the module power supplies turned off. The functioning of the temperature interlock unit was tested without a module using just a 10 k $\Omega$  NTC directly connected to the input. The unit was triggered heating the NTC with a hot air gun and the unit relays opened their electrical contacts for the low voltage and high voltage as expected.

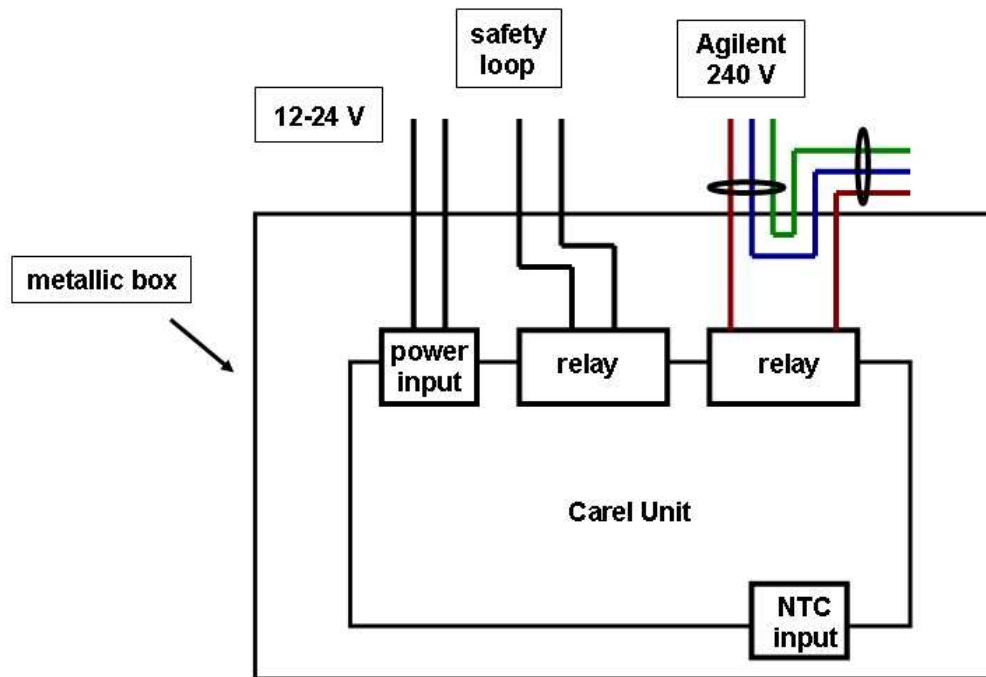


Figure 3.11: Temperature interlock schematic and pictures of the unit. The input signal was the resistance read from one NTC on the hybrid. The current temperature was shown in the front panel display. The unit used two relays to interlock both high voltage and low voltage units. On the back panel the HV safety loop and Agilent power cable were connected. In case of module overheating both connections would open and turn off the module power supplies.

Table 3.4: BROICE relay parameters list.

| Parameter           | Values         |
|---------------------|----------------|
| Input voltage range | 0.5 - 10.0 V   |
|                     | 3.0 - 60.0 V   |
|                     | 30.0 - 600.0 V |
| Over voltage        | 0 - 100%       |
| Hysteresis          | 5 - 50%        |
| Time delay          | 0.1 - 3 s      |
| Reset time          | 60 ms          |
| Latching facility   | selectable     |
| Relay inversion     | selectable     |

### Pressure Interlock Unit

The pressure interlock unit was composed of two BROICE 45050 unit relays [102]. They could operate in two modes. This model was able to operate in three different input voltage ranges. In the burn-in setup the latching mode was used in such a way that if they were triggered it would be necessary to manually turn them off and restart again. The overvoltage, hysteresis and time delay from a fault were adjustable. The latching facility and relay inversion were selectable features. Table 3.4 lists the possible values the parameters mentioned could assume.

The relays were triggered via the 5 V delivered by the Controller 201 device in case of a vacuum system failure. Figure 3.12 illustrates the electrical connections of the unit. On the front panel of the pressure interlock unit values for the hysteresis could be set. A set of two 230 V plugs (male and female) and two banana plugs were available at the back to connect the Iseg safety loop and the Agilent power cable. One BROICE unit was used to interlock the low voltage supply and the other was used to interlock the high voltage safety loop. The mains power cable connection for the unit was also located at the back panel.

The pressure interlock was verified using the burn-in vacuum system but also without a module mounted. The pumps were turned off and the pressure hardware interlock relays opened their electrical contacts for the low voltage and high voltage as expected.

### 3.3.6 Control and Data Acquisition

This section describes the data acquisition setup (DAQ) used in the burn-in facility. The burn-in DAQ was able to fully operate the electronics of the module and to acquire data from both sides of the module simultaneously inside the vacuum chamber. The electronics used was quite similar to the ones that are used in the LHCb experiment. Figure 3.13 illustrates how

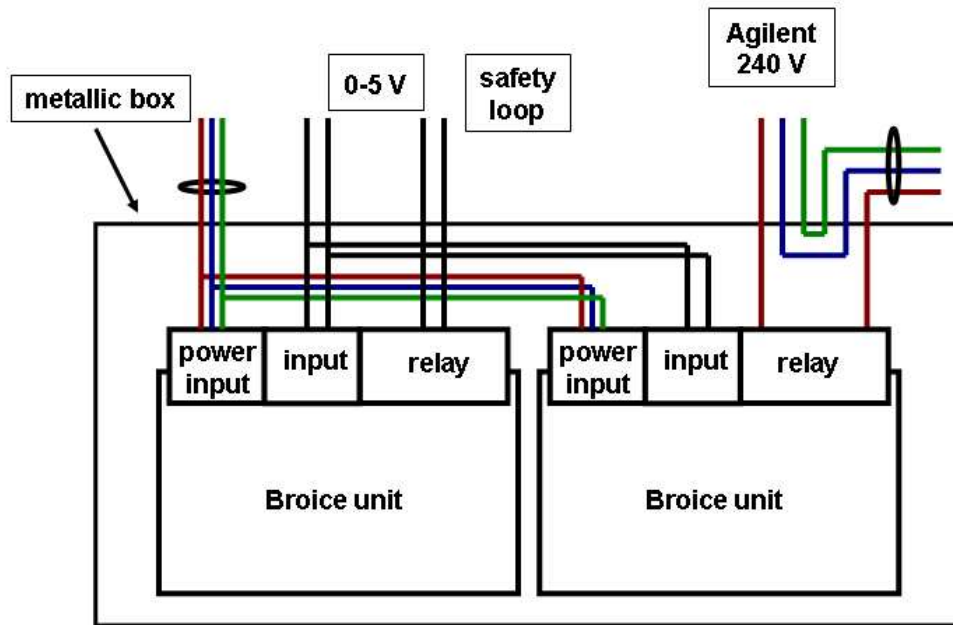


Figure 3.12: The top picture shows the pressure interlock schematic. The input signal was the 0-5 V delivered by the Controller 201 unit in the vacuum pump system. It used two relays to interlock both high voltage and low voltage units. The state of the relays could be verified from the LEDs on the front panel. The overvoltage and hysteresis were tuned on the front panel buttons. On the back panel the HV safety loop and Agilent power cable were connected.

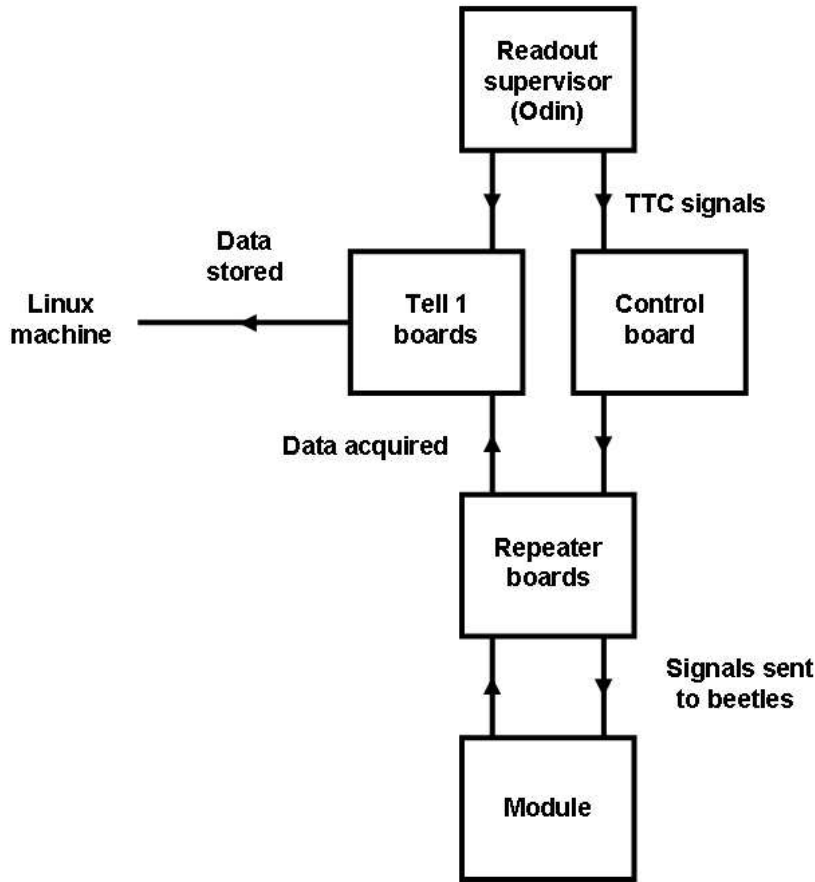


Figure 3.13: Diagram of the DAQ system in the burn-in. The readout supervisor sends TFC signals to the Beetle front-end chips in order to configure them. The data acquired is received and digitised by the Tell1 boards and then stored in binary files in a Linux machine.

the DAQ used in the burn-in was set up. Section 3.3.6.1 briefly describes the DAQ readout used in the burn-in system and its components function. The software used to control the DAQ system is introduced in section 3.3.6.2.

The Odin readout supervisor was responsible for the control of the module readouts [91]. It was performed by sending the timing and fast control (TFC) signals to the control board [103] and Tell1 mother boards [90] as illustrated in figure 3.13. The control board sent these signals to the Beetle chips in the modules via the repeater boards in order to configure and operate them. The data acquired from the module were sent back to the Tell1 boards passing through the repeater boards. The Tell1 boards digitised the data and this was finally acquired by a Linux machine by means of Gigabit Ethernet cards. The Linux machine saved the data

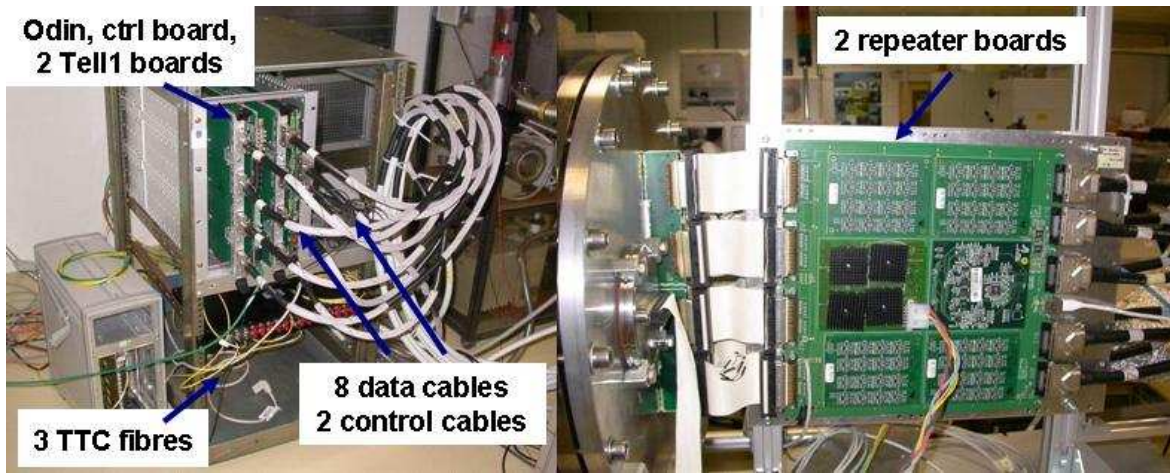


Figure 3.14: The DAQ setup in the burn-in system. Main components are indicated.

in binary files for further analysis. The full data was saved, i.e. non-zero suppression was performed.

### 3.3.6.1 Data Readout

The burn-in DAQ system was composed of electronic boards and parts which were specifically developed to perform the VELO data acquisition in the LHCb experiment. This section describes the DAQ used in the burn-in facility and how it was implemented. The functionalities provided by the DAQ components used in the burn-in system are also detailed.

The DAQ hardware consisted of two Tell1 mother boards, two repeater boards, one control board and one Odin readout supervisor. The Tell1 mother boards, control board and readout supervisor were located in a single crate. The repeater boards were placed close to the chamber lid. Figure 3.14 shows the complete setup. The Tell1 boards were connected to the repeater boards via 8 data cables each 5 m long. Two control cables 20 m long connected the repeater boards to the control board. To connect the repeater boards to the hybrid four PCB patch cards were plugged on the lid of the vacuum tank and sealed on the outside and inside of the chamber. Between the PCB patch cards and repeater boards there were 8 flat 50 pin cables 10 cm long with strain relief connectors. Finally the module kapton cables were connected directly to the patch cards inside the vacuum chamber.

In the LHCb experiment, the TFC system distributes the information that has to arrive synchronously at different points of the experiment [104]. In the burn-in system the readout supervisor was the component responsible for the distribution to the front-end electronics of the timing, trigger and control commands necessary for the synchronous readout. In the experiment it also controls the trigger rate avoiding buffer overflows using the status of the different components of the system.

The timing signals and fast commands from the readout supervisor were received by the



control board and distributed to the L0 electronics. There was only one control board in the burn-in system since each control board can support up to 6 VELO modules. The configuration data on the control board were translated and distributed to the configurable components via I<sup>2</sup>C by the Specs Slave on the board [105]. Specs is a 10 Mbit/s serial link based on a master multi-slave paradigm designed for the configuration of remote electronics elements. It is used to read the configuration of the electronics located on the detector. It allows fast, efficient and error safe communication between electronic elements. In the experiment the monitored voltages are digitised on the control board and sent to the experiment control system (ECS).

The repeater boards amplify the TFC signals and configuration commands from the control board. They also amplify the data signals read from the detector front-end. The control commands to the repeater boards were sent only by the control board. These boards also contain drivers and multiplexers for monitoring signals, which are of two types: temperature and voltage monitoring signals. In the LHCb experiment the monitoring signals are routed either to the so-called temperature board or to the control board. The temperature monitoring and interlock of the modules and repeater board are performed by the temperature board. However, in the burn-in system the temperature monitoring was performed using a Keithley and the temperature interlock was performed by a custom made unit (see sections 3.3.4 and 3.3.5).

A FPGA based acquisition board was developed for the LHCb experiment. The so-called Tell1 board is used on all sub-detectors of the LHCb experiment. Its design and functionality was constrained by the maximum L0 output event rate of 1.1 MHz. It makes the interface between the sub-detectors front-end electronics and the DAQ network. It can also perform data preprocessing but this feature was not implemented in the burn-in system.

The Tell1 board works as a receiver card of the front-end electronics signals. On the VELO the data is delivered via analogue electronic signals which are digitised on the analogue receiver side. The Tell1 board can accept electrical or optical signal input cards depending on the sub-detector it reads out. To perform the main preprocessing of the 1.1 MHz L0 accepted data the Tell1 boards have 4 PP-FPGAs (Pre Processor FPGAs). Some of the data processing steps that the Tell1 can perform on the data from the Beetle chips on the VELO modules are: pedestal subtraction, data reordering, common mode correction, clusterization, and finite impulse response filter correction (FIR). In the burn-in facility only the digitised raw data was saved and the processing was performed afterwards. The data from the PP-FPGAs went through the so-called SyncLink-FPGA which assembled the data fragments into events. Then various events were put together into multiple event packages (MEP) before its transmission to the DAQ network. The data was then delivered to the DAQ network via a Gigabit Ethernet card (GBE).

A Linux machine equipped with a GBE card was used to acquire the data from the Tell1

boards and to write it in binary files. The files were analysed with the Gaudi<sup>‡</sup> based Vetra package [107]. It was used to perform processing stages such as the pedestal evaluation and the common mode suppression of the data, saving the results in ROOT files. The final analysis to estimate noise, signal to noise and number of bad strips on the silicon sensors was performed by using ROOT scripts (see chapter 4).

### 3.3.6.2 Software

The software panels to control the hardware in LHCb are made within the PVSS framework [108]. It is an application that allows the development of supervisory control and data acquisition systems (SCADA). It is widely used on industrial applications to control distributed systems from a master location. PVSS is used by all LHC experiments and in LHCb it is mainly used to access the DAQ hardware slow controls such that it can be initialised, configured and operated. It can connect to the hardware devices, acquire data and monitor their behaviour.

The communication between the PVSS applications and the DAQ hardware in the burn-in laboratory was performed with the client-server paradigm. These applications allowed the user to initialise and operate all the boards in order to run the data acquisition system. Hence, the VELO module operation was also controlled by the system user via the PVSS applications.

Credit-card sized personal computers (CCPC) are used to control and monitor the electronic boards in LHCb. As in LHCb, each board was equipped with a CCPC which was connected via Ethernet to a control PC in the burn-in laboratory. The CCPCs provided the buses towards the electronics [109].

The CCPCs ran a server while the PVSS applications ran clients. By means of the client the application demanded the server to execute some task it could perform according to the functionality it had implemented. To perform the FPGAs programming directly, a generic server was available on the CCPCs. It was referred to as the DIM server since it was implemented with the Distributed Information Management package [110].

To operate the whole DAQ system a set of servers had to be initialised. To set up the Odin one had to start its server and depending on the type of task it should perform different recipes were loaded. The Odin server ran automatically on the readout supervisor board. In order to operate the control board correctly the Specs server had to be running properly and in the burn-in system it had to be started manually since the implementation of this server was not complete. In the final experiment the Tell1 boards also run servers but they are operated by direct Linux commands in the burn-in lab.

---

<sup>‡</sup>Gaudi is the framework used to develop the algorithms of the LHCb experiment [106].

### 3.4 Conclusion

A facility was developed and commissioned to perform the reception, visual inspection and burn-in of the VELO modules. The reception and visual inspection checks aimed to verify the physical integrity of the modules on their arrival and after the burn-in tests. The burn-in setup was used to perform a long term evaluation of the modules in environmental conditions similar to those in the LHCb experiment. The modules were thermally stressed in order to uncover any latent weakness intrinsic to the components of the module or introduced during the assembly phase.

Procedures and suitable mechanics were developed for the safe handling of the modules during reception and visual inspection. A transfer jig and an aluminium frame with a base compatible with the module attachment points were produced. When the module was mounted on this frame transparent plastic plates were used to protect the module. The frame fitted safely under the microscope to allow visualisation of the different elements of the module.

The burn-in setup was composed of vacuum, cooling, DAQ, interlock and monitoring systems. These components were developed to allow the modules to be operated under the required environmental conditions. Satisfactory performance of these components was achieved such that the VELO modules could be operated according to the requirements specified for the burn-in tests.

The vacuum system consisted of a set of vacuum pumps and a vacuum chamber. The obtained values of pressure obtained in the burn-in setup were adequate to test the module in a environment similar to the LHCb experiment. The system achieved pressure levels of the order of  $5\text{-}10 \times 10^{-5}$  mbar within a period of 20 to 40 minutes. Running overnight values of about  $0.5\text{-}1 \times 10^{-5}$  mbar were reached.

The cooling system was designed to provide appropriate heat transfer from the module to the coolant liquid used. The critical part of the design of this system was the cooling block. A set of mechanical constraints led the cooling block to be a two piece copper pipe connected by a U tube. This connection allowed the cooling pipe to expand and contract according to the temperature changes without applying mechanical stress on the module. The final cooling block was able to cool down a mounted module from  $30.0\text{ }^{\circ}\text{C}$  to  $-20.0\text{ }^{\circ}\text{C}$  in about 20 minutes. A similar period of time was necessary to bring the module temperature up again.

The burn-in DAQ system was used to acquire data from the modules. It read out both sides of the module simultaneously using two Tell1 boards. To set up the correct chip configuration a control board was used. Repeater boards were necessary to shape and amplify the signals read out from the Beetle chips and serve the modules with voltages and currents. The acquired data were digitised by the Tell1 boards and then saved onto disk using Gigabit Ethernet cards to transfer the data to the Linux machine available in the laboratory. Afterwards

the data were stored and analysed with the ROOT software that was developed.

A set of possible failure modes were identified in the burn-in system and to protect the modules against any possible malfunction an interlock system was developed. It consisted of two units which were used to monitor the temperature of the modules inside the tank and the pressure. In the case of a failure in the cooling system causing overheating the temperature hardware interlock would shut down the low voltage and high voltage supply to the module. If the vacuum system stopped pumping down, raising the pressure, then the pressure hardware interlock units would also turn off the module.

The Glasgow burn-in facility was commissioned and achieved the requirements necessary to allow the testing of the VELO modules, suitably replicating the LHCb environment. The vacuum system provided the low pressure needed within a reasonable time scale. The cooling system was able to thermally cycle the cooling block and control the hybrid temperature. A DAQ system to read out both sides of the module simultaneously was operated. The safety of the modules during the tests was ensured by a hardware interlock system monitoring both pressure and temperature of the module.

### 3.5 Future Improvements

A facility for the long term evaluation and quality assurance of the LHCb VELO modules was designed, commissioned and successfully operated. No significant failures occurred during the complete testing of all the production modules and all the procedures went smoothly (see chapter 4). The only failure during operation was of the rotary pump, which was replaced.

It is planned that a replacement set of sensors will be produced for the VELO. This section describes recommended changes to the burn-in facility for the testing of these future sensors. These improvements can be implemented in order to increase the reliability of the system and extend the range of tests that can be performed. In addition some elements (such as the vacuum system) should be serviced again before long-term operation. The main possible improvements are related to the cooling system, the fragile PCBs installed on the vacuum chamber lid and the operation of the monitoring software.

The cooling system was capable of keeping the modules at a safe and stable temperature level. However, the minimum temperature that was reached was strongly dependent on the mounting procedure of the cooling block on the module. Improving the flatness of the cooling block would allow a better thermal interface with the module. A thermal gel pad was used between the cooling block and the module. A thin plastic layer was kept in between, so removing this layer would improve the thermal conduction. However, it would need to be checked that this pad would not leave a sticky residue on the modules.

Four PCB cards were used to supply the modules with low and high voltages. The PCBs were placed in the lid of the vacuum chamber and sealed with Variant Torr Sealant. Inside the

vacuum chamber, short kapton cables were used to connect the PCB cards to the modules. As PCB cards are quite fragile the procedure of attachment of the short kapton cables was difficult and could potentially break one of the cards. Fortunately no such problem occurred during the burn-in operation. However, the replacement of one of these PCB cards and installation in the chamber lid would be time consuming. An additional mechanical support could be manufactured in order to avoid stresses on the PCB cards during the kapton cable attachment.

The monitoring software used was satisfactory for the burn-in purposes but its operation was temperamental and its full capabilities were not explored yet. So far, a number of temperatures and the high voltage were measured using the software algorithms. However, algorithms were also developed to measure the pressure, low voltages and currents and address the software stability issues. This second version of the software was not deployed during the burn-in operation as the continuity of operation was considered to be more important. This software should be tested and employed for the future use of the burn-in system.

# Chapter 4

## VELO Modules Characterisation

This chapter describes the inspection, thermal and electrical tests which were performed on the LHCb VELO modules before they were mounted onto the final VELO detector mechanics. The tests described and the results presented in this chapter were performed using the burn-in facility detailed in chapter 3.

As discussed in chapter 3 it was necessary to burn-in each of the VELO modules in an environment similar to the LHCb experiment to check for problems which could lead to module failure. The main problems that were checked for were electrical problems, thermal stress, degradation or any possible damage due to the transport of the module. These tests were of significant importance as they were the final testing stage before the modules were mounted on the detector halves. Once the module was permanently mounted onto the detector half it was very difficult to remove the module for inspection or debugging purposes.

This chapter is organised as follows. The introduction section 4.1 gives a brief overview of the LHCb VELO modules tests, the timeline from production to assembly and the general aims of the Glasgow burn-in tests. Section 4.1 describes and details the procedures that were applied during each test and stage of the Glasgow burn-in measurements. The high resolution inspections were performed using the equipment which was described in section 3.2 and details of the electrical testing setup were given in section 3.3.6.

Sections 4.2 - 4.8 detail the results that were found for each tested VELO module in the burn-in facility. Section 4.2 lists the problems that were found through the high resolution visual inspections. Thermal images of the modules were taken and compared. Temperature distributions of the modules, and the change in the distributions due to the burn-in tests are described in section 4.3. The signal to noise ratio measured by the front end chip header provided an estimation of the performance of the sensors on each module. An investigation into the signal to noise ratios is fully described in section 4.4. The effect of the burn-in procedures upon the signal to noise ratios was studied. For four modules the effect on the signal to noise ratio of varying the sensor bias voltage is also described.

The pre-irradiation leakage current of the sensors can highlight early problems with the modules. Results on the leakage current measurements are provided in section 4.5, and

section 4.6 explores possible correlations between high leakage current modules and the sensor cutting or the sensor's position on the original wafer. Section 4.7 characterises the pulse shapes from a n-on-n VELO module and compares it to a VELO module with a n-on-p sensor technology. The pulse shapes were analysed over a range of front end chip parameter settings. Section 4.8 lists the results of the electronic channels characterisation in terms of the number of bad channels for each module. Section 4.9 draws the conclusions from all the tests performed in the burn-in laboratory.

Each module was extensively tested in the burn-in laboratory and details of the tests are summarised in this chapter. After the module burn-in, each module was hand delivered to the assembly laboratory which was also located at CERN. The module was then mounted onto the VELO detector half and underwent another electrical test. Both fully populated VELO detector halves were sent to metrology to obtain alignment constants for the start-up phase of the experiment. The detector was then installed and commissioned in the LHCb experiment.

## **4.1 Burn-in Procedures**

In order to evaluate the quality of the delivered modules three different procedures were performed. First the modules underwent reception checks, then a visual inspection was done and finally electrical and thermal tests were performed. These procedures are described in sections 4.1.1, 4.1.2, 4.1.3. The burn-in time scale is described in section 4.1.4.

### **4.1.1 Reception**

The modules were unpacked from the custom built transport box and transferred to a storage box upon their arrival in the burn-in laboratory. During the transfer a checklist was followed to document the integrity of the modules upon arrival. The following items were checked by eye.

- Each module was shipped with its own uniquely fitted pair of kapton cables. For each cable the cable number was compared to the cable number in the University of Liverpool database [111], the copper-beryllium kapton clamps and the connectors were inspected for damage and the cable was inspected under a grazing light to check for indents into the surface of the kapton plane or for scratches on the surface.
- The transport box was checked to ensure that it was still filled with nitrogen and that the box had no loose components inside.
- The module had a full low resolution inspection performed of the paddle, the kapton clamp connectors, the cooling face, the hybrid components, the kapton connectors and the silicon surface. The hybrid was also inspected for any signs of delamination.

- A low resolution inspection with grazing light was performed on the bond wires to identify any lifted bonds that may have become loose during transport.

The full reception tests and transfer to the module storage box took 30-45 minutes per module.

#### **4.1.2 Visual Inspection**

A high resolution visual inspection was performed to the two sensors, hybrids and all wire bonding. The visual inspection of the modules was performed by using the equipment described in section 3.2. The following list provides details of what was visually inspected on each module.

- The two female kapton connectors on each side of the hybrid were checked for pin alignment, debris and scraping of the pin feet.
- The surface mounted components on each side of the hybrid were inspected.
- The high voltage (HV) return lines (one line on the  $\Phi$ -sensor with two sets of bond wires and two independent lines on the R-sensor where each line had two sets of bond wires).
- The scratch pads were inspected for any loose bond wires that could move during operation in vacuum.
- The surfaces of each one of the 16 front end Beetle chips on each side of the hybrid were checked for scratches, debris or any other visual problems.
- The pitch adaptors which route the silicon strips to the front end Beetle chips were checked for scratches, discolouration or debris.
- The silicon surface and the multiple floating guard rings were visually inspected for scratches, debris or stains.
- The Back End Bonds (BEB) of the Beetle chip were checked. The BEBs provide auxiliary signals such as the ground to the chip.
- The Front End Bonds (FEB) of the Beetle chip were visually inspected. The 128 FEBs were in 4 rows of 32 channels and the wire bonds connect the Beetle chip channel to the pitch adaptor.
- The Sensor End Bonds (SEB) between the silicon strip and the pitch adaptor channel were visually inspected. The SEBs were also in 4 rows of 32 channels.



Surface debris was carefully removed with nitrogen. Care was taken not to have a flow of nitrogen perpendicular to any bond wire or to blow the debris into a region of bond wires. The visual inspection lasted between 1.5 to 3 hours for every delivered module.

After the thermal and electrical tests were performed the modules were visually inspected for a second time. During the second inspection only the BEBs, the silicon surface and the specific FEBs and SEBs that were associated with channels that had failed any part of the electrical or thermal tests were inspected. The second visual inspection lasted only 15 minutes per module.

### 4.1.3 Electrical and Thermal Tests

After the visual inspection was performed the electrical and thermal tests were performed. The DAQ system used to perform the electrical tests with the VELO modules was described in section 3.3.6. The full testing procedure that was implemented is described below. For some modules an optimised version of the procedure was used and the differences between the two procedures are also indicated below. The change in procedure was motivated by the performance of the first 6 modules and the required throughput of modules.

- The module was mounted into a custom built frame. The 5 screws which are used in the LHCb experiment to secure the cooling connection were removed. The individually matched kapton cables were connected to the hybrid, and the silicon and hybrid were covered with an aluminium hood to minimise the chance of damage to the hybrid during the mounting procedures. Procedures were developed for handling the modules while mounting and dismounting them in the burn-in setup. Once mounted in the chamber, the module could be cooled, slid into the vacuum chamber, thermally imaged or electrically tested. The cooling system was described in section 3.3.2 and the vacuum system was described in section 3.3.1.
- Thermal images of each side of the module were taken in air with the front-end Beetle chips powered and configured. During the imaging the protective hood that covered the hybrid and the silicon was removed. Approximate camera alignment procedures were established to recreate the position of the camera relative to the silicon for every module that was imaged. The purpose of the thermal analysis was to spot Beetle chips that had a high or low current consumption, and to identify regions on the silicon of high temperature. The analysis that was performed is described, along with the results in Section 4.3. This procedure was removed for the optimised burn-in procedures.
- Electrical data and the behaviour of the sensors leakage current were recorded in air and then again in vacuum. The procedure for taking data and measuring the leakage current is described in Section 4.1.3.1.

- The module was thermally cycled four times. The chiller was set to temperature extremes of  $-37^{\circ}\text{C}$  and  $+30^{\circ}\text{C}$  which approximately corresponded to hybrid temperatures of  $-22^{\circ}\text{C}$  and  $+28^{\circ}\text{C}$ , depending on the quality of the cooling connection made during the module mounting procedure. The temperature was held at each extreme for 15 minutes and the time to ramp between the extremes was approximately 20 minutes. This procedure was included in the burn-in to thermally stress the module.
- Electrical data and the leakage current behaviour were measured in vacuum only at this stage and the procedure which was followed is described in Section 4.1.3.1. This step was removed for the optimised burn-in procedures.
- The Beetle chips were powered and configured and the cooling was turned on. No high voltage was applied to the sensors. The module was left for a chip burn-in procedure which lasted between 16-24 hours at pressures of around  $10^{-6}$  Torr. This test was designed to catch early chip failures.
- Electrical data and the leakage current behaviour were measured in vacuum and then in air to compare the performance after the thermal and electrical tests to the performance before. During the optimised burn-in procedure, data was not taken in air, but only in vacuum. The procedure that was followed is described in Section 4.1.3.1.
- The module was thermally imaged again so that when the image was compared to the first image, a differential image could be created. The differential image highlighted possible areas of change during the burn-in procedure. Again, the protective hood that covers the hybrid and the silicon during the burn-in procedure was removed. The thermal imaging stages were removed for the optimised burn-in procedures.
- The module was carefully dismantled according to written procedures. During the dismantling a second visual inspection was performed.

A description of the data acquisition procedures and analysis of the data taken with the modules in the burn-in laboratory is given in sections 4.1.3.1 and 4.1.3.2.

#### **4.1.3.1 Electrical Data and Leakage Current Measurements**

Electrical data and the behaviour of the sensors leakage current were recorded either in air or in vacuum. The following procedure was used to apply the bias voltage to the silicon sensors of the VELO modules and to acquire electrical data.

The appropriate cooling was applied and the Beetle chips were powered and configured. The current-bias voltage relationship was measured using ramp speeds of between  $0.4\text{--}0.8\text{ Vs}^{-1}$  and both the ramp up and ramp down were recorded. The bias voltage that was applied to the sensor in air was the larger of either 100 V or the depletion voltage as measured from

capacitance - voltage measurements plus 50 V. The maximum bias voltage applied in vacuum was 250 V. The temperature of the hybrid was measured during the recording of the leakage current as a function of the bias voltage. Electronic data was recorded when the maximum bias voltage was applied to the sensors.

The data was analysed immediately and the raw noise and the common mode corrected noise values were plotted. These quantities were calculated for each channel on both sides of the hybrid. An estimate of the signal to noise ratio was made using the Beetle header(see section 4.4). A list of channels which failed some set of specified cuts were listed as bad channels. There were three cuts implemented: an absolute maximum and minimum value cut of the raw noise measured in ADC counts; a maximum percentage deviation above the average common mode corrected noise calculated for a single link (a link is 32 channels); a percentage deviation below the average raw noise calculated for a single link. The list of bad channels were compared to the list of problem channels in the Liverpool database for each module. The results are given in section 4.8. During the optimised burn-in procedure, this stage was performed only in vacuum.

#### **4.1.3.2 Burn-in Data Processing**

As explained in section 3.3.6 the raw data acquired was received and digitised by the Tell1 boards. By means of Gigabit Ethernet cards installed on the Tell1 boards and on a Linux desktop machine the multi-event packages (MEP) were dumped and stored on a hard disk in binary file format. The binary files were processed with the VETRA package [107] which provided all the algorithms used to perform the data analysis.

In the burn-in analysis there were three main algorithms which ran in sequence to get access to and then analyse the ADC and headers values which were acquired from each Tell1. The first algorithm accessed the raw ADC and header values organising them into histograms according to their corresponding Analogue Receiver Card (ARC), Link and Beetle chip number (0..15). The second algorithm accessed the common mode suppressed ADC and header values before and after the pedestal subtraction stage. This information was also saved according to the ARC, Link and Beetle chip. The third algorithm estimated the pedestals and noise before and after the common mode suppression for even and odd events.

#### **Common Mode Suppression**

The common mode suppression was evaluated for all 2048 channels in the 16 Beetle chips for each side of the module (section 2.2.1.4). Each Beetle chip had 128 channels which were divided in 4 ports or links which contained 32 channels per link. The common mode suppression was calculated for each individual link. The common mode suppression calculation was broken down into 3 steps.

- i The average ADC value ( $\langle \text{ADC} \rangle$ ) was calculated over the 32 channels on each link.

- ii A new average ( $\langle \text{ADC}' \rangle$ ) was calculated excluding all channels in the link that differed significantly from the original average calculated in step 1 ( $\sim 5 \sigma$ ). This was performed in order that the common mode suppression was not biased by strips containing test pulses.  $\langle \text{ADC}' \rangle$  was the common mode suppression value.
- iii The common mode suppressed ADC ( $\text{CMSADC}_i$ ) for each channel was calculated by subtracting the common mode suppression value from the ADC of the channel  $i$ . Denoting the original ADC value of each channel as  $\text{ADC}_i$ ,  $\text{CMSADC}_i = \text{ADC}_i - \langle \text{ADC}' \rangle$ .

In the final experiment two stages of common mode suppression are used, one in electronic channel order and one in strips order. One is a mean common mode algorithm similar to that described here, the other also allows a common mode slope across channels.

### **Pedestal subtraction**

A pedestal map was obtained using 1000 events and the mean pedestals were subtracted afterwards. The pedestal subtraction was calculated directly on the CMSADC. It was given by the difference between the CMSADC and the average pedestal calculated over the 32 channels in the corresponding link.

The output of the analysis algorithms were stored in a single ROOT file. All the histograms and profiles that were obtained were saved in a directory structure. This structure was used to relate the data with its respective Tell1 board. The output of the three algorithms were stored in different branches inside each of the directories.

In the final experiment the pedestal subtraction is performed before the common mode subtraction, and the pedestal is calculated separately for each individual channel.

### **4.1.4 Burn-in Time Scale**

The full procedure lasted around 42.5 hours if the steps were performed sequentially with no delays. The optimised procedure which excluded the thermal pictures analysis lasted between 29-32 hours.

The type of electrical testing which the module received depended on the delivery date of the module. The first 9 delivered modules were electrically tested, having their noise and leakage current measured, and were then sent to a test beam for long term running and temperature cycling. The next 6 modules underwent the full burn-in procedure which was described in section 4.1.3. The remaining 30 modules underwent the optimised burn-in procedure which was also described in section 4.1.3.

The dates of each module reception, visual inspection and full burn-in are shown in Figure 4.1. The qualification tests successfully managed to follow the module delivery rate, through the Glasgow burn-in team working in shifts.

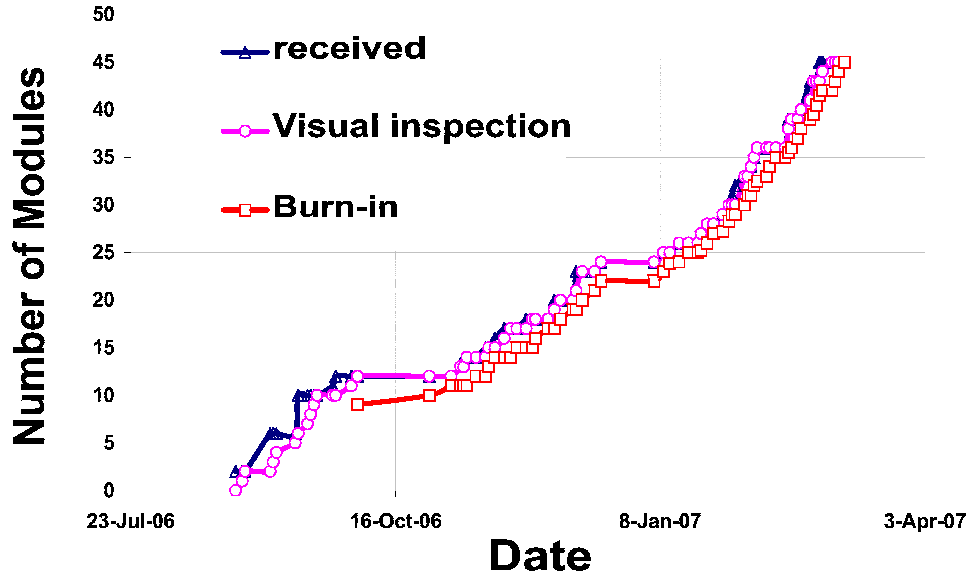


Figure 4.1: The dates on which the VELO modules were received, visually inspected and their burn-in completed.

## 4.2 Visual Inspections

The visual inspections of each VELO module were an important component of the module procedures. Section 3.2 described the visual inspection setup and section 4.1.2 provided the details of the visual inspection procedure that was performed on every module. The following sections detail some of the results from the module visual inspections.

### 4.2.1 Kapton Damage

The procedure for attaching and removing the kapton cables onto the kapton connectors on the module was performed using two tools. The Liverpool group designed these tools to minimise mechanical stress on the hybrid during the attaching/removing routines. The kapton attachment tool used a parallel force applied simultaneously to the loosely placed kapton cables on both sides of the hybrid. The removal tool had a similar shape to a tuning fork and was used to remove one kapton cable at a time by sliding the tool along the outside of the connector and forcing the hybrid and the cable to separate. The first version of this removal tool was made of aluminium and it was found during the visual inspections of the first modules that the feet on the outside of the hybrid kapton connectors were being scraped and some of the feet were being broken. This was discovered early and a version of the kapton removal tool fabricated from plastic was made. This version avoided the scraping on the feet of the hybrid kapton connectors of the subsequent modules.

### 4.2.2 HV Return Lines

The two HV return lines on the R-side of the hybrid and the one HV return line on the  $\Phi$ -side of the hybrid were inspected on all modules (as described in section 4.1.2). The bond wires on some of the first modules were found to be deformed and in some cases the bonds were broken. This was traced back to a holding jig at the production site in University of Liverpool. When the module was suctioned down on to the jig under vacuum, the HV return bonds positioned at the edge of the hybrid were being deformed by the edge of the jig. The jig was quickly altered to allow a larger opening for the hybrid to be placed on. The visual inspections of subsequent modules revealed the problem had been rectified and the HV return bonds were not damaged.

### 4.2.3 Silicon Surfaces

Any surface debris that was found was gently blown off with a nitrogen gun. The most common problems that were found with the silicon surfaces were small surface scratches due to production and stains from handling. The guard ring area was carefully inspected for cracks or scratches on each sensor but no problems were found.

### 4.2.4 Pitch Adaptors

The most common problems that were noted with the pitch adaptors was damage to the traces by scratches. Occasionally the scratches were deep enough to put a break in the pitch adaptor trace of a single channel. Debris was noted but not removed due to the difficult positioning of the pitch adaptors in between the FEBs and the SEBs. Surface damage like excess epoxy glue was not found to affect the electrical performance of any channels (figure 3.3).

### 4.2.5 Bonding

Both ends of approximately half a million bond wires were visually inspected. There were a small number of discrepancies between the bad channel lists that were compiled in University of Liverpool by laser measurements and the visual inspection that was performed in the burn-in laboratory. The main problems that were found for the bonds were lifted bonds, electrical shorts between a few channels due to metallic debris on the SEBs and deformation in the bonds where the deformation occasionally resulted in two bonds being electrically shorted. The lifted BEBs were usually not problematic since most of the auxiliary signals were duplicated and therefore due to the redundancy in the design, the lifted bond was left (figure 3.3). No intervention was possible in the burn-in laboratory in the case of lifted FEBs or SEBs due to the complexity of the bonding pattern. The maximum percentage of bad channels for any side of the modules was approximately 1.7 %, however, the majority of

modules had much less than this value. See Section 4.8 for details of the bad channels that were electrically measured.

Two separate cases were visually found where one of the pre-amplifier bonds on the BEBs of a Beetle chip was found to be burnt and broken. Each Beetle chip had 6 pre-amplifier bonds. In each of the two cases the fragments of the burnt bonds were removed and the chip was thoroughly electrically re-tested.

### 4.3 Thermal Images

The first 6 modules which received the full burn-in procedure were thermally imaged both before and after the thermal and electrical tests. The thermal images were taken in air and with the front end Beetle chips turned on and configured. Images of each side of the hybrid which were taken before and after the burn-in were inspected for areas of non-uniformity. The differential image which resulted from the subtraction of the images taken before and after the burn-in procedure was also obtained.

The temperature of the chiller was set to 15 °C, and depending on the quality of the cooling connection that was achieved during the module mounting, the hybrid temperature was around 34 °C. The temperature of the hybrid varied slightly between the thermal images taken before and after the burn-in, usually the effect was around 1-2 °C. An alignment procedure for the thermal camera was set-up using a well positioned jig for the thermal camera and fine alignment was performed by eye for the angular field of vision. The edge of the silicon was used as the reference for alignment. The typical alignment achieved was a few millimetres between objects in the thermal image of one side of the hybrid before and after the burn-in.

Figure 4.2 shows examples of the thermal images that were taken before and after the burn-in procedure, as well as an example of the differential image that was the result of the subtraction of the thermal images taken before and after the burn-in.

Figure 4.3 shows the average temperature of each Beetle chip on the R and the  $\Phi$ -hybrids of a module. The Beetle chips positioned closest to the edge of the hybrid were slightly hotter than the middle chips which were positioned further away from the cooling block. No irregularities were found in any of the images for all of the six modules that were imaged.

The average temperatures of the Beetle chips were measured on the differential thermal images and the distributions from the R and  $\Phi$ -hybrids are shown in figure 4.4. The temperature difference in each Beetle chip was less than 2 °C for all chips. The thermal images check aimed to find any possible degradation of the thermal contact between the Beetle chips and the hybrids after the modules thermal stress.

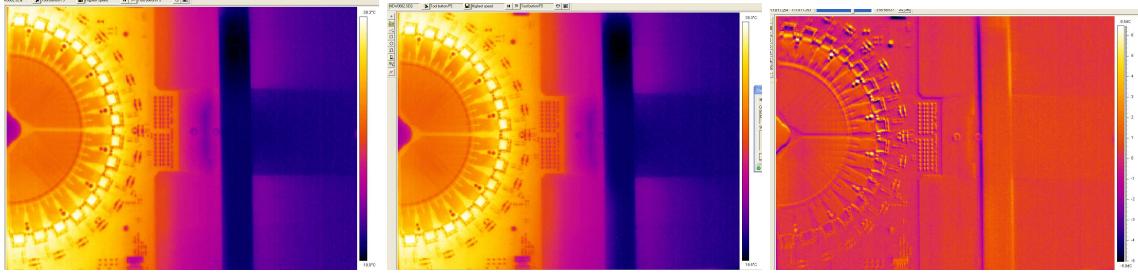


Figure 4.2: Three thermal images of the R-side of a module (module 25). The silicon (orange semicircles on the left), 16 Beetle chips (16 bright yellow squares positioned around the silicon), the hybrid, some of the hybrid components and the cooling block are visible in the first two thermal images. The first thermal image was taken before the burn-in procedure and the second image was taken after the burn-in procedure. The temperature range for the first two images is between 19-39 °C. The third image is a pixel-by-pixel subtracted image between the first and second thermal images and the temperature range is between -6.5 and -5 °C.

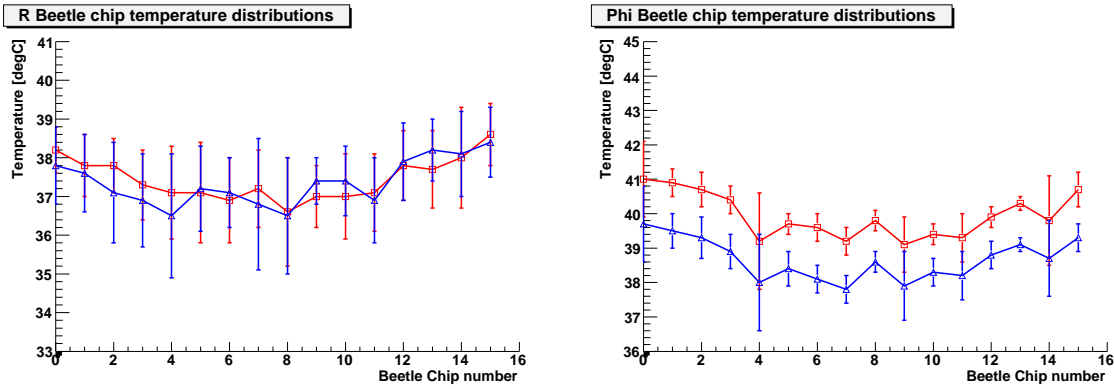


Figure 4.3: The average temperature of each of the 16 Beetle chips on the R (left plot) and  $\Phi$ -side (right plot) of a module. The blue triangle markers are the average temperatures before the burn in and the red squares are after the burn-in procedure. The Beetle chips are numbered sequentially from the top of the hybrid. In this case the average temperature of the silicon on the R-side was  $30.3 \pm 0.4$  °C before the burn-in and  $30.4 \pm 0.4$  °C after the burn-in. The average temperature of the silicon on the  $\Phi$ -side was  $32.2 \pm 0.4$  °C before the burn-in and  $33.9 \pm 0.4$  °C after the burn-in.

## 4.4 Signal to Noise Ratio

The signal to noise ratio was estimated using header signals from the Beetle chips. Details of the output characteristics and readout modes of the Beetle are given in [78]. The peak-to-peak header amplitude was constant over time and approximately the same for all Beetle chips. It was verified that the amplitude of the last header bit in the analogue mode was



### Beetle chip differential temperature distributions

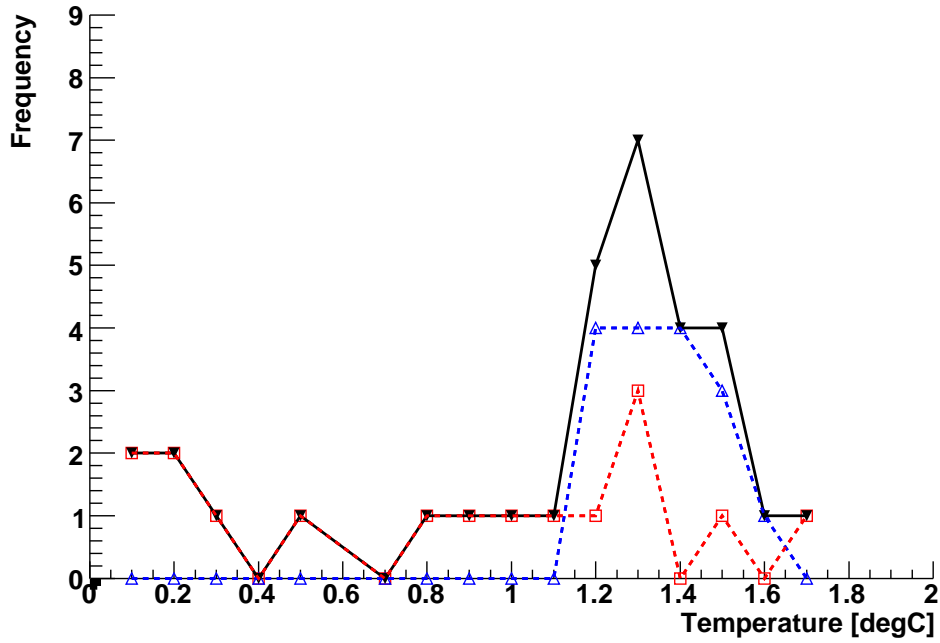


Figure 4.4: A histogram of the average temperature difference of each chip measured on the thermal images before and after the burn-in procedure. The red dashed line with open red square markers shows the distribution of the 16 Beetle chips on the R-side of the hybrid and the blue dashed line with triangle markers shows the contribution from the 16 Beetle chips on the  $\Phi$ -side. The black solid line shows the total for all chips on module 32.

equivalent to  $3.0 \pm 0.4$  times the amplitude resulting from the charge that a minimum ionising particle (MIP) would deposit in  $291 \mu\text{m}$  of silicon [112]. The signal to noise ratio was therefore defined by the difference of the averages of the high and low amplitudes divided by three times the average common mode suppressed noise for each link of the hybrid. All signal to noise ratio plots shown throughout this chapter were performed as per the calibration given in [112]. Figure 4.5 shows typical plots of the noise for each of the 2048 channels on each hybrid before and after the common mode subtraction.

Figure 4.5 shows the noise and the common mode corrected noise as a function of both the electronic chip channel and the geometric sensor position strip number ordered by software. The two channel orderings differ by a rearrangement only. The capacitance of the inner and the outer strips on the  $\Phi$ -sensor were different due to the difference in the strip length. This can be seen in the measured noise of the first 683 software channels of the  $\Phi$ -sensor in figure 4.5. The R-sensor had 4 sectors of 512 channels which increased in strip length across the 512 channels. The pattern of the 4 sectors with increasing noise can be seen in the bottom right hand plot of figure 4.5.

As an illustration, the signal to noise distribution for each link on module 55 \* is shown

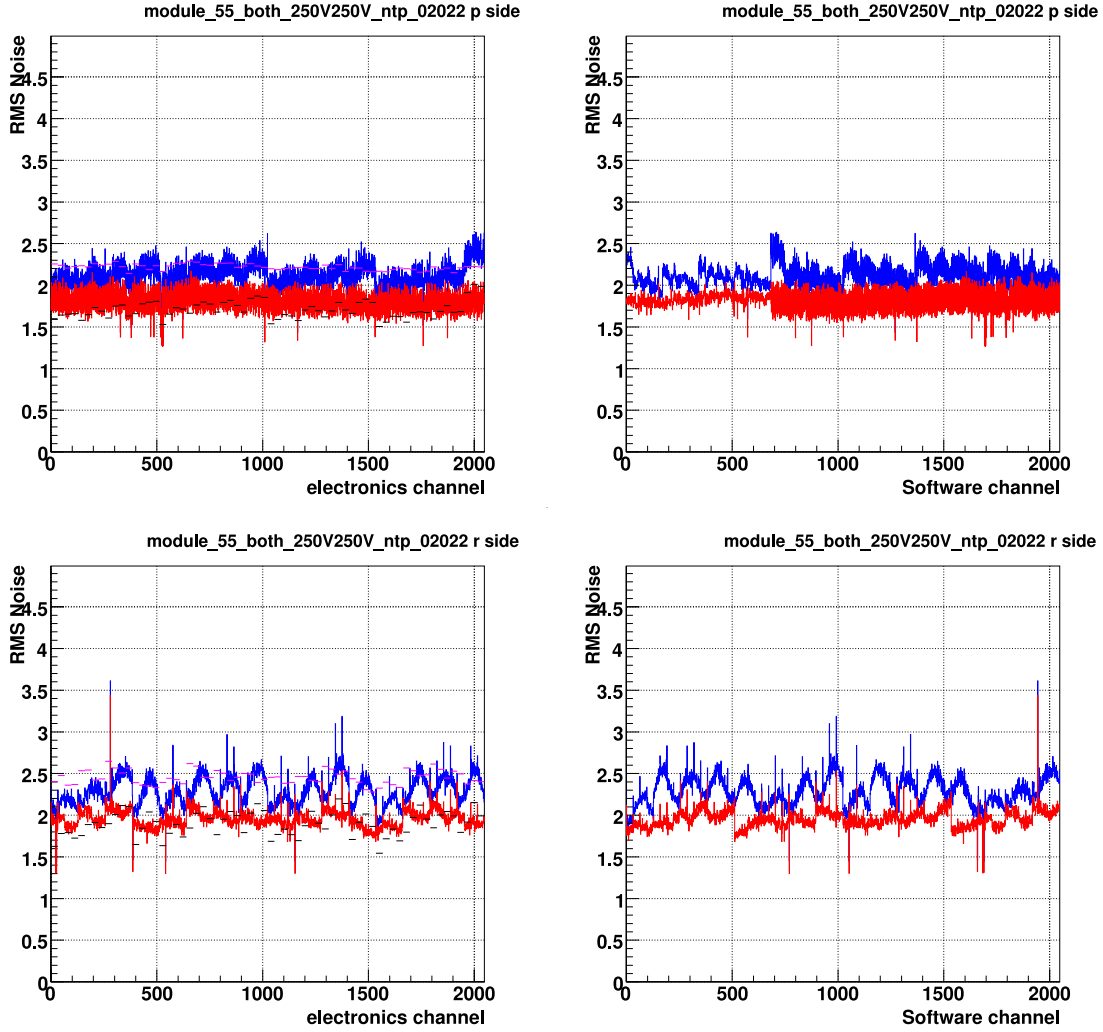


Figure 4.5: The top two plots show the noise (blue) and the common mode corrected noise (red) for each channel on the  $\Phi$ -side of module 55 and the bottom two plots show the noise (blue) and the common mode corrected noise (red) for the R-side of the hybrid. The two plots on the left show the noise as a function of the electronic channel and the two plots on the right side show the noise as a function of the software channel. The pink and black horizontal lines on the plots are respectively the maximum deviation of the common mode suppressed ADC values and minimum deviation of the raw ADC for each link. A full description of these analysis criteria are provided in section 4.8.

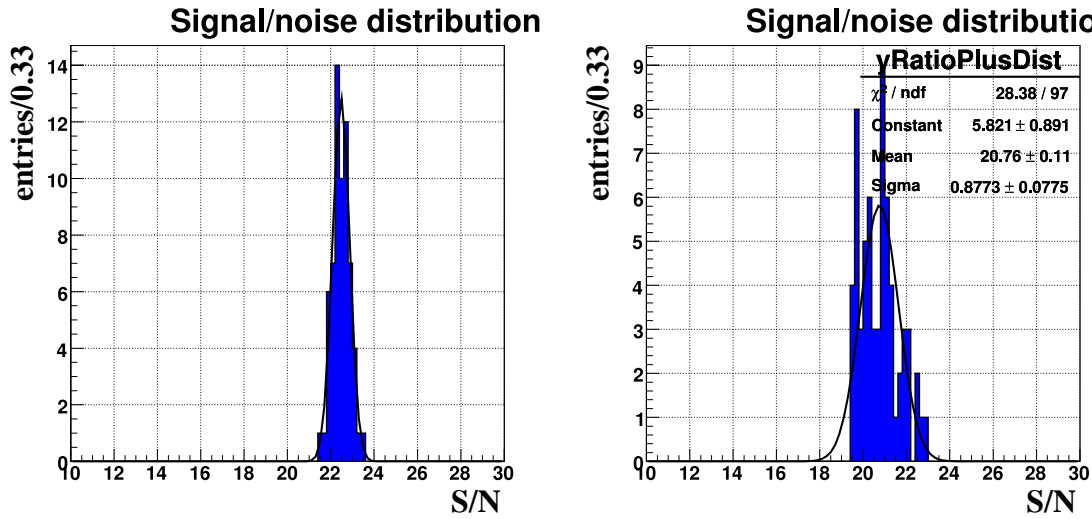


Figure 4.6: The signal to noise distribution per link of module 55 is shown on the left for the  $\Phi$  sensor and on the right for the R-sensor.

in figure 4.6 for both the R and the  $\Phi$ -hybrids.

All of the modules that were tested in the burn-in laboratory had their signal to noise ratio estimated before and after the burn-in procedure. Figure 4.7 shows the signal to noise calculated for both the R and  $\Phi$ -sensors as a function of the module number for the module before it was burned-in and after the module had been through the burn-in procedure. No degradation in the signal to noise was observed due to the burn-in procedure for any side of any module. The signal to noise ratio was higher for the  $\Phi$ -side of the modules compared to the R-side. Figure 4.7 also shows the distributions for the signal to noise ratios for the modules measured before the burn-in and after the burn-in procedures.

The mean of the signal to noise distribution obtained via a Gaussian fit was the same before ( $20.39 \pm 0.03 \pm 2.86$ ) and after ( $20.44 \pm 0.03 \pm 2.87$ ) the burn-in procedure for the R-sensor. The first uncertainty on the means of the distributions and on the following widths come from the uncertainty in the fit and the second uncertainty comes from the calibration given in [112] for 291  $\mu\text{m}$  thick silicon. The mean of the Gaussian fits to the distribution for the  $\Phi$ -sensor was also relatively unchanged with a mean of  $22.45 \pm 0.06 \pm 3.15$  before the burn-in and  $22.37 \pm 0.06 \pm 3.14$  after the burn-in. The width of the R-sensor distributions was  $0.15 \pm 0.03 \pm 0.02$  before and  $0.18 \pm 0.03 \pm 0.03$  after the burn-in procedure and the width of the Gaussian fit to the  $\Phi$ -sensor signal to noise ratio distribution was  $0.35 \pm 0.04 \pm 0.05$  before and  $0.33 \pm 0.04 \pm 0.05$  after the burn-in procedures.

The signal to noise ratios estimated in the burn-in system were compatible with the values obtained in previous measurements [112] and with estimates later obtained with test beam data analyses [113]. The results of the burn-in indicated that the VELO modules signal to

---

\*The module number corresponds to the its production number.

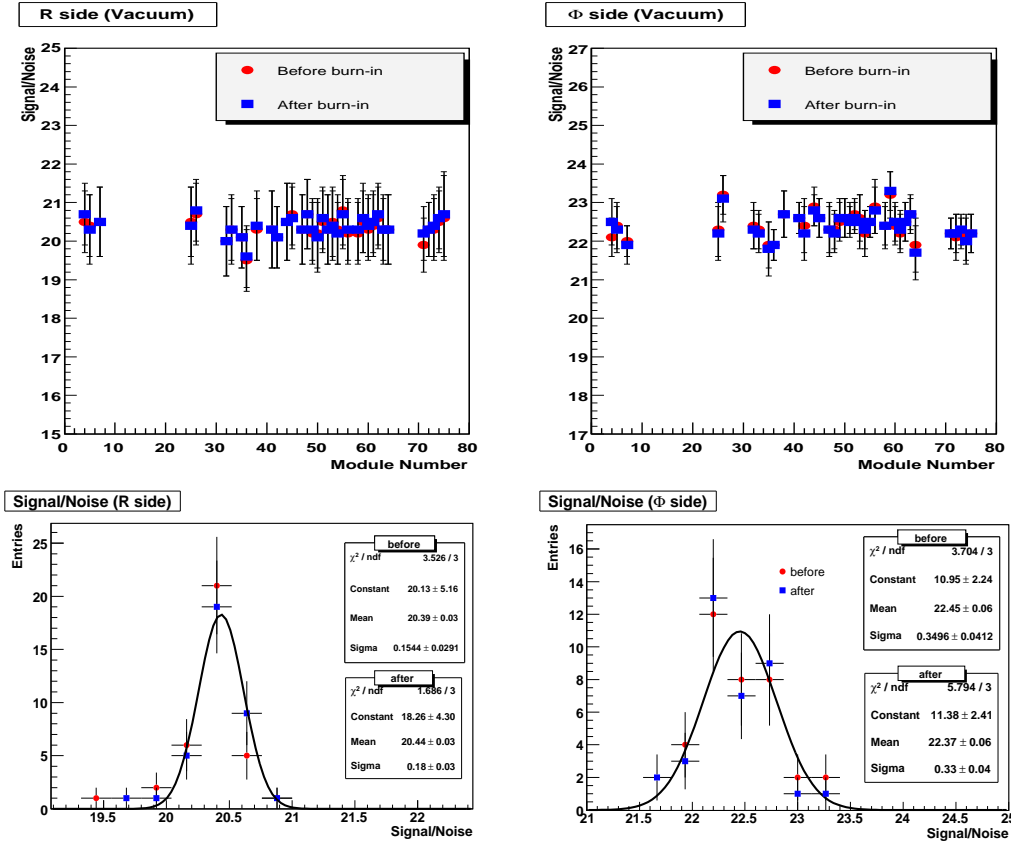


Figure 4.7: The top two plots show the estimated signal to noise ratio from the Beetle header as a function of the module number. The red circular markers are the measurements from before the burn-in procedure and the blue square markers are from after the burn-in procedure. The bottom two plots show the distribution of the signal to noise ratio for the measurements made before the burn-in (red circular markers) and after the burn-in (blue square markers). The Gaussian fit is shown for the fit to the signal to noise distribution after the burn-in. The plots on the left are for the R-side and the plots on the right are for the  $\Phi$ -side.

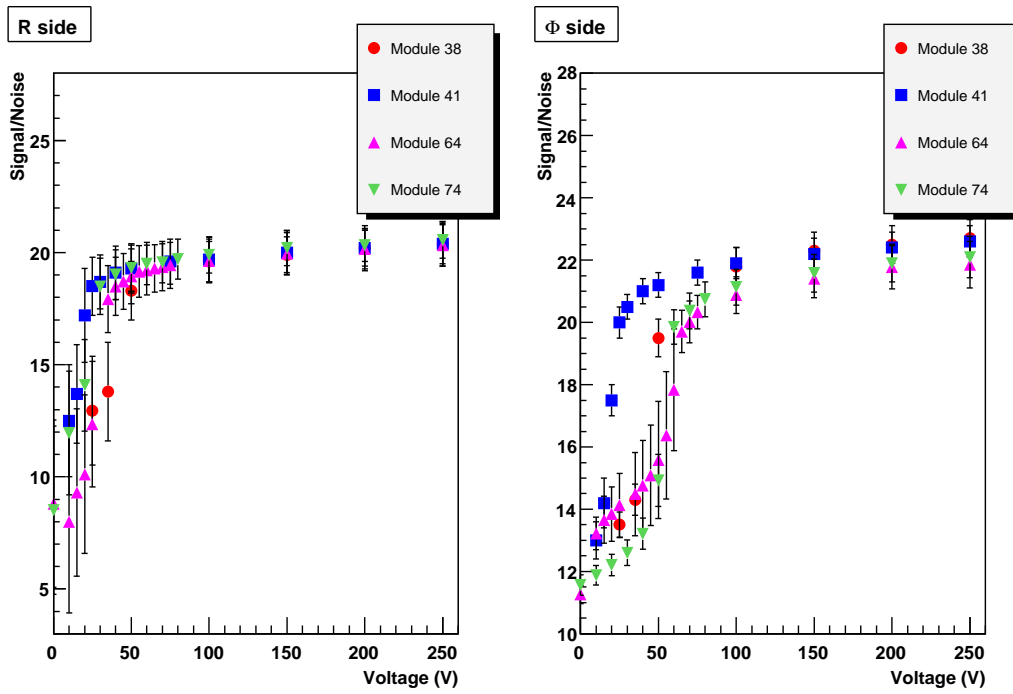


Figure 4.8: The signal to noise ratio as a function of the bias voltage applied on silicon sensors for the R-sensors (left) and the  $\Phi$ -sensors (right).

noise ratio satisfied the LHCb requirement  $\text{Signal/Noise} > 14$ . The Signal/Noise ratios well above the LHCb requirement should allow the modules to sustain radiation damage in the LHCb environment and to be operated efficiently for the expected period of data taking (section 2.2.1.2).

#### 4.4.1 High Voltage Scans

Electronic data were taken at a range of bias voltages for a few modules. The signal to noise ratio as a function of bias voltage was therefore extracted. Four modules in total were measured in such a manner and the curves obtained are shown in figure 4.8. The voltage at which the signal to noise ratio starts to plateau provides an indication of the approximate point of device depletion, although this method did not provide as good accuracy in determining the depletion voltage as other methods such as measuring the charge collection efficiency.

Each of the four modules began to plateau at bias voltages of 50 V for the R-sensors and 80 V for the  $\Phi$ -sensors. Figure 4.9 shows the depletion voltage which was measured at University of Liverpool as a function of the module number. The R-sensors of modules 38, 41, 64 and 74 had depletion voltages between 30 - 50 V which agreed well with the signal to noise ratio voltage scans for the R-sensors shown in figure 4.8. The  $\Phi$ -sensors had depletion voltages less than 80 V, which also agreed with the signal to noise ratio voltage scans for

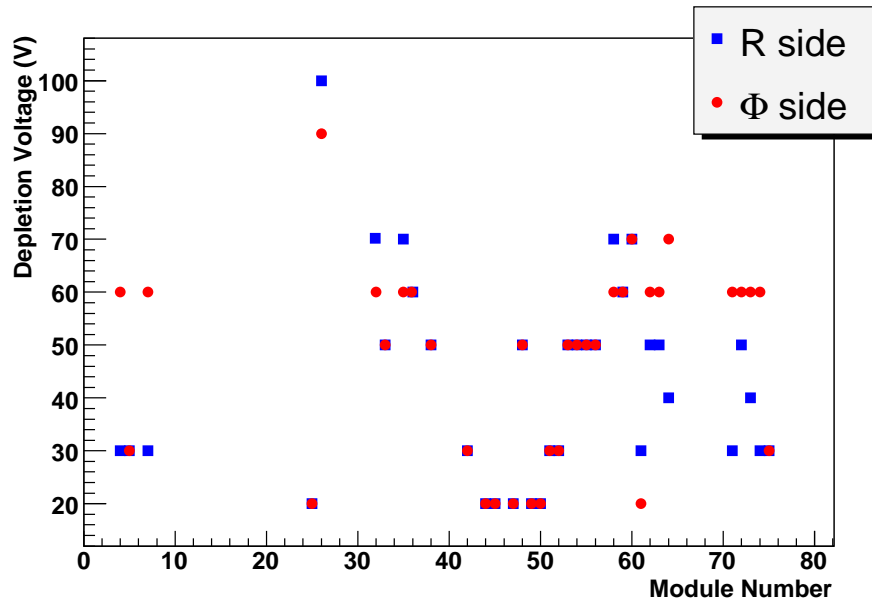


Figure 4.9: The depletion voltage for the R (blue square markers) and  $\Phi$ -sensors (red circle markers) as a function of the module number. The depletion voltage was measured using the capacitance-voltage method in University of Liverpool.

the  $\Phi$ -sensors shown in figure 4.8. The shape of the high voltage scans from three of the  $\Phi$ -sensors (modules 38, 64 and 74) were as expected for an  $n^+$ -in-n sensor which was read out through the segmented  $n^+$ -implants and before irradiation, see figure 4.8. However, due to the low depletion voltage of the R-sensors and one of the  $\Phi$ -sensors (module 41) the curves shown in figure 4.8 plateau at a low bias voltage.

This method was used to estimate the starting operation voltage of the sensors during the assembly of the modules in the VELO ( $\sim 100$  V). In future this approach will be used as a complementary method to monitor the depletion voltage of the silicon sensors. This means the depletion voltage will be evaluated also when no LHC beam is available.

## 4.5 Leakage Current

The VELO modules leakage current was measured in order to verify its values were within the expected limits and it did not degrade during the burn-in procedures. The Iseg unit (see section 3.3.3) was used to provide the bias voltage to the sensors and to acquire the leakage current data used to obtain the results presented in this section. Section 4.5.1 describes the method used to compare the measurements performed at different temperatures. Section 4.5.2 presents the results on the monitoring of the leakage current during the burn-in procedure. The accuracy on the measurements of the leakage current was  $\sim 0.4 \mu\text{A}$ .

### 4.5.1 Temperature Corrections

To compare multiple measurements on one sensor, or compare modules to each other it was necessary to make temperature corrections to the leakage current measurements. Depending on whether the original or optimised burn-in strategy was used the number of measurements of the leakage current-bias voltage behaviour was between 2-5. Each measurement of the same module was made at a slightly different temperature. The temperature of the silicon dramatically affected the leakage current. The measured current from the detector had a contribution from the bulk silicon and a contribution from the surface of the silicon. Unfortunately due to the bonding scheme of the VELO modules it was not possible to distinguish between these two contributions. The temperature dependence of the two sources of leakage current were very different. If the leakage current was dominated by the leakage of charge carriers across the band gap,  $E_g$ , of the silicon, as was the case with leakage current generation in the bulk, the following equation could be used to scale the leakage current measured:

$$I(T_{ref}) = I(T) \cdot \left(\frac{T_{ref}}{T}\right)^2 \cdot \exp\left(\left(\frac{-E_g}{2k_B}\right)\left[\frac{1}{T_{ref}} - \frac{1}{T}\right]\right). \quad (4.1)$$

where  $T_{ref}$  is the reference temperature,  $T$  is the measurement temperature and  $k_B$  is the Boltzmann constant.

For further analysis it was useful to compare the leakage current of a single sensor measured several times during the burn-in procedure, and also to compare the leakage current between sensors. Therefore, it was necessary to establish how well the leakage current obeyed equation 4.1.

Two modules were studied to establish the temperature behaviour of the sensors; module 64 and module 26. Module 64 was a standard n-on-n production VELO module and module 26 was a production module but made with two n-on-p sensors. The leakage current was measured at 250 V bias on the R and the  $\Phi$ -sensors while the Beetle chips were turned off. The temperature was varied using the cooling block on the hybrid and the temperature of the NTC on the hybrid was noted. Figure 4.10 shows the measured leakage currents as a function of the hybrid temperature.

The leakage current, which was measured at 27.3 °C, was then scaled using equation 4.1 to the other hybrid temperatures and was compared to the measured data in figure 4.10. While not a perfect agreement, both the R and the  $\Phi$ -sensors show a similar trend between the scaled and measured leakage currents.

The same procedure was performed on module 26 and figure 4.11 shows the comparison between the measured and the scaled leakage currents for module 26. The measured and the scaled trend of the temperature of the R-sensor of module 26 agreed roughly. However, the  $\Phi$ -sensor leakage current of module 26 did not agree with the temperature scaling. The leakage current of this sensor was quite high (around 50  $\mu$ A) and actually decreased with increasing temperature. It could be concluded that for this sensor the leakage current was

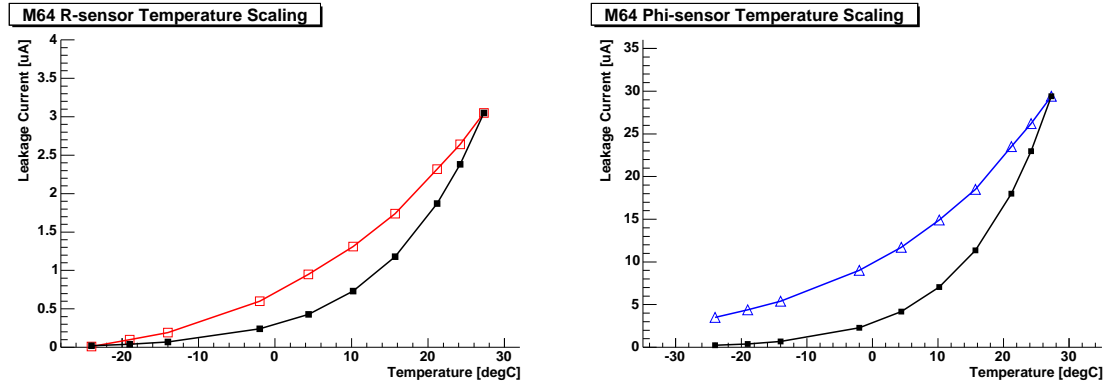


Figure 4.10: The temperature dependence of the leakage current measured at 250 V bias of module 64 is shown for the R-sensor leakage current on the left (red open square markers) and the  $\Phi$ -sensor leakage current on the right (blue open triangle markers). The black solid square markers on both plots are the temperature scaled leakage current starting from the measured leakage current at 27.3 °C.

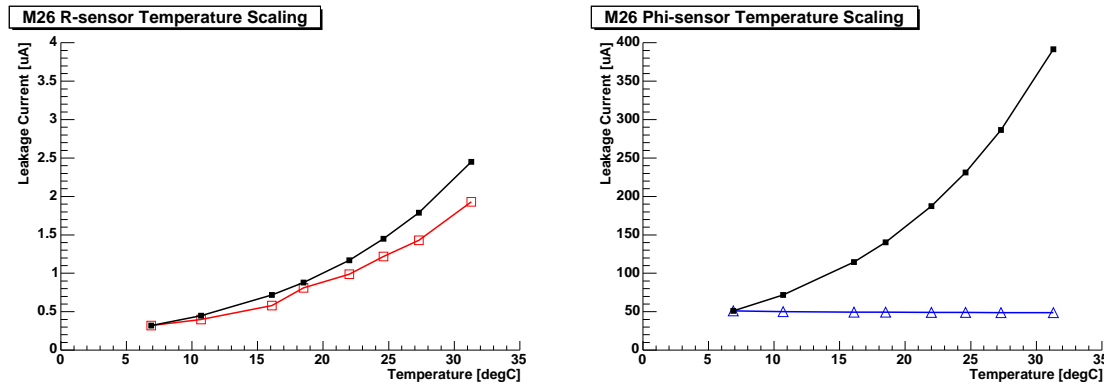


Figure 4.11: The temperature dependence of the leakage current measured at 250 V bias of module 26 is shown for the R-sensor leakage current on the left (red open square markers) and the  $\Phi$ -sensor leakage current on the right (blue open triangle markers). The black solid square markers on both plots are the temperature scaled leakage current starting from the measured leakage current at 6.9 °C.

not dominated by the leakage of charge carriers across the band gap of the silicon but there should be another source of the large leakage current. Figure 4.12 shows a zoom of the measured leakage current at 250 V bias for the  $\Phi$ -sensor and indeed the leakage current was found to decrease slightly with increasing hybrid temperature.

Most of the VELO production modules were found to have leakage currents which approximately scaled with temperature according to the exponential term which described the leakage of charge carriers across the band gap. Module 26 was found to have anomalous leakage current behaviour, and one further sensor on module 64 was also found to behave in



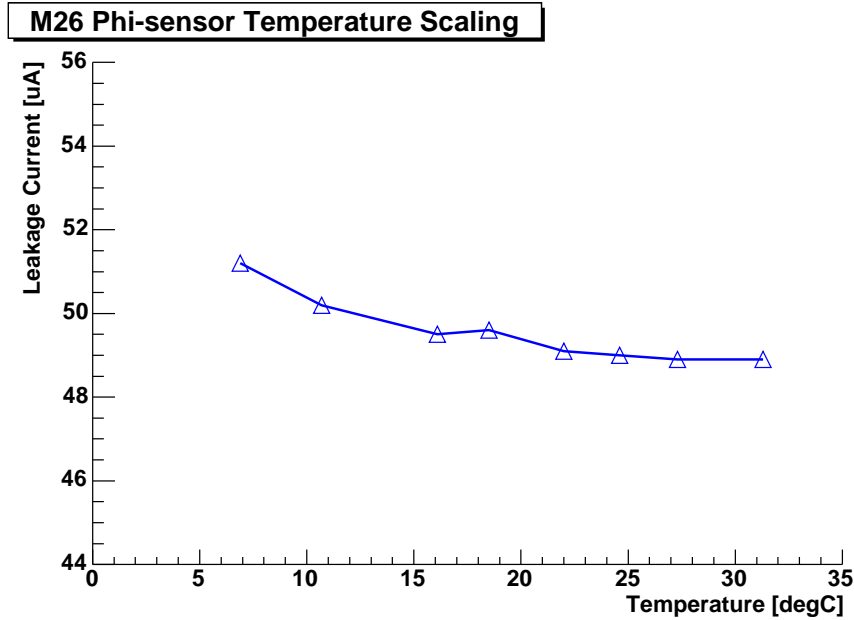


Figure 4.12: The temperature dependence of the leakage current measured at 250 V bias of module 26 is shown for the  $\Phi$ -sensor leakage current.

a similar manner which is described in section 4.5.2. Therefore, these two high leakage current sensors were found not to scale with temperature and indeed, the leakage currents were found to decrease with increasing hybrid temperature. Some of the subsequent analysis in this chapter uses the temperature scaled leakage current. Wherever possible, both the scaled and the measured currents are provided.

### 4.5.2 Current Degradation

Measurements of the leakage current were performed on the VELO modules to investigate if there was any degradation in the leakage current behaviour at different stages of the burn-in tests. The leakage current was measured at the University of Liverpool before the transport of the modules to the burn-in laboratory, and then additional measurements were made before and after (and for some modules during) the burn-in procedure. This analysis studied the leakage current on both the R and  $\Phi$ -sensors for the VELO modules.

Two basic quantities were used to characterise the leakage current behaviour of the VELO sensors: the absolute value of the leakage current measured as a function of bias voltage; and the percentage change in the measured leakage current between two stages of the production line. For the majority of the sensors the applied voltage on the silicon was 250 V, although a lower bias voltage was applied for high leakage currents (100  $\mu$ A was the maximum current drawn from any sensor).

As already mentioned in section 4.5.1, the current generated in the sensor due to the

leakage of charge carriers across the band gap depended on the temperature of the sensor. The method described in section 4.5.1 was used to compare the measured values of the sensor leakage current for many sensors or to compare the leakage current of one sensor at various measurement stages at different temperatures. The chosen temperature for scaling all leakage current measurements was 20.0 °C since this was the approximate temperature when the leakage current measurements were performed at the University of Liverpool. Figure 4.13 shows the leakage measured and temperature corrected leakage currents on the R-sensors as a function of the module number. Figure 4.13 also shows the leakage currents which were measured at the University of Liverpool and just before the Glasgow burn-in procedures. The percentage change in the measured and scaled leakage currents due to the difference in the Liverpool and the first burn-in laboratory measurement are shown in figure 4.13. The percentage change in the measurements between the leakage current measurement performed before and after the burn-in procedure are also shown in figure 4.13 for the R-sensor.

The top right hand plot in figure 4.13 shows that there were no high leakage current measured on the R-sensors since all measured currents were less than 16  $\mu\text{A}$ , both in Liverpool and in the burn-in laboratory. The temperatures of the silicon during the Liverpool measurements were approximately constant for all modules at 20 °C, whereas the temperature of the hybrid for the burn-in measurements was highly dependent on the quality of the cooling connection that was made to the module during the mounting procedure. Therefore due to the large variation in the temperature of the burn-in laboratory measurement the centre left plot of figure 4.13 shows changes in the leakage current of up to 450 % between the Liverpool and burn-in measurements. The large variation in the burn-in measurements was corrected for in the temperature scaled percentage change in the leakage current which only showed variations up to 100 %, as shown on the middle right plot of figure 4.13. As expected for this plot the overall spread was around zero, however, since the absolute values of the measured leakage currents were small (less than 16  $\mu\text{A}$  for all sensors but most of the sensors were measured to draw less than 5  $\mu\text{A}$ ) a percentage change of 100 % in the current does not indicate any unexpected behaviour or large degradation in the sensor performance. The percentage change in the leakage current measured before and after the burn-in procedure was within  $\pm 100$  % for all R-sensors and the temperature corrected changes were similar since the measurements performed before and after the burn-in were performed at very similar hybrid temperatures. The bottom right plot of figure 4.13 shows that for the majority of the R-sensors the leakage current increased slightly after all of the burn-in tests.

The analogous plots for the  $\Phi$ -sensors are shown in figure 4.14. The top left plot in figure 4.14 shows some sensors with high leakage current measurements (40 - 100  $\mu\text{A}$ ). As mentioned in section 4.5.1 the leakage current on two high leakage current sensors did not obey the scaling law. The  $\Phi$ -sensor on module 26 is such a sensor and hence the large current shown for module 26 on the scaled plot on the top left plot of figure 4.14 is not meaningful. Modules 35 and 36 also showed high leakage currents. The measured current

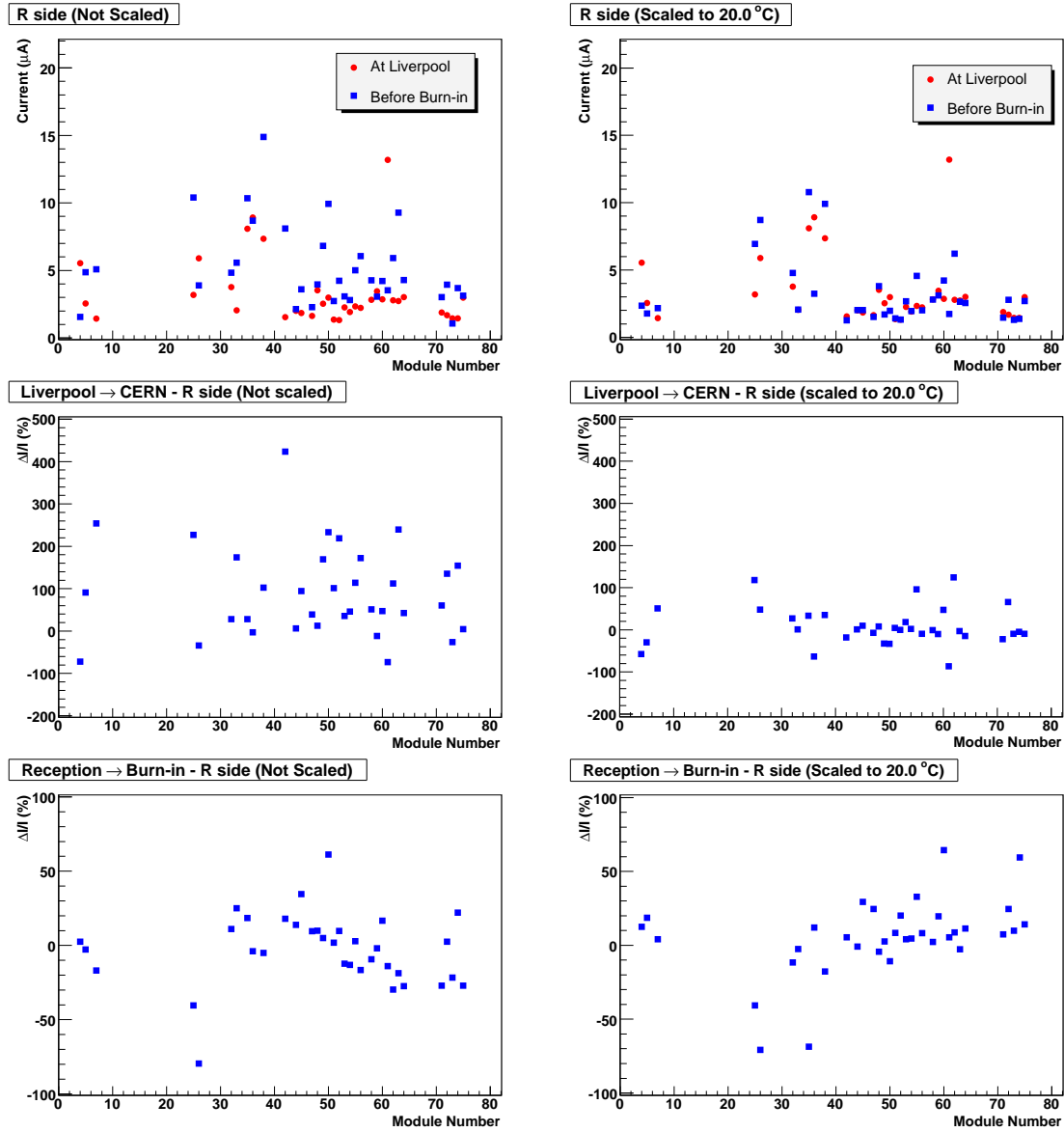


Figure 4.13: The top two plots show the measured (left plot) and temperature scaled (right plot) leakage current as a function of VELO module number for the R-sensors. The leakage current measured in Liverpool are the red circle markers and the leakage current measurements performed in the burn-in laboratory before the burn-in procedure are shown by the blue square markers. The middle two plots show the percentage change in the measured (left plot) and temperature scaled (right plot) leakage current between the measurements made in University of Liverpool and before the burn-in procedure. The bottom two plots show the percentage change in the measured (left plot) and temperature scaled (right plot) leakage current between the measurements made before and after the burn-in procedures. The plots of the leakage currents were scaled to 20.0 °C.

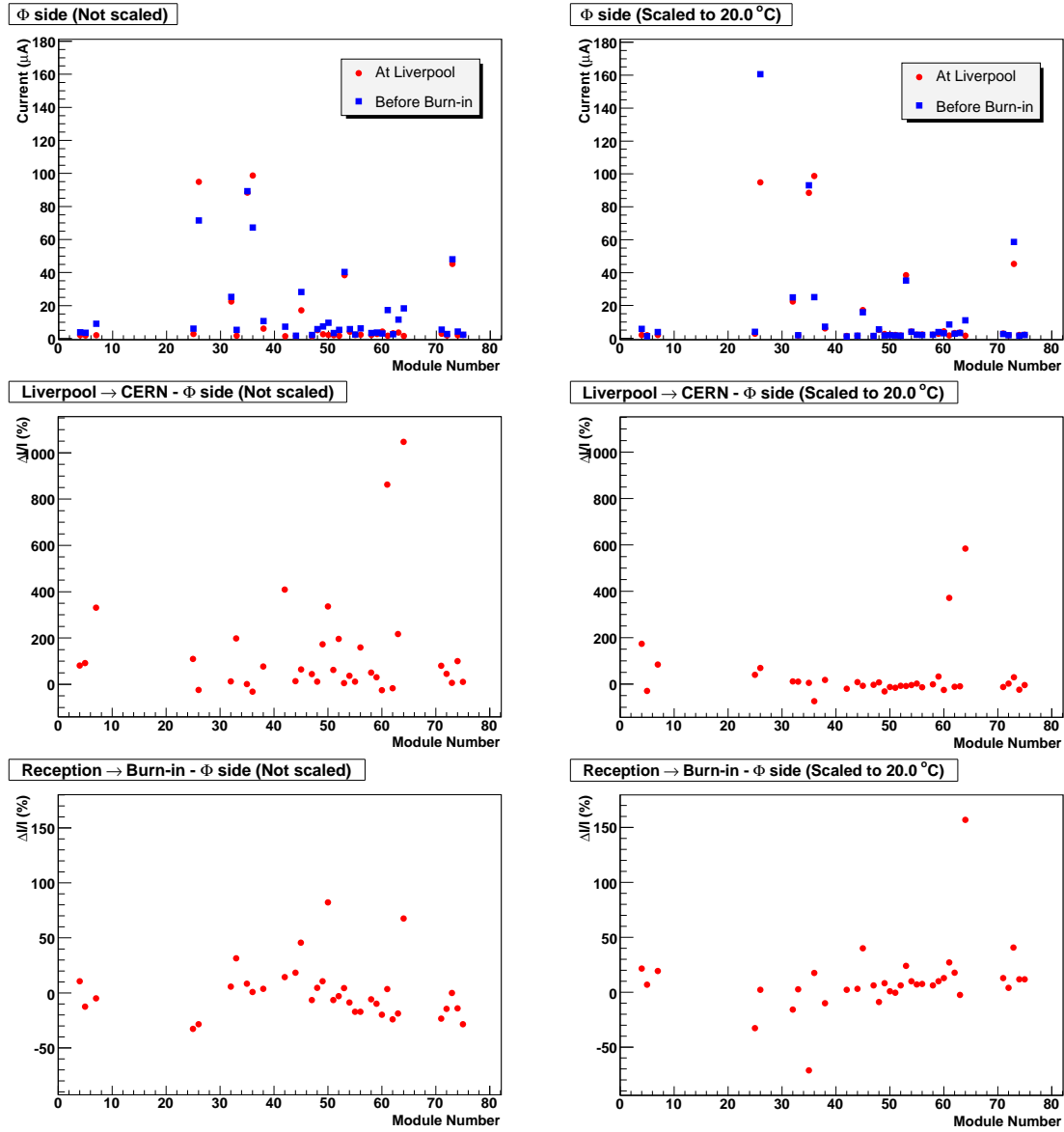


Figure 4.14: The top two plots show the measured (left plot) and temperature scaled (right plot) leakage current as a function of VELO module number for the  $\Phi$ -sensors. The leakage current measured in Liverpool are the red circle markers and the leakage current measurements performed in the burn-in laboratory before the burn-in procedure are shown by the blue square markers. The middle two plots show the percentage change in the measured (left plot) and temperature scaled (right plot) leakage current between the measurements made in University of Liverpool and before the burn-in procedure. The bottom two plots show the percentage change in the measured (left plot) and temperature scaled (right plot) leakage current between the measurements made before and after the burn-in procedures. The plots of the leakage currents were scaled to 20.0 °C.

for module 35 at Liverpool and before the burn-in were quite similar, hence the middle right plot of figure 4.14 shows a small percentage change in the leakage current. Module 36 was one of the very few cases where the measured current before the burn-in procedure was lower than the current which was measured at University of Liverpool. The two plots on the bottom row of figure 4.14 shows that the leakage current of modules 35 and 36 decreased between the measurements made before and after the burn-in procedures, which was in contrast to the slight increase in the leakage current that was measured for most of the  $\Phi$ -sensors during the burn-in procedures.

Modules 61 and 64 showed a significant increase in leakage current between the measurement made at University of Liverpool and the first burn-in measurement, see the middle left plot in figure 4.14, but the absolute values for the sensor currents were lower than  $20\text{ }\mu\text{A}$ . The  $\Phi$ -sensor of module 64 showed an increase of 1000 % in the measured leakage currents in Liverpool and the burn-in laboratory and an increase of 600 % in the temperature scaled leakage current. Due to these large degradations in leakage current, module 64 was withheld from the normal assembly and re-tested. The leakage current was measured after the burn-in procedure at 10 different hybrid temperatures over the range of  $7 - 32\text{ }^{\circ}\text{C}$ , while the Beetle chips were not operated, see the left plot on figure 4.10. The module was then temperature cycled 3 times between  $+30\text{ }^{\circ}\text{C}$  and  $-37\text{ }^{\circ}\text{C}$  and then the leakage current was remeasured at three different hybrid temperatures with the Beetle chips turned off. The module was then thermally cycled a third time for two cycles between  $+30\text{ }^{\circ}\text{C}$  and  $-37\text{ }^{\circ}\text{C}$  and then the leakage current was remeasured at four different hybrid temperatures with the Beetle chips turned off. The leakage currents which were measured after each thermal cycle are shown in figure 4.15.

Figure 4.15 shows that the  $\Phi$ -sensor of module 64 showed no further degradation in the leakage current with subsequent thermal cycles. For safety the module was kept as a spare module and not used as a production module.

The  $\Phi$ -sensor of module 75 showed a 50 % increase in the temperature scaled leakage current, as shown on the bottom right plot of figure 4.14. Figure 4.16 shows the current measured on the  $\Phi$ -sensor of module 75 for three different temperatures. It did not scale as expected using equation 4.1. The leakage current was measured to be constant over an  $8\text{ }^{\circ}\text{C}$  temperature range(see figure 4.16). Therefore the scaled graphs could not be considered as a correct representation of the leakage current for this sensor. This module was mounted in the final VELO detector, as very few spare sensors were available.

In summary, the leakage current of all of the R and  $\Phi$ -sensors were investigated at University of Liverpool and before and after the Glasgow burn-in procedure. The R-sensors behaved well and most of the sensors had a leakage current less than  $16\text{ }\mu\text{A}$ . Maximum changes of around 50 % due to any two consecutive measurements were observed for R-sensors. The  $\Phi$ -sensors contained a few high leakage current sensors. The  $\Phi$ -sensor of module 26 and module 75 were found not to scale according to the expected temperature dependence. Only

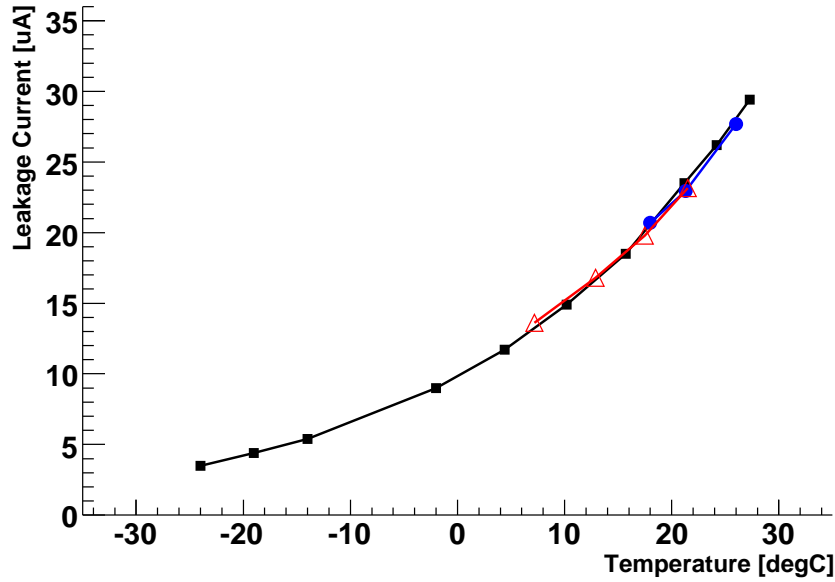


Figure 4.15: The temperature dependence of the leakage current measured at 250 V bias of module 64 is shown for  $\Phi$ -sensor leakage current. The leakage current measured after the standard burn-in thermal cycle (4 cycles) are shown with the black solid square markers. The leakage current measured after a second thermal cycle (3 cycles) are shown in the blue solid circles. The leakage current measured after a third thermal cycle (2 cycles) is shown in the red empty triangles.

a few  $\Phi$ -sensors showed significant degradation in the leakage currents during burn-in but after further tests on these sensors, only module 64 was not used for production and was held as a spare.

## 4.6 Metrology

As discussed in section 4.5, a few modules showed a higher than normal leakage current on the  $\Phi$ -side. In some cases the modules showed a high leakage current before the burn-in procedures began but in some cases the current increased during the electrical and thermal tests. A correlation study with the Liverpool metrology measurements was performed to test if the increase in the leakage current was related to any mechanical stress in the sensors during module assembly.

Four different sets of variables were investigated. The first set was a collection of measurements made of the sensors with respect to the baseline or Liverpool metrology reference frame. Table 4.1 shows all the variables that were used and their respective definitions according to the Liverpool database.

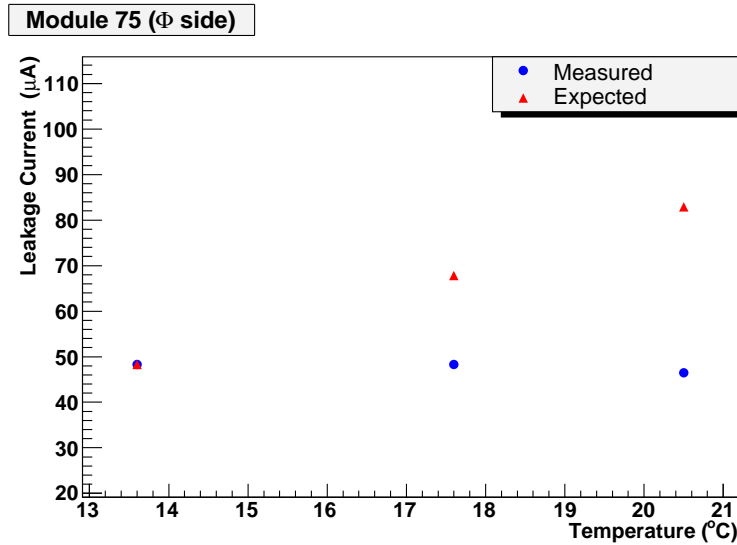


Figure 4.16: The measured (blue circle markers) and temperature scaled (red triangle markers) leakage current measured on  $\Phi$ -sensor of module 75 for 3 different temperatures.

Table 4.1: Module metrology parameters

| Parameter | Definition   |
|-----------|--|
| Twist     | Rotation on x axis (mrad)                                      |
| Tilt      | Rotation on y axis (mrad)                                      |
| Z maximum | Maximum z on top of the module (mm)                            |
| Z minimum | Minimum z on top of the module (mm)                            |
| Tilt 1    | Top module displacement wrt baseline at initial Metrology (mm) |
| Tilt 2    | after cabling (mm)   |
| Tilt 3    | after tests without cabling (mm)                               |

Figures 4.17 and 4.18 show the distribution of the metrology parameters as a function of the leakage current and the percentage change in the temperature normalised leakage current. Both figures show the temperature normalised current versus the metrology variables in the left column. The right column shows the change in the percentage of the leakage current due to the thermal and electrical tests as function of the metrology parameters. The red circles were the modules which presented either high leakage current levels or large increases during the burn-in procedures. No correlation was identified with any of the module parameters

The second set of metrology variables that were investigated were the contour shape measurements of the sensors. Table 4.2 lists all the parameters from the contour and surface measurements that were used.

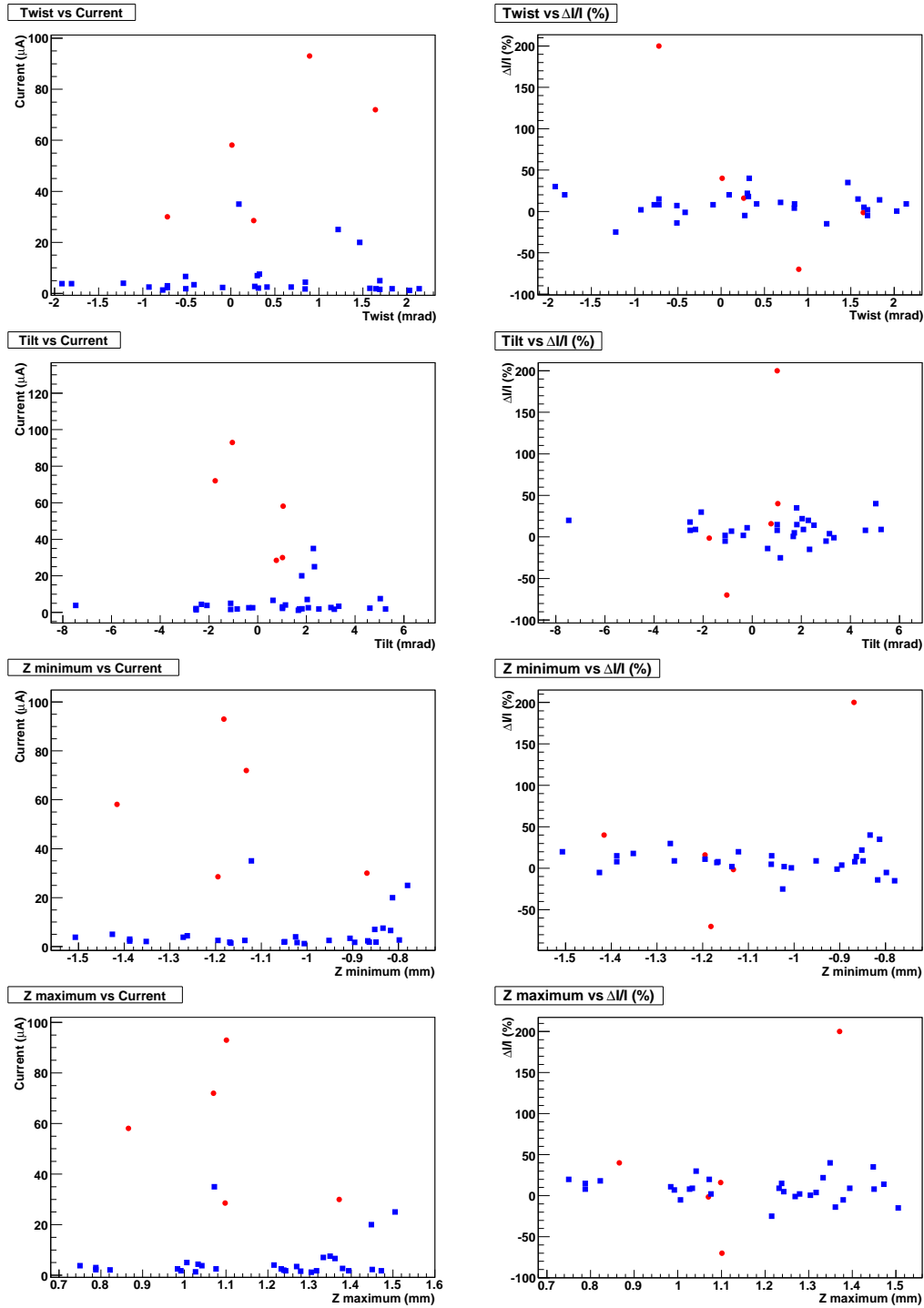


Figure 4.17: The left column shows the leakage current versus the various metrology parameters. The right column shows the percentage change in the leakage current due to the burn-in procedure as a function of the metrology parameters. The red circles are the modules which had either a high leakage current or a large increase in current during the burn-in procedures. No correlation was found between the higher leakage current sensors and the module metrology parameters.



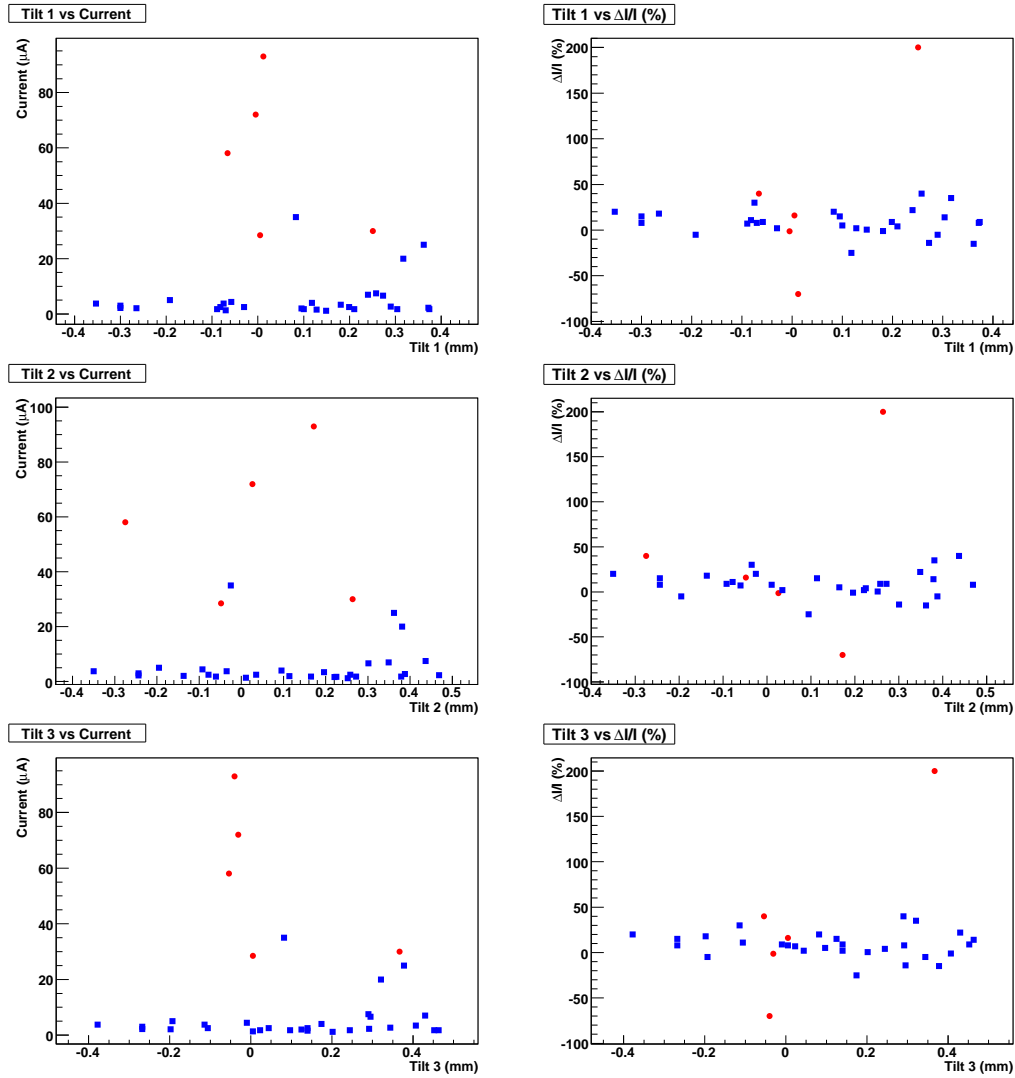


Figure 4.18: The left column shows the leakage current versus the various metrology parameters. The right column shows the percentage change in the leakage current due to the burn-in procedure as a function of the metrology parameters. The red circles are the modules which have either a high leakage current or a large increase in current during the burn-in procedures. No correlation was found between the higher leakage current sensors and the module metrology parameters.

Table 4.2: Sensor metrology parameters

| Parameter   | Definition                                      |
|-------------|---|
| Rotation    | Sensor rotation wrt frame (mrad)                |
| X shift     | Sensor X shift wrt frame (mm)                   |
| Y shift     | Sensor Y shift wrt frame (mm)                   |
| Total shift | Sensor total shift wrt frame (mm)               |
| Sagitta     | Maximum surface dist<br>to reference plane (mm) |

During the Liverpool metrology there were two different fits that were performed to evaluate the contour of the sensors. In the first fit the measurements were performed with respect to the fiducial on the silicon and in the second fit the metrology measurements were compared to a reference frame which sits on the centre position of the sensor. A total of 20 positions were measured on the  $\Phi$ -sensors and were compared to an ideal module. The statistical results on the residuals for each position were also analysed. Figure 4.19 shows the plots of the parameters from the sensor shape fit and figure 4.20 shows some of the plots obtained from four example positions on the sensor. All 20 positions on each  $\Phi$ -sensor were measured and 160 similar plots to the ones shown in figure 4.20 were created in order to uncover any possible correlations. No conclusive information was extracted; in the worst case the high leakage current modules had one of these statistical quantities values located just on the edge of the distribution and not considerably displaced with respect to the other points.

The third set of metrology variables that were investigated were the curvatures of the sensors. The sensor curvature was evaluated by comparing the fit of the sensor surface to a reference plane. The sagitta extracted was used in the correlation studies. Again, there was no explicit dependency between the higher current sensors and their sagitta values, as can be seen in figure 4.21.

A fourth set of variables that was investigated were the positions of the silicon on the wafers during manufacturing. Two different mask sets were produced, one for  $\Phi$ -sensors the other for R-sensors. The  $\Phi$ -sensor mask sets allowed for the fabrication of 3 sensors per wafer (labelled  $A, B, C$ ). The R-sensor mask set had only 2 sensors per wafer (labelled  $D, E$ ). Figure 4.22 shows the wafer masks of the VELO sensors. Figure 4.23 clearly shows that all the modules with higher current levels (red circular markers) were in wafer position  $A$ , with the sole exception of module 64 which was in position  $B$  on the same wafer. Sensors from  $B$  and  $C$  positions on the  $\Phi$ -wafer faced each other, almost making a circle. This was the same layout for the R-sensors where the  $D$  and  $E$  positions were facing each other, almost completing a circle. Position  $A$  on the  $\Phi$ -sensor was placed vertically beside positions  $B$

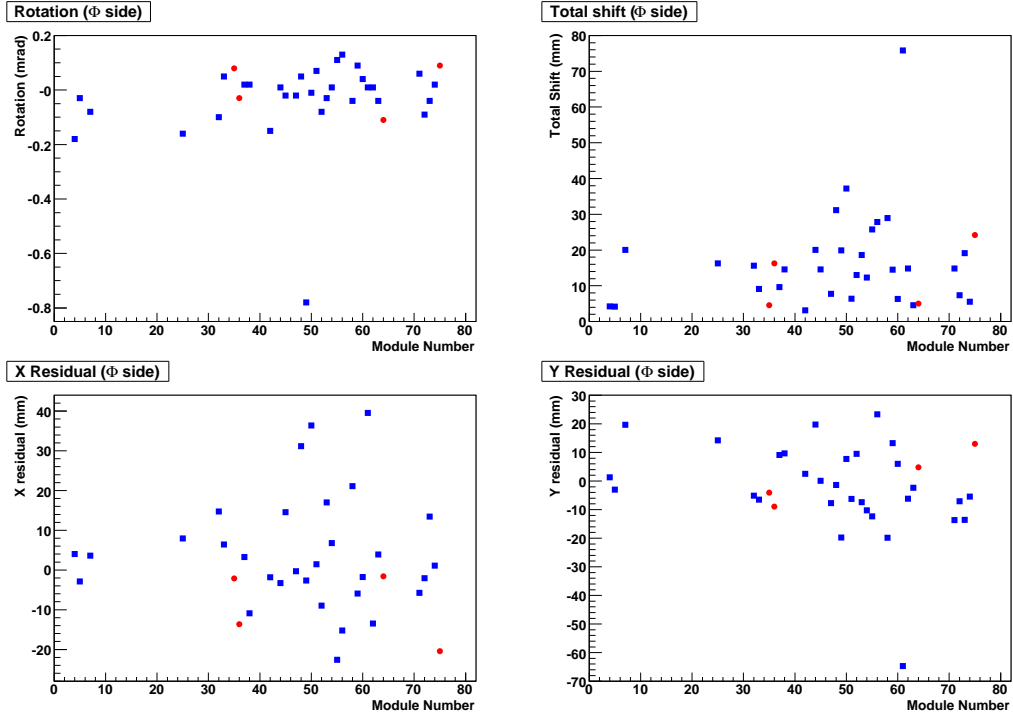


Figure 4.19: Each plot shows one of the first four sensor metrology variables listed in table 4.2 as a function of the module number. The red circles are the modules which have either a high leakage current or a large increase in current during the burn-in procedures. No correlation with the shape fit parameters has been observed.

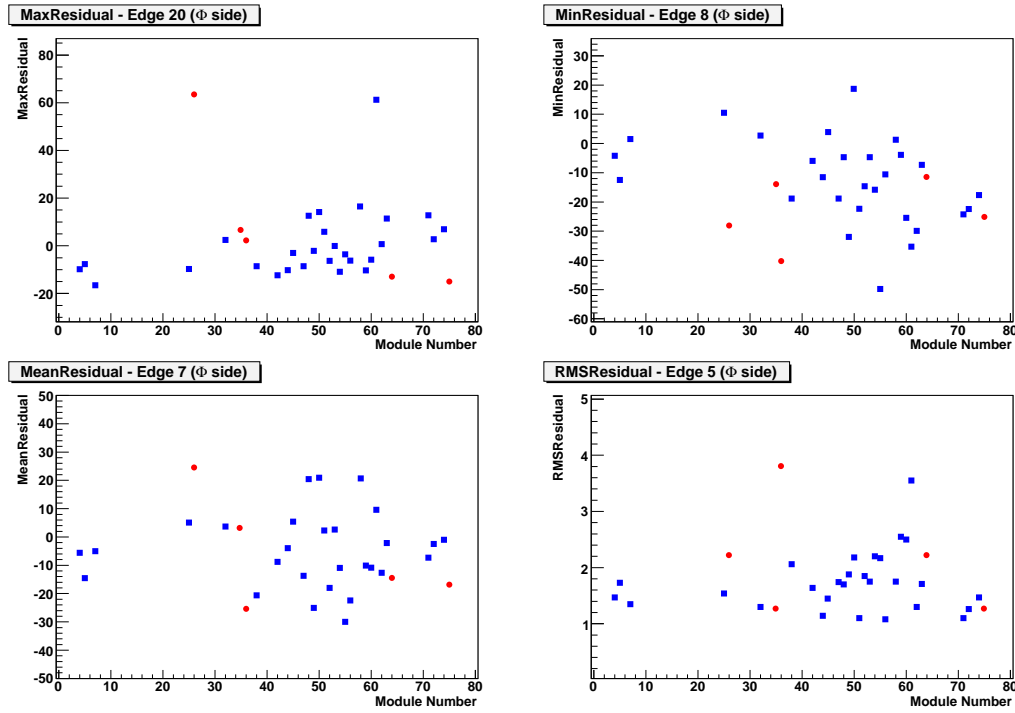


Figure 4.20: The maximum residual (top left), the mean residual (bottom left), the minimum residual (top right) and the RMS of the residual (bottom right) as a function of the module number for four different positions measured on the sensors. The red circle markers are the modules which have either a high leakage current or a large increase in current during the burn-in procedures and the blue square markers were measured to have a normal leakage current behaviour. For further details see text.

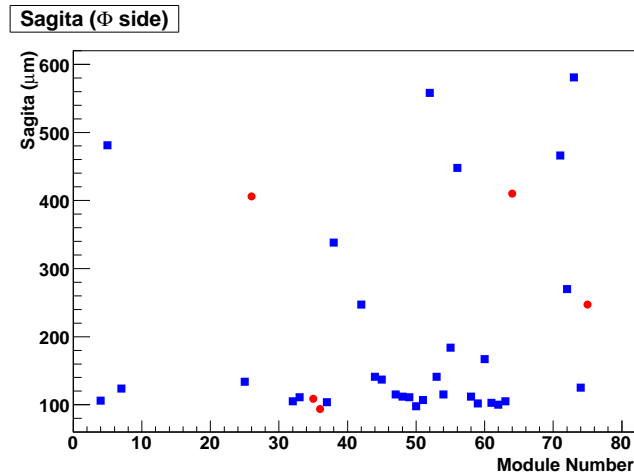


Figure 4.21: The sagitta of the sensor as function of the module number. The red circles are the modules which have either a high leakage current or a large increase in current during the burn-in procedures.

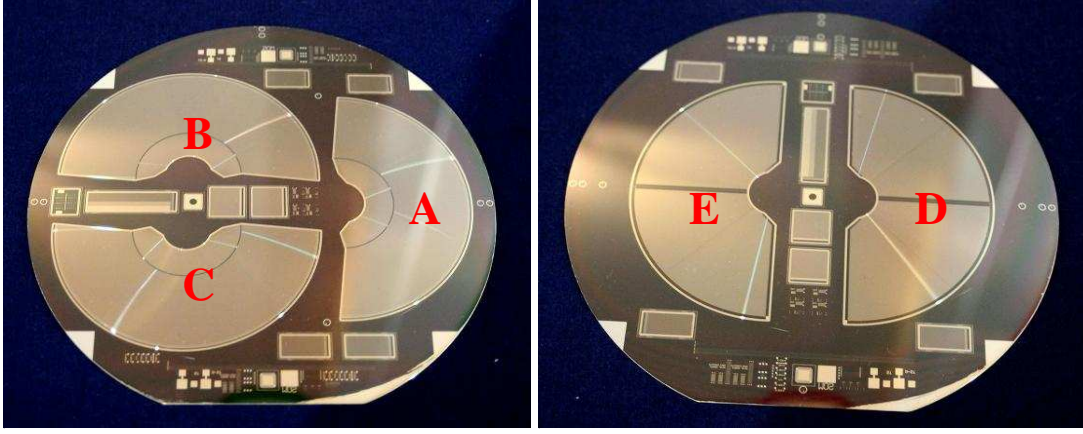


Figure 4.22: Wafer masks of the silicon sensors. The mask of the  $\Phi$ -sensors is shown on the left-hand side. The A position on the mask is indicated. The mask of the R-sensors is shown in the right-hand side.

and *C*. Figure 4.23 shows that all high leakage current sensors except one were from wafer position *A*.

Figure 4.24 shows the measured leakage current as a function of the date of the first leakage current test in Liverpool. It shows that the high leakage current sensors were not tested during the same period. Therefore the high current could not be associated to a particular fault that may have occurred during a specific short period of time (biasing method of the silicon sensors).

So in conclusion, there were no correlations found between the modules with a high leakage current and any of the 4 sets of metrology variables that were studied. The only correlation that was found was that the majority of the high leakage current sensors were found to come from the wafer position *A* during manufacturing. Since most sensors from the *A* position were good and just few sensors with high leakage current were found, it was not worth rejecting all sensors from that particular position.

## 4.7 Pulse Shape Studies

As discussed in section 2.2.1.4, the Beetle chip integrates low-noise charge-sensitive pre-amplifiers and shapers. The chip also implements a charge injector to test the chip and for calibration purposes. Figure 4.25 shows the typical test pulse shape obtained with the VELO modules. Peak amplitude, rise time and spillover are indicated. These quantities were estimated and are presented in this section. Another quantity studied was the undershoot which corresponds to the part of the pulse amplitude below the baseline (negative).

Data was taken using test pulses with VELO modules in order to evaluate the characteristics of the Beetle chip parameters and to compare the response of n-on-n and n-on-p VELO

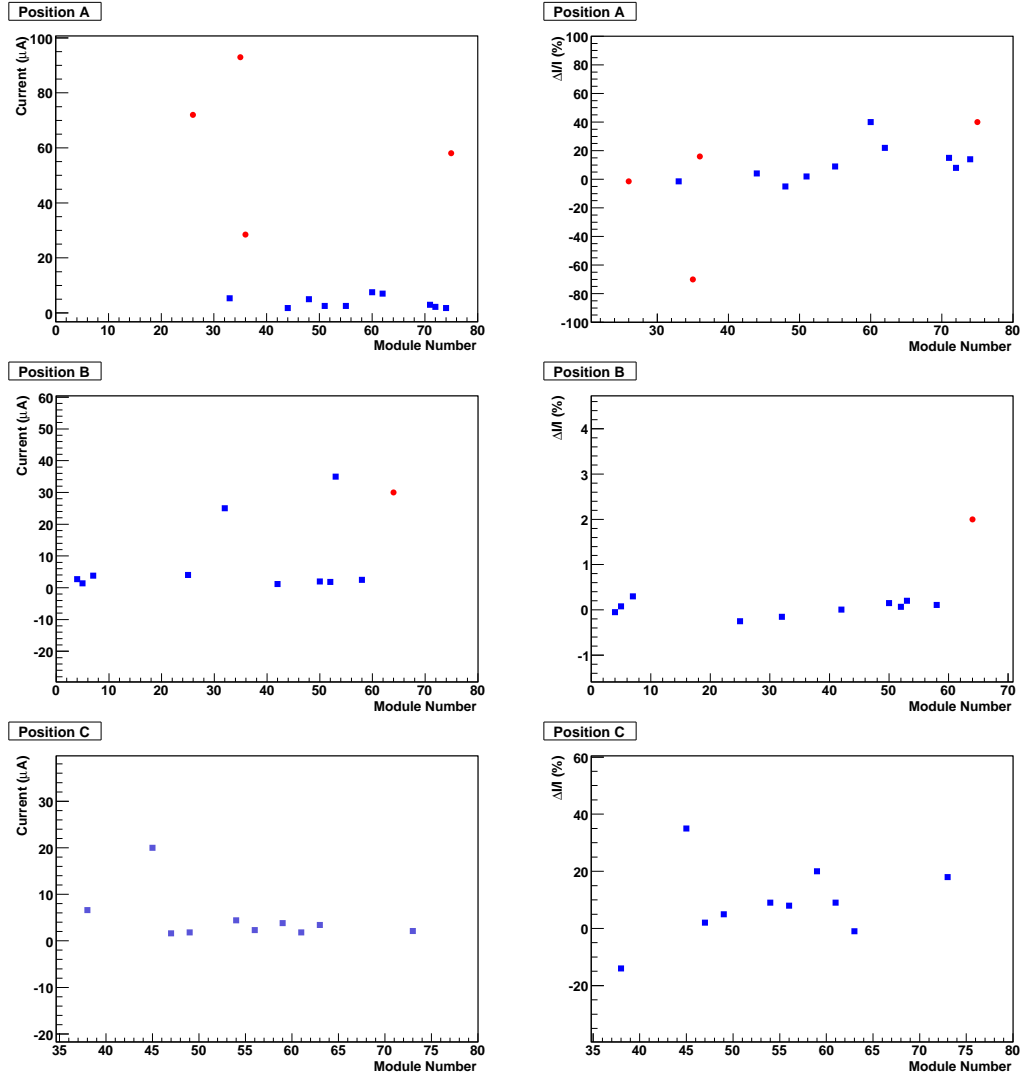


Figure 4.23: Each plot on the left hand column shows the temperature normalised leakage current as a function of the module number for each of the 3  $\Phi$ -wafer positions. The right hand column shows the same plot with the vertical axis showing the percentage change in the leakage current due to the thermal and electrical tests. The red circles are the modules which have presented either a high leakage current or a large increase in current during the burn-in procedures. Most modules with higher currents were in position *A* with just one module in wafer position *B*.

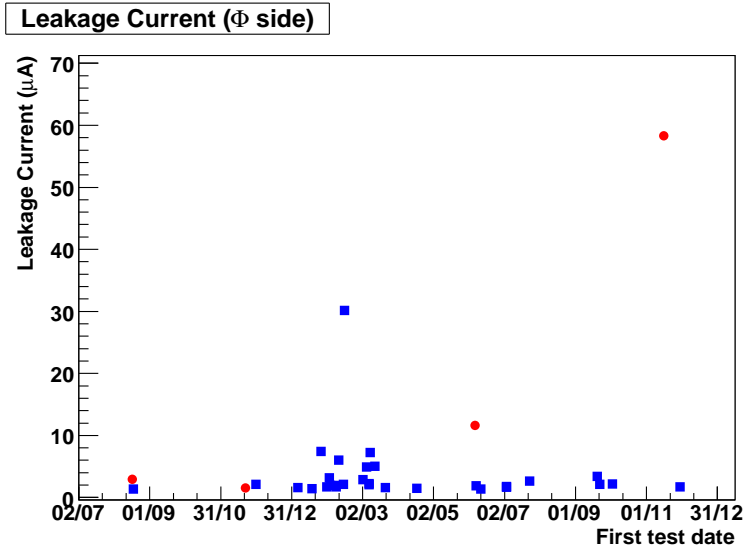


Figure 4.24: Leakage current of the  $\Phi$ -sensors as a function of the date of the first leakage current measurement at University of Liverpool. The red circles were the modules which presented either high leakage current levels or large increases during the burn-in procedures and all other modules are shown with blue square markers.

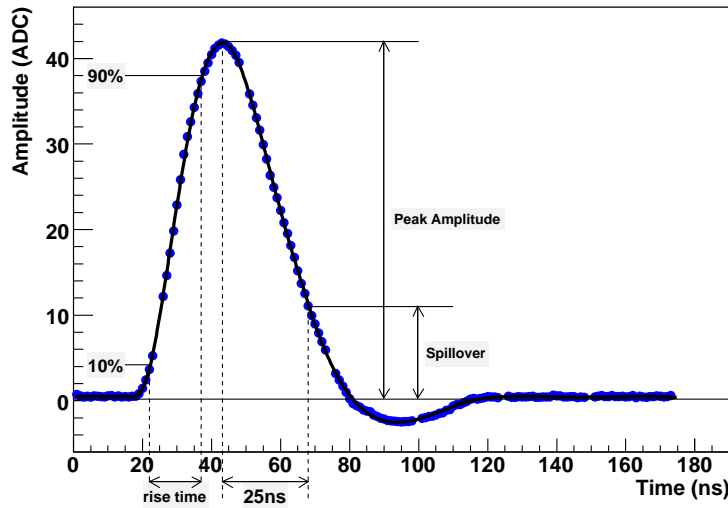


Figure 4.25: Test pulse shape of a Beetle chip installed in a VELO module. The peak amplitude, spillover and rise time are indicated. The rise time is the time it takes the pulse to rise from 10% to 90% of the peak amplitude. The spillover is the pulse amplitude 25 ns after the peak of the pulse.

modules. The test pulse signal height and the *spillover* were extracted from the sets of data taken with different values for various Beetle chip parameters. The *spillover* was defined as

the pulse amplitude at 25 ns after the pulse peak.

A detailed description of the Beetle chip and its relevant parameters can be obtained from [78] and a further explanation of the Beetle parameters can also be found in [114]. The following Beetle parameters were analysed:

- Pre-amplifier feedback voltage ( $V_{fp}$ ): The effect of  $V_{fp}$  is seen on the undershoot region of the pulse shape. The maximum undershoot reduces and the return to the baseline is faster as  $V_{fp}$  increases.
- Shaper amplifier feedback voltage ( $V_{fs}$ ): An increase in  $V_{fs}$  results in longer rise-times, higher peak signals and increased spillover.
- Pre-amplifier bias current ( $I_{pre}$ ): The rise time and fall time of the signal reduces when  $I_{pre}$  is increased. Hence it reduces the spillover and increases the undershoot.
- Shaper amplifier bias current ( $I_{sha}$ ): An increase in  $I_{sha}$  reduces the rise-time and undershoot.

The Beetle chip characteristics described were verified by changing the values of the chip parameters. The default values for the Beetle parameters that were used in the standard burn-in laboratory measurements, as well as the additional values used in the tests are listed in table 4.3. The default parameters that are used for the Beetle chip in the LHCb experiment are 200 mV and 550 mV for the  $V_{fp}$  and  $V_{fs}$  parameters respectively, which unfortunately were outside the range of parameters tested in this analysis.

Table 4.3: The standard values and the tested set of Beetle chip parameters.

| Parameter            | Definition                     | Default | Other tested values |
|----------------------|--------------------------------|---------|---------------------|
| $V_{fp}$ (mV)        | Pre-amplifier feedback voltage | 0       | 20, 40              |
| $V_{fs}$ (mV)        | Shaper feedback voltage        | 700     | 600, 650, 750, 800  |
| $I_{pre}$ ( $\mu$ A) | Pre-amplifier bias current     | 600     | 400, 800            |
| $I_{sha}$ ( $\mu$ A) | Shaper bias current            | 80      | 120, 150            |

Figure 4.26 shows the test pulse shape on the electronic channel 23 of the first link of the first Beetle chip (chip 0). The signal is given in ADC units. The test pulse for the n-on-p and n-on-n modules on both the R and  $\Phi$ -sides of each of the two VELO modules is shown. These plots were obtained by performing a Gaussian fit to the data in each time slice and extracting the mean of the fit. The errors on the mean were of the order of 0.1 ADC counts. The uncertainties shown in the plots were the sigmas obtained from the fit. The default Beetle chip parameters were used to make this comparison. Apart from the signal height, no considerable differences on the characteristics of the pulse shapes were observed.



The difference in the test pulse peak signal between n-on-n and n-on-p technologies was measured to be  $6.7 \pm 0.5$  % with a sigma of  $3.2 \pm 0.5$  on the R-side and  $6.9 \pm 0.4$  % with a sigma of  $3.1 \pm 0.3$  on the  $\Phi$ -side using the default Beetle chip configuration. These numbers were obtained by averaging over a total of 64 channels per sensor. Four channels were pulsed on each Beetle chip. Module 24 had n-on-p sensors and module 64 had n-on-n sensors. Each chip had 4 links and one single channel was pulsed per link (see section 2.2.1.4).

Figures 4.27, 4.28, 4.29 and 4.30 show the test pulse shapes for the studied configurations of chip parameters. In each of these figures, only one of the chip parameters was changed while the others were set to the default values.

A 6<sup>th</sup> order polynomial was fitted to the test pulse shape in a time range of 80 ns to obtain the signal peak and estimate the spillover. The range was set so that the lower limit was approximately 15 ns before the peak. In order to get the peak of the signal and estimate its uncertainty the fit parameters from the polynomial were smeared according to their uncertainties. The function which was fitted to the test pulse shapes was

$$f(t) = A_0 + A_1t + A_2t^2 + A_3t^3 + A_4t^4 + A_5t^5 + A_6t^6, \quad (4.2)$$

where  $f$  was the pulse amplitude and  $t$  was the time in nanoseconds. Table 4.4 shows the values of the polynomial parameters and their fractional uncertainties.

The spillover fraction was estimated using the fitted 6<sup>th</sup> order polynomial given in Equation 4.2. This spillover was calculated using

$$Spillover = \frac{f(t_{spillover})}{f(t_{peak})}, \quad (4.3)$$

where  $f(t_{peak})$  was the peak amplitude and  $f(t_{spillover})$  was the spillover amplitude with  $t_{spillover} = t_{peak} + 25$  ns. The spillover uncertainty was also obtained by smearing the polynomial fit parameters.

The undershoot was calculated using a similar approach as for the spillover calculation. The only difference was that the pulse amplitude on the undershoot region was parametrised as a 6<sup>th</sup> polynomial fitted on the time range between 80 and 140 ns. The minimum value of this fitted polynomial gave the undershoot amplitude. On both the  $R$  and the  $\Phi$ -sensors it was estimated to be of the order of 17% with respect to the signal peak. This number was calculated for all configurations of the Beetle parameters tested.

The signal peak and the spillover were calculated using the tested n-on-n module and n-on-p module using the range of Beetle parameters settings and on both  $R$  and  $\Phi$ -sensors. Figures 4.31, 4.32, 4.33 and 4.34 show the signal and spillover as a function of the Beetle parameters for both types of VELO modules and for both sides of the hybrid.

The signal peak was measured to be higher for most of the Beetle parameters that were tested on the n-on-p module compared to the n-on-n module. The estimated spillover for both technologies were quite similar - only a few percent higher with the n-on-p technology

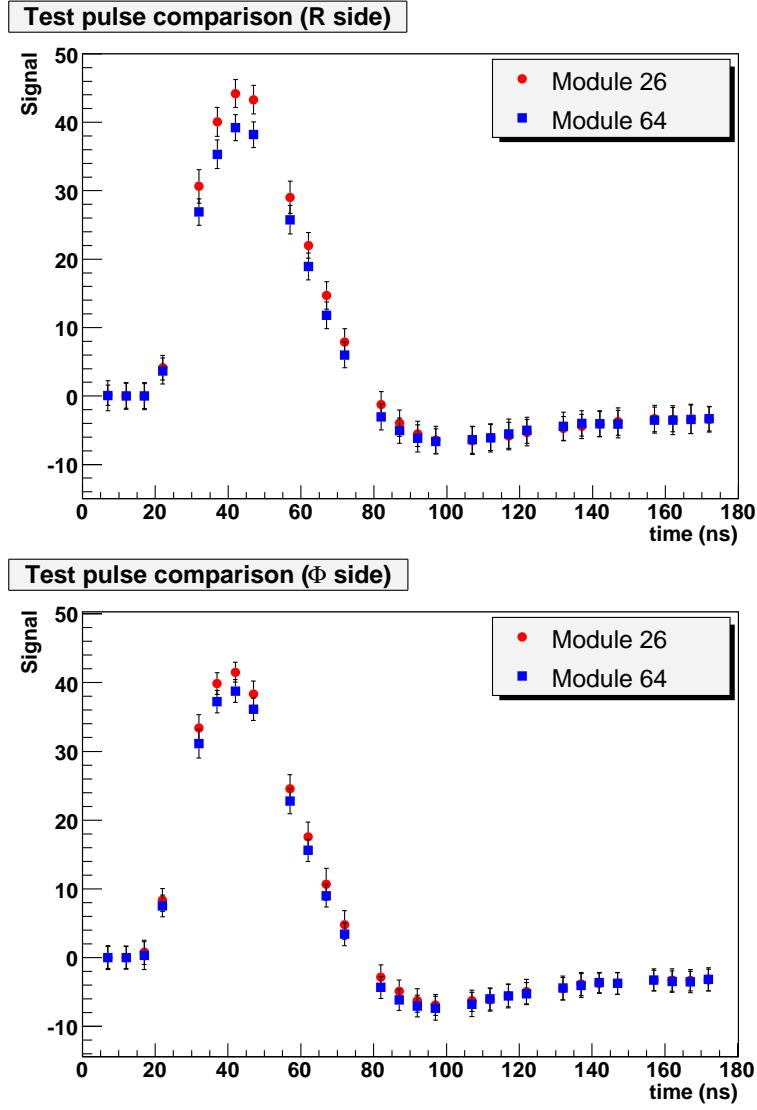


Figure 4.26: The signal measured in response to test pulses in the Beetle chips using the default Beetle parameters. The red circular markers correspond to the n-on-p module and the blue square markers correspond to the n-on-n module. The top plot compares the R-sides from the two tested modules and the bottom plot compares the  $\Phi$ -sides from the two tested modules.

in most of the values set for the chip parameters.

The observed increase of the signal peak was about 3 ADC units with the increase in  $V_{fs}$  from 0 to 40 mV. This was observed for both n-on-n and n-on-p modules and on both sides (R and  $\Phi$ -hybrids). On the R-side the spillover increased by about 9 % on the n-on-n module and by about 13 % on the n-on-p module. On the  $\Phi$ -side the spillover change was 11 % and 10 % respectively. The uncertainty on these variations was estimated to be  $\pm 4$  %. No significant change in the signal and spillover was observed for the different tested values

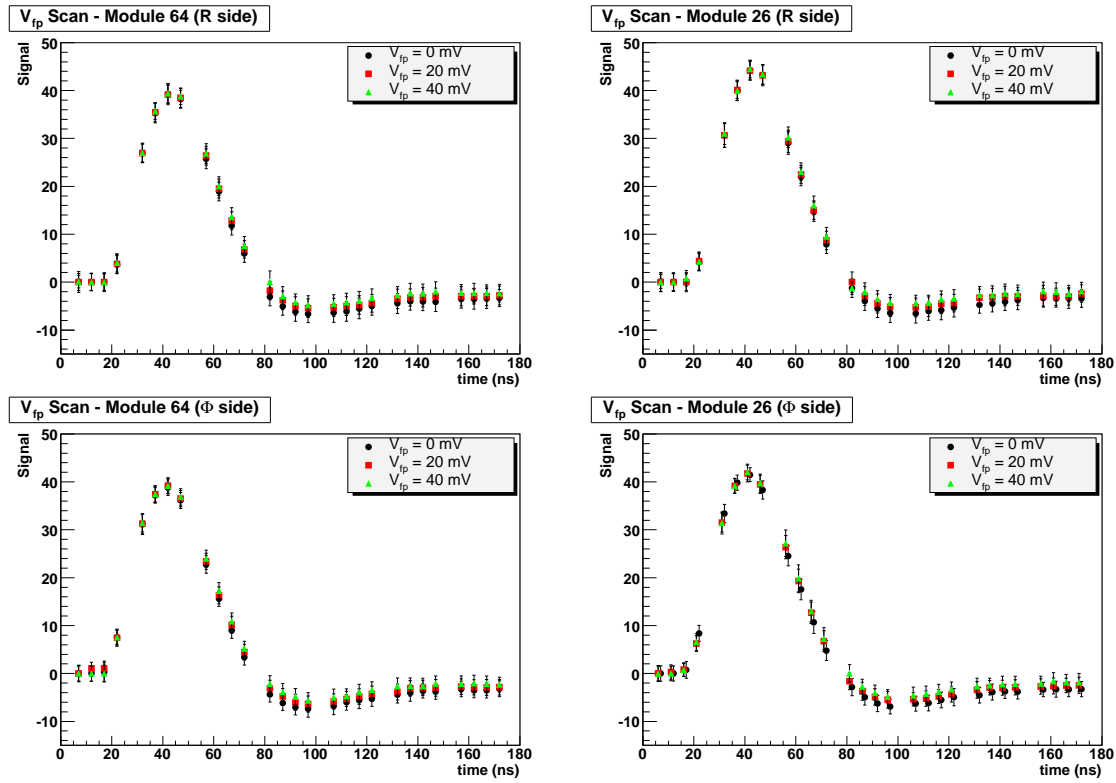


Figure 4.27: Pulse shapes for different values of  $V_{fp}$ . The top two plots show the measured signal for the R side and the bottom two plots show the measured signal for the  $\Phi$  side. The plots in the left column show the measured signal for the n-on-n module (module 64) and the measured signal for the n-on-p module (module 26) are shown in the plots on the right column.

of  $V_{fp}$ ,  $I_{pre}$  and  $I_{sha}$ . The variations obtained agree with those in [114] which studied Beetle parameter settings on a 300  $\mu\text{m}$  R-measuring VELO prototype module.

The peak of the pulse and the spillover were also calculated as a function of the strip length of the R-sensors using the default Beetle parameter settings. Figure 4.35 shows the test pulse peak and spillover calculated as a function of strip length for both the n-on-n and n-on-p modules. It was not possible to evaluate the dependence of the pulse amplitude and spillover with strip length as the routing lines contribution should also be taken into account. The length of the strips were calculated using the VELO Detector Element package which provided a geometric description of the active area of the sensors [115]. The radius and  $\Phi$ -angle of the strips was obtained via the DeVeloRType class as a function of the strip number. Hence the length of the strips was obtained as the product of the radius and the  $\Phi$ -angle of the strip. The association between the chip channels and the strips number was also available via a method within this class.

The peak amplitude was approximately constant across the range of strip lengths (4 mm - 34 mm) for both the n-on-n and n-on-p modules. As already discussed, the n-on-p module

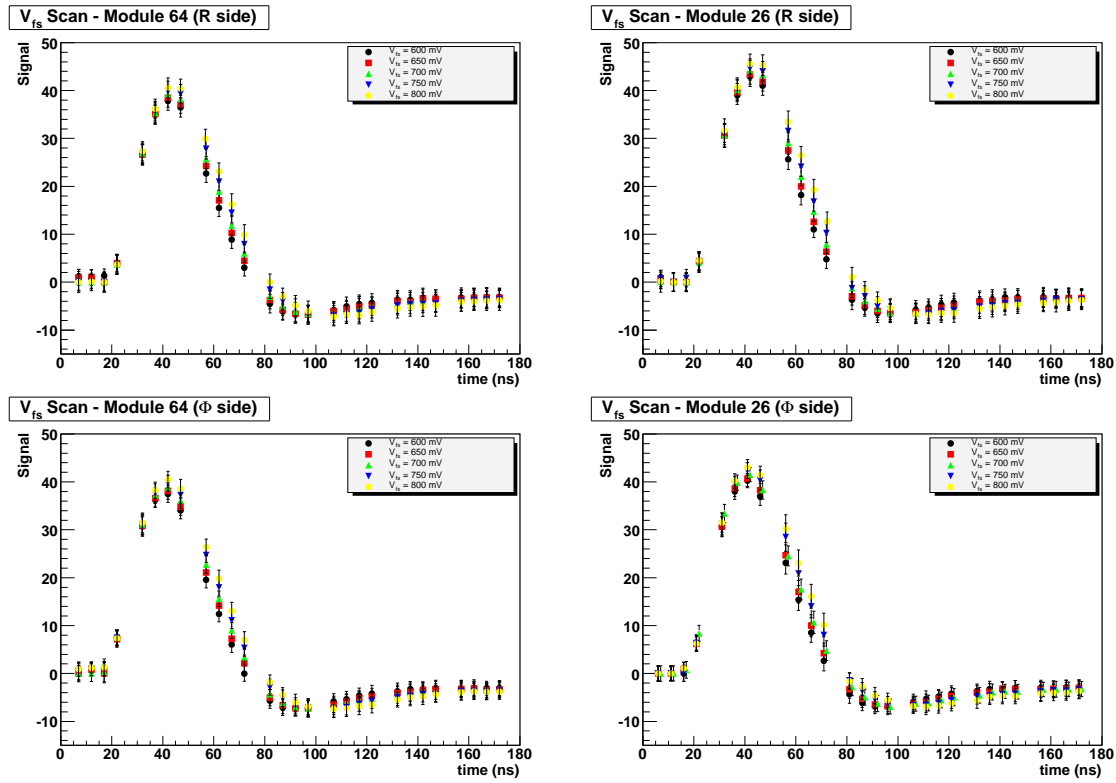


Figure 4.28: Pulse shapes for different values of  $V_{fs}$ . The top two plots show the measured signal for the R side and the bottom two plots show the measured signal for the  $\Phi$  side. The plots in the left column show the measured signal for the n-on-n module (module 64) and the measured signal for the n-on-p module (module 26) are shown in the plots on the right column.

had slightly higher ADC values compared to the n-on-n module for almost all strip lengths. The spillover was approximately 30% for both the n-on-n and n-on-p modules for all measured strip lengths, with the default parameters.

Figure 4.36 shows the ratio of the pulse amplitude as a function of time and the pulse peak for the n-on-n module given as a percentage. This ratio was calculated in steps of 25 ns after the pulse peak and for all Beetle chip parameters tested.

Full return to the baseline of the signal was still not achieved after 180 ns, for all of the parameters which were tested.  $V_{fp}$  was seen to have an effect on the spillover and undershoot regions, where the maximum undershoot was reduced as  $V_{fp}$  was increased.  $V_{fs}$  was also seen to reduce the maximum undershoot as  $V_{fs}$  was reduced, although no effect on the rise time and peak signal was measured. The rise time and fall time of the signal was seen to reduce and the maximum undershoot was increased as  $I_{pre}$  was increased. Finally, the shaper amplifier bias current,  $I_{sha}$ , reduced the rise time and reduced the maximum undershoot as the settings were increased from 80 to 150  $\mu$ A.

To operate the LHCb experiment at a 25 ns bunch crossing rate, the Beetle chips param-

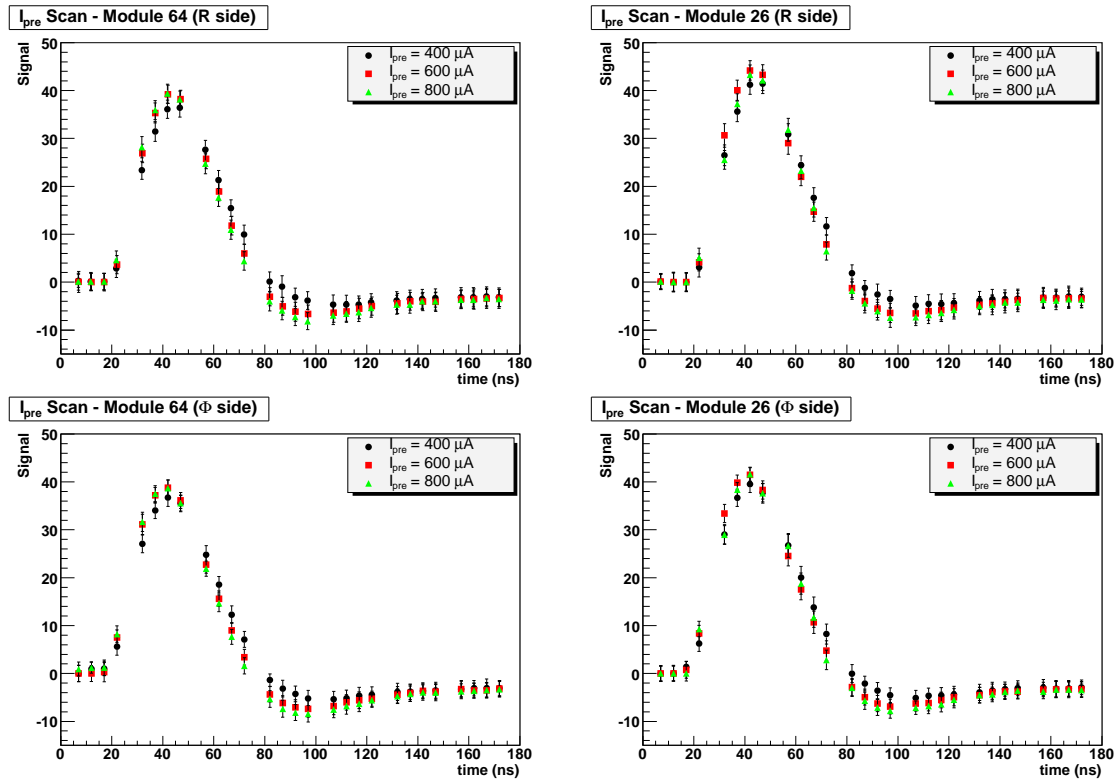


Figure 4.29: Pulse shapes for different values of  $I_{pre}$ . The top two plots show the measured signal for the R side and the bottom two plots show the measured signal for the  $\Phi$  side. The plots in the left column show the measured signal for the n-on-n module (module 64) and the measured signal for the n-on-p module (module 26) are shown in the plots on the right column.

eters have to be tuned to minimise spillover. The values used for the chip parameters depend on the silicon sensors characteristics, which might change as the detectors will be irradiated during the detector operation.

## 4.8 Bad Channels Analysis

The aim of analysing the electronic data from before and after the burn-in procedure for each channel on the sensors was to identify any new problematic channels and to determine if any extra problem had occurred during burn-in. The bad channel list was also cross-checked against the Liverpool test list produced during the modules production to see if any new problems had occurred. The list of bad channels combined observations from bond inspections made during the visual inspection of the modules and the noise measurements made during the electronic data taking. As mentioned previously in section 4.2, the visual inspection identified non-bonded or shorted channels. During the electrical measurements noisy

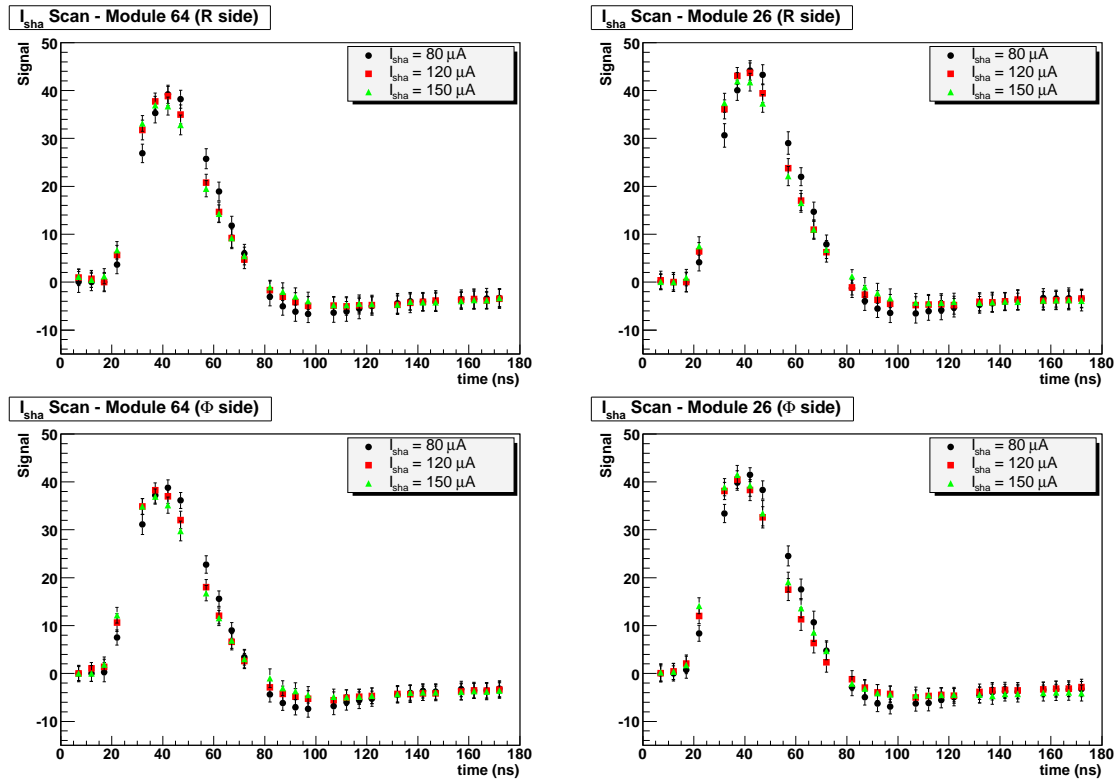


Figure 4.30: Pulse shapes for different values of  $I_{sha}$ . The top two plots show the measured signal for the R side and the bottom two plots show the measured signal for the  $\Phi$  side. The plots in the left column show the measured signal for the n-on-n module (module 64) and the measured signal for the n-on-p module (module 26) are shown in the plots on the right column.

and dead channels were found by applying specific cuts on the estimated noise depending on the corresponding strip position.

### 4.8.1 Liverpool Classifications

The first list of bad channels was compiled during the module assembly phase at the University of Liverpool. A high-resolution visual inspection, laser scan and noise analysis were performed in order to uncover the possible problems that could cause channels to have a bad performance. These tests provided information on the physical integrity of the channels and their actual functionality.

The bad channels were classified into five categories according to the different results obtained from the three procedures at the University of Liverpool. The channel categories were listed as the following:

- Dead channels: these were usually identified through the laser scan when the measured signal was too low or when the raw noise was low;

Table 4.4: List of fit parameters,  $P$ , and the absolute value of the ratio between the associated errors and the parameters.

| Parameter number | Parameter Value        | $ \delta P/P $       |
|------------------|------------------------|----------------------|
| $A_0$            | $-3.53 \times 10^2$    | $4.1 \times 10^{-3}$ |
| $A_1$            | $2.39 \times 10^1$     | $1.8 \times 10^{-3}$ |
| $A_2$            | $-4.48 \times 10^0$    | $1.2 \times 10^{-3}$ |
| $A_3$            | $1.60 \times 10^{-3}$  | $4.2 \times 10^{-3}$ |
| $A_4$            | $3.39 \times 10^{-5}$  | $2.3 \times 10^{-3}$ |
| $A_5$            | $-3.53 \times 10^{-7}$ | $2.3 \times 10^{-3}$ |
| $A_6$            | $9.71 \times 10^{-10}$ | $7.5 \times 10^{-4}$ |

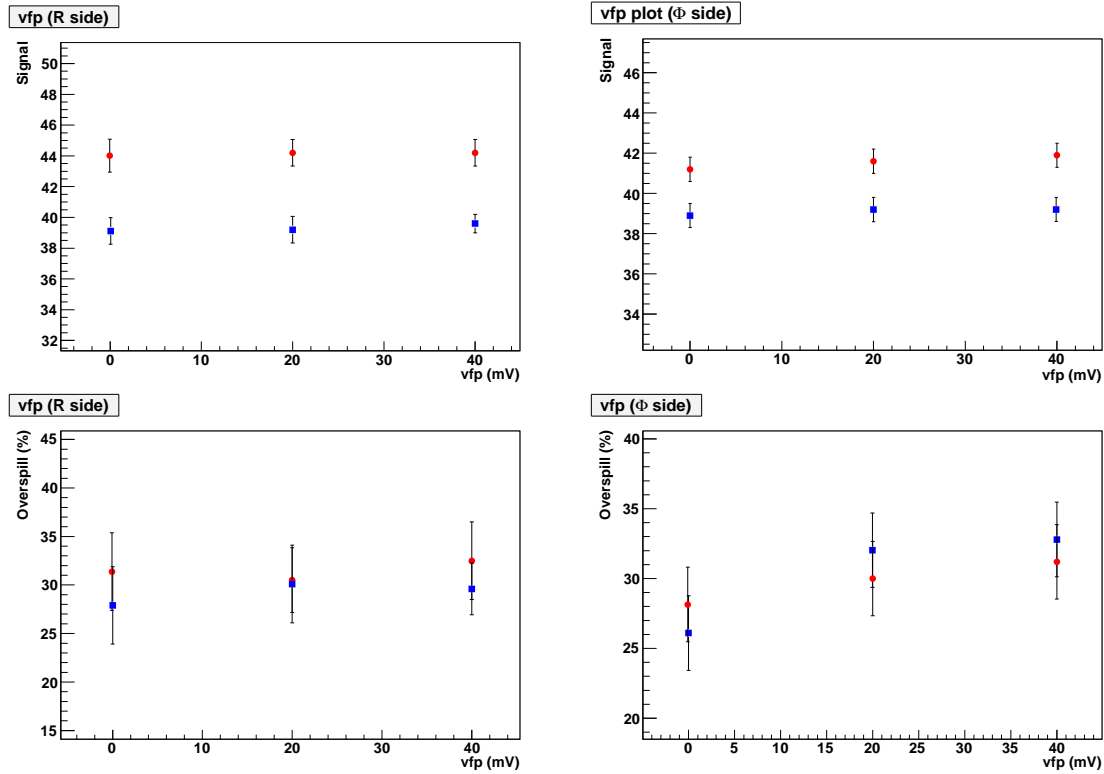


Figure 4.31: The top (bottom) two plots show the measured signal (spillover) from Beetle test pulses as a function of  $V_{fp}$  on both the  $R$  and the  $\Phi$ -sides of the module. The red circle markers correspond to the n-on-p modules and the blue square markers correspond to the n-on-n module.

- Noisy channels: these were identified to be when the readout channels had a noise higher than the usual limits.
- Low Gain channels: these were identified by the laser scan and were defined as occur-

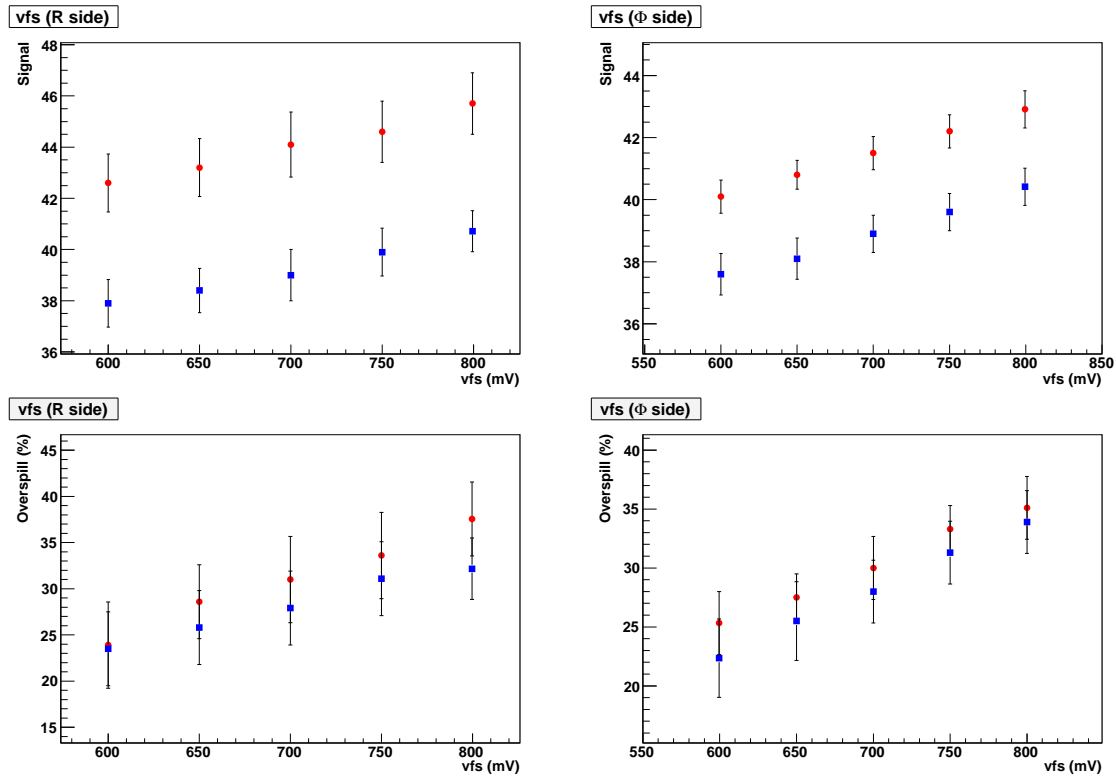


Figure 4.32: The top (bottom) two plots show the measured signal (spillover) from Beetle test pulses as a function of  $V_{fs}$  on both the  $R$  and the  $\Phi$ -sides of the module. The red circle markers correspond to the n-on-p modules and the blue square markers correspond to the n-on-n module.

ring when a response was received but the signal amplitude was below the expected values.

- Open channels: these occurred when the Front-End Bond or the Sensor-End Bond was not connected.
- Shorted channels: these occurred when the channel was connected to another channel in its vicinity. These were identified by measurements of charge sharing during the laser tests or through the high resolution visual inspections.

## 4.8.2 Burn-in Electrical Tests

The noise analysis procedure was performed on both the  $R$  and  $\Phi$ -sensors. The procedure was identical for both sensors: the same set of variables was used though the values of the applied limits differed slightly from one sensor type to the other. The values of the ADC limits applied also varied depending if the strip was in the inner region or in the outer region of the  $\Phi$ -sensors.



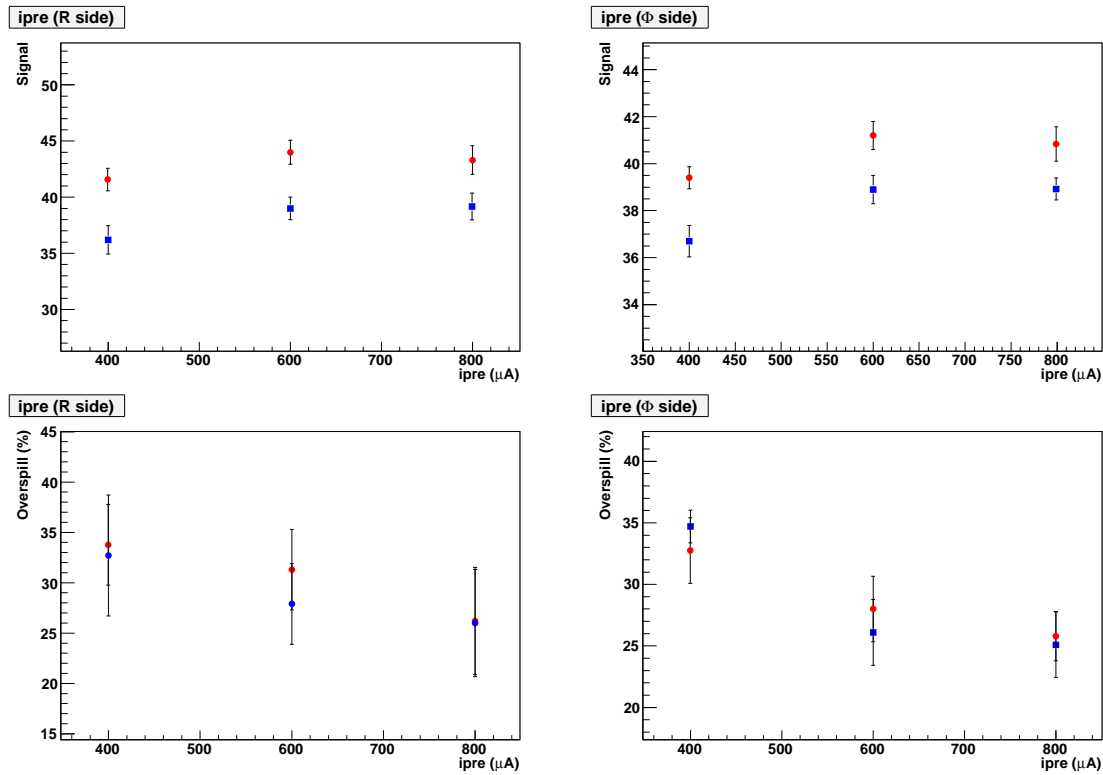


Figure 4.33: The top (bottom) two plots show the measured signal (spillover) from Beetle test pulses as a function of  $I_{pre}$  on both the  $R$  and the  $\Phi$ -sides of the module. The red circle markers correspond to the n-on-p modules and the blue square markers correspond to the n-on-n module.

The noise for each channel was calculated with the raw data and with the common mode suppressed data. A channel was considered dead if its raw noise was below a minimum limit or it was classified as noisy if the common mode suppressed noise is above a maximum limit.

Each channel also had its raw noise and common mode suppressed noise compared to the average noise obtained over all channels in its link.

A limit was applied to the difference between the average raw noise in the link and the measured raw noise from a single channel. If this difference was below the limit imposed the channel was classified as dead, i.e. if the raw noise of a channel in the R-sensor was more than 0.4 below the average noise for that link it was defined as dead. A limit was applied on the difference between the common mode corrected noise and the average common mode suppressed noise in the link. The channel was classified as noisy if the difference was above the limit imposed. The values of the cuts used for different sensors and regions are listed in table 4.5. The limits calculated for module 55 were shown in figure 4.5.

Three different quantities were estimated in order to provide an overview of the channels performance of the VELO sensors. The first of the three quantities was the absolute number of bad channels.

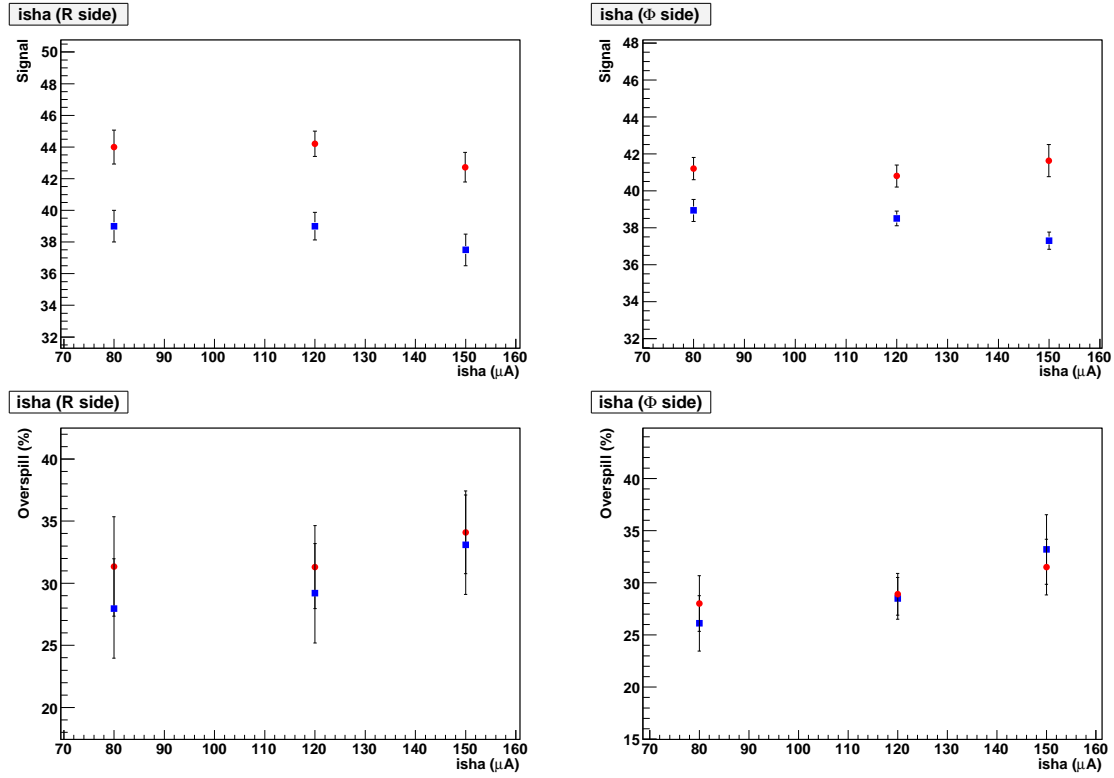


Figure 4.34: The top (bottom) two plots show the measured signal (spillover) from Beetle test pulses as a function of  $I_{\text{sha}}$  on both the  $R$  and the  $\Phi$ -sides of the module. The red circle markers correspond to the n-on-p modules and the blue square markers correspond to the n-on-n module.

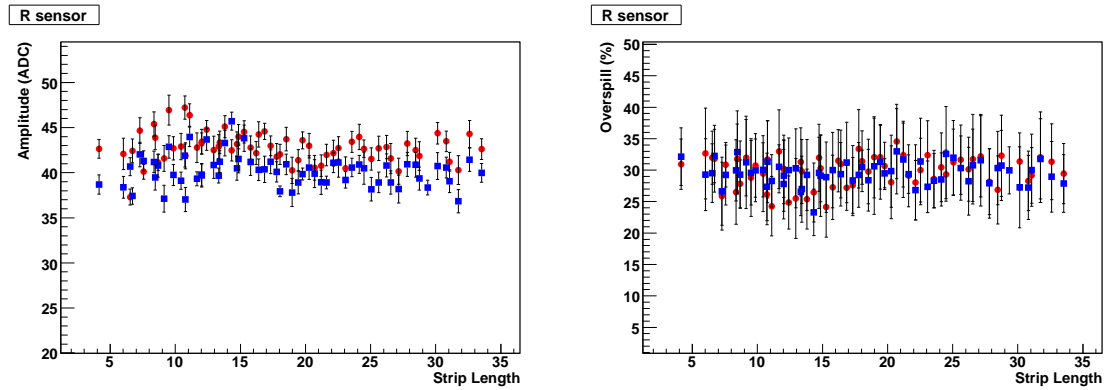


Figure 4.35: Test pulse peak (left) and spillover (right) as a function of the strips length in millimetres on R-sensors. The blue square markers are the values calculated for the n-on-n module and red circular markers are the values calculated for the n-on-p module. The default Beetle parameters were used.

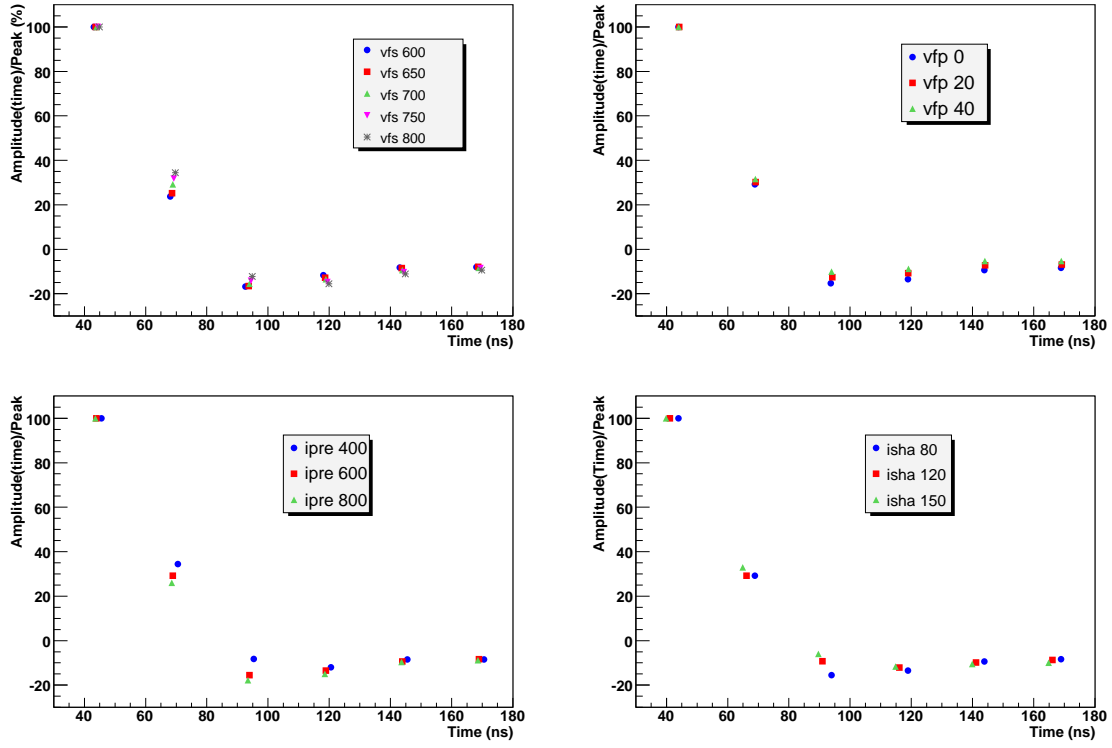


Figure 4.36: The ratio between the pulse amplitude as a function of the time and the pulse peak expressed as a percentage. The top left plot used the default Beetle parameters for  $V_{fp}$ ,  $I_{pre}$  and  $I_{sha}$  and varied the  $V_{fs}$  parameter, where the tested values for  $V_{fs}$  are shown in the legend. The other 3 plots had the same format, where the parameter in the legend was varied and the default Beetle settings were used for the other 3 parameters.

The second quantity calculated was the ratio

$$\frac{N_{New}}{N_{Agreement}}, \quad (4.4)$$

where  $N_{New}$  is number of new bad channels found in the burn-in since the Liverpool measurements and  $N_{Agreement}$  is the number of channels found in agreement with Liverpool and the burn-in bad channels lists.

The third quantity was the ratio

$$\frac{N_{Not\ rejected}}{N_{Agreement}}, \quad (4.5)$$

where  $N_{Not\ rejected}$  is the number of channels categorised as bad in Liverpool but were not identified as bad in the burn-in analysis. Figure 4.37 shows these three quantities as a function of the module number for both R and  $\Phi$ -sensors.

Figure 4.37 shows that the total number of bad channels on the R-sensors was less than 35 for all sensors (equivalent to less than 1.7 % bad channels) and less than 21 bad channels

Table 4.5: Rejection criteria for bad strips on the R and  $\Phi$ -sensors.

| Cut   | R       | $\Phi$ (inner) | $\Phi$ (outer) |
|---|---------|----------------|----------------|
| Raw Noise [ADC]   | $< 1.5$ | $< 1.5$        | $< 1.5$        |
| CMS noise [ADC]   | $> 2.7$ | $> 2.7$        | $> 2.7$        |
| $\langle \text{Raw Noise} \rangle - \text{Raw Noise}$ [ADC] | $> 0.4$ | $> 0.45$       | $> 0.65$       |
| CMS Noise - $\langle \text{CMS Noise} \rangle$ [ADC]        | $> 0.5$ | $> 0.45$       | $> 0.45$       |

for all  $\Phi$ -sensors (equivalent to less than 1.0 % bad channels). Almost all of the new bad channels found in the burn-in were typically on the edge of the cuts. On the other hand the cuts used were crudely optimised to reject as many genuine problem channels while not enforcing too tight cuts so that good channels were rejected. The total number of bad channels found in Liverpool and in the burn-in were respectively 435 and 451 on the R-sensor and 336 and 342 on the  $\Phi$ -sensors. An overall agreement of 79% with the Liverpool bad strips list was found for the combined results of the R and  $\Phi$ -sensors. Table 4.6 shows the total number of bad channels found in University of Liverpool and the burn-in laboratory, the number of channels in agreement between the two bad channels lists, the percentage of the number of new bad channels compared to the channels in agreement and the percentage of the number of selected bad channels in Liverpool that were not rejected by cuts on the electrical data analysis in the burn-in laboratory compared to the channels in agreement.

Table 4.6: The total number of bad channels found at the University of Liverpool and the burn-in laboratory, the number of channels in agreement between the two bad channels lists, the percentage of the number of new bad channels compared to the channels in agreement and the percentage of the number of selected bad channels in Liverpool that were not rejected by cuts on the electrical data analysis in the burn-in laboratory compared to the channels in agreement.

|        | Total <sub>Burn-in</sub> | Total <sub>Liverpool</sub> | Agreement | $\frac{\text{New Problem}}{\text{Agreement}}$ | $\frac{\text{Not Rejected}}{\text{Agreement}}$ |
|--------|--------------------------|----------------------------|-----------|---|--|
| R      | 451                      | 435                        | 328       | 0.37  | 0.18   |
| $\Phi$ | 342                      | 336                        | 278       | 0.29  | 0.39   |

Table 4.6 shows that the total number of bad channels that were found was higher for both sensor types compared to the lists compiled in University of Liverpool. Most of the differences were due to the cuts that were applied and in hindsight, the cuts applied in the burn-in could have been slightly tighter to allow for more of an agreement with the bad channel list compiled in University of Liverpool.

According to the numbers obtained from the burn-in analysis the mean number of bad

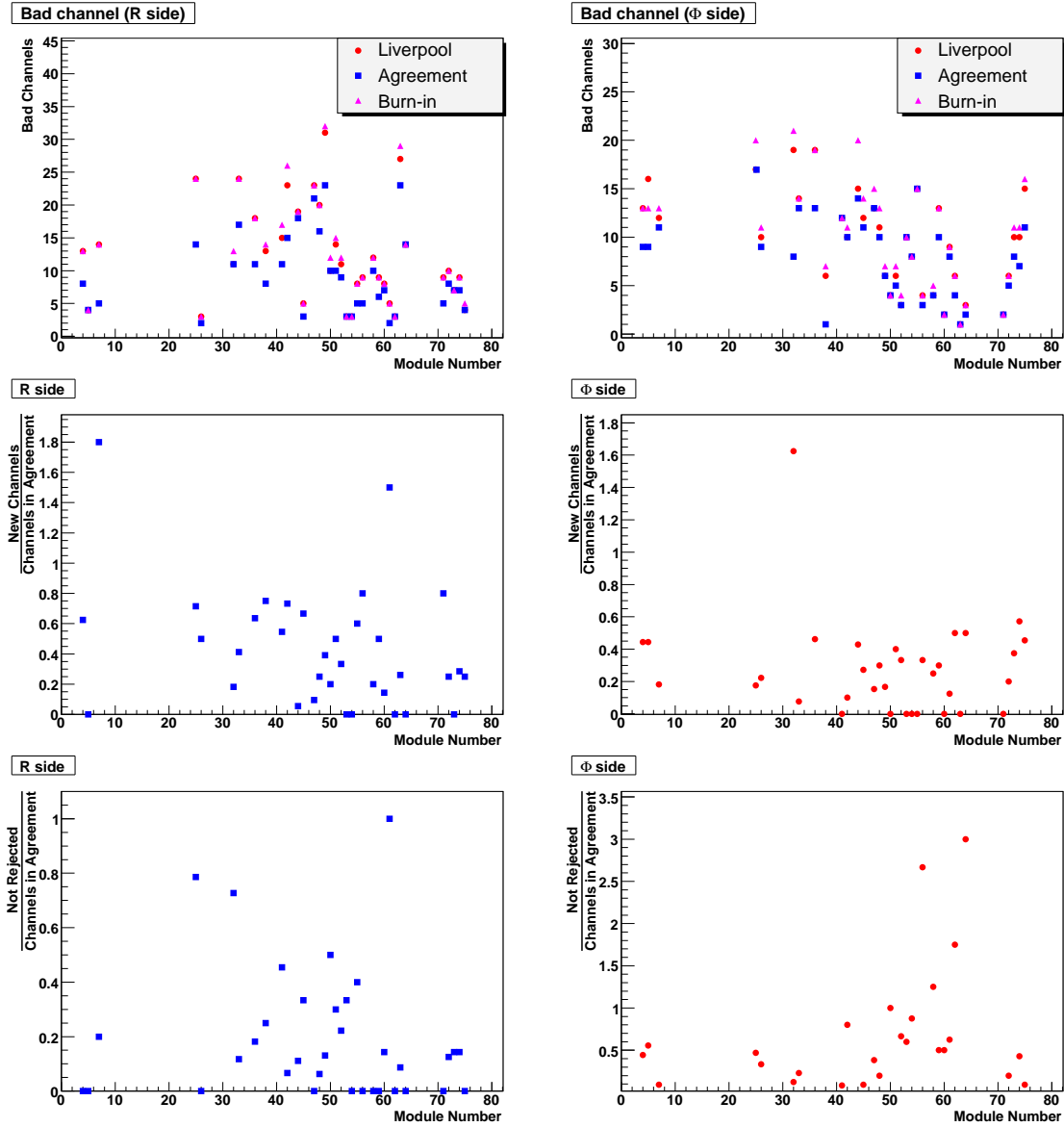


Figure 4.37: Top row: The number of bad channels as a function of the module number for both the R (left plot) and the  $\Phi$ -sensors (right plot). The red circle markers are the bad channels classified in Liverpool, the purple triangle markers are the bad channels found in the burn-in laboratory and the blue square markers are the number of bad channels that were in agreement. Centre row: The ratio between the number of new problematic channels found in the burn-in and the number of channels found in agreement with Liverpool on the R (left) and  $\Phi$ -sensors (right). Bottom row: The ratio between the number of channels categorised as bad in Liverpool but not rejected in the burn-in analysis and the number of channels in agreement with Liverpool on the R (left) and  $\Phi$ -sensors (right).

strips per module was estimated to be 14 on the  $R$ -sensors and 10 on the  $\Phi$ -sensors. An uncertainty of 20% on the number of bad strips was estimated by varying the cuts applied

on the analysis selection. Therefore the average percentage of problem strips in the whole VELO was measured to be  $0.7 \pm 0.1\%$  for the  $R$ -sensors and  $0.5 \pm 0.1\%$  for the  $\Phi$ -sensors. The number of channels which were measured to be shorted were 60 in total for all  $R$ -sensors measured and 51 channels for all  $\Phi$ -sensors\*, which was equivalent to 13% and 15% of the total number of bad channels found in the  $R$  and  $\Phi$ -sensors in the burn-in laboratory tests. If the shorted channels were used they would have a degraded resolution performance compared to a fully working channel. However, these channels form a significant proportion of the total bad channels measured and perhaps they could be used in the future operation of the VELO, with careful tuning of the clustering algorithm.

## 4.9 Conclusions

The VELO modules were extensively tested in the burn-in laboratory. The testing rate successfully managed to follow the production delivery rate and hence did not delay the detector assembly rate. A few problem features on the modules were picked up during the detailed visual inspections and the results were fed back into the University of Liverpool production, such as an early problem with a vacuum holding jig which was deforming the high voltage return bonds on early production modules.

Six of the 42 production modules were thermally imaged before and after the electrical and thermal burn-in tests and all of the images showed no problems on the front end chips or areas of non-uniformity. Throughout the electrical tests the signal to noise ratio was calculated from the header and the ratio was monitored and no problems were found.

The leakage current of the sensors were carefully measured and compared throughout the personal history of each module. A few of the  $\Phi$ -sensors were found to suffer from a thermally induced increase in leakage current and one of these modules was withheld from the final system and used as a spare. No correlation was found between the metrology performed in University of Liverpool and the leakage current of the sensors. The majority of the high leakage current sensors were  $\Phi$ -sensors and it was found that most of these high leakage current  $\Phi$ -sensors originated from wafer position  $A$  which was near the edge of the wafer.

The Beetle Front-End chip control parameters were scanned and compared for an n-on-n VELO module and an n-on-p module. The behaviour of the n-on-p and n-on-n modules were found to be very similar, i.e. capacitances are the same. The variation of the pulse shapes with the Beetle chip parameters is useful for the tuning the VELO for different stages of its lifetime. Bad channels were analysed using information from both the visual inspections and the electrical tests. The agreement between the list of bad channels found in University of Liverpool and the burn-in laboratory was good. Overall there were 0.7% and 0.5% bad channels measured in the burn-in laboratory on the  $R$  and  $\Phi$ -sensors respectively.

---

\*Two channels that were shorted together counted as two

The modules were fully exercised and operated as in the LHCb experiment. The overall performance of the VELO modules was excellent. There were very few problems discovered during the burn-in testing. The testing performed in the burn-in improved the confidence with which the VELO detector could be operated. The burn-in results were later used as guidelines for the commissioning of the VELO detector to verify the performance of the modules. Leakage current measurements and noise estimates were made during the commissioning stage and compared to the burn-in results.

# Chapter 5

## Analysis of the $B_d \rightarrow K^* \mu^+ \mu^-$ decay

This chapter presents preparatory studies for an analysis of the  $B_d \rightarrow K^* \mu^+ \mu^-$  decay in the LHCb experiment. As discussed in section 1.5 the  $B_d \rightarrow K^* \mu^+ \mu^-$  decay can be sensitive to possible new physics (NP) effects. Quantities which are affected by NP effects in this decay are: the dimuon mass squared distribution; and Forward-Backward Asymmetry distribution (FBA).

The aim of this analysis was to evaluate the quality of the measurements of the  $B_d \rightarrow K^* \mu^+ \mu^-$  decay in the LHCb experiment. This analysis contains estimates of the signal selection efficiency, annual yields and discusses the dependence of these quantities with the LHCb luminosity. Resolution studies were performed to evaluate whether or not the uncertainties of the detector measurements can distort the dimuon mass squared and FBA distributions. A novel approach to determine the FBA distribution was developed. This method was also extended to correct effects due to acceptance and background.

Section 5.1 describes the current LHCb data simulation. Sections 5.2 and 5.3 describe the trigger and the particle identification respectively. Sections 5.4 and 5.4.1 present the results which were obtained on the signal selection of the  $B_d \rightarrow K^* \mu^+ \mu^-$  decay in LHCb. The annual yield estimate is an important quantity which was used in the studies discussed in this chapter.

Section 5.5 presents estimates of the selection efficiency and annual yield in this channel as a function of the LHCb instantaneous luminosity. The evaluation of the performance of the LHCb detector at higher luminosities relates to a possible upgrade of the detector. Operating the LHCb detector at higher luminosities would allow a significant increase in statistics. As a result an overall improvement of the physics measurements could be achieved. Section 5.6 presents the calculations of the resolution of the different variables used in the analysis.

A non-parametric unbinned method was developed to measure the FBA distribution in LHCb. This approach provided access to the shape of the distributions without assuming any specific distribution. The FBA zero point was extracted directly from the obtained curve. This method and its features are described in section 5.7. The estimated sensitivity of the LHCb detector to measure the dimuon mass squared distribution and FBA distribution are



presented.

The LHCb selection algorithms must apply cuts to efficiently accept signal events and to avoid background contamination. These cuts can affect the dimuon mass squared distribution and hence the FBA distribution. These effects are commonly referred to as acceptance effects. In section 5.8 the unbinned approach was used to evaluate acceptance effects in the  $B_d \rightarrow K^* \mu^+ \mu^-$  decay. Such effects can be corrected on the measured distributions.

Although selection algorithms are developed to accept only signal events, a small fraction of the background events can be wrongly selected. This small amount of background can affect the measured distributions. This issue was addressed in the study discussed in section 5.9.

Section 5.10 summarises the main results of the  $B_d \rightarrow K^* \mu^+ \mu^-$  analysis presented. Section 5.11 discusses the LHCb prospects for the  $B_d \rightarrow K^* \mu^+ \mu^-$  decay measurements, possible impact on new physics models and future developments in the analysis.

## 5.1 The LHCb Simulation

The studies performed for the  $B_d \rightarrow K^* \mu^+ \mu^-$  decay in this thesis are based on the analysis of Monte Carlo (MC) event simulations. The MC simulation provides a realistic description of the physics process and detector performance, and hence allows an assessment of the potential of the experiment of measuring this physics process.

The complete LHCb event generation is broken down in a number of steps. It extends from the proton-proton collisions up to the event reconstruction performed by the detector. The products of the collisions are generated in the reference frame of the detector. Then the response of the detector to the particles passing through its material is simulated. The data acquisition process is also simulated. The information from the different parts of the detector are finally assembled in a full event ready to analyse.

The so called offline analysis is the part of the LHCb software which performs the signal event selection and extraction of physics parameters. By using simulated data it is possible to evaluate efficiencies by comparing the number of selected events and the number of generated events. In LHCb, the MC method is also used to estimate background rejection rates and to evaluate the resolution of measurements or elements such as vertex positions, particle momenta, etc. The following sections briefly describe the MC event production used in this analysis.

### Event generation and Detector simulation

The Gauss package [116] is the event generator used for LHCb simulation. The event generation was divided in two parts to provide a realistic description of the LHCb data taking:

- generation of the proton-proton collisions and the decay of the unstable particles produced;

- simulation of the passage of particles through the detector material.

The proton-proton collisions were generated with the PYTHIA 6 package [117]. The decay of the produced particles was simulated by using the EvtGen package [118]. EvtGen is a software library dedicated to  $b$ -hadron decay simulation.

The simulation of the detector response to the particles passing through its material was performed with the GEANT4 package [119]. This part of the simulation contained a detailed description of the detector material and described the interaction of the particles with the detector components.

### Digitisation

The LHCb digitisation simulated the readout of the signals produced by the particle hits in the sensitive parts of the detectors. It included the response of the readout electronics to these signals and the analogue to digital conversions. This part of the simulation was performed by the Boole package [120].

### Reconstruction

The LHCb event reconstruction application processed the output from the digitisation algorithm (Boole). This part of the LHCb software reconstructed the tracks and the Cherenkov rings using the raw data acquired by the DAQ system. The output of the reconstruction was recorded in data summary tape files (dst) and were used by the offline analysis algorithms. In the LHCb experiment this application processes the data from the DAQ system.

Events generated with the complete LHCb data simulation were used to evaluate the detector efficiency to select signal events (see section 5.4). To evaluate the LHCb sensitivity on the FBA measurement a toy Monte Carlo simulation using only the output from the event generation was used. The effect of the detector reconstruction was later included in the toy Monte Carlo through acceptance functions, as described in section 5.8.

## 5.2 Trigger

The strategy for the trigger selection of the  $B_d \rightarrow K^* \mu^+ \mu^-$  events is summarised in this section. The trigger system is discussed in section 2.2.7.

The  $B_d \rightarrow K^* \mu^+ \mu^-$  events are first selected by the L0 muon trigger. The L0 processor finds the muon tracks in the event by searching for hits defining a straight line through the five muon stations and pointing towards the interaction point. The determination of the track's  $P_T$  is performed using the first two muon stations. An event is accepted by the L0 muon trigger if one track with  $P_T > 1.2 \text{ GeV}/c$  is found or two tracks satisfying the requirement  $P_T^{\mu_1} + P_T^{\mu_2} > 1.0 \text{ GeV}/c$  are found. The majority of the  $B_d \rightarrow K^* \mu^+ \mu^-$  events are accepted by the L0 single muon selection.

In the HLT trigger there are few possibilities being studied to select the  $B_d \rightarrow K^* \mu^+ \mu^-$  decay. As mentioned in section 2.2.7 the HLT is divided in two stages. In the HLT1 the signal events can be selected via the single muon alley or through a  $\mu + track$  alley. Both use events accepted by the L0 single muon trigger as input. The HLT1 single muon alley uses cuts on the muon  $P_T$  and  $IP$  of the muon. The  $\mu + track$  alley also implements cuts on  $P_T$  and  $IP$  of a companion track and includes vertex cuts. The performance of both alleys are estimated to be quite similar. The HLT2 is still under development but results using the inputs from both single muon and  $\mu + track$  alleys should be the same.

The effect of the trigger in the selection efficiency is discussed in section 5.5. The effects of the trigger selection on the dimuon mass squared distribution and hence the FBA distribution are presented in section 5.8.3.

### 5.3 Particle Identification

In the LHCb experiment the particle identification (PID) is implemented at the end of the event reconstruction. PID algorithms are developed to assign a particle type to the reconstructed tracks. These specific algorithms store their final results for each subdetector (RICH, calorimeters and muon system) in summary objects. The main output of the identification algorithms are the so-called PID data objects which summarise the PID results for each track. The following identification procedures are performed using the information of the subdetectors.

- Hadronic identification: the Cherenkov rings measured in the RICH system are used to evaluate particle type hypotheses for the tracks of the hadronic particles. Averaged over the full momentum range the performance with pion and kaon efficiencies is  $\sim 95\%$  and mis-identification rates are below 5%;
- Muon identification: it is performed by extrapolating the tracks reconstructed within the muon detector. By searching for hits close to the extrapolated track in the detector chambers it is possible to build a likelihood for the muon hypothesis. The muon identification is 94% efficient with a misidentification rate of 3%;

The final stage of the particle identification is called global PID. All the sources of PID information from the subdetectors are merged to provide optimised global PID estimators. A log-likelihood difference is used as a selection variable to differentiate between the possible PID types assigned to the same particle track.

### 5.4 Event Selection and Efficiency

The LHCb offline analysis was performed by the Da Vinci package [121]. This package provided the tools necessary to perform the reconstruction and the selection of the  $b$ -hadrons.

Da Vinci algorithms perform basic analysis tasks such as vertex reconstruction. It also contains algorithms to perform the event selection of specific decays.

The selection of the  $B_d \rightarrow K^* \mu^+ \mu^-$  signal events was performed by combining the information of the measured charged particles to reconstruct their mother particles. In this case the  $K^*$  was obtained by combining its  $K^+$  and  $\pi^-$  daughter particles. In the case of the  $\bar{B}_d \rightarrow \bar{K}^* \mu^+ \mu^-$  then the  $\bar{K}^*$  decays to its  $K^-$  and  $\pi^+$  daughter particles. The  $B_d$  meson was then obtained by combining the two muons and the  $K^*$ . Figure 5.1 shows the  $B_d \rightarrow K^* \mu^+ \mu^-$  with the  $B_d$  obtained in a typical production event.

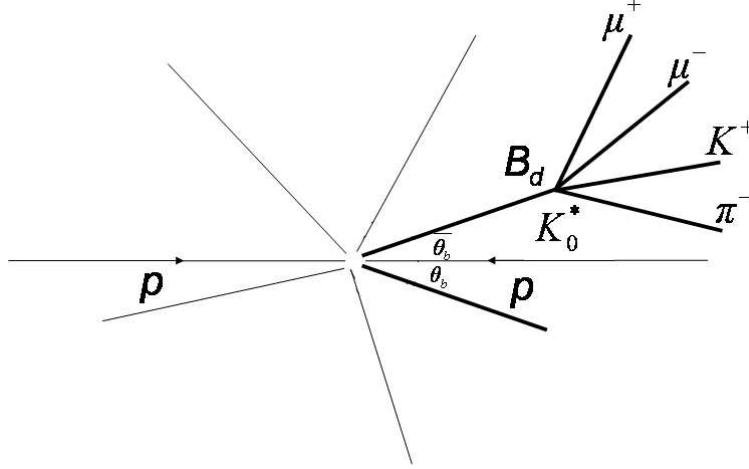


Figure 5.1: Diagram of a  $B_d \rightarrow K^* \mu^+ \mu^-$  event produced in a proton-proton collision. The angle of production of the quarks  $p$  and  $\bar{p}$  is indicated.

To select the signal  $B_d \rightarrow K^* \mu^+ \mu^-$  events and to reject background events a set of selection criteria have to be used. The cuts used were those proposed in [122]<sup>‡</sup>. The signal selection criteria were based on the particular topology of the decay. In general the muons produced in B decays have  $P_T$  higher than those from the primary vertex. The two muons in the  $B_d \rightarrow K^* \mu^+ \mu^-$  decay were required to have their transverse momenta  $P_T$  to be higher than a certain minimum value and to have their origin from the same decay vertex. The decay vertex of the dimuon was required to be displaced from the collision vertex ensuring the dimuon was from a B meson. Similar constraints were imposed to the  $K$  and  $\pi$ . The invariant mass obtained with the  $K$  and  $\pi$  should be close to the  $K^*$  resonance mass. The reconstructed decay vertex of the  $K^*$  was required to be displaced from the collision vertex. The reconstructed  $B_d$  was also required to satisfy some cuts in order to be selected. Table 5.1 shows the cuts applied to all the particles involved in this decay. A total of  $\sim 62800$  signal events were used in this study. The number of selected events was  $4027 (1.15 \text{ fb}^{-1})$ .

As the VELO detector reconstructs the tracks of the particles and primary vertices with

<sup>‡</sup>Similar results were previously obtained at [123] and recently by a new selection which is being developed using the latest LHCb simulation [124].

Table 5.1:  $B_d \rightarrow K^* \mu^+ \mu^-$  selection criteria. Particle types, selection variables and cut value are listed. The selection criteria were proposed in order to select signal events and to reject background events.

| Particle      | Selection Criterion           | Cut value                          |
|---------------|-------------------------------|------------------------------------|
| $\mu^\pm$     | p                             | $>4000 \text{ MeV/c}$              |
|               | $p_T$                         | $>500 \text{ MeV/c}$               |
|               | $IP/\delta IP \text{ (3D)}^*$ | $>2.0$                             |
| $\mu^+ \mu^-$ | flight-distance <sup>†</sup>  | $>1.0 \text{ mm}$                  |
|               | vertex $\chi^2/\text{ndf}$    | $<20.0$                            |
|               | $J/\Psi(1S)$ mass-rejection   | $2900\text{-}3200 \text{ MeV/c}^2$ |
|               | $J/\Psi(2S)$ mass-rejection   | $3650\text{-}3725 \text{ MeV/c}^2$ |
| $\pi^\pm$     | p                             | $>2000 \text{ MeV/c}$              |
|               | $p_T$                         | $>250 \text{ MeV/c}$               |
|               | $IP/\delta IP$                | $>3.0$                             |
| $K^\pm$       | p                             | $>2000 \text{ MeV/c}$              |
|               | $p_T$                         | $>400 \text{ MeV/c}$               |
|               | $IP/\delta IP$                | $>3.0$                             |
| $K^*$         | $p_T$                         | $>300 \text{ MeV/c}$               |
|               | vertex $\chi^2/\text{ndf}$    | $<30.0$                            |
|               | flight-significance           | $>1.0$                             |
|               | $IP/\delta IP$                | $>1.5$                             |
|               | mass-window                   | $\pm 100 \text{ MeV/c}^2$          |
| $B_d$         | $p_T$                         | $>250 \text{ MeV/c}$               |
|               | vertex $\chi^2/\text{ndf}$    | $<20$                              |
|               | flight-significance           | $>6$                               |
|               | $IP/\delta IP$                | $<5$                               |
|               | mass-selection                | $\pm 50 \text{ MeV/c}^2$           |

great precision, quantities such as the particles  $IP/\delta IP^*$ , flight-distance<sup>†</sup> and secondary vertex position can be calculated and used as selection criteria (see section 2.2.1).

Figure 5.2 shows the reconstructed mass distribution of the  $K^*$  and  $B_d$  mesons. The  $K^*$  mass was estimated to be  $m_{K^*}^{\text{rec}} = 895.50 \pm 0.54 \text{ MeV/c}^2$  and its full width  $\Gamma = 51 \pm 11 \text{ MeV/c}^2$  through a Breit-Wigner distribution fit. The input value in the simulation was  $m_{K^*} = 896 \text{ MeV/c}^2$ . The mass of the  $B_d$  meson was estimated to be  $m_{B_d}^{\text{rec}} = 5279.6 \pm$

\*The  $IP/\delta IP$  is the impact parameter significance. The impact parameter is defined as the minimum distance (in 3D) between the trajectory of a particle with respect to the primary vertex.

†The flight-distance is defined as the distance between the decay vertex and the primary vertex.

0.3 MeV/c<sup>2</sup> with a resolution of  $\sigma = 17.74 \pm 0.22$  MeV/c<sup>2</sup> by means of a Gaussian fit. The input value was  $m_{B_d} = 5279.5$  MeV/c<sup>2</sup>. The results were in good agreement with the input value in the simulation. No biases due to the detector reconstruction were observed.

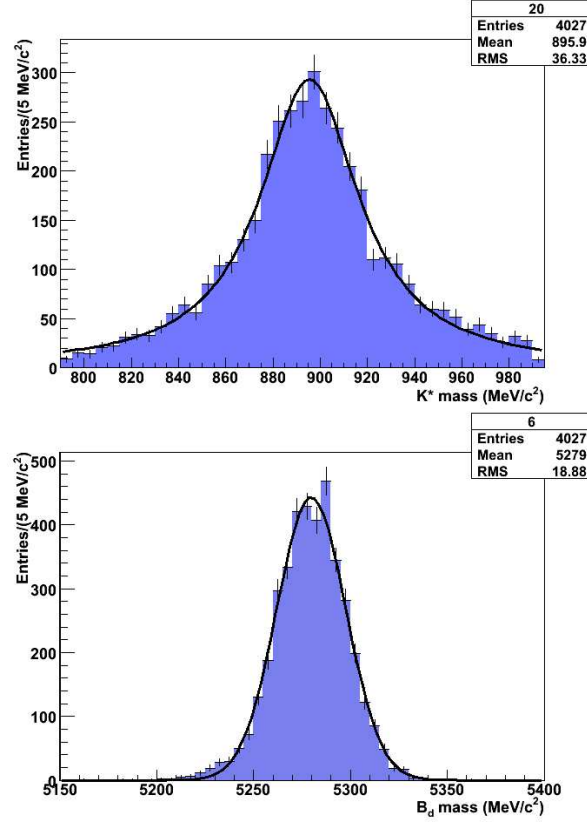


Figure 5.2: Reconstructed mass distribution of the  $K^*$  and  $B_d$  mesons from simulated  $B_d \rightarrow K^* \mu^+ \mu^-$  events. The fitted curve for the  $K^*$  ( $B_d$ ) mass resonance is a Breit-Wigner (Gaussian) curve. The corresponding luminosity is  $1.15 \text{ fb}^{-1}$ . The selection cuts are described in the text.

The cuts listed in table 5.1 were chosen in order to optimise the ratio  $S/\sqrt{B}$  for each variable (see [122]), where  $S$  is the number of signal events and  $B$  is the number of background events. For example, the  $\text{IP}/\delta\text{IP}$  cut applied on muons, kaons and pions ensures the selected particles are not produced in the primary vertex. This reduces drastically the use of particles which are not genuine products of the  $B_d \rightarrow K^* \mu^+ \mu^-$  decay. Cuts applied on the  $\chi^2/\text{ndf}$  of the vertex fit of the dimuon,  $K^*$  and  $B_d$  are used to avoid combinations of particles produced in different vertices. The cut on the flight-distance or significance helps to distinguish whether or not the reconstructed dimuon and  $K^*$  are from a  $B$  meson. It also ensures the reconstructed  $B_d$  is displaced from the primary vertex reducing the background.

The dimuon invariant mass is subject to cuts in order to avoid contamination from  $B \rightarrow J/\psi(1S)X$  or  $B \rightarrow \Psi(2S)X$  decays. The reconstructed  $K^*$  mass is also required to have a value close to the expected  $K^*$  mass rejecting spurious  $K\pi$  combinations that could pass the

other cuts. A similar cut is performed to the reconstructed mass of the  $B_d$ . For the analysis presented in this chapter the background levels used were from [122](see table 5.3).

### 5.4.1 Selection Efficiency and Yield

The selection efficiency was given as the ratio of the number of selected events divided by the number of generated events. A multiplicative geometric factor was required because in the LHCb simulation the  $B_d$  meson and its decay products were generated within the geometric acceptance of the detector. Mathematically:

$$\epsilon_{sel} = \frac{\text{Selected Events}}{\text{Generated Events}} \times f_{\text{geometry}}, \quad (5.1)$$

where  $f_{\text{geometry}}$  is the expected ratio between the number of events generated inside the detector acceptance and the total of produced events in  $4\pi$  steradian. The selection efficiency was estimated to be  $\epsilon_{sel} = 1.12 \pm 0.02\%$ .

The number of signal events expected to be selected after one year of data taking was calculated according to the following equation:

$$N_{sel}^{year} = \mathcal{L}^{year} \times \sigma_{b\bar{b}} \times 2 \times \text{Prob}(\bar{b} \rightarrow B_d) \times \text{BR}(B_d \rightarrow K^* \mu^+ \mu^-) \times \epsilon_{sel}, \quad (5.2)$$

where  $\mathcal{L}^{year}$  is the expected integrated luminosity after one full year of data taking,  $\sigma_{b\bar{b}}$  is the estimated cross section of  $b\bar{b}$  production,  $\text{Prob}(\bar{b} \rightarrow B_d)$  is the probability of the hadronization of the  $\bar{b}$  quark into a  $B_d$  meson and  $\text{BR}(B_d \rightarrow K^* \mu^+ \mu^-)$  is the estimated branching ratio of the signal decay. The factor 2 is required to account for the signal originating from both  $b$  and  $\bar{b}$  quarks.  $N_{sel}^{year}$  was estimated to be  $\sim 7.0 \pm 0.1 \times 10^3$ . Table 5.2 shows the values used in the LHCb simulation and for these calculations [72].

Table 5.2: Parameters used in the annual yield evaluation.

|  |                       |
|--|-----------------------|
| $\mathcal{L}(\text{cm}^{-2}\text{s}^{-1})$   | $2 \times 10^{32}$    |
| $\mathcal{L}^{year}(\text{cm}^{-2})$         | $2 \times 10^{39}$    |
| $\sigma_{b\bar{b}}(\text{cm}^2)$             | $5 \times 10^{-28}$   |
| $\text{Prob}(\bar{b} \rightarrow B_d)$       | 0.398                 |
| $\text{BR}(B_d \rightarrow K^* \mu^+ \mu^-)$ | $1.38 \times 10^{-6}$ |
| $f_{\text{geometry}}$                        | 1/0.1747              |

The values for  $\epsilon_{sel}$  and  $N_{sel}^{year}$  were estimated with the detailed simulation of the experiment which included not only the proton-proton collisions and the decays of the particles produced but also the response of the detector to the charged particles passing through its material, as described in section 5.1.

## 5.5 Luminosity Dependence of Selection Efficiency

The LHCb experiment will operate at a instantaneous luminosity of  $2 \times 10^{32} \text{ cm}^{-2}\text{s}^{-1}$ . However an upgrade has been suggested that could run at  $2 \times 10^{33} \text{ cm}^{-2}\text{s}^{-1}$  [125]. In order to evaluate the selection efficiency of the  $B_d \rightarrow K^* \mu^+ \mu^-$  decay as a function of the luminosity an analysis was performed using two different simulation data sets at different luminosities. The results that were obtained using the current detector setup are presented in this section.

As already mentioned the data sets which were used were the final result of the detailed simulation of the LHCb experiment. On average it takes about 70 seconds to simulate one event in LHCb[126]. Due to this huge time consumption it was not possible to generate many sets of data with enough statistics for different values of luminosity. Hence, an alternative approach to estimate this efficiency as a function of the luminosity was used. This approach consisted of evaluating the efficiency as a function of the number of proton-proton interactions in the event.

Two sets of data were used for this study: the signal data set with  $\mathcal{L} = 2 \times 10^{32} \text{ cm}^{-2}\text{s}^{-1}$ ; and a set of 74000 signal events containing at least one  $B_d \rightarrow K^* \mu^+ \mu^-$  decay at a luminosity of  $5 \times 10^{32} \text{ cm}^{-2}\text{s}^{-1}$ . The efficiency as a function of the number of generated primary vertices was obtained with these data sets. Figure 5.3 shows the number of selected events as a function of the number of primary vertices. It also shows the values of efficiency obtained as a function of the number of generated primary vertices per event with both data sets. Note the efficiency for events with a number of primary vertices per event higher than 5 could not be accurately estimated with the  $\mathcal{L} = 2 \times 10^{32} \text{ cm}^{-2}\text{s}^{-1}$  data set.

It is possible to calculate the efficiency as a function of luminosity once the efficiency as a function of the number of primary vertices per event is already known. The average number of primary vertices and the luminosity are related by

$$\langle PV \rangle = \frac{\sigma_{interaction} \times \mathcal{L}}{R_{cross}}, \quad (5.3)$$

where  $\langle PV \rangle$  is the mean number of primary vertices,  $\sigma_{interaction}$  gives the interaction probability,  $\mathcal{L}$  is the luminosity and  $R_{cross}$  is the bunch crossing rate. The values for  $\sigma_{interaction} = 80 \text{ mb}$  and  $R_{cross} = 30 \text{ MHz}$  were taken from [28].

The efficiency as a function of the luminosity can be written in terms of the efficiencies obtained for different numbers of primary vertices per event as:

$$\epsilon(\mathcal{L}) = \sum \epsilon(PV) \times P(PV, \langle PV \rangle). \quad (5.4)$$

In this formula  $\epsilon(\mathcal{L})$  and  $\epsilon(PV)$  are the efficiencies in terms of the luminosity and the number of primary vertices.  $P(PV, \langle PV \rangle)$  is the Poisson distribution for the number of primary vertices. Figure 5.4 shows the efficiency and the expected number of selected events per year (annual yield) obtained as a function of the luminosity. The annual yields were



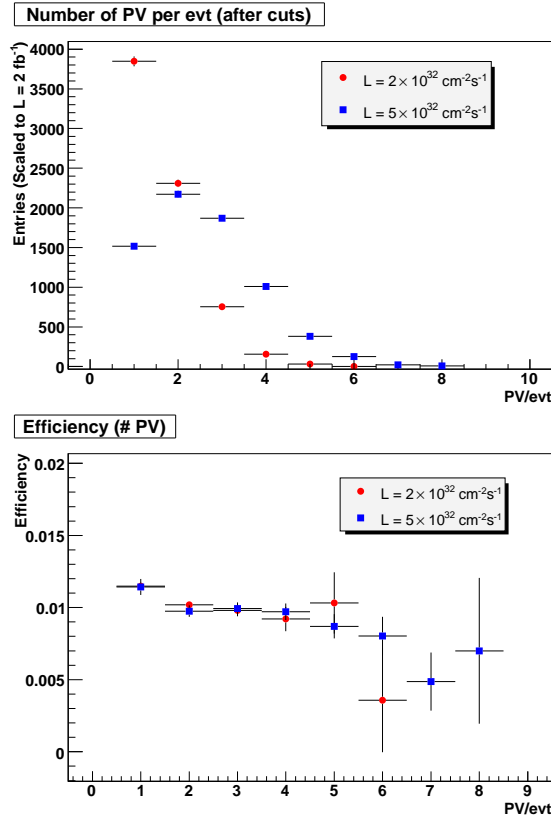


Figure 5.3: Number of selected events and efficiency as a function of the number of primary vertices per event. The red dots represent the points calculated with the  $2 \times 10^{32} \text{ cm}^{-2}\text{s}^{-1}$  data set and blue squares calculated with the  $5 \times 10^{32} \text{ cm}^{-2}\text{s}^{-1}$  data set.

calculated using equation 5.2, replacing  $\epsilon_{sel}$  with the luminosity dependent  $\epsilon(L)$  of equation 5.4.

As can be seen from the graphs the efficiency would decrease by about 22% of its value if the luminosity was increased from  $2 \times 10^{32} \text{ cm}^{-2}\text{s}^{-1}$  (nominal luminosity) to  $14 \times 10^{32} \text{ cm}^{-2}\text{s}^{-1}$ . The annual yield at  $14 \times 10^{32} \text{ cm}^{-2}\text{s}^{-1}$  was estimated to be  $\sim 5$  times higher than at nominal LHCb luminosity, assuming the trigger efficiency remained constant. In these estimates no further optimisation of the event selection to improve the efficiency at higher luminosities (or multiple primary vertices) was performed.

### Trigger Efficiency

The results presented in the previous sections do not include trigger simulations. As discussed in section 2.2.7 the LHCb trigger system is implemented in two levels. The L0 trigger has already been implemented while the HLT is still under development. Previous studies show the L0 efficiency on the  $B_d \rightarrow K^* \mu^+ \mu^-$  channel is  $\sim 93\%$  [122, 123]. Studies have been performed in order to estimate the L0 efficiency as a function of luminosity assuming constant bandwidth [125]. Figure 5.5 shows the L0 trigger yield as a function of the

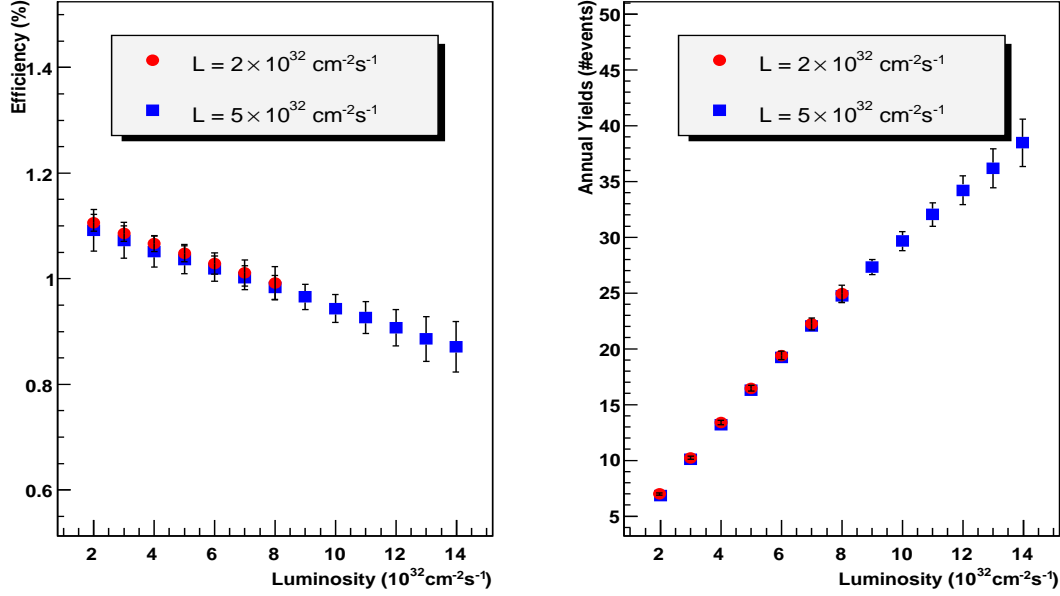


Figure 5.4: Efficiency and annual yields as a function of the luminosity. The yields are equivalent to the number of events selected during a period of one year of data taking ( $10^7$  s). The red dots (blue squares) represent the efficiencies and annual yields calculated as a function of the luminosity using the  $2 \times 10^{32} \text{ cm}^{-2} \text{ s}^{-1}$  data set.

luminosity. The combined efficiency of the L0 trigger and HLT trigger system is expected to be higher than 80% at nominal LHCb luminosity. No strong dependence on luminosity is expected, so the combination of both the L0 and HLT efficiencies should simply change the efficiency from  $\epsilon_{L0} \sim 93\%$  to  $\epsilon_{L0+HLT} \sim 80\%$ .

### Discussion

As a result of the studies performed in this section it was demonstrated that a significant improvement on the number of selected  $B_d \rightarrow K^* \mu^+ \mu^-$  events can possibly be achieved by running the detector at higher luminosities. The selection efficiency remains high at higher luminosities and the trigger on muons scales with the instantaneous luminosity. Hence, the original detector design could be used to collect increased data samples in the case of the  $B_d \rightarrow K^* \mu^+ \mu^-$  decay and also other muonic channels. Radiation damage and background increase are issues that still need to be investigated in future. As discussed in section 2.2.1 the VELO sensors performance will vary with radiation exposure. Increasing the luminosity will increase the radiation damage and it might reduce the performance of the sensors such that the improvement of the signal yield obtained may be lower than estimated. Background can increase significantly with luminosity, however further development of the selection algorithms to cope with multiple PV events can be made.

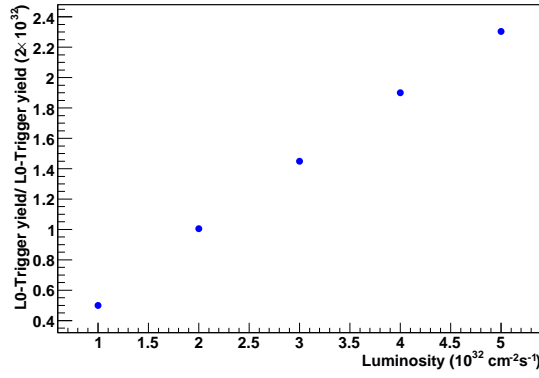


Figure 5.5: L0 trigger yield as function of the luminosity for the  $B_d \rightarrow K^* \mu^+ \mu^-$  channel. Analysis values were extracted from [125].

The results obtained in this section do not apply to hadronic decays where the efficiency is expected to drop significantly as the luminosity increases due to the trigger efficiency. Hence the current detector could run at  $5 \times 10^{32} \text{ cm}^{-2} \text{ s}^{-1}$  only for muonic channels.

## 5.6 Resolution

As discussed in chapter 2, the LHCb experiment was designed to reconstruct the particles produced inside its angular acceptance with good precision. In this section the resolutions obtained for the quantities critical for this analysis (particles momenta, dimuon mass and  $\theta_l$  angle<sup>§</sup>) are presented. The mass resolution of the  $B_d$  has already been presented in section 5.4. Comments on the particle identification are given in section 5.3.

### 5.6.1 Momentum Resolution

It was possible to evaluate the measurement resolution of the detector by using MC simulation comparing the results from the reconstruction simulation with their values assigned at the event generation. Figures 5.6 and 5.7 show the momentum resolutions of the charged particles of the  $B_d \rightarrow K^* \mu^+ \mu^-$  decay. Figure 5.7 also shows the momentum resolutions for the  $B_d$  resonance.  $\Delta P_x/P_x$  is the resolution for the transverse component perpendicular to the magnetic field (see section 2.2.3),  $\Delta P_y/P_y$  is the resolution of the transverse component parallel to the magnetic field and  $\Delta P_z/P_z$  is the resolution of the longitudinal component.

A fit of a double Gaussian function was performed on the distributions shown in figures 5.6 and 5.7. The sigma of the core Gaussian ( $p_2$ ) was the estimate of the momentum resolution. The resolution in  $\Delta P/P$  obtained for all particles was  $< 0.7\%$ . The value for the

<sup>§</sup>The  $\theta_l$  angle was defined in section 1.5.2.1. It is the angle between the positive lepton and the B meson in the dimuon mass rest frame.

mean of both Gaussians converged to zero since no bias or asymmetry was expected on the distributions.

### 5.6.2 Dimuon Mass Resolution

It was found that the dimuon mass resolution depends on the dimuon mass value. Therefore this resolution was calculated in different dimuon mass ranges. This dependence was understood to be a consequence of the momentum uncertainties.

The uncertainties of the momenta were approximately proportional to its value ( $\delta p_{x,y,z} = A |p_{x,y,z}|$ ). Figure 5.8 shows the momentum uncertainty as a function of the momentum magnitude. As the momenta uncertainties increased with the momenta magnitude it was also expected the overall dimuon mass uncertainty to increase with the dimuon mass. This parametrisation was also used to estimate the uncertainties of the  $\theta_l$  angle (section 5.6.4).

Figure 5.9 shows the obtained dimuon mass resolution integrated over the whole dimuon mass range. Note this distribution exhibits a very narrow peak and relatively long side bands. The narrow peak corresponds most to events at low dimuon mass values while the long side bands correspond to events at higher dimuon mass values.

Figure 5.10 shows the resolution of the dimuon mass as a function of the dimuon mass itself. A double Gaussian fit was performed to obtain the resolution which was given as the sigma of the core Gaussian<sup>¶</sup>. The RMS of the distribution is also shown.

The values for the core sigma obtained for  $15 \text{ GeV}^2/c^4$  and  $17 \text{ GeV}^2/c^4$  were slightly smaller than the expected. That was because of the double Gaussian shape assumed for the distribution was not appropriate at higher dimuon values. The dimuons mass squared range analysed in this chapter is  $0 - 10 \text{ GeV}^2/c^4$ .

Although the sigma and RMS values increased with the dimuon mass when compared to the values at the lowest dimuon mass range, the absolute values obtained for the sigmas were sufficiently small that they should not introduce any considerable bias into analyses performed as a function of the dimuon mass.

### 5.6.3 $\theta_l$ Resolution

As described in section 1.5.2.1 the  $\theta_l$  angle is the angle between the positive lepton and the B meson in the dimuon mass rest frame. The  $\theta_l$  angle resolution is shown in figure 5.11. The resolution distribution calculated for a particular range of  $\theta_l$  is shown as a continuous line on the top panel ( $\pi/2 < \theta_l < 2\pi/3$ ). A double Gaussian fit was performed to evaluate the resolution in different ranges of  $\theta_l$ . The resolution as a function of  $\theta_l$  is shown on the bottom panel. The average obtained for the  $\theta_l$  resolution is  $4.5 \pm 0.3 \text{ mrad}$ . No dependence on  $\theta_l$  was found.

---

<sup>¶</sup>The core Gaussian returns the smallest value of the fitted sigma.

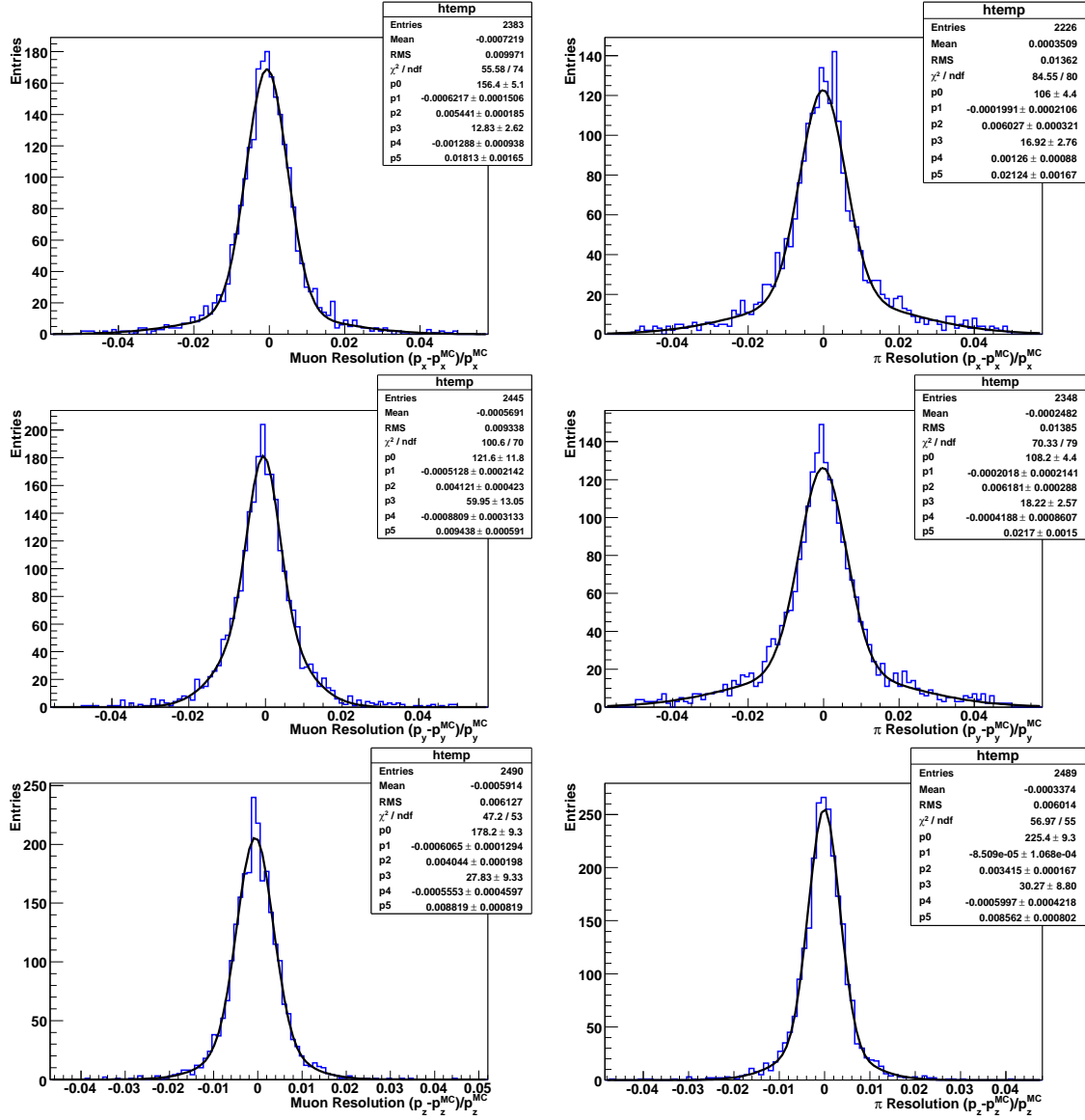


Figure 5.6: Momentum resolution of the muon and pion from  $B_d \rightarrow K^* \mu^+ \mu^-$  decay. The left-hand side column show the momentum resolutions for muons. The right-hand side column shows the momentum resolutions for pions. The fitted lines are double Gaussians. The parameters  $p_0$ ,  $p_1$  and  $p_2$  were the height, mean and sigma of the core Gaussian respectively. The parameters  $p_3$ ,  $p_4$  and  $p_5$  were the height, mean and sigma of the second Gaussian respectively.

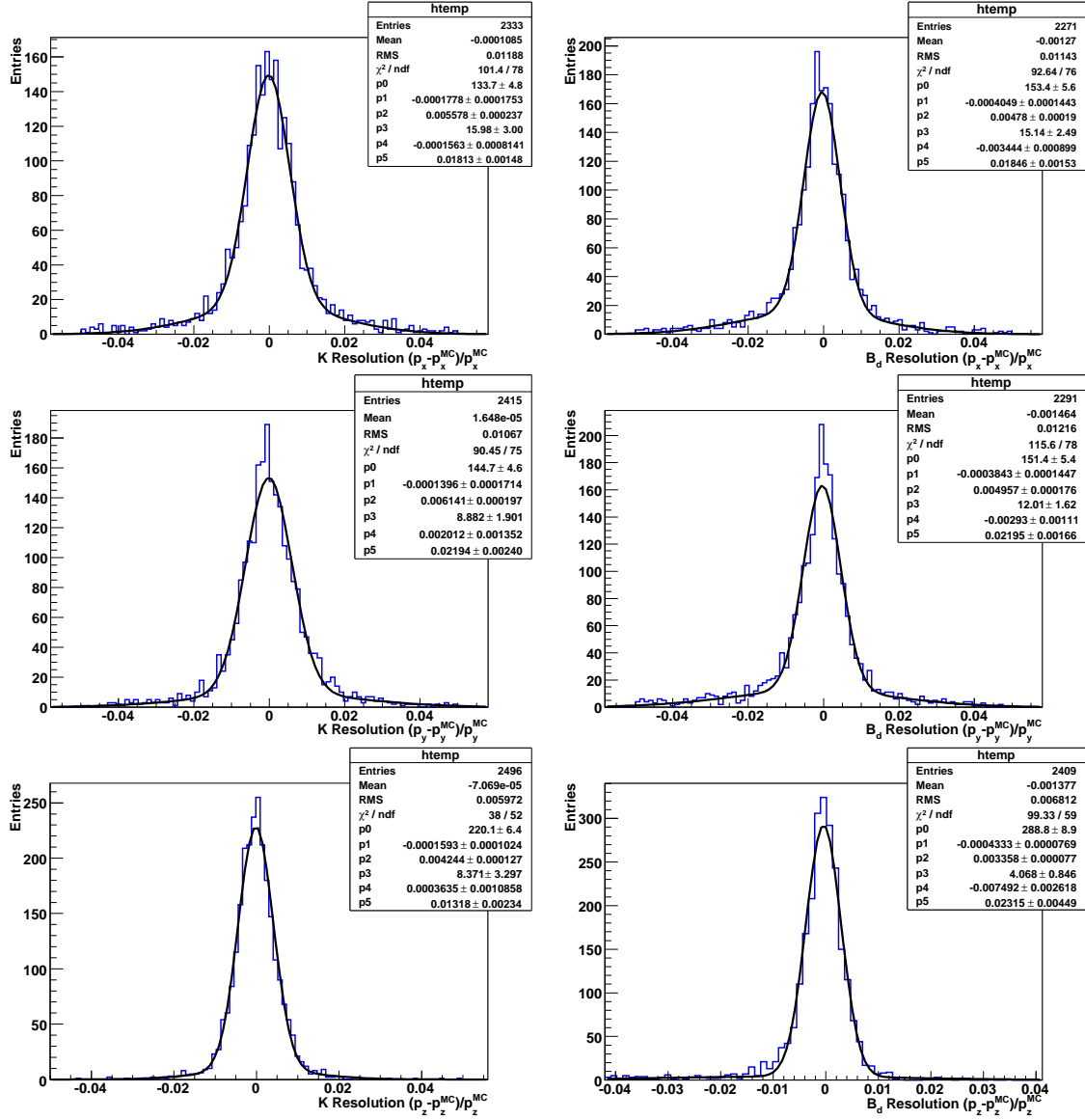


Figure 5.7: Momentum resolution of the kaon and reconstructed  $B_d$ . The left-hand side column shows the momentum resolutions for kaons. The right-hand side column shows the momentum resolutions for the reconstructed B mesons. The fitted lines are double Gaussians. The parameters  $p_0$ ,  $p_1$  and  $p_2$  were the height, mean and sigma of the core Gaussian respectively. The parameters  $p_3$ ,  $p_4$  and  $p_5$  were the height, mean and sigma of the second Gaussian respectively.

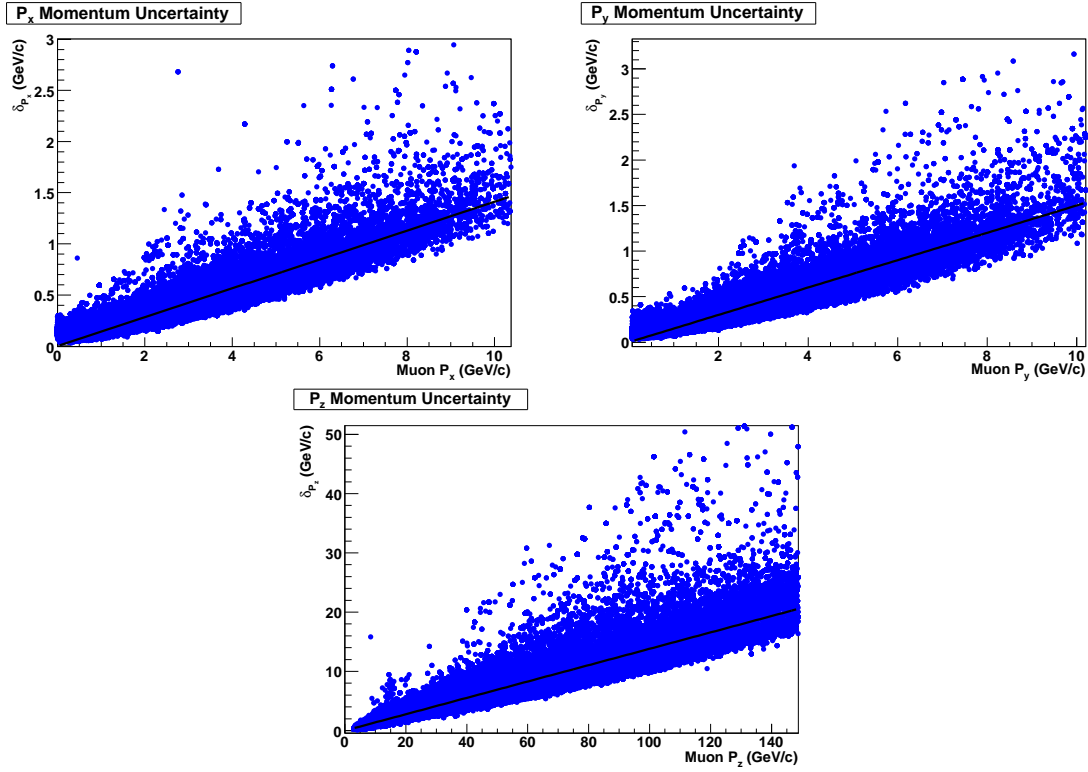


Figure 5.8: Momentum uncertainties of the muons which are products of the  $B_d \rightarrow K^* \mu^+ \mu^-$  decay. The solid line shows the uncertainty parametrisation  $\delta p_{x,y,z} = A |p_{x,y,z}|$  fit.

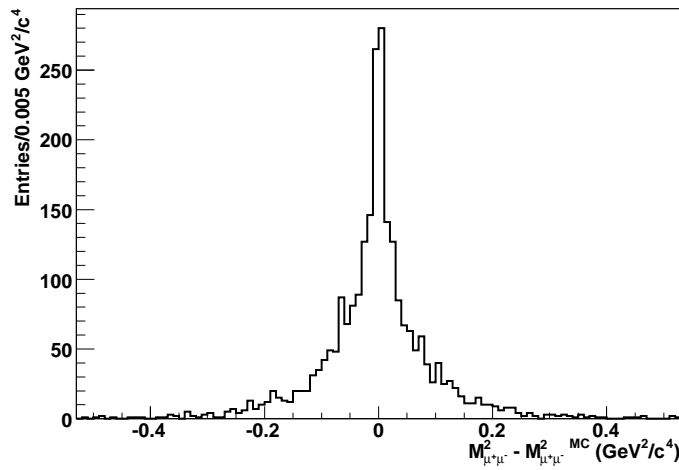


Figure 5.9: Dimuons mass squared resolution distribution.

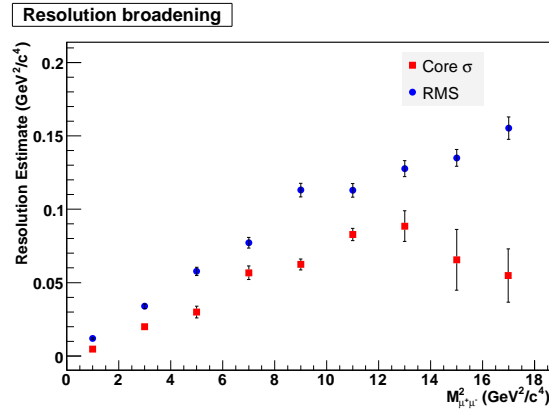


Figure 5.10: Dimuon mass resolution broadening. The red squares represent the resolution estimates and the blue dots represent the RMS of the distributions.

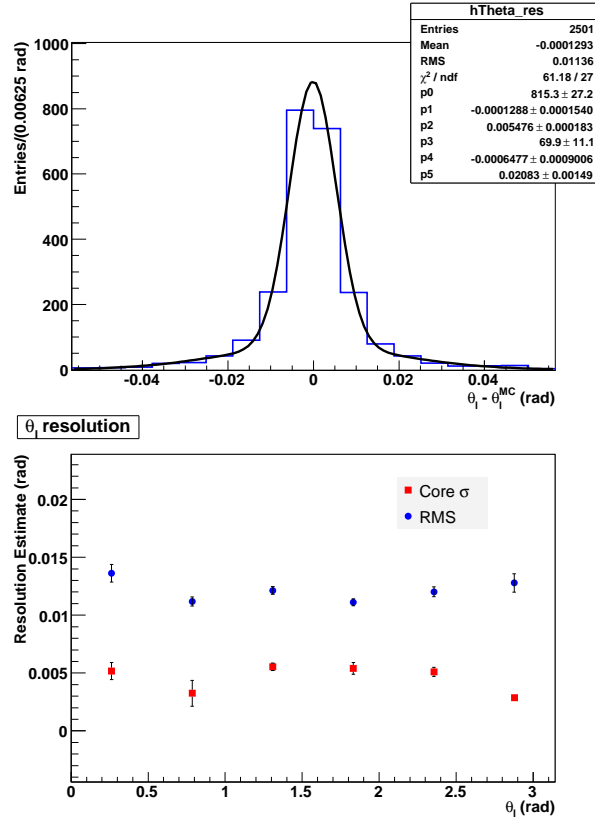


Figure 5.11:  $\theta_l$  angle resolution. The  $\theta_l$  resolution calculated for the range  $\pi/2 < \theta_l < 2\pi/3$  is shown as a continuous line on the top panel. The resolution calculated for different ranges of  $\theta_l$  is shown as a histogram on the bottom panel. The blue dots represent the RMS obtained in each range and the red squares represent the resolution obtained from the fit.



### 5.6.4 $\theta_l$ Uncertainty

The uncertainty of  $\theta_l$  was also roughly estimated using only the results from the reconstruction simulation. It was obtained by simply propagating the uncertainties of the particle's momenta. In this calculation no correlations were taken into account and the momenta uncertainties were parametrised by the expression  $\delta p_{x,y,z} = A |p_{x,y,z}|$  as discussed in section 5.6.2. This parametrisation is shown in figure 5.8. The uncertainty for the  $\theta_l$  angle obtained with this approach is shown in figure 5.12. The average uncertainty of the  $\theta_l$  angle was estimated as  $4.6 \pm 0.1$  mrad and the distribution RMS was about 1.8 mrad. This estimate is in good agreement with the resolution obtained in section 5.6.3.

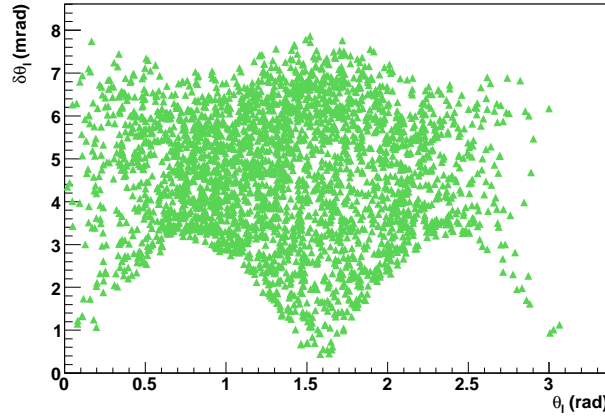


Figure 5.12:  $\theta_l$  angle uncertainty estimate. The average uncertainty obtained was  $\sim 4.6 \pm 0.1$  mrad.

Together with the dimuon mass, the  $\theta_l$  angle is an important quantity to evaluate the FBA distribution. It is important that the reconstruction of this angle is accurate as estimated. With the precise LHCb momentum measurements it is possible to reconstruct this angle in LHCb such that the FBA distribution can be determined. Section 5.7.2 discusses the LHCb sensitivity to measure the FBA of the  $B_d \rightarrow K^* \mu^+ \mu^-$  decay.

## 5.7 The Forward Backward Asymmetry in LHCb

As defined in section 1.5.2.3, the FBA is the difference between the number of forward and backward events as a function of the dimuon mass squared. Previously the FBA dependence with the dimuon mass squared was obtained by dividing the dimuon mass squared range in bins. This approach was used in the Babar and Belle analyses, reported in section 1.5.3, and also in the previous studies in LHCb described in [123, 122]. In this section an alternative approach to measure the FBA is described. This novel technique is a non-parametric unbinned method used to estimate the FBA distribution.

To develop the unbinned method a simplified MC simulation was used to generate signal events without including the detector reconstruction simulation. With this simulation a first estimate of the LHCb sensitivity to measure the FBA was obtained.

The results obtained through these studies are presented as follow. Section 5.7.1 describes the toy MC used to develop the unbinned method. Section 5.7.2 explains the implementation of the unbinned method and how it is used to calculate the FBA. The estimates obtained for the FBA and its uncertainties are presented. The effects of the detector reconstruction are presented in section 5.8. A discussion of how these effects can be taken into account in terms of acceptance corrections is presented. Section 5.9 discusses the possible effects due to the presence of background events selected as signal events. The results obtained in this subject include sensitivity degradation and systematic effects.

### 5.7.1 Simplified Monte Carlo

A toy MC simulation was used to develop the unbinned method and to calculate the uncertainties on the estimates provided. In this simplified model no detector simulation was included. This reduced the simulation time drastically and allowed the toy MC to generate the number of events necessary to perform the analysis proposed in a short period of time<sup>§</sup>.

The results from section 5.6 indicated that the dimuon mass and the  $\theta_l$  angle are determined to a high precision in LHCb. Therefore, no significant distortions on the shape of the generator level distribution of these variables are expected after the LHCb event reconstruction. This also indicates the results obtained with the toy MC should not differ significantly from what would be expected with the complete LHCb simulation.

In this analysis 100 data sets were generated. Each set contained the number of signal events equivalent to the estimated annual yield of 7k events, as obtained in section 5.4.1. Using each of these data sets it was possible to perform the analysis described in section 5.7.2. In this analysis the FBA and its zero point were estimated. The LHCb sensitivity to measure the FBA was estimated by repeating the same analysis over the 100 data sets.

### 5.7.2 Unbinned Method

This section describes the unbinned method developed to obtain the FBA distribution in the  $B_d \rightarrow K^* \mu^+ \mu^-$  analysis. To calculate the FBA it was necessary: to evaluate which events were forward or backward; to obtain the dimuon mass squared distribution for the forward and backward events; and to use the obtained distributions to evaluate the FBA according to equation 5.5.

---

<sup>§</sup>The time necessary to generate a single event with the complete LHCb simulation is  $\sim 70$  s. This time is mostly consumed by the LHCb reconstruction simulation.

The FBA distribution is given by:

$$\text{FBA}(M_{\mu^+ \mu^-}^2) = \frac{\text{Forward}(M_{\mu^+ \mu^-}^2) - \text{Backward}(M_{\mu^+ \mu^-}^2)}{\text{Forward}(M_{\mu^+ \mu^-}^2) + \text{Backward}(M_{\mu^+ \mu^-}^2)}, \quad (5.5)$$

where Forward (Backward) is the differential number of forward (backward) events<sup>¶</sup>.

The following sections describe the nonparametric unbinned method developed to measure the FBA. Section 5.7.2.1 introduces the unbinned method and its features. Section 5.7.2.2 discusses the convergence of the method applied to the dimuon mass and FBA distributions. Sections 5.7.2.3 and 5.7.2.4 explain how the unbinned method was used to analyse the  $2 \text{ fb}^{-1}$  simulated data sets and presents the results obtained.

### 5.7.2.1 Kernel Density Estimator

In this section a method to evaluate probability density functions (pdf) is introduced. This approach is a nonparametric unbinned method which does not assume a specific shape for the distribution. Such a method is very useful in cases where the distribution is unknown or difficult to parametrise with a reduced number of parameters.

The pdf is obtained by using a sequence of independent and identically distributed random events. Given a data set represented as  $x_1, x_2, x_3, \dots, x_n$  distributed according to  $f(x)$  one can estimate the pdf as:

$$f_n(x) = \frac{1}{nh} \sum_{i=1}^n K\left(\frac{x_i - x}{h}\right), \quad (5.6)$$

where  $K$  are kernel functions defined such

$$\begin{aligned} K(x) &\geq 0, \quad K(x) = K(-x), \\ \lim_{|x| \rightarrow \infty} xK(x) &= 0, \quad \int_{-\infty}^{\infty} K(x)dx = 1, \end{aligned}$$

and  $h$  is the smoothness<sup>||</sup>. Theoretical background on the convergence of this kind of estimator and further generalisations related to relaxed conditions of continuity can be found at [127, 128, 129].

The value of  $h$  depends on the total number of events used to calculate the pdfs and on the shape of the distribution itself. To obtain sensible results the value for the  $h$  parameter used must be within an acceptable range,  $h_{\min} < h < h_{\max}$ . The range of suitable  $h$  values becomes broader as the number of events used for the pdfs calculation increases. If  $h$  is outside this range two problems can occur: overfit and underfit. Overfit means that statistical

<sup>¶</sup>As defined in section 1.5.2.3, if  $0 > \theta_l < \pi/2$  ( $\pi/2 \geq \theta_l < \pi$ ) the event is classified as a forward (backward).

<sup>||</sup>The formula given by equation 5.6 can be referred to as the expression of the Kernel Density Estimator. It is also called Parzen Estimator, named after Emanuel Parzen who developed this method in [127].

fluctuations are reproduced as true features of the pdf ( $h < h_{min}$ ). Underfit ( $h > h_{max}$ ) results in the loss of information in the calculation of the distribution. Figure 5.13 illustrates the overfit and underfit effects. The red lines are the values calculated with the kernel density estimator and the blue markers represent a histogram estimate of the same distribution. On the left-hand side an example of the overfit effect is shown. On the right-hand side the underfit effect is shown. The bottom row of figure 5.13 shows the pdf estimate when  $h$  satisfies the constraint  $h_{min} < h < h_{max}$ .

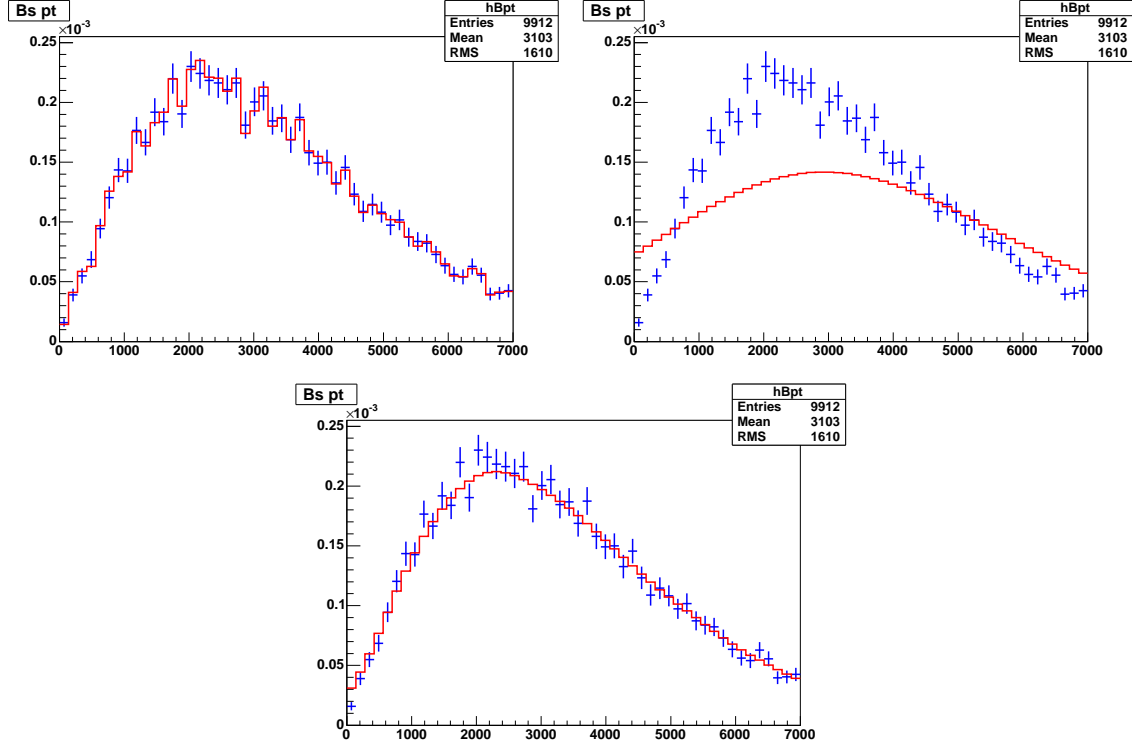


Figure 5.13: Comparison between kernel density estimator and histogram. On the top row overfit and underfit examples are shown. On the left-hand side an example of the overfit effect is shown. On the right-hand side the underfit effect is shown. The bottom row figure shows the pdf estimate using an appropriate  $h$ . Extracted from [130].

The  $h$  parameter is in general defined as a function of  $x$ . Hence, it can depend on the shape of the distribution. In cases where the distributions have regions with narrow peaks or steep gradients the appropriate  $h$  values to use are smaller than those used in the distribution's tails.

Note the role of the  $h$  parameter is similar to the bin width when using histograms. Overfit and underfit also occur with histograms if the bin width is not appropriate. With histograms the bin width can be reduced as the number of events increases. The bin width choice is also constrained by the shape of the distribution as is the  $h$  parameter: the bins used to describe sharp peaks are in general smaller than those used in the distribution's tails.

The advantages of the unbinned method are: it provides better access to the distribution's shape; it converges to the true distribution with less (or at worst the same) number of events as with histograms. As a consequence of these features the FBA zero point calculation needs no further model-dependent fit or parametrisation. In the previous LHCb analyses the FBA zero point was obtained by fitting polynomials to a binned distribution. The determination of the zero point provided by these fits depends on the dimuon mass squared range used in the fit and on the order of the polynomial.

The convergence of the kernel density estimator on the dimuon mass and FBA distribution estimate is discussed in section 5.7.2.2. The results presented were obtained with  $\sim 700k$  events in order to get a very accurate estimate of the true distributions and to reduce any dependence on the  $h$  parameter.

In the  $B_d \rightarrow K^* \mu^+ \mu^-$  analysis a Gaussian function was used as the kernel  $K$ . The criteria used to evaluate the appropriate  $h$  to be used in the analysis with limited number of events (annual yield) are discussed in section 5.7.2.3. The FBA estimate obtained with the unbinned method is presented in section 5.7.2.4.

### 5.7.2.2 Method Convergence

A set of  $\sim 700k$  events was used to evaluate the dimuon mass and FBA distributions with the unbinned method. This high number of events allowed the pdf estimate to be  $h$  independent. The results were compared with estimates obtained with histograms in order to verify the convergence of the method.

Figure 5.14 shows the comparison between the dimuon mass squared distributions calculated with the unbinned method and by using histograms. In the case of very high statistics the distributions converge to the same result.

The FBA distribution was evaluated by using the obtained dimuon mass distributions in the formula given by equation 5.5. The FBA formula was then written as

$$FBA(M_{\mu^+\mu^-}^2) = \frac{N_{forward} f_{forward}(M_{\mu^+\mu^-}^2) - N_{backward} f_{backward}(M_{\mu^+\mu^-}^2)}{N_{forward} f_{forward}(M_{\mu^+\mu^-}^2) + N_{backward} f_{backward}(M_{\mu^+\mu^-}^2)}, \quad (5.7)$$

where  $N_{forward}$  ( $N_{backward}$ ) was the total number of forward (backward) events selected and  $f_{forward}$  ( $f_{backward}$ ) was the dimuon mass squared distribution of the forward (backward) events.

Figure 5.15 shows the comparison between the FBA distribution obtained with the unbinned method and with coarse binned histograms for high statistics. Note that the unbinned method and the histogram method provided similar estimates for the FBA. However the unbinned method provided access to the complete shape of the FBA distribution and the zero point could be extracted directly from the curve obtained. In the binned method the FBA zero point is typically extracted by fitting a straight line through a number of points in this

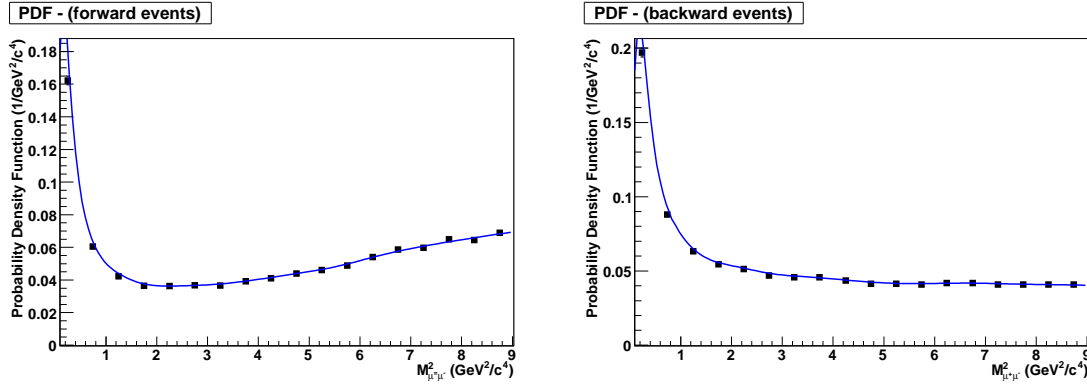


Figure 5.14: Dimuon mass squared distribution. Comparison between unbinned estimate and coarse histogram in the case of very high statistics. The curved line shows the unbinned method estimate and the black squares indicate the binned histogram estimates. On the left-hand side the distributions for the forward events are shown. On the right-hand side the distributions for the backward events are shown.

region. Hence, the binned method assumes a straight line shape, an assumption not required in the unbinned method.

### 5.7.2.3 $h$ Estimate

To evaluate the FBA with an amount of data equivalent to  $2 \text{ fb}^{-1}$  it was necessary to estimate the appropriate  $h$  value to be used. This section discusses the procedures used to estimate the  $h$  parameter as a function of the dimuon mass squared.

The  $h$  parameter was roughly estimated through a  $\chi^2$  approach. The basic idea of this estimate was to compare the calculated pdf obtained with the unbinned method and the pdf obtained by counting events within a coarse bin. For a given value of the dimuon mass squared ( $M^2_{\mu^+\mu^-}$ ) the following  $\chi^2$  formula was used:

$$\chi^2(h, M^2_{\mu^+\mu^-}) = \sum_{j=0}^N \frac{1}{N-1} \left( \frac{f(h, M^2_{\mu^+\mu^-}) - \langle f(M^2_{\mu^+\mu^-}) \rangle}{\sigma} \right)^2, \quad (5.8)$$

where  $\langle f(M^2_{\mu^+\mu^-}) \rangle$  and  $f(h, M^2_{\mu^+\mu^-})$  are estimates of the distribution of interest and  $\sigma$  is the uncertainty of  $\langle f(M^2_{\mu^+\mu^-}) \rangle$ .

$\langle f(M^2_{\mu^+\mu^-}) \rangle$  is the pdf value obtained by counting events within a coarse bin centred at  $M^2_{\mu^+\mu^-}$ . It is defined by

$$\langle f(M^2_{\mu^+\mu^-}) \rangle = \frac{n_{events}}{n_{Total} \Delta M}, \quad (5.9)$$

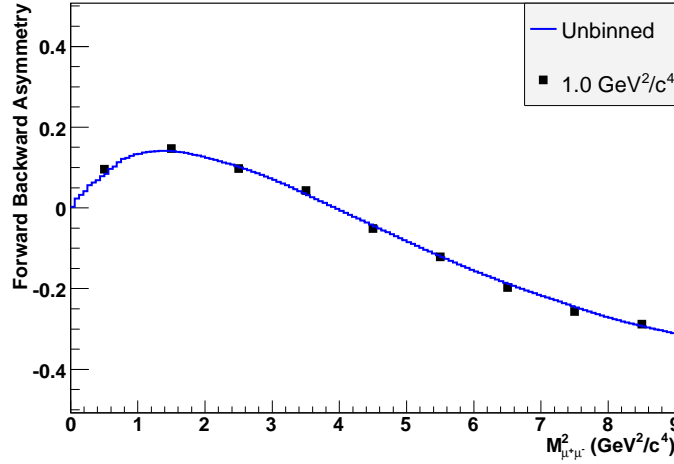


Figure 5.15: FBA distribution. Comparison between unbinned and coarse histogram estimates. The curved line shows the unbinned method estimate. The black squares indicate the binned histogram estimates at  $1 \text{ GeV}^2/\text{c}^4$  intervals.

where  $n_{events}$  is the number of events within the coarse bin,  $n_{Total}$  is the total number of events in the sample and  $\Delta M$  is the width of the coarse bin.

$f(h, M_{\mu^+\mu^-}^2)^j$  is the pdf calculated with the unbinned method for  $M_{\mu^+\mu^-}^2$  values defined within the range of the coarse bin. The  $M_{\mu^+\mu^-}^2$  values are defined by

$$M_{\mu^+\mu^-}^2{}^j = M_{\mu^+\mu^-}^2 - \Delta M \left( \frac{1}{2} - \frac{j}{N} \right). \quad (5.10)$$

The expression given by equation 5.8 is a summation which compares the value of the unbinned pdf evaluated at the different  $M_{\mu^+\mu^-}^2$  and  $\langle f \rangle$ . The  $M_{\mu^+\mu^-}^2$  values are within the range of the coarse bin. Mathematically:

$$M_{\mu^+\mu^-}^2 - \Delta M/2 < M_{\mu^+\mu^-}^2{}^j < M_{\mu^+\mu^-}^2 + \Delta M/2. \quad (5.11)$$

The values used for the bin width and sum steps in equation 5.8 were  $\Delta M = 1.25 \text{ GeV}^2/\text{c}^4$  and  $N = 15$ .

Note that equation 5.8 is not equivalent to a comparison between the average value of the pdf evaluated with the unbinned method and  $\langle f \rangle$ . Equation 5.8 was used instead of such a comparison because it provided a smooth  $\chi^2$  curve as can be seen in figure 5.16. These graphs were obtained with one data set equivalent to  $2 \text{ fb}^{-1}$ .

The  $h_{min}$  and  $h_{max}$  values were determined as the points where  $\chi^2 = 0.3$ , this is illustrated in figure 5.16. This value for the  $\chi^2$  was such that overfit and underfit could be

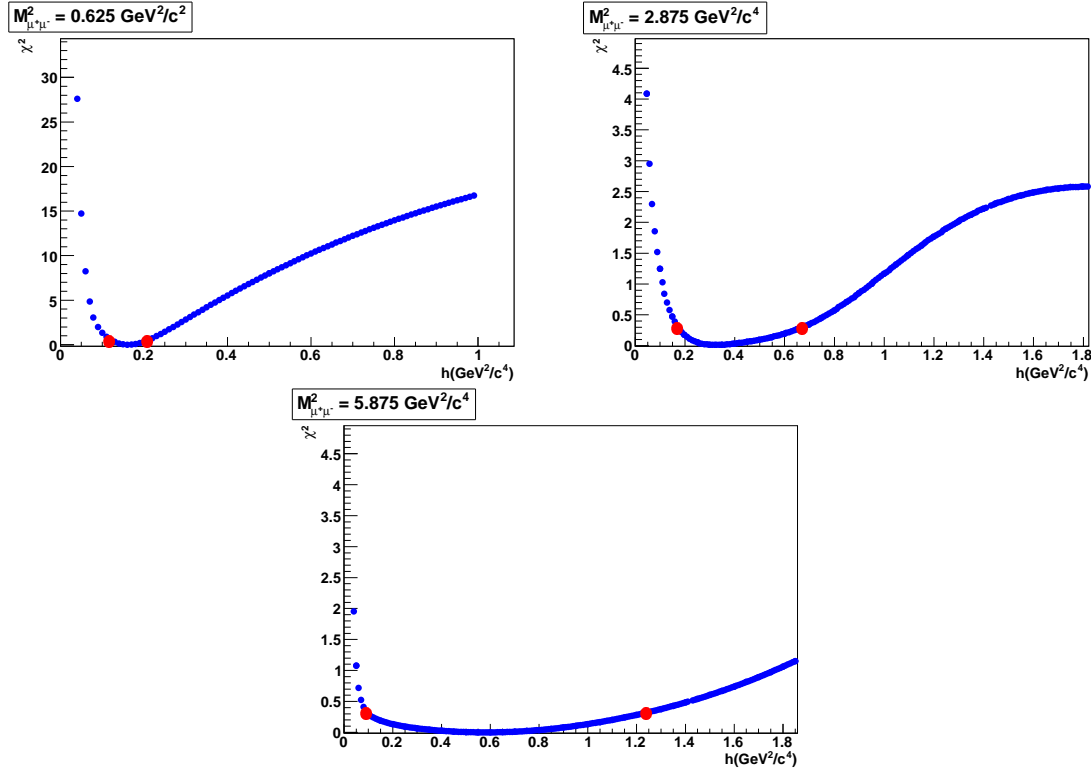


Figure 5.16:  $h$  optimisation.  $\chi^2$  distribution as a function of the  $h$  parameter at three different values of  $M^2_{\mu^+\mu^-}$ . The red dots show the points where ( $\chi^2 = 0.3$ ), which are used to determine the  $h_{min}$  and  $h_{max}$  values.

avoided. The value adopted for the  $h$  parameter was calculated as

$$h = \frac{\int_{h_{min}}^{h_{max}} h e^{-\chi^2} dh}{\int_{h_{min}}^{h_{max}} e^{-\chi^2} dh}. \quad (5.12)$$

The  $h$  parameter was obtained as a function of the  $M^2_{\mu^+\mu^-}$  by repeating this procedure for different values of  $M^2_{\mu^+\mu^-}$ . Figure 5.17 shows  $h$  as a function of  $M^2_{\mu^+\mu^-}$ . It provides a rough estimate of the  $h$  values. The values for  $h$  did not vary significantly along the  $M^2_{\mu^+\mu^-}$  axis. However small values of  $h$  had to be adopted at the lower  $M^2_{\mu^+\mu^-}$  since the pdf distribution was very steep at that region with a pole at zero. A 3<sup>rd</sup> order polynomial was fitted to the distribution of  $h$  as a function of  $M^2_{\mu^+\mu^-}$ . The  $h$  functions obtained were used to evaluate the FBA distribution in the following sections.

#### 5.7.2.4 FBA Estimate

In this section the results obtained for the FBA using  $2 \text{ fb}^{-1}$  simulated data sets are presented. The  $h$  functions for the forward and backward events as discussed in section 5.7.2.3 were used to evaluate the dimuon mass distributions. The FBA was estimated by using the dimuon distributions together with equation 5.7.



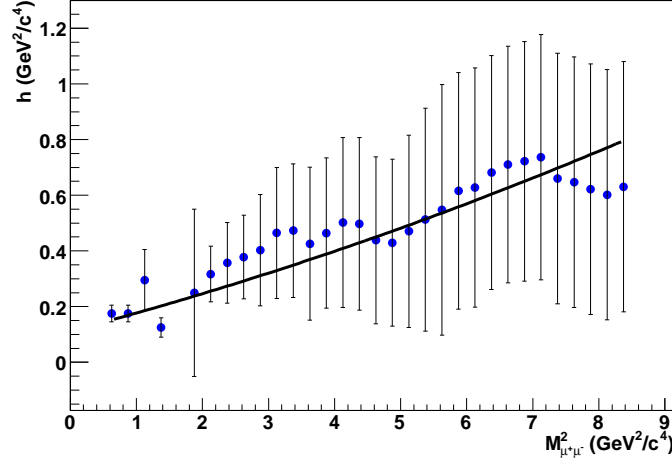


Figure 5.17:  $h$  as a function of  $M_{\mu^+\mu^-}^2$ . The blue dots indicate the optimal values of  $h$  calculated with equation 5.12. The errors indicate the  $[h_{\min}, h_{\max}]$  range. The solid line is a fit performed with a 3<sup>rd</sup> order polynomial.

Figure 5.18 shows the FBA obtained with 4 simulated data sets each equivalent to  $2 \text{ fb}^{-1}$ . The curves are compared with the expected FBA distribution calculated using 700k events as described in section 5.7.2.2.

The uncertainties shown in figure 5.18 were calculated by using a simplified toy MC. For each  $2 \text{ fb}^{-1}$  data set the obtained dimuon mass distributions were used to sample about 100 new data sets with the same number of events. The FBA distribution was then evaluated for each of these new data sets and the uncertainties were calculated as the RMS of each point of the curve. The quoted errors correspond to a  $2 \text{ fb}^{-1}$  data sample. Alternatively, estimate of the uncertainty from a single data sample could be extracted using the jackknife method [131].

The data sets from the toy MC simulation described in 5.7.1 were also used to calculate the FBA zero point sensitivity. Figure 5.19 shows the distribution of the values obtained for the zero point with all the data sets, i.e. split into  $2 \text{ fb}^{-1}$  data sets. The value obtained for the zero point was obtained through a Gaussian fit. The sigma from this fit is the estimate of the LHCb sensitivity to the measurement of the zero point. The zero point was estimated to be  $S_0 = 3.95 \pm 0.05 \text{ GeV}^2/c^4$  with a sigma of  $\sigma_{S_0} = 0.41 \pm 0.04 \text{ GeV}^2/c^4$ . The  $B_d \rightarrow K^* \mu^+ \mu^-$  decay model in the LHCb event generator was based on reference [132]. In this model the FBA zero point was estimated to be  $3.98 \pm 0.05 \text{ GeV}^2/c^4$ .

Although the total number of events per data set used to evaluate the FBA plays a major role on this measurement, the results quoted in this section are optimistic as they do not include reconstruction, selection and background effects. In the following sections those effects are discussed. Section 5.8 discusses the effects of the reconstruction of the particles

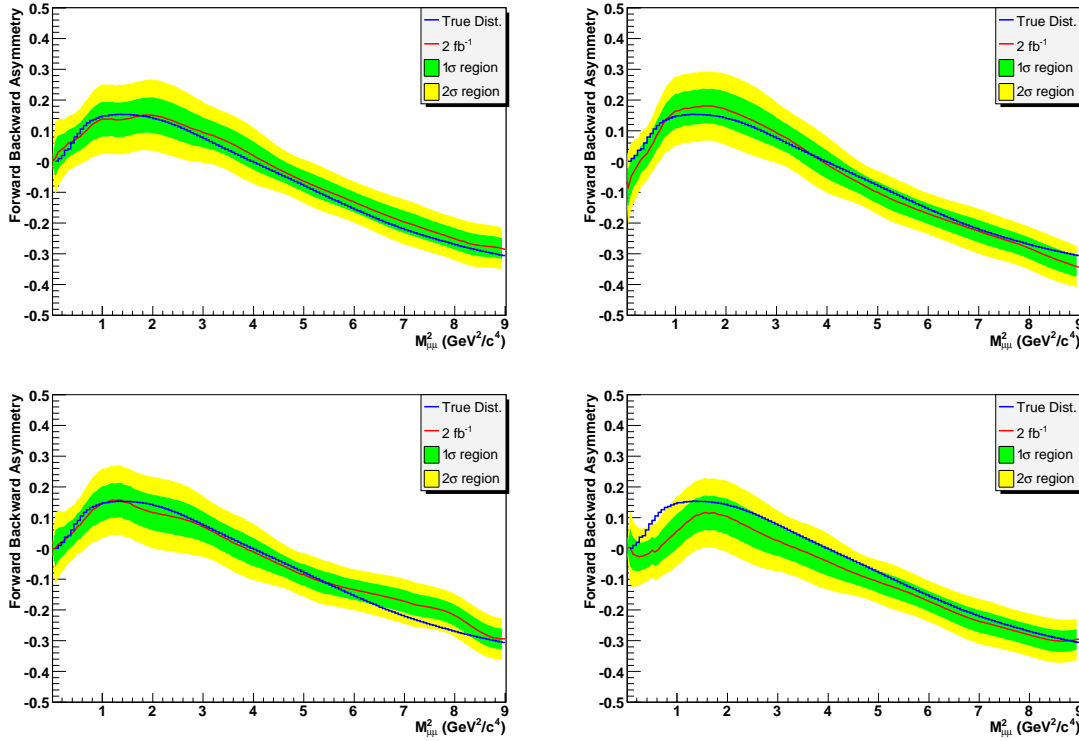


Figure 5.18: FBA obtained with  $2 \text{ fb}^{-1}$  data sets. Each graph was produced with a single data set. The red line represents the FBA calculated with a  $2 \text{ fb}^{-1}$  simulated data sample. The green and yellow areas represent  $1\sigma$  and  $2\sigma$  areas. The blue line represents the FBA as obtained in section 5.7.2.2, with large statistics.

and event selection on the FBA distribution in terms of acceptance functions. Section 5.9 evaluates the possible effects due to the presence of background events wrongly selected as signal events.

## 5.8 Acceptance Effects

One way to evaluate if the measurements of the FBA are affected by any biasing effect in LHCb is through the calculation of acceptance functions. This section presents the results of a study that was carried out to evaluate these effects by including a data set of the complete LHCb simulation in the analysis. It also describes how corrections to these effects can be applied in the unbinned FBA extraction method.

In this study an amount of  $\sim 8 \text{ fb}^{-1}$  of signal events were used. These events were generated using the complete LHCb simulation which included the detector simulation (see section 5.1). The dimuon mass and FBA distributions calculated with this data set were compared with the expected distributions shown in section 5.7.2.2 in order to evaluate any possible acceptance effects.

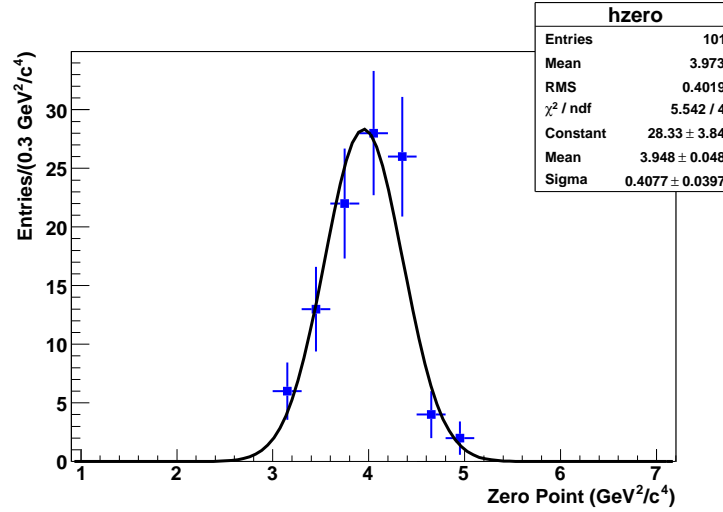


Figure 5.19: FBA zero point distribution. The FBA was estimated from 100 data samples each corresponding to  $2 \text{ fb}^{-1}$  data. A Gaussian function was fitted to the distribution in order to estimate the expected value for the zero point and sensitivity. The fit outputs are also shown in the picture.

The dimuon mass and FBA distributions could be affected in many stages of the event reconstruction and selection. These effects could be due to trigger cuts, particle identification and selection cuts. The results presented in this section mainly relate to the offline event selection. However, effects due to the cuts applied on the momenta of the muons in both trigger and particle reconstruction are also discussed.

The following sections present the results obtained in the acceptance studies. Section 5.8.1 shows the acceptance effects due to the selection cuts obtained with the complete LHCb data simulation. Section 5.8.2 describes how the muon momentum and particle identification are correlated. Section 5.8.3 shows some estimates obtained for the effects caused by the cuts on the momentum of the muons at the L0 trigger level. Section 5.8.4 discusses the results and possible strategies to evaluate the acceptance effects from LHCb data.

### 5.8.1 Selection Cuts

The complete LHCb simulation was used to evaluate if any selection cut could potentially bias the dimuon mass distribution and the FBA distribution. The approach consisted in the comparison of the distributions obtained with and without a given cut applied while the other cuts used in the selection were not altered.

The cuts used in this study were the same as listed in table 5.1. Figure 5.20 shows the FBA evaluated with the complete LHCb simulation data and the distribution obtained with the event generator. The data set was equivalent to an integrated luminosity of  $8 \text{ fb}^{-1}$ . The back solid line is the FBA obtained after applying all selection cuts and the blue dashed line

is the expected curve. The lines were in reasonable agreement but there were some regions where the difference between the curves amounted up to  $1.8 - 2\sigma$  for the results of analysing  $8 \text{ fb}^{-1}$ . The zero point was shifted from the expected position by about  $\sim 2\sigma$ . While the statistics available were not conclusive on whether there were significant biases or not it was possible to use it as a reference in the evaluation of the acceptance effects due to single cuts.

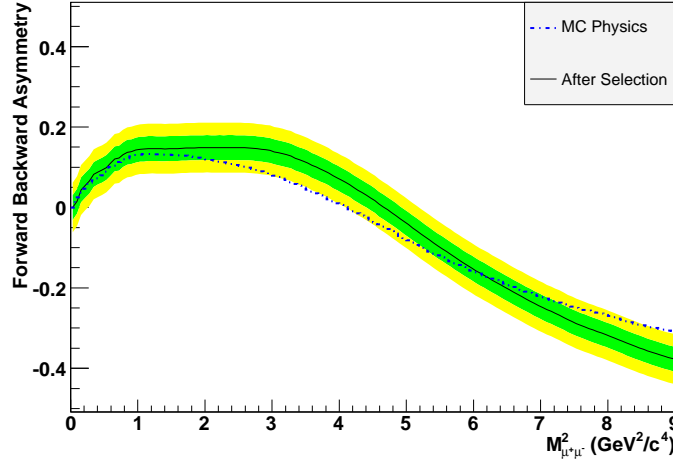


Figure 5.20: FBA distribution after selection cuts. The blue line is the expected curve and the black line is the curve obtained with the complete LHCb simulation. The green and yellow areas are the  $1\sigma$  and  $2\sigma$  regions with  $8 \text{ fb}^{-1}$ .

The comparison between distributions was performed checking the effect of each cut applied individually to the particles produced in the  $B_d \rightarrow K^* \mu^+ \mu^-$  decay. From these comparisons only the  $P_T$  cuts applied to the single muons were observed to affect the dimuon mass squared distribution. Figure 5.21 shows the ratio between the dimuon mass squared distributions before and after the  $P_T$  cuts. On the left-hand side the ratio calculated for the forward events is shown and on the right-hand side the ratio calculated for the backward events is shown. On both graphs a slope as a function of the dimuon mass squared is observed. The difference between the maximum and minimum values of the graphs are  $\sim 5 - 10\%$ .

The dimuon mass squared distributions obtained with all the selection cuts applied were then scaled with the result shown in figure 5.21 to apply an acceptance correction. The difference between the FBA obtained and the expected curve reduced to  $\sim 1.2 - 1.8\sigma$  and the zero point shift was reduced to  $\sim 1\sigma$ .

Figure 5.22 shows the ratios obtained by performing the same procedure but using the cut on  $P$  or the cut on  $IP/\sigma$ . In both cases the distributions obtained were flat and no significant effect on the FBA was observed. Similar results were obtained with cuts applied to the dimuons, kaons and pions.

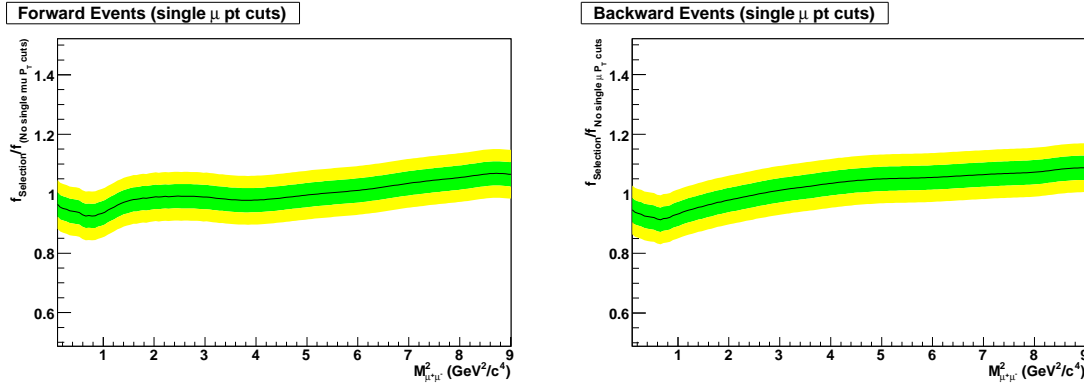


Figure 5.21: Ratio between the dimuon mass squared distribution before and after the muon  $P_T$  cut at selection level. The acceptance effect for the forward events is shown on the left-hand side and for the backward events it is shown on the right-hand side.

### 5.8.2 Muon Identification

A study of possible acceptance effects due to the muon identification was carried out as a consequence of the effect observed on single muon  $P_T$  cuts at selection level (see section 5.8.1). This section shows the result obtained by including the muon identification in the analysis.

One global variable available to control how loose or tight the muon identification could be was the so-called difference of log-likelihood for muon and pion hypotheses ( $DLL(\mu - \pi)$ ). This variable is calculated by the particle identification algorithms (see section 5.3). Figure 5.23 shows the distribution of the  $DLL$  versus  $P_T$  and their respective cuts.

The  $DLL$  and  $P_T$  variables were correlated and both cuts had similar effects on the dimuon mass squared distribution. By loosening the  $DLL$  and  $P_T$  it was possible to identify the contribution to the acceptance function, keeping the correlation between these two variables. Figure 5.24 shows the ratio between the dimuon mass squared distributions with and without the  $DLL$  and  $P_T$  cuts. The effect was similar to that observed for muon  $P_T$  in figure 5.21 but the shapes were now more pronounced. The difference between the maximum and minimum values of the graphs are  $\sim 20 - 25\%$ . The overall FBA shape after scaling the dimuon mass squared distributions with the results obtained in figure 5.24 was very similar to applying the correction derived from figure 5.21. The maximum deviations of the obtained FBA curve with respect to the expected distribution was  $\sim 1.1 - 1.8\sigma$ . The shift on the zero point was also  $\sim 1\sigma$ .

### 5.8.3 L0 Trigger

The simplified MC data set used in section 5.7.1 was also used to make a rough estimate of the possible effects of the L0 trigger  $P_T$  cuts on the acceptance. Since the momentum

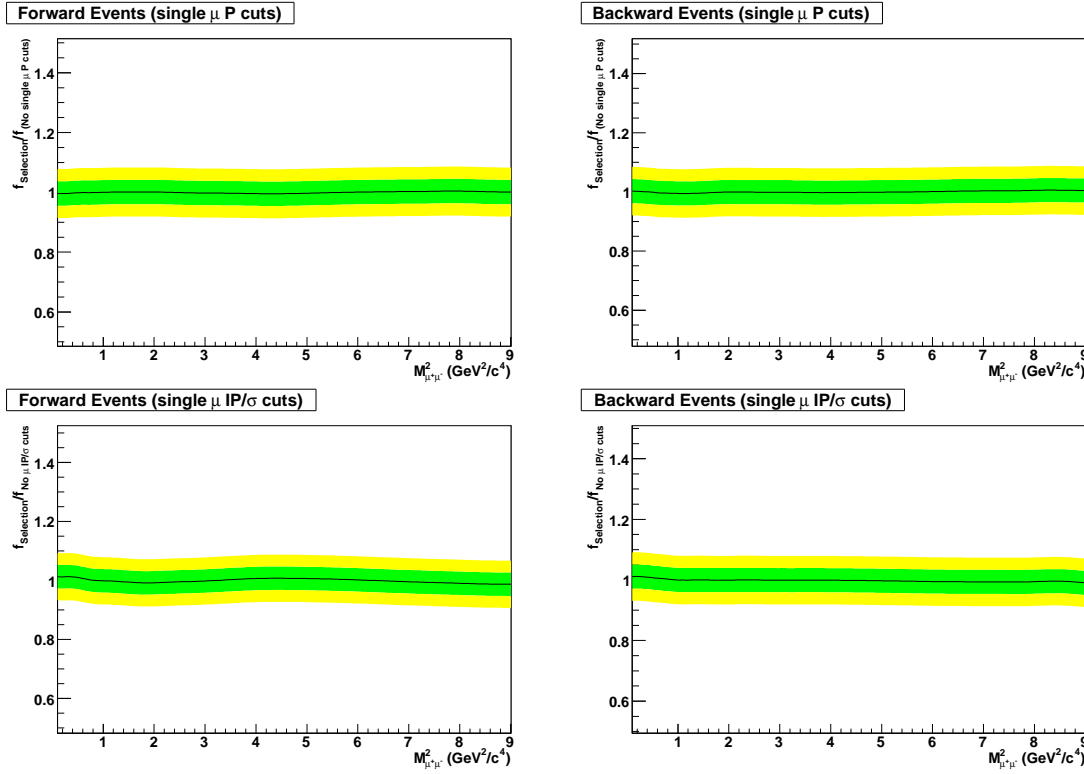


Figure 5.22: Ratio between the dimuon mass squared distribution before and after the muon  $P$  or  $IP/\sigma$  cut at selection level. The acceptance effect for the forward events is shown on the left-hand side and for the backward events it is shown on the right-hand side. No significant acceptance effect was observed.

resolution of the particles can be neglected, as shown in section 5.6, these estimates were obtained using the generator level momentum only.

Two  $P_T$  cuts were implemented in the L0 trigger. The event could either be accepted if at least one muon had  $P_T > 1.2$  GeV/c or if two muons satisfied the constraint  $P_T^{\mu_1} + P_T^{\mu_2} > 1.0$  GeV/c. Figure 5.25 shows the acceptance effect in both cases. The effect on the single muon  $P_T$  cut was similar to that observed on the offline events selection. No significant effect on the two muons cut was observed.

#### 5.8.4 Proposal for Single Muon Calibration

The acceptance results shown in sections 5.8.1, 5.8.2, 5.8.3 suggested that the major components of the acceptance effects in the FBA measured with the  $B_d \rightarrow K^* \mu^+ \mu^-$  decay were due to the cuts applied to single muons. Therefore it should be possible to evaluate these effects on the single muon distributions with LHCb data. To perform this evaluation it would be necessary to select a set of muons without using the muon identification and avoiding the use of selection cuts. Such a data set would allow the evaluation of the acceptance effects

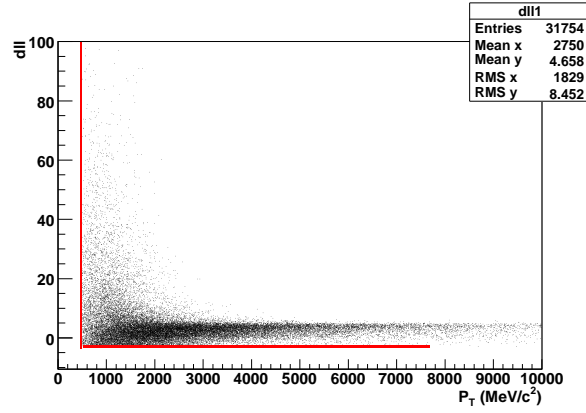


Figure 5.23: Correlation between muon  $P_T$  and  $DLL$  variables. Cut values are indicated in the figure ( $P_T > 500$  MeV/c and  $DLL > -2$ ).

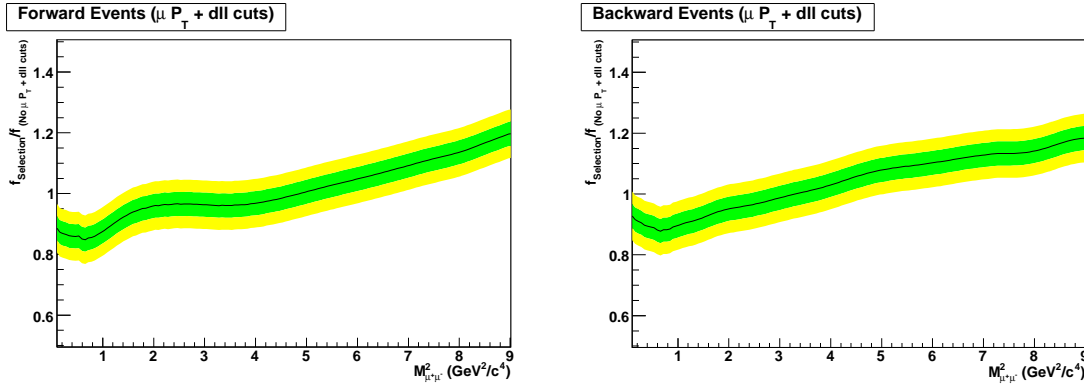


Figure 5.24: Ratio between the dimuon mass squared distribution before and after the muon  $P_T$  and  $DLL$  cuts. The acceptance effect for the forward events is shown on the left-hand side and for the backward events it is shown on the right-hand side.

on single muons and also provide information for the calibration of the LHCb MC simulation. This section suggests a strategy to select muons for this calibration based on the use of  $J/\psi \rightarrow \mu^+ \mu^-$  samples.

One way to perform the procedure of selecting muons without applying cuts would be through events with a clear signature in the detector. The proposal to select a set of muons with  $J/\psi \rightarrow \mu^+ \mu^-$  is described here. In this analysis only events selected by the L0 single muon trigger<sup>††</sup> should be used. The particle triggered in L0 should also be confirmed as a muon by the muon identification algorithm. Other cuts could also be applied to this muon. Then another particle track with opposite charge should be combined with the identified muon. In principle the charged track should not pass through any kind of particle identification or selection algorithm. If this combination of particles have a very good vertex fit and the resulting invariant mass is close to the  $J/\psi$  mass the charged particle should be selected

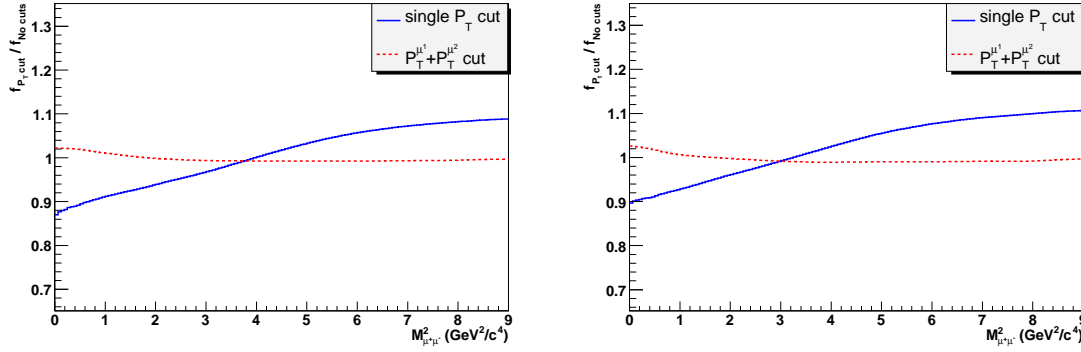


Figure 5.25: Ratio between the dimuon mass squared distribution before and after the muon  $P_T$  cuts on the L0 trigger. The blue solid (red dashed) line shows the acceptance effect due to the single (double) muon  $P_T$  cut. The acceptance effect for the forward events is shown on the left-hand side and for the backward events it is shown on the right-hand side.

as a muon.

A simplified version of this method was attempted as a proof of principle. The  $P_T$  distribution of the muons was reproduced by just loosening the muon identification and relaxing the muon cuts. Figure 5.26 shows the effect of the  $DLL$  cut on the  $P_T$  distribution of the muons on cases where the muons were obtained with a  $J/\psi \rightarrow \mu^+ \mu^-$  sample and with a  $B_d \rightarrow K^* \mu^+ \mu^-$  signal data. The  $DLL$  cut effect was significant up to 4000 MeV/c in the  $J/\psi \rightarrow \mu^+ \mu^-$  data, exactly as for the  $B_d \rightarrow K^* \mu^+ \mu^-$  data. The size of the error bars in the  $J/\psi \rightarrow \mu^+ \mu^-$  plot was due to the reduced number of events used ( $\sim 13000$  events). In the LHCb experiment a copious number of this type of event should be produced ( $\sim 10^9$  events).

However, background rejection for prompt  $J/\psi$  events produced at the primary vertex was found to be challenging. Hence, in order to reduce the contamination of the sample by pions produced in the PV the reconstructed  $J/\psi$  should be required to be displaced by a certain distance from the PV. This means only events of the type  $B \rightarrow J/\psi(\mu^+ \mu^-)X$  would be used. In terms of number of produced events in LHCb this is, for example, equivalent to  $\sim 47 \times 10^6$   $B \rightarrow J/\psi(\mu^+ \mu^-)K^*$  events per year. The total number of events of the type  $B \rightarrow J/\psi(\mu^+ \mu^-)X$  available for the analysis would be of the order of  $10^8$ .

To reduce background as much as possible very tight cuts should be applied on the triggered muon and on the reconstructed  $J/\psi$ . This would also reduce the signal selection efficiency drastically. However the number of  $B \rightarrow J/\psi \rightarrow (\mu^+ \mu^-)X$  events produced and selected in LHCb per year should be satisfactory. This number has not been calculated yet but conservative assumptions can be made to estimate the number of events available to the analysis.

This proposal offers significant advantages from the point of view of understanding the

<sup>††</sup>The event is selected with only one muon being required to have  $P_T > 1.2$  GeV/c.



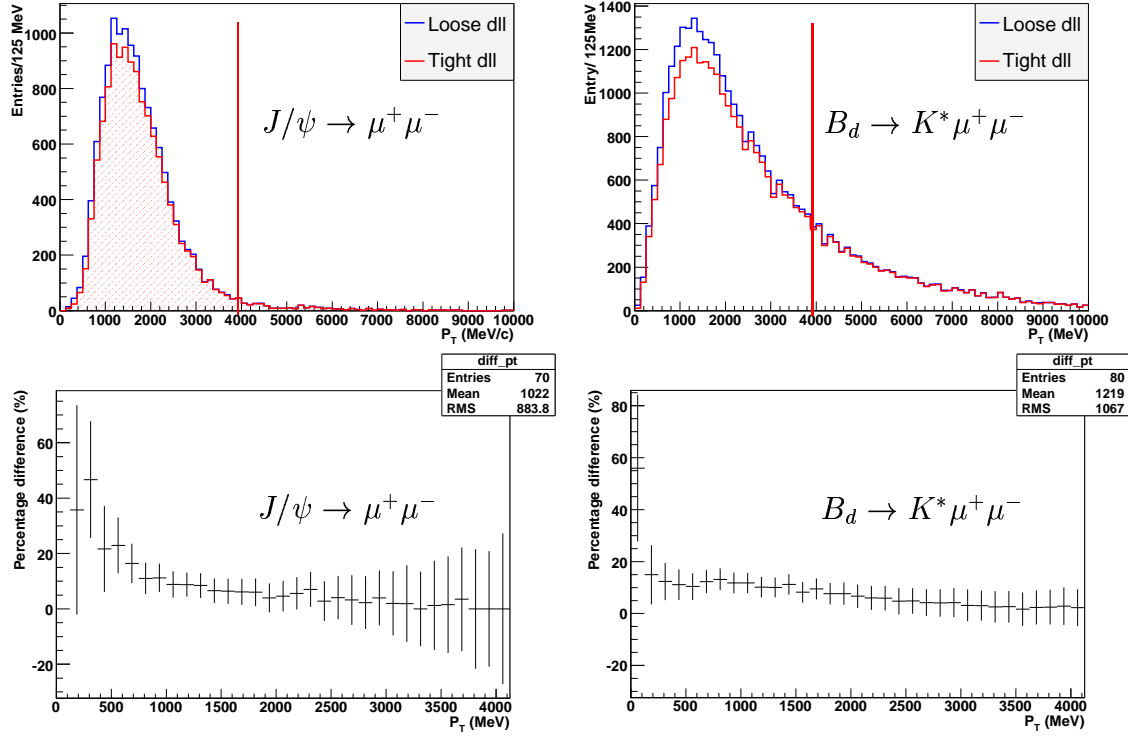


Figure 5.26: Comparison of muon  $P_T$  distributions before and after particle identification. On the top row the  $P_T$  distributions loose (blue) and tight (red) the  $DLL$  cuts are seen. The bottom row shows the percentage difference between the distributions. The left column shows the graphs obtained with the  $J/\psi \rightarrow \mu^+ \mu^-$  sample and the right column shows the graphs for  $B_d \rightarrow K^* \mu^+ \mu^-$ .

data in LHCb. However, further investigations are necessary in order to evaluate the feasibility of this calibration method. The main issue is to evaluate if it is possible to achieve suitable efficiency and S/B to perform the analysis on  $B \rightarrow J/\psi(\mu^+ \mu^-)X$ . It is also necessary to understand how to propagate the acceptance effects on the single muons to the dimuon mass distribution. A method to correctly weight the distributions on an event-by-event basis according to the  $P_T$  values of the muons would be required.

## 5.9 Background Effects

Studies were carried out to evaluate the effects of the background events in the FBA distribution measurement. These studies were performed using the unbinned method described in section 5.7.2.1. The unbinned method was adapted in order to perform the background subtraction.

The background estimates obtained with the LHCb simulation were very limited in the case of the rare  $B_d \rightarrow K^* \mu^+ \mu^-$  decay. This was because the number of simulated back-

ground events was very small when compared to the number of events expected to be produced in LHCb ( $\sim 1.7\%$  of  $2 \text{ fb}^{-1}$ )\*. Therefore the background estimates for  $2 \text{ fb}^{-1}$  were obtained by scaling the results from the background simulation within a 95% confidence level range.

In the studies performed in [122]<sup>†</sup> the total number of background events expected for  $2 \text{ fb}^{-1}$ , within the range  $0 \text{ GeV}^2/c^4 < M_{\mu^+\mu^-}^2 < 9 \text{ GeV}^2/c^4$ , was factor of  $\sim 0.3 \pm 0.09$  smaller than the number of signal events in the same  $M_{\mu^+\mu^-}^2$  range ( $\sim 1100$  events). These events were classified according to their  $\theta_l$  angle distribution. Events where the dimuon was a combination of muons coming from different decays were classified as symmetric background since they were equally distributed as forward and backward events. However, part of the background events were of the type  $b \rightarrow \mu c(\rightarrow \mu X)$  and a fraction of these were observed to be asymmetrically distributed. From the total of background events  $\sim 75\% \pm 20\%$  were classified as symmetric events and  $\sim 25\% \pm 13\%$  were classified as asymmetric. These numbers were used as input for the analysis presented in this section. A list of the numbers used in this analysis is given in table 5.3.

Table 5.3: Background event types used as input for the FBA analysis.

| Background type       | Number of events |
|-----------------------|------------------|
| Symmetric             | $827 \pm 205$    |
| Asymmetric (forward)  | $215 \pm 95$     |
| Asymmetric (backward) | $70 \pm 46$      |

Because the remaining number of background events after the selection cuts was too small it was not possible to evaluate the dimuon mass squared distribution of the forward and backward background events. Hence three different distributions were used in the analysis to evaluate the possible variations on the results. The following type of distributions were used:

- i Signal like: A  $M_{\mu^+\mu^-}^2$  distribution similar to the distribution of the signal events.
- ii Peak: A  $M_{\mu^+\mu^-}^2$  distribution with most events concentrated in the region close to the zero point of the FBA.
- iii Flat: A homogeneous distribution with events populating the distribution spectrum equally.

Figure 5.27 shows the three distributions used in the analysis.

---

\*The number of background events generated in the LHCb simulation were equivalent to  $\sim 0.1 - 10$  hours with  $\mathcal{L} = 2 \times 10^{32} \text{ cm}^{-2}\text{s}^{-1}$  depending on the data sample.

<sup>†</sup>As mentioned in section 5.7 similar results were previously obtained at [123] and recently by [124].

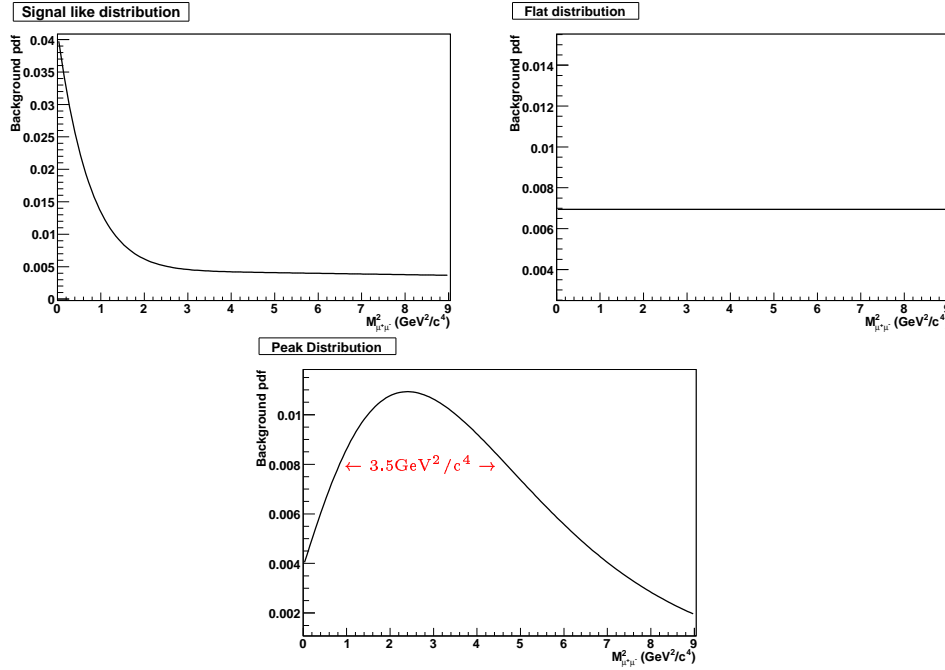


Figure 5.27: Background  $M^2_{\mu^+\mu^-}$  distributions. Three different distribution shapes were used to evaluate the background effects. The signal like distribution is shown on the left-hand side of the top row and the flat distribution is shown on the right-hand side of the top row. The peak distribution is shown in the bottom row. The width of the peak distribution is also illustrated.

### 5.9.1 Background Subtraction

The background was taken into account in the evaluation of the FBA distribution through the following expression:

$$FBA = \frac{(N_f^{total} f_f - N_f^{back} f'_f{}^{back}) - (N_b^{total} f_b - N_b^{back} f'_b{}^{back})}{(N_f^{total} f_f - N_f^{back} f'_f{}^{back}) + (N_b^{total} f_b - N_b^{back} f'_b{}^{back})}, \quad (5.13)$$

where  $N_{f(b)}^{total}$  was the total number of forward (backward) events including signal and background,  $f_{f(b)}$  was the pdf evaluated using signal and background events for forward (backward) events.  $N_{f(b)}^{back}$  was the estimated number of background and  $f'_{f(b)}{}^{back}$  was the background pdf estimated for the forward (backward) events.

By using the explicit expression of  $f$  as given by equation 5.6 the terms between brackets in expression 5.13 could be written as:

$$N^{total} f - N^{back} f'^{back} = \frac{1}{h} \sum_{i=1}^{N^{total}} K \left( \frac{M_{\mu^+\mu^-}^2{}^i - M_{\mu^+\mu^-}^2}{h} \right) - N^{back} f'^{back} \quad (5.14)$$

However, the first term on the right-hand side of equation 5.14 was broken down as:

$$\begin{aligned} \frac{1}{h} \sum_{i=1}^{N^{total}} K \left( \frac{M_{\mu^+ \mu^-}^2 - M_{\mu^+ \mu^-}^2}{h} \right) &= \frac{1}{h} \sum_{i=1}^{N^{signal}} K \left( \frac{M_{\mu^+ \mu^-}^2 - M_{\mu^+ \mu^-}^2}{h} \right) + \\ &\quad \frac{1}{h} \sum_{j=1}^{N^{back}} K \left( \frac{M_{\mu^+ \mu^-}^2 - M_{\mu^+ \mu^-}^2}{h} \right) \\ &= N^{signal} f^{signal} + N^{back} f^{back} \end{aligned}$$

and expression 5.14 became:

$$\begin{aligned} N^{total} f - N^{back} f'^{back} &= N^{signal} f^{signal} + N^{back} (f^{back} - f'^{back}) \\ &= N^{signal} f^{signal} + N^{back} \Delta f^{back} \\ &\simeq N^{signal} f^{signal}, \end{aligned} \tag{5.15}$$

since  $\Delta f^{back}$  tends to zero.

This result implies that equations 5.7 and 5.13 are statistically equivalent. Therefore, the expression given by equation 5.13 is the correct formula to obtain the FBA. The functions  $f^{back}$  and  $f'^{back}$  should cancel out in expression 5.15 because they represent the same background distribution but evaluated with different data sets.  $f^{back}$  was the background contribution to the dimuon mass squared distribution calculated with the events accepted by the selection algorithm.  $f'^{back}$  was the background distribution estimate, which in LHCb should be estimated using the so-called side bands technique. This technique relies on the estimation of the number of background events and its distributions by analysing the background events which are reconstructed with a  $B_d$  mass within a range of values adjacent to the selection band of the signal. The numbers and distributions obtained are then extrapolated to the signal band. This method was used in the  $B_d \rightarrow K^* \mu^+ \mu^-$  analyses performed by BELLE, BABAR and CDF collaborations [4, 5, 55].

The following sections describe how the extended unbinned method was used to evaluate the effects of the background on the FBA. These effects were investigated for both cases where  $f'$  was assumed to be either correctly estimated or mismeasured. These studies allowed the estimate of the precision to which the background distributions have to be determined in LHCb in order to avoid significant distortions of the FBA distribution.

## 5.9.2 Symmetric Background

To evaluate the effects of the symmetric background on the FBA, 300 sets of toy background events were generated. The number of events per set was equivalent to  $2 \text{ fb}^{-1}$ . By using these data sets it was possible to evaluate the average values of the FBA distribution and zero point sensitivity, assuming the amount of background mentioned at the start of section 5.9.

Figure 5.28 shows the effects of the symmetric background on the FBA obtained for the cases where no background subtraction was performed. The legend indicates the different dimuon mass squared distributions used. As expected, in none of the three cases was the

FBA zero point shifted. No significant deformation on the FBA distribution was observed although a small reduction of the FBA amplitude could be seen.

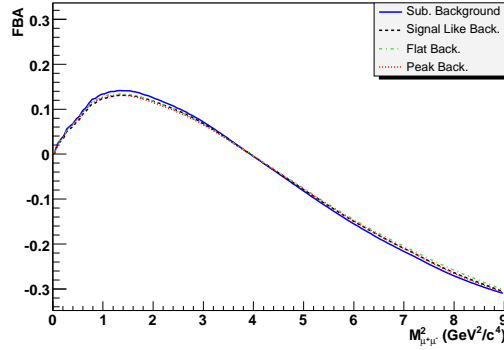


Figure 5.28: Effect on FBA due to symmetric background. Three different background distributions were assumed. The solid blue line corresponds to the FBA distribution with the background subtracted correctly. The dashed lines correspond to the FBA calculated for the three background distributions without background subtraction.

The same exercise was performed but using equation 5.13 for the background subtraction and using the possible  $f'^{back}$  distributions. As a result the sensitivity to the FBA zero point degraded when compared to the result without background ( $\sigma_{S_0} = 0.41 \text{ GeV}^2/\text{c}^4$  - see section 5.7.2.4). Figure 5.29 shows the degradation in the sensitivity on the zero point for the three different distributions. The sensitivity degradation with the signal-like distribution is shown on the left-hand side of the top row ( $0.027 \text{ GeV}^2/\text{c}^4$ ). The degradation with the flat distribution is shown on the right-hand side of the top row ( $0.031 \text{ GeV}^2/\text{c}^4$ ). On the bottom row the sensitivity degradation with the peak distribution is seen ( $0.032 \text{ GeV}^2/\text{c}^4$ ).

### Background Mismeasurement

The effects of a possible background mismeasurement of the symmetric background were evaluated. To perform these calculations only a fraction of the total background was subtracted. The FBA zero point value and sensitivity were calculated as a function of the fraction of background subtracted.

Figure 5.30 shows the FBA zero point and sensitivity as a function of the fraction of the background subtracted. No significant shift of the FBA zero point value ( $< 0.006 \text{ GeV}^2/\text{c}^4$ ) or extra degradation of the sensitivity of the zero point were observed. However the amplitude of the FBA distribution was reduced in a similar way to that shown in figure 5.28. As indicated in the figure, the three types of background distributions were used.

### Background Increase

The FBA zero point value and the degradation of the sensitivity to this were also eval-

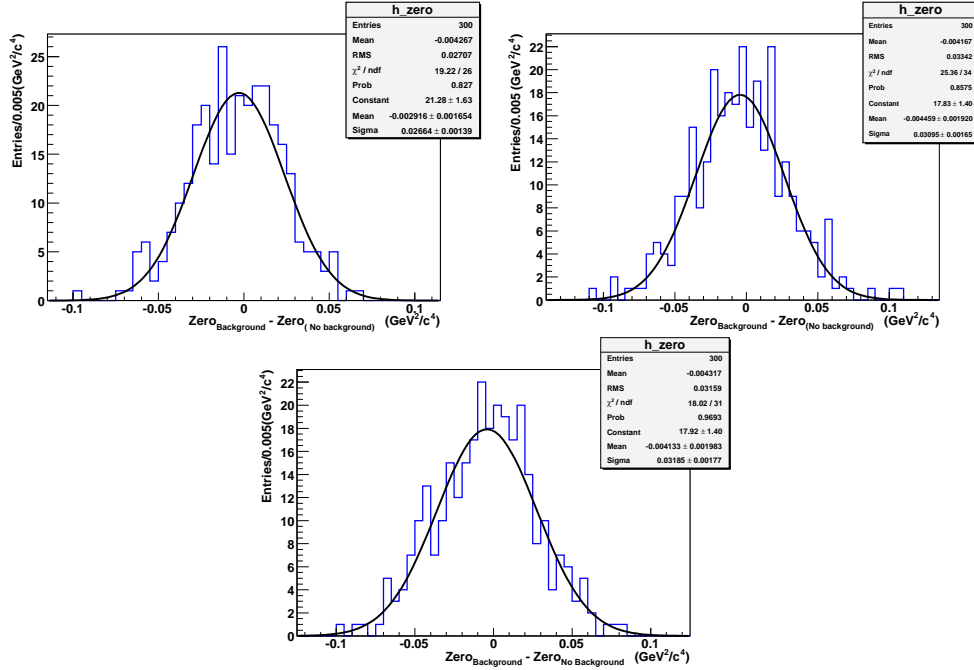


Figure 5.29: Degradation of the FBA zero point sensitivity due to the symmetric background. Further explanation is given in the text.

uated as a function of the background level. These estimates were calculated because the amount of background in the  $B_d \rightarrow K^* \mu^+ \mu^-$  channel is not well estimated yet and could potentially be higher than that estimated with the current LHCb simulation<sup>‡</sup>.

Figure 5.31 shows the FBA zero point value and the degradation of the sensitivity as the background increases. The legend in the figure indicates the background distributions used. On the left-hand side the FBA zero point as a function of the  $\sqrt{B}/S$  ratio is shown. No significant shift was observed ( $< 0.018 \text{ GeV}^2/c^4$ ). On the right-hand side the sensitivity degradation of the zero point is shown. Note the increase on  $\sigma_{\text{Zero Point}}$  was linear with  $\sqrt{B}/S$  and the slope of the curve did not depend on the background dimuon mass squared distribution.

### 5.9.3 Asymmetric Background

This section presents the results obtained with the studies of the possible effects caused by the asymmetric background on the FBA.

The degradation of the sensitivity by the asymmetric background was evaluated. It was increased by  $0.013 \text{ GeV}^2/c^4$ ,  $0.019 \text{ GeV}^2/c^4$ ,  $0.016 \text{ GeV}^2/c^4$  with the signal like, peak and flat distributions respectively. These numbers were evaluated with the correct background

<sup>‡</sup>The background estimates presented in [123, 122] were based on LHCb simulations. These numbers strongly depend on the physics models used and the simulation of the LHCb detector.

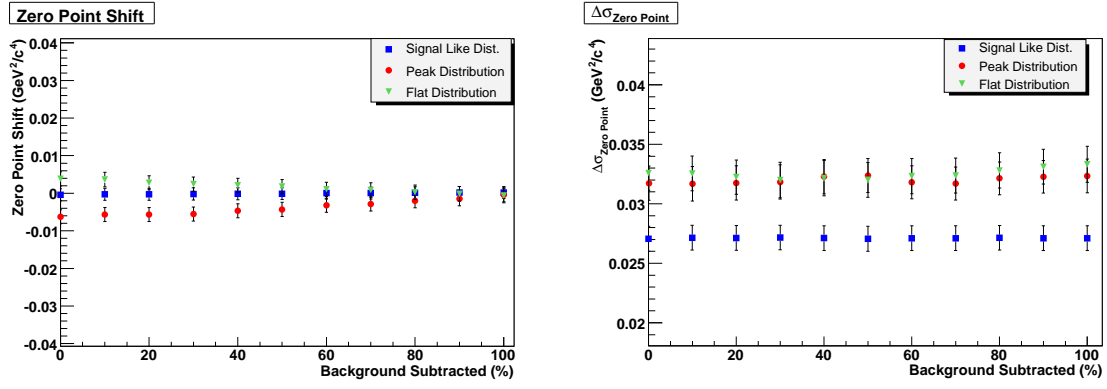


Figure 5.30: FBA zero point value and sensitivity as a function of the fraction of background subtracted. No significant variation on these quantities was observed.

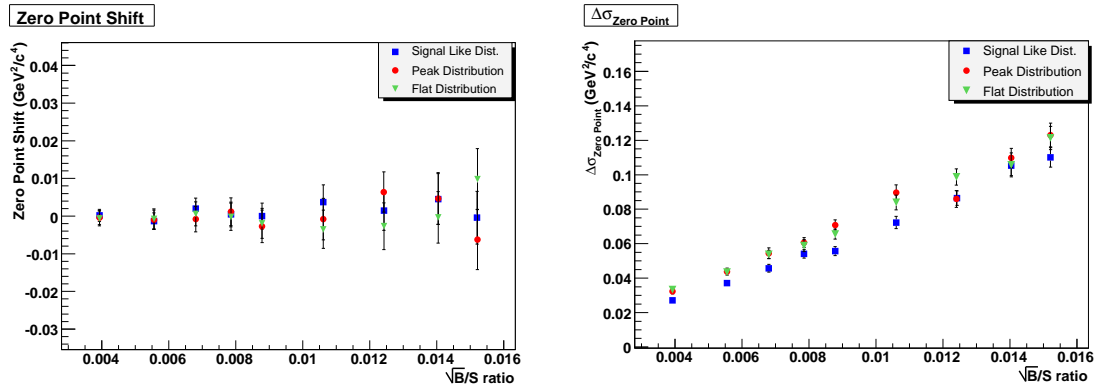


Figure 5.31: FBA zero point value and sensitivity as a function of the  $\sqrt{B}/S$  ratio. No significant shift on the FBA zero point was observed. The degradation on the sensitivity was linear with  $\sqrt{B}/S$ .

subtraction. No significant bias on the FBA zero point was observed.

Although the estimated amount of asymmetric background was small when compared to the signal and to the symmetric background its mismeasurement could significantly affect the FBA. That was because it could add extra contribution to the FBA distribution and shift the FBA zero point. A study including asymmetric background mismeasurement was performed to evaluate to which precision the background has to be determined in order to avoid a significant shift of the FBA zero point.

The following procedure was implemented to evaluate the effects of the asymmetric background mismeasurement on the FBA distribution:

- The background mismeasurement was introduced in  $f'^{back}$  as it represented the background knowledge acquired from the  $B_d$  mass side bands in the LHCb data.
- The background mismeasurement was implemented by transferring a fraction of the

asymmetric background from the forward events side to the backward events side.

- The number of asymmetric background events was not changed.

Figure 5.32 illustrates the procedure used to implement the asymmetric background studies. The background in the forward and backward bands are shown on the left-hand side of the diagram. The bars represent the value of the  $f$  distribution for a fixed dimuon mass value. The red region on the forward band shows the fraction of the background which was transferred from the forward band to the backward band to calculate the  $f'$ . The right-hand side of the diagram describes the  $f'$  distributions used with the background mismeasurement included.

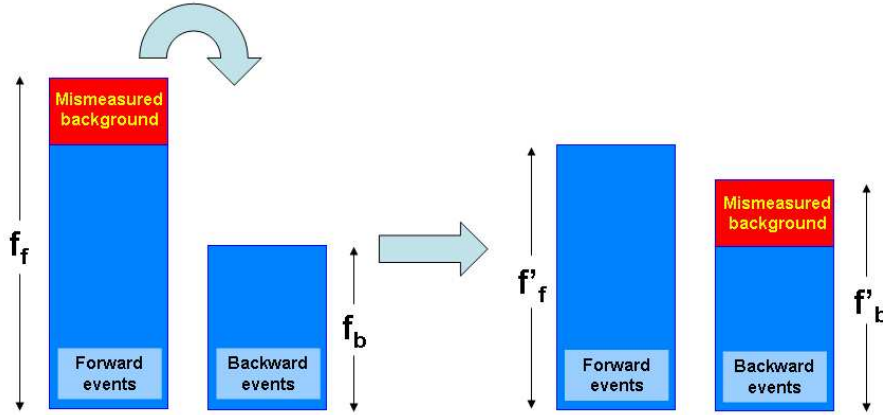


Figure 5.32: Diagram illustrating the asymmetric background mismeasurement algorithm. The algorithm is explained with more detail in the text.

This procedure was performed using the three distributions described at the introduction of section 5.9. The same distribution was used for the forward and backward events. Only the number of events in each of these bands was different. Figure 5.33 shows the shift of the FBA zero point due to the mismeasurement of the asymmetric background. The  $x$  axis of the graph represents the fraction of the total asymmetric background which was transferred from the forward band to the backward band. The  $y$  axis represents the FBA zero point shift. The shift effect could be significant with any of the background distributions depending on the mismeasurement fraction. It could be dominant with fractions above  $\sim 50\%$  depending on the background distribution. The shift for the peak background distribution was  $\sim \sigma_{\text{ZeroPoint}} = 0.40 \text{ GeV}^2/c^4$  with a fraction of mismeasured background of  $\sim 50\%$ .

By comparing this fraction of the asymmetric background with the total background level it was possible to roughly set the minimum precision required on the background evaluation of the  $B_d \rightarrow K^* \mu^+ \mu^-$  decay channel. This minimum was calculated as

$$\Delta_{\text{Background}} = f_{\text{asymmetric}} \times f_{\text{mismeasured}} \quad (5.16)$$



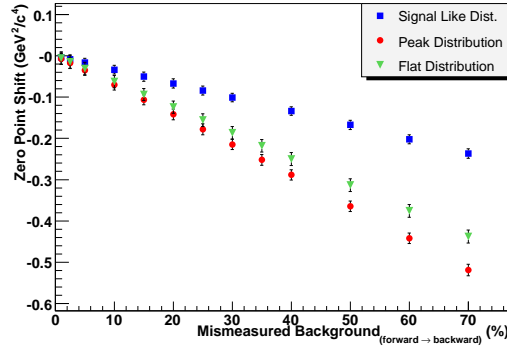


Figure 5.33: FBA zero point shift as a function of the fraction of asymmetric background mismeasured. The  $x$  axis represents the fraction of the asymmetric background transferred from the forward band to the backward band. The  $y$  axis is the FBA zero point shift.

where  $\Delta_{Background}$  is the background uncertainty,  $f_{asymmetric}$  is the fraction of the asymmetric background with respect to the total of the background and  $f_{mismeasured}$  is the fraction of mismeasured asymmetric background necessary to shift the zero point by about  $1\sigma_{Zero\ Point}$ . The result of this calculation was  $\sim 25\% \times 50\% = 12.5\%$ . Hence, in order to avoid systematic shifts on the FBA zero point measurement the background in the  $B_d \rightarrow K^* \mu^+ \mu^-$  analysis should be determined to a precision better than 12.5%.

The shape of the FBA distribution was also distorted by the mismeasurement of the asymmetric background. Figure 5.34 shows a comparison between the FBA distribution with and without the correct background subtraction. To produce these distributions an amount of 50% mismeasurement of the asymmetric background was used as input.

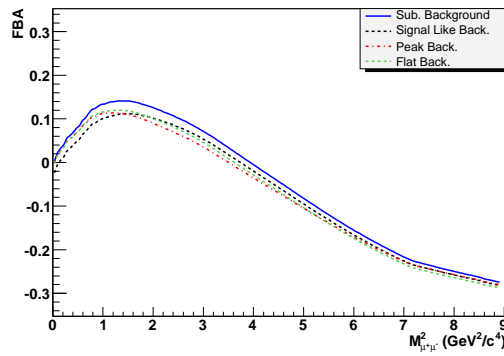


Figure 5.34: FBA comparison with and without asymmetric background subtraction. The solid blue line corresponds to the FBA distribution calculated subtracting the background correctly. The dashed lines correspond to the FBA calculated for the three types of background distribution with 50% mismeasurement.

## 5.10 Conclusions

An analysis was developed to estimate the FBA distribution of the  $B_d \rightarrow K^* \mu^+ \mu^-$  decay in LHCb. This analysis was implemented employing the LHCb data simulation. Using this simulation it was possible to estimate the signal efficiency and the total number of selected events for a given integrated luminosity. These estimates were necessary to develop a toy Monte Carlo to estimate the LHCb sensitivity to the measurement of the FBA distribution and its zero point.

The reconstructed masses of the  $K^*$  and  $B_d$  resonances were obtained using an event selection algorithm. The results on simulated data were  $\delta m_{K^*} = 0.54 \text{ MeV}/c^2$  with  $\delta \Gamma = 11.4 \text{ MeV}/c^2$  and  $\delta m_{B_d} = 0.3 \text{ MeV}/c^2$  with resolution  $\sigma = 17.74 \pm 0.22 \text{ MeV}/c^2$ . The selection efficiency and the annual yield were  $\epsilon_{\text{sel}} = 1.12 \pm 0.02\%$  and  $N_{\text{sel}}^{\text{year}} = 7.0 \pm 0.1\text{k}$ .

An investigation of the dependence of the selection efficiency and annual yield with the instantaneous luminosity was also performed. The efficiency reduced by only  $\sim 22\%$  when increasing the luminosity up to  $14 \times 10^{32} \text{ cm}^{-2} \text{ s}^{-1}$ . As a result the annual yield increase factor was estimated to be  $\sim 5$  times higher for this luminosity value. In summary the LHCb experiment could run at  $\sim 5 \times 10^{32} \text{ cm}^{-2} \text{ s}^{-1}$  selecting muonic channels without reduction of the selection efficiencies and increasing the signal yield significantly.

A study of the reconstruction resolution of the variables used to calculate the FBA was performed. The aim of this analysis was to evaluate if the LHCb measurement resolution would contribute significantly to the FBA uncertainties. As a result of this analysis the resolution of the dimuon mass squared and the  $\theta_l$  angle were found to be good and could not contribute significantly to the FBA uncertainties. The momenta resolution of the particles produced in the  $B_d \rightarrow K^* \mu^+ \mu^-$  were observed to be smaller than  $0.7\%$ . The dimuon mass squared resolution was estimated to be  $\sim 0.006 \text{ GeV}^2/c^4$  at the lower dimuon mass squared range ( $0 - 2 \text{ GeV}^2/c^4$ ) and  $\sim 0.08 \text{ GeV}^2/c^4$  at the range ( $10 - 12 \text{ GeV}^2/c^4$ ). The obtained  $\theta_l$  resolution was  $4.5 \pm 0.3 \text{ mrad}$ .

A non-parametric unbinned method was developed to evaluate the FBA distribution. The unbinned method provided access to the dimuon mass squared distributions and to the FBA distribution as continuous curves. A toy Monte Carlo simulation was used to evaluate the LHCb sensitivity to measure the FBA distribution. The FBA zero point sensitivity obtained was  $\sigma_{S_0} = 0.41 \text{ GeV}^2/c^4$  for a integrated luminosity of  $2 \text{ fb}^{-1}$ .

Acceptance effects due to cuts on the  $P_T$  of the muons were studied. These effects were observed in the different stages of the particles reconstruction and selection. At the event selection these effects were solely due to the cut on the muons  $P_T$ . No acceptance effect due to other cuts was observed in the event selection level. Similar results were observed at the reconstruction level but effects due to other variables still need to be investigated. The acceptance effect on the distribution of dimuon mass squared was found to be significant. This effect was similar on both forward and backward distributions, hence, the overall ef-

fect on the FBA was partially cancelled. The FBA zero point shift was partially recovered ( $\sim 0.25 \text{ GeV}^2/c^2$ ) by weighting the dimuon mass squared distribution according to  $P_T$  acceptance. These effects would become significant after  $\sim 6 - 8 \text{ fb}^{-1}$  of data taking when the statistical uncertainties become smaller than the estimated bias on the FBA.

The effects of the background on the  $B_d \rightarrow K^* \mu^+ \mu^-$  distributions were also investigated. The direct effect of the background on the FBA was the degradation of the zero point sensitivity. A small increase on the  $\sigma_{\text{Zero Point}}$  of the order of  $8 - 10\%$  was found. No significant bias on the FBA zero point was found when the background subtraction was performed assuming the correct distributions. However a compromising effect was found if the background was assumed mismeasured in such a way that it would introduce an additional asymmetry displacing the FBA zero point. In this case the shape of the FBA distribution was also considerably affected. To avoid this effect it was estimated that the overall background distributions for the  $B_d \rightarrow K^* \mu^+ \mu^-$  decay should be determined with a precision better than  $\sim 12.5\%$  in LHCb.

## 5.11 LHCb Outlook

The results of the analysis of the  $B_d \rightarrow K^* \mu^+ \mu^-$  decay channel were presented in this chapter. It was shown that LHCb will improve significantly the understanding of this decay channel. The measurement of the FBA distribution is the most important quantity to be obtained since it allows sensitive searches for new physics effects. In this section the prospects and future improvements for the analysis of  $B_d \rightarrow K^* \mu^+ \mu^-$  decay in LHCb are discussed.

At early stages of LHCb data taking ( $\sim 1$  month) the branching ratio of the  $B_d \rightarrow K^* \mu^+ \mu^-$  decay should be determined with uncertainties better than the current measurements. An amount of  $0.5 \text{ fb}^{-1}$  data will allow the evaluation of whether or not the FBA zero point exists. In other words it will improve considerably the constraints of the  $\mathcal{C}_7$ ,  $\mathcal{C}_9$  and  $\mathcal{C}_{10}$  coefficient values. The correct sign of the coefficients might be determined at this stage, however the absolute values of the Wilson coefficients will improve with more data. At  $2 \text{ fb}^{-1}$  the measurements will be much more refined. The unbinned method can provide access to the shape of the FBA distribution without assuming any specific model. This feature is important because a direct comparison between data and theoretical models is possible and easier than performing various fits for the different models. At this level it will be feasible to directly compare the FBA zero point measurement with the expected values from the different theoretical models. Beyond  $2 \text{ fb}^{-1}$  the full angular analysis (including other angles and correlations) could be implemented and should provide its first results which will improve over the years of LHCb data taking and analysis [133]. The experimental uncertainties should be comparable to the current SM theoretical predictions after  $6 \text{ fb}^{-1}$ .

Of course it is not possible to determine which amount of data will be necessary to find new physics effects with the  $B_d \rightarrow K^* \mu^+ \mu^-$  decay measurements. However, depending

on the NP signature (if any) it is possible to estimate some rough limits. For example, in the case of NP flipping the FBA distribution with respect to SM prediction this could be quickly detected. However, this possibility was already ruled out by previous measurements from BELLE and BABAR (see figure 1.14). Another possibility is that NP is such that there is no FBA zero point. In that scenario evidence of NP effects should be found within one year of data taking ( $< 2 \text{ fb}^{-1}$ ) since LHCb can determine the FBA shape. In case NP does not change the FBA shape drastically when compared to the SM prediction, then it might be necessary to analyse  $2 - 10 \text{ fb}^{-1}$  of data to spot any NP effect by looking at the FBA distribution and its zero point [9].

The improvements on the  $B_d \rightarrow K^* \mu^+ \mu^-$  measurements due to a luminosity upgrade can be significant as demonstrated in section 5.5. However it is necessary to understand how the performance of the VELO evolves with the radiation exposure of the silicon sensors. This will determine the performance of the detector at higher luminosities. The LHCb data will help to understand the background contributions to this channel. An optimisation of the selection algorithm is necessary to reduce background and improve signal selection when analysing events with multiple primary vertices.

To perform a cleaner measurement of the dimuon mass squared and FBA asymmetry it will be necessary to improve the understanding of the acceptance effects on the  $B_d \rightarrow K^* \mu^+ \mu^-$  decay. For this the calibration proposed in section 5.8.4 can be used to understand the acceptance effects on the single muon cuts. The results can be used to compare with the MC estimates or to calibrate the simulation correctly using the LHCb data.

# Chapter 6

## Conclusions & Outlook

Scheduled to start operation in the spring of 2009 the LHC accelerator will allow the production of a copious number of  $b$ -hadrons inside the LHCb detector. This will enable precise measurements of CP violation and rare decays in the  $b$  sector. This chapter summarises the subjects discussed and results presented in this thesis. Possible future developments of the projects presented in this thesis are also discussed.

### 6.1 Summary

#### Chapter 1: Theory Review

The Standard Model of particle physics was introduced in chapter 1. The main priorities of the physics programme of the LHCb experiment were discussed. Emphasis was placed to the theory of the  $b \rightarrow s$  transitions. The phenomenology of the  $B_d \rightarrow K^* \mu^+ \mu^-$  was introduced describing the most important quantities to be measured with this channel. These quantities include the dimuon mass squared distribution and the FBA distribution. The recent experimental results on the  $B_d \rightarrow K^* \mu^+ \mu^-$  channel were given.

#### Chapter 2: The LHCb Experiment

The LHCb detector and its subsystems were described in chapter 2. A more detailed description of the Vertex Locator (VELO) system was presented: the technology of the silicon sensors and the complete VELO modules were discussed. The trigger and online systems were also described.

#### Chapter 3: A facility for long term evaluation of the LHCb Vertex Detector modules

As discussed in chapter 3 a facility to perform the reception, visual inspection and burn-in of the VELO modules was developed. The reception and visual inspection aimed to verify the physical integrity of the modules on their arrival and at the end of the burn-in tests was described. The design requirements of this facility were such that it was necessary to develop

a vacuum system, cooling system, hardware interlocks and DAQ system.

The performance of each part of the burn-in system allowed the operation and tests of the LHCb VELO modules to be executed within a time scale which matched the module's production pace. The vacuum system provided the appropriate vacuum to perform the burn-in of the modules. Pressure levels of  $\sim 5 - 10 \times 10^{-5}$  mbar within a period of 20 to 40 minutes were achieved. After long running periods, values of about  $0.5 - 1 \times 10^{-5}$  mbar were reached. The cooling system met all the mechanical requirements and was able to cool down a mounted module from 30.0 °C to -20.0 °C in about 20 minutes. The burn-in DAQ system was used to acquire data from the modules, reading out both sides of each module simultaneously. The data acquired were digitised and saved onto disk as binary files. A set of analysis scripts were later used to analyse the data. To protect the modules against malfunction two interlock units were used to monitor the temperature of the modules and the pressure inside the tank. An overheating failure or a significant pressure raise would shut down the low voltage and high voltage supplies to the module.

Based on requirements for the VELO operation it was decided that replacement modules for the VELO should be produced and tested in the burn-in system. These sensors are currently being manufactured. To improve the overall performance of the burn-in in future operation, a set of guidelines were developed. These guidelines envisaged the manufacturing and/or improvement of parts of the system in particular the cooling block and the PCB cards attached to the vacuum chamber lid. An update of the control software was also proposed.

#### **Chapter 4: VELO Modules Characterisation**

In chapter 4 the procedures used to test the modules were described and the results obtained were given. The aim of these tests was to evaluate whether or not the VELO modules would perform as expected in the LHCb experiment. The overall performance of the VELO modules was excellent. There were very few problems discovered during the burn-in testing. The testing performed in the burn-in has increased the group's confidence that the VELO detector can be successfully operated. The modules were characterised through the burn-in procedures, which included checking for: electrical problems, thermal stress, outgassing in vacuum, degradation or any damage due to the transportation of the module.

The leakage current of the sensors was measured and compared throughout the history of each module. The leakage current of the R and  $\Phi$ -sensors were investigated at the University of Liverpool, before and after the burn-in procedure at CERN. The R-sensors had a low leakage current (less than 16  $\mu$ A) and no significant increase was observed after the Glasgow burn-in procedure. However, a few  $\Phi$ -sensors showed degradation in their leakage currents during burn-in, and two  $\Phi$ -sensors were observed to have high leakage current. No correlation between the parameters obtained from the sensor's metrology and the leakage current was found. However, it was found that most of the high leakage current sensors originated from the same wafer position.

Signal to noise ratios were calculated for the modules' sensors. The values obtained were  $20.4 \pm 0.03 \pm 2.9$  for R-sensors and  $22.4 \pm 0.06 \pm 3.1$  for  $\Phi$ -sensors. These values were estimated using the signal calibration given in [112]. A list of bad channels was compiled using information from both visual inspection and noise measurements. There were 0.7% and 0.5% bad channels measured on the R and  $\Phi$ -sensors respectively. The number of bad channels was in agreement with the LHCb requirement ( $< 1\%$ ).

A test pulse analysis was performed with both n-on-n and n-on-p technologies. Most of the results obtained with both modules were broadly similar. The values of the spillover varied between 24 – 33% with uncertainties of  $\sim 3\%$  depending on the Beetle parameters used. The undershoot was estimated to be  $\sim 17\%$  for both types of sensor\*. The dependence of these quantities with the Beetle parameters was also found to be the same on both sensors. The results of this analysis will allow to change the shape of the pulse shape in order to reoptimise the ratio  $S/N$  and spillover during the detector operation (see section 6.2.1).

### Chapter 5: Analysis of the $B_d \rightarrow K^* \mu^+ \mu^-$ decay

Chapter 5 presented the analysis developed to evaluate the LHCb sensitivity to measure the FBA distribution. The main results in this chapter were calculated assuming the value obtained for the signal annual yield. A study to evaluate the LHCb performance to measure the  $B_d \rightarrow K^* \mu^+ \mu^-$  decay running at higher luminosities was performed. It was found that LHCb can run at  $\mathcal{L} = 14 \times 10^{32} \text{cm}^{-2} \text{s}^{-1}$  to select muonic channels increasing the signal yield by a factor of  $\sim 5$ . The consequences of these results on the future operation of LHCb are discussed in section 6.2.

A novel method was implemented to calculate the dimuon mass squared distribution and the FBA distribution from the  $B_d \rightarrow K^* \mu^+ \mu^-$  decay. The LHCb sensitivity to the FBA zero point with  $2 \text{ fb}^{-1}$  was estimated to be  $\sigma_{\text{ZeroPoint}} = 0.41 \text{ GeV}^2/\text{c}^4$ . Taking into account background, the sensitivity degraded to  $\sigma_{\text{ZeroPoint}} = 0.45 \text{ GeV}^2/\text{c}^4$ . Effects due to acceptance and background mismeasurement were also implemented. It was found that acceptance effects could significantly affect the dimuon mass squared distributions. However, no significant effects on the FBA distribution was found due to acceptance. The acceptance effects were observed in the different stages of the selection of the muons of the  $B_d \rightarrow K^* \mu^+ \mu^-$  decay. It was found that the background in the  $B_d \rightarrow K^* \mu^+ \mu^-$  channel should be determined with a precision better than  $\sim 13\%$  in order to avoid significant biases on the FBA distribution.

---

\*Spillover was given as the ratio between the pulse amplitude 25 ns after the peak and the peak amplitude. The undershoot was given as the ratio between the minimum of the pulse shape with respect to the baseline and the peak amplitude. Both quantities were defined in section 4.7.

## 6.2 Outlook

This section discusses the possible developments and prospects for the burn-in facility and  $B_d \rightarrow K^* \mu^+ \mu^-$  analysis presented in this thesis. Section 6.2.1 describes the relevance of the results obtained for the commissioning of the VELO system and preparation for the  $B_d \rightarrow K^* \mu^+ \mu^-$  data analysis. Section 6.2.2 describes how these projects might evolve during the first phase of data acquisition of the LHCb. Section 6.2.3 discusses the possible upgrade of the LHCb experiment depending on the outcoming results of the LHC experiments during the first data taking period.

### 6.2.1 VELO Commissioning and Physics Analysis Preparation

The LHCb detector commissioning is in its final stages and the data acquisition of physics events should now take place in 2009. The burn-in system contributed to the quality assurance of the VELO modules and provided measurements to monitor their performance during the commissioning stages of the VELO system. The results obtained in the burn-in system allowed the evaluation of the performance of the VELO modules in the LHCb environment. Some of these results have been used in the commissioning of the VELO system, for example the leakage current and depletion voltage measurements results discussed in chapter 4 are used as references for the system operation. Furthermore, the analysis developed here will be used to monitor the performance of the silicon sensors during the operation of the experiment. The bad channel monitoring and noise with voltage analyses are currently being set up for the final system. The close monitoring of the VELO system is of paramount importance both for the safety of the experiment but also to obtain the best performance from the system (e.g., by tuning the Beetle chip parameters as discussed in section 4.7).

The VELO system has already been tested and it was used recently to reconstruct first tracks induced by the LHC beam. An example event display showing the reconstructed tracks is seen in figure 6.1. Initial studies on the collected data suggest that the sensor performance is as expected from the burn-in tests and beam test results.

The performance of the VELO must be maintained as it will translate directly to the quality of the physics analysis results produced. As discussed in section 5.4 the variables used to select signal  $B_d \rightarrow K^* \mu^+ \mu^-$  events and to reject background rely upon the track impact parameters and the primary and secondary vertices reconstructed by the VELO. As demonstrated in sections 5.6 and 5.7 the signal yield and background levels are the main variables which define the quality of the measurements of the  $B_d \rightarrow K^* \mu^+ \mu^-$  decay channel in LHCb. The quantities estimated in this thesis have shown that the LHCb experiment will measure the  $B_d \rightarrow K^* \mu^+ \mu^-$  decay with great precision (see sections 5.4, 5.6). These results were obtained assuming the current knowledge of the detector systems. As a direct consequence the studies performed in section 5.6 are being extended by the Glasgow group to understand the effects of any possible VELO misalignments in the particle's reconstruction.



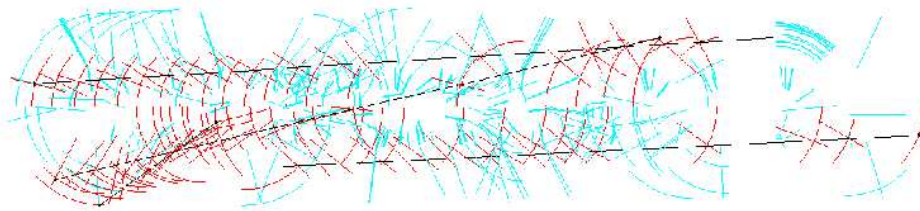


Figure 6.1: Tracks induced by the LHC beam reconstructed by the VELO detector. The particles were obtained from colliding the LHC beam with an absorber placed 300 m before the LHCb detector. Three tracks, represented by the black lines, are shown. The red crosses show the reconstructed cluster positions for clusters on the track. Extracted from [134].

### 6.2.2 First Phase of Operation

The procedures to operate the LHCb detector will be defined during the first phase of data acquisition. In this period problems such as beam accidents and radiation damage can occur damaging the silicon modules which would need replacement. As mentioned in section 6.1 the silicon sensors for the production of replacement modules are being manufactured. The burn-in system will be used to perform quality assurance of the new modules. The tests and results presented in chapter 4 will serve as a baseline to the operation of the burn-in system testing the replacement modules. The upgrades suggested for the burn-in facility in section 3.5 will allow new measurements and correlation studies between the variables monitored during the electrical tests of the modules.

The monitoring of the performance of the silicon sensors installed in the VELO is also important for the long-term future operation of the detector. As the  $S/N$  ratio estimated in section 4.4 was well above the LHCb requirements it might be possible to run the experiment at higher luminosities, as discussed in section 5.5. However, it is still necessary to understand how the  $S/N$  ratio will evolve with the cumulative radiation damage. This evaluation will be provided through the monitoring of the silicon sensors during the initial operation of the detector ( $0-2 \text{ fb}^{-1}$ ).

As discussed in section 5.11 the branching ratio of the  $B_d \rightarrow K^* \mu^+ \mu^-$  decay should be better determined than the current measurements with a month of data acquisition. The evaluation of the dimuon mass squared distribution and FBA distribution should be well determined within a few months of data acquisition. Using the unbinned method it is possible to determine the FBA zero point or to test NP models where the coefficient  $\mathcal{C}_7$  has flipped sign (no FBA zero point). These studies will be performed using the unbinned method which does not require parametrised fits. Assuming the Standard Model (SM), the LHCb sensitivity to the FBA zero point is estimated as 0.73, 0.45, 0.27  $\text{GeV}^2/\text{c}^4$  for 0.5, 2, 6  $\text{fb}^{-1}$

respectively. Systematic effects are likely to become significant at  $6\text{-}8\text{ fb}^{-1}$ . This means LHCb can potentially find signals of NP on the  $B_d \rightarrow K^* \mu^+ \mu^-$  decay channel with less than  $2\text{fb}^{-1}$ .

### 6.2.3 LHCb Replacement and Upgrade

In section 5.5 it was shown that running at higher luminosity might be feasible. For measurements of muonic channels it could be even achieved with the current detector. For hadronic channels it would be necessary a 40 MHz readout displaced vertex trigger to run at higher luminosities. However radiation hardness issues still have to be addressed for both types of event (muonic and hadronic). In the particular case of the  $B_d \rightarrow K^* \mu^+ \mu^-$ , the operation at higher luminosities would allow a significant improvement of the analysis. Sensitivities could be much improved and a multivariate angular analysis could be implemented.

In the physics analyses side the upgrade targets will be defined according to what is found in the first phase. Two main scenarios are possible and in both cases flavour physics plays a major role, therefore, the LHCb analysis of the  $B_d \rightarrow K^* \mu^+ \mu^-$  decays can make important contributions. The first scenario is if none of the LHC experiments finds NP signatures. In that case flavour physics may be the only way of probing higher mass scales. The second scenario is if NP is found during the first phase of operation in the LHC experiments. In that case flavour physics is needed to disentangle and understand the nature of the discovery. In both scenarios FCNC loop processes such as the  $B_d \rightarrow K^* \mu^+ \mu^-$  decay can be important elements of these studies. In summary LHCb, with its resolution and detector performance, is poised to measure the FBA from  $B_d \rightarrow K^* \mu^+ \mu^-$  decays and search for NP in this channel with unprecedented accuracy.

# Bibliography

- [1] A. D. Sakharov. Violation of CP invariance, C asymmetry, and baryon asymmetry of the universe. *JETP*, 5:24–27.
- [2] N. Cabibbo. Unitary Symmetry and Leptonic Decays. *Phys. Rev. Lett.*, 10:531–533, 1963.
- [3] M. Kobayashi and K. Maskawa. CP-Violation in the Renormalizable Theory of Weak Interaction. *Prog. Theor. Phys.*, 49:652, 1973.
- [4] A. Ishikawa et al. Observation of  $B \rightarrow K^* l^+ l^-$ . *Phys. Rev. Lett.*, 91, 2003.
- [5] B. Aubert et al. Measurements of branching fractions, rate asymmetries, and angular distributions in the rare decays  $B \rightarrow K l^+ l^-$  and  $B \rightarrow K^* l^+ l^-$ . *Phys. Rev. D*, 73, 2006.
- [6] A. Ali, E. Lunghi, C. Greub, and G. Hiller. Improved model-independent analysis of semileptonic and radiative rare B decays. *Phys. Rev. D*, 66(034002), 2002.
- [7] W.-M. Yao et al. 2006 Review of Particle Physics. *Journal of Physics G*, 33(1), 2006.
- [8] M. Beneke, T. Feldmann, and D. Seidel. Systematic approach to exclusive  $B \rightarrow V l^+ l^-$ ,  $V \gamma$ . *Nucl. Phys. B*, 612:25–58, 2001.
- [9] A. Ali, P. Ball, L. T. Handoko, and G. Hiller. Comparative study of the decays  $B \rightarrow K, K^* l^+ l^-$  in the Standard Model and supersymmetric theories. *Phys. Rev. D*, 61(074024), 2000.
- [10] G. Altarelli and M. W. Grunewald. Precision Electroweak Tests of the Standard Model. *Phys. Rept.*, 403-404:189–201, 2004.
- [11] J. Bluemlein. QCD Precision Tests in Deeply Inelastic Scattering. In *KEK symposium, Towards precision QCD physics*, Tsukuba, March 2007.
- [12] G. Barbagli. Model Dependent Searches for New Physics at Hera. In *Rencontres de Moriond EW 2008*, La Thuile, March 2008.

- [13] C. Quigg. *Gauge Theories of the Strong, Weak, and Electromagnetic Interactions*. Addison Wesley Pub. Co., 1983.
- [14] I. J. R. Aitchison and A. J. G. Hey. *Gauge Theories in Particle Physics : A Practical Introduction*. Adam Hilger, 1990.
- [15] S. L. Glashow. Partial-symmetries of Weak Interactions. *Nucl. Phys. B*, 22, 1961.
- [16] S. Weinberg. A Model of Leptons. *Phys. Rev. Lett.*, 19, 1967.
- [17] A. Salam. Elementary Particle Theory: Relativistic Groups and Analicity. In *Proceedings of the 8<sup>th</sup> Nobel Symposium*, Estocolmo, 1968.
- [18] M. E. Peskin and D. V. Schroeder. *An Introduction to Quantum Field Theory*. Addison-Wesley, 1995.
- [19] Y. Fukuda et al. Evidence for oscillation of atmospheric neutrinos. *Phys. Rev. Lett.*, 81:1562–1567, 1998.
- [20] P. W. Higgs. Broken symmetries, massless particlees and gauge fields. *Phys. Lett.*, 12:132–133, 1964.
- [21] S. L. Glashow, J. Iliopoulos, and L. Maiani. Weak Interactions with Lepton-Hadron Symmetry. *Phys. Rev. D*, 2.
- [22] C. S. Wu. Experimental Test of Parity Conservation in Beta Decay. *Phys. Rev.*, 105:1413–1415, 1957.
- [23] L. D. Landau. On the conservation laws in weak interactions. *Nucl. Phys. 3*, 3(127), 1957.
- [24] J. W. Cronin. CP Symmetry Violation - The search for its origin. In *Nobel lecture*. Les Prix Nobel, 1980.
- [25] A. Abashian et al. The Belle Detector. *NIM A*, 479:117, 2002.
- [26] The BABAR Collaboration. The BABAR Detector. *NIM A*, 479:1, 2002.
- [27] A. Angelopoulos et al. First direct observation of time-reversal non-invariance in the neutral-kaon system. *Phys. Lett.*, 444.
- [28] LHCb Technical Proposal. (CERN-LHCC-98-004).
- [29] L. Wolfenstein. Parametrization of the Kobayashi-Maskawa Matrix. *Phys. Rev. Lett.*, 51:1945, 1983.

- [30] A. Hocker et al. A new approach to a global fit of the CKM matrix. *Eur. Phys. J. C*, 21:225, 2001.
- [31] E. Barberio et al. Averages of b-hadron properties at the end of 2005. *hep-ex/0603003*.
- [32] J. Charles et al. CP Violation and the CKM Matrix: Assessing the Impact of Asymmetric B Factories. *Eur. Phys. J. C*, 41:1–131, 2005.
- [33] R. K. Ellis, W. J. Stirling, and B. R. Webber. *QCD and collider physics*. Cambridge University Press, 1996.
- [34] A. Abulencia et al. Observation of  $B_s^0$ - $\bar{B}_s^0$  Oscillations. *Phys. Rev. Lett.*, 97, 2006.
- [35] P. Koppenburg. Study of Rare Semileptonic B decays on LHCb. (CERN-LHCb-2002-017).
- [36] K. G. Wilson and W. Zimmermann. Operator Product Expansion and Composite Field Operators in the General Framework of Quantum Field Theory. *Commun. Math. Phys.*, 24:87, 1972.
- [37] E. Witten. Short Distance Analysis of Weak Interactions. *Nucl. Phys. B*, 122:109, 1977.
- [38] K. S. M. Lee, Z. Ligeti, I. W. Stewart, and F. J. Tackmann. Extracting short distance information from  $b \rightarrow sl^+l^-$ . *Phys. Rev. D*, 75:034016, 2007.
- [39] C. Bobeth, P. Gambino, M. Gorbahn, and U. Haisch. Complete NNLO QCD Analysis of  $B \rightarrow X_sl^+l^-$  and Higher Order Electroweak Effects. *JHEP*, 0404:71, 2004.
- [40] C. T. H. Davies et al. High-Precision Lattice QCD Confronts Experiment. *Phys. Rev. Lett.*, 92:022001, 2004.
- [41] P. Ball and R. Zwicky.  $B_{d,s} \rightarrow \rho, \omega, K^*, \phi$  decay form factors from light-cone sum rules reexamined. *Phys. Rev. D*, 71:014029, 2005.
- [42] G. Buchalla, A. J. Buras, and M. E. Lautenbacher. Weak Decays beyond Leading Logarithms. *Rev. Mod. Phys.*, 68:1125, 1996.
- [43] A. J. Buras. Flavour Dynamics: CP Violation and Rare Decays. (hep-ph/0101336), 2001.
- [44] A. Ali, G. Kramer, and G. Zhu.  $B \rightarrow K^*l^+l^-$  in soft-collinear effective theory. *Eur. Phys. J. C*, 47:625, 2006.
- [45] Y. Nir. The Physics of Heavy Flavors. In *Second CERN-Fermilab Hadron Collider Physics Summer School*, CERN, 2007.

- 
- [46] D. E. Kaplan. Particle Physics Beyond the Standard Model. In *Second CERN-Fermilab Hadron Collider Physics Summer School*, CERN, 2007.
  - [47] T. M. Aliev, C. S. Kim, and Y. G. Kim. A Systematic Analysis of the Exclusive  $B_d \rightarrow K^* \mu^+ \mu^-$  Decay. *Phys. Rev. D*, 62:014026, 2000.
  - [48] F. D. Steffen. Supersymmetric Dark Matter Candidates - The Lightest Neutralino, the Gravitino, and the Axino. (hep-ph/07111240).
  - [49] Dark Matter Portal.  
<http://lpsec.in2p3.fr/mayet/dm.php>,  
 April 2008.
  - [50] J. L. Hewett and J. D. Wells. Searching for Supersymmetry in rare  $B$  decays. *Phys. Rev. D*, 55:5549, 1997.
  - [51] M. Ciuchini, G. Degrandi, P. Gambino, and G. F. Giudice. Next-to-Leading QCD Corrections to  $B \rightarrow X_s \gamma$  in Supersymmetry. *Nucl. Phys. B*, 534:3, 1998.
  - [52] E. Lunghi, A. Masiero, I. Scimemi, and L. Silvestrini.  $B \rightarrow X_s l^+ l^-$  decays in Supersymmetry. *Nucl. Phys. B*, 568:120, 2000.
  - [53] G. Buchalla, G. Hiller, and G. Isidori. Phenomenology of non-standard  $Z^0$  couplings in inclusive semileptonic  $b \rightarrow s$  transitions. *Phys. Rev. D*, 63:014015, 2001.
  - [54] P. Ball and V. M. Braun. Exclusive Semileptonic and Rare B-Meson Decays in QCD. *Phys. Rev. D*, 58:094016, 1998.
  - [55] The CDF Collaboration. Search for the Rare Decays  $B^+ \rightarrow \mu^+ \mu^- K^+$ ,  $B_d^0 \rightarrow \mu^+ \mu^- K^*$  and  $B_s^0 \rightarrow \mu^+ \mu^- \phi$ . (CDF note 8543), 2006.
  - [56] A. Ishikawa et al. Measurement of Forward-Backward Asymmetry and Wilson Coefficients in  $B \rightarrow K^* l^+ l^-$ . *Phys. Rev. Lett.*, 96, 2006.
  - [57] Jui-Te Wei. Radiative Electroweak Penguins at Belle. In *34<sup>th</sup> International Conference on High Energy Physics*, Philadelphia, July-August 2008.
  - [58] G. Eigen. Inclusive and Exclusive  $b \rightarrow s l l$ . In *Flavor Physics & CP Violation*, Taipei, May 2008.
  - [59] The Babar Collaboration. Direct CP, Lepton Flavor and Isospin Asymmetries in the Decays  $B \rightarrow K^{(*)} l^+ l^-$ . (BaBar-PUB-08/022).
  - [60] The Large Hadron Collider.  
<http://lhc-new-homepage.web.cern.ch/lhc-new-homepage/>,  
 December 2006.
-

- [61] European Organization for Nuclear Research.  
<http://public.web.cern.ch/Public/Welcome.html>,  
December 2006.
- [62] CERN - LEP: the Z factory.  
<http://public.web.cern.ch/public/en/Research/LEP-en.html>,  
December 2006.
- [63] CERN Hadron Linacs.  
<http://linac2.home.cern.ch/linac2/>,  
February 2007.
- [64] The Proton Synchrotron Booster.  
<http://ab-dep-op-psb.web.cern.ch/ab-dep-op-psb/>,  
February 2007.
- [65] The Proton Synchrotron.  
<http://public.web.cern.ch/public/en/Research/PS-en.html>,  
February 2007.
- [66] The Super Proton Synchrotron.  
<http://public.web.cern.ch/public/en/Research/SPS-en.html>,  
February 2007.
- [67] R. Schmidt. Accelerator Physics and Technology of the LHC. (CERN-OPEN-2000-148), February 2007.
- [68] A Augusto Alves et al. The LHCb Detector at the LHC. *JINST*, 3(S08005), 2008.
- [69] G A et al. The ATLAS experiment at the CERN Large Hadron Collider. *JINST*, 3(S08003), 2008.
- [70] S Chatrchyan et al. The CMS experiment at the CERN LHC. *JINST*, 3(S08004), 2008.
- [71] K Aamodt et al. The ALICE experiment at the CERN LHC. *JINST*, 3(S08002), 2008.
- [72] Reoptimized LHCb Detector Design and Performance TDR. (CERN-LHCC-2003-030).
- [73] LHCb Technical Design Report: Vertex Locator. (CERN-LHCC-2001-011).
- [74] J. Singh. *Semiconductor Devices: An Introduction*. McGraw-Hill, 1994.
- [75] Performance of an irradiated n-on-n Hamamatsu prototype VELO detector. (CERN-LHCb-2001-039).

- [76] A. Bates. *Development of Silicon Detectors and their impact on LHCb Physics Measurements*. PhD thesis, University of Glasgow, Glasgow, Scotland, 2003.
- [77] LHCb Liverpool Home.  
<http://hep.ph.liv.ac.uk/lhcb/index.html>,  
November 2006.
- [78] The Beetle Manual Reference. (CERN-LHCb-2005-105), 2006.
- [79] LHCb Technical Design Report: RICH. (CERN-LHCC-2000-037).
- [80] T. Gys et al. First operation of a hybrid photon detector prototype with electrostatic cross-focussing and integrated silicon pixel readout. *NIM A*, 449:48–59, 2000.
- [81] LHCb Technical Design Report: Magnet. (CERN-LHCC-2000-007).
- [82] LHCb Technical Design Report: Inner Tracker. (CERN-LHCC-2002-029).
- [83] LHCb Technical Design Report: Outer Tracker. (CERN-LHCC-2001-024).
- [84] LHCb Technical Design Report: CALO. (CERN-LHCC-2000-036).
- [85] LHCb Technical Design Report: Muon System. (CERN-LHCC-2001-010).
- [86] LHCb Addendum to the Muon System Technical Design Report. (CERN-LHCC-2003-002).
- [87] LHCb Technical Design Report: Trigger System. (CERN-LHCC-2003-031).
- [88] LHCb Technical Design Report: Online System - Data Acquisition and Experiment Control. (CERN-LHCC-2001-040).
- [89] Addendum to the LHCb Online System Technical Design Report. (CERN-LHCC-2005-039).
- [90] Tell1 Specification for a common read out board for LHCb. (CERN-LHCb-2003-007).
- [91] Readout Supervisor design specifications. (CERN-LHCb-2001-012).
- [92] Test Method for Standard Microcircuitry. (MIL-STD-883F).
- [93] General Environmental Specification for STS, ELV payloads, Subsystems and Components. (GEVS-SE. Rev. A).
- [94] VELO module transport box document and operational guide. *Syracuse University note*, (SU-LHCb 2006-02-03).



- [95] Vacuum studies with a VELO module. (CERN-LHCb-2007-104).
- [96] Huber, Peter Huber Kaultemaschinenbau GmbH, Werner-von-Siemens-Strasse 1, D-77656 Offenburg, Germany. *Operating instructions for units with CC1, CC2, CC3*, 1.0 / 05 edition.
- [97] Huber webpage.  
<http://www.huber-online.com/>,  
October 2005.
- [98] C++ GUI Programming with Qt 3. ISBN 0-13-124072-2.
- [99] René Brun et al. ROOT: An Object-Oriented Data Analysis Framework, October 2005.
- [100] QTROOT - Qt Interface to ROOT.  
<http://wwwlinux.gsi.de/~go4/qtroot/html/qtroot.html>,  
December 2005.
- [101] CAREL, Via del'Industria, 11 - 35020 Brugine - Padova, Italy. *Universal Infrared Series user manual*.
- [102] BROICE, Broyce Control Ltd., Pool Street, Wolverhampton, West Midlands WV2 4HN, England. *45050 voltage relay instructions*.
- [103] Control and Monitoring of VELO and Pile-Up Level 0 Electronics. (EDMS 596194).
- [104] The LHCb Timing and Fast Control System. (CERN-LHCb-2001-016).
- [105] SPECS: the Serial Protocol for the Experiment Control System of LHCb. (CERN-LHCb-2003-004).
- [106] CERN, CERN. *Gaudi: LHCb Data Processing Applications Framework*, 9 edition.
- [107] Description of the Vetra Project and its Application for the VELO Detector. (CERN-LHCb-2008-022).
- [108] PVSS Introduction for Newcomers.  
<http://itcobe.web.cern.ch/itcobe/Services/Pvss/Documents/PvssIntro.pdf>,  
August 2006.
- [109] R. Beneyton. Controlling Front-End Electronics Boards Using Commercial Solutions. *IEEE Transactions on Nuclear Science*, 49(2):474:477.

- [110] Distribution Information Management System.  
<http://dim.web.cern.ch/dim/>,  
August 2006.
- [111] Liverpool University LHCb VELO module database.  
<http://velodb.ph.liv.ac.uk/lhcb/index.html>,  
April 2007.
- [112] Absolute calibration of Beetle1.3 test-pulse, noise and header using MIP signals from an ATLAS reference detector. (CERN-LHCb-2004-068).
- [113] O. Behrendt. The LHCb vertex locator. In *The 2007 Europhysics Conference on High Energy Physics*, Manchester, July 2007.
- [114] Pulseshape characteristics of a 300  $\mu\text{m}$  PR03 R-measuring VELO sensor read out with a beetle 1.3 chip. (CERN-LHCb-2004-068).
- [115] M. Tobin. The VELO Detector Element.  
<http://mtobin.home.cern.ch/mtobin/LHCb/VeloDet.html>,  
February 2007.
- [116] I. Belyaev et al. *Gauss: LHCb Simulation Program*. LHCb, CERN, 1 / 1.4 edition.
- [117] T. Sjostrand. PYTHIA 6.4: Physics and Manual. (hep-ph/0603175).
- [118] David J. Lange. The EvtGen particle decay simulation package. *NIMA*, 462:152–155, 2001.
- [119] G. Cooperman et al. Geant4: A simulation toolkit. *NIMA*, 3:250–303, 2003.
- [120] The BOOLE Project.  
<http://lhcb-release-area.web.cern.ch/LHCb-release-area/DOC/boole/>,  
June 2008.
- [121] The DaVinci Project.  
<http://lhcb-release-area.web.cern.ch/LHCb-release-area/DOC/davinci/>,  
June 2008.
- [122] J. Dickens et al. Selection of the decay  $B_d \rightarrow K^* \mu^+ \mu^-$  at LHCb. (CERN-LHCb-2007-038).
- [123] J. H. Lopes. Study of the rare decay  $B_d \rightarrow K^* \mu^+ \mu^-$  decay with the LHCb detector. (CERN-LHCb-2003-104).

- [124] H. Skottowe. Rare  $B_d \rightarrow K^* \mu^+ \mu^-$  decays at LHCb. In *IoP High Energy Particle Physics Conference*, Lancaster, April 2008.
- [125] The LHCb Collaboration. Expression of Interest for an LHCb Upgrade. (CERN-LHCC-2008-007).
- [126] F. Andrianala. Performance Monitoring of Gauss, The Simulation Software in LHCb. In *HEP-MAD07*, Antananarivo, September 2007.
- [127] E. Parzen. On estimation of a probability density function and mode. *Ann. Math. Statist.*, 33:1065–1076, 1962.
- [128] V. K. Murthy. Estimation of probability density. *Ann. Math. Statist.*, 36:1027–1031, 1965.
- [129] V. K. Murthy. Estimation of jumps, reliability and hazard rate. *Ann. Math. Statist.*, 36:1032–1040, 1965.
- [130] F. Marinho. Studies on Sensitivity of the  $B_s \rightarrow \mu^+ \mu^-$  decay with the reoptimized LHCb detector. Master’s thesis, IF, UFRJ, September 2005.
- [131] B. Efron. Nonparametric estimates of standard error: The jackknife, the bootstrap and other methods. *Biometrika*, 68:589–599, 1981.
- [132] A. Ali et al. A Comparative Study of the Decays  $B \rightarrow (K, K^*) l^+ l^-$  in Standard Model and Supersymmetric Theories. *Phys. Rev.*, D61(074024), 2000.
- [133] William Reece. Extracting Angular Correlations from the Rare Decay  $\bar{B}_d \rightarrow \bar{K}^* \mu^+ \mu^-$  at LHCb. (CERN-LHCb-08-021).
- [134] LHCb VELO group. First tracks reconstructed from LHC beam in the LHCb VELO. In *PSD08*, Glasgow, September 2008.